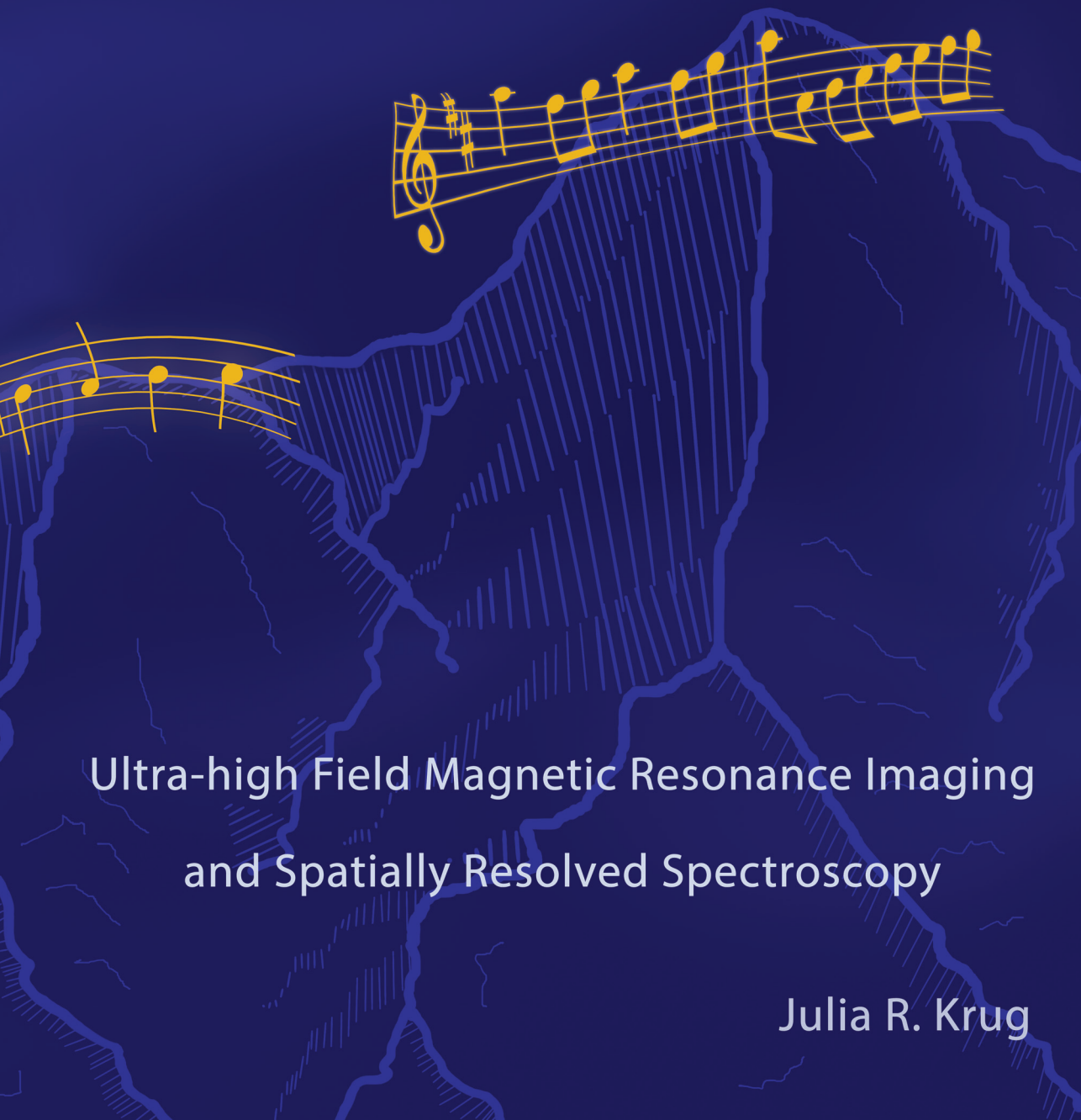


# Higher, Better, Faster!?



Ultra-high Field Magnetic Resonance Imaging  
and Spatially Resolved Spectroscopy

Julia R. Krug

# Propositions

1. Increased magnetic field strength for MRI accompanied by optimised hardware allows for increased temporal and spatial resolutions.  
(this thesis)
2. In MRI, the concept of signal-to-noise ratio per experimental acquisition time has to be expanded to include time for preparation, pre-scan adjustments and data processing.  
(this thesis)
3. In the evaluation of academic publications, authorship order has to be replaced by authorship contribution statements.
4. In the 'Doctor of Philosophy' education in Natural Sciences, the component of philosophy should be re-introduced.
5. Increasing diversity in an organisation is only effective when the associated change is embraced by the organisation itself.
6. The rationale behind a rule is more important than the rule itself.

Propositions belonging to the thesis, entitled

Higher, Better, Faster!?

Ultra-high Field Magnetic Resonance Imaging and Spatially Resolved Spectroscopy

Julia R. Krug

Wageningen, 24 April 2020



# **Higher, Better, Faster!?**

## **Ultra-high Field Magnetic Resonance Imaging and Spatially Resolved Spectroscopy**

Julia R. Krug



## **Thesis committee**

### **Promotor**

Prof. Dr A.H. Velders

Professor of BioNanoTechnology

Wageningen University and Research

### **Co-promotor**

Dr H. Van As

Associate Professor at the Laboratory of Biophysics

Wageningen University and Research

### **Other members**

Prof. Dr H.H.M. Rijnaarts, Wageningen University and Research

Prof. Dr A.P.M Kentgens, Radboud University Nijmegen

Dr L. van der Weerd, Leiden University Medical Center

Dr S. Haber-Pohlmeier, Research Centre Jülich, Germany

This research was conducted under the auspices of the Graduate School for Socio-Economic and Natural Sciences of the Environment (SENSE)

**Higher, Better, Faster!?**  
**Ultra-high Field Magnetic Resonance Imaging**  
**and Spatially Resolved Spectroscopy**

Julia R. Krug

**Thesis**

submitted in fulfilment of the requirement for the degree of doctor  
at Wageningen University  
by the authority of the Rector Magnificus,  
Prof. Dr A.P.J. Mol,  
in the presence of the  
Thesis Committee appointed by the Academic Board  
to be defended in public  
on Friday 24 April 2020  
at 4 p.m. in the Aula.

Julia R. Krug

Higher, Better, Faster!?

Ultra-high Field Magnetic Resonance Imaging and Spatially Resolved Spectroscopy

254 pages

PhD thesis, Wageningen University, Wageningen, The Netherlands (2020)

With references, with summaries in English, Dutch and German

ISBN: 978-94-6395-298-9

DOI: <https://doi.org/10.18174/512982>

# **Higher, Better, Faster!?**

## **Ultra-high Field Magnetic Resonance Imaging and Spatially Resolved Spectroscopy**

### **Content**

<b>List of Abbreviations</b>	1
<b>Chapter 1</b> General Introduction	3
Abstract	
1.1 History of Nuclear Magnetic Resonance, or NMR Explained with a Piano	
1.2 Basics of MRI and Spatially Resolved Spectroscopy	
1.3 What is Magnetic Resonance Microscopy?	
1.4 How to increase the Signal-to-Noise-Ratio in MR Microscopy?	
1.5 Other Benefits and Challenges at Ultra-high Field MRI	
1.6 Motivation and Outline of this Thesis	
1.7 References	
<b>Chapter 2</b> Assessing Spatial Resolution, Acquisition Times and Signal-to-Noise Ratios for Commercial Microimaging Systems at 14.1, 17.6 and 22.3 T	29
Abstract	
2.1 Introduction	
2.2 Experimental Methods	
2.3 Results	
2.4 Discussion	
2.5 Outlook and Conclusion	
2.6 Acknowledgements	
2.7 Supporting Information	
2.8 References	

**Chapter 3** Magnetic Resonance Microscopy using Microcoils at 22.3 T: A Method Protocol for Sample Preparation and Coil Calibration 57

Abstract

3.1 Introduction

3.2 Protocol for Microcoil and Sample Preparation

3.3 Determining Coil Characteristics

3.4 Magnetic Resonance Imaging: A Comprehensive Overview for Starting with a Readily Calibrated System

3.5 Representative Results

3.6 Discussion

3.7 Conclusion and Outlook

3.8 Acknowledgements

3.9 References

**Chapter 4** 3D Biofilm Visualisation and Quantification on Granular Bioanodes with Magnetic Resonance Imaging 87

4.0 Preamble, or How to Deal with Artefacts

4.1 Abstract

4.2 Introduction

4.3 Experimental Methods

4.4 Results

4.5 Conclusions

4.6 MRI of Bioanodes Beyond 14.1 T – A Mission Impossible?

4.7 Acknowledgements

4.8 Supporting Information

4.9 References

**Chapter 5** Magnetic Resonance Microscopy at Cellular Resolution and Localised Spectroscopy of *Medicago truncatula* at 22.3 Tesla 137

Abstract

5.1 Introduction

5.2 Experimental Methods

5.3 Results

5.4 Discussion	
5.5 Conclusion	
5.6 Acknowledgements	
5.7 Supporting Information	
5.8 References	

## **Chapter 6 CEST-MRI at (Ultra-)high Magnetic Field Systems: Analysis of Metabolite Specificity** 169

Abstract	
6.1 Introduction	
6.2 Experimental Methods	
6.3 Results	
6.4 Discussion	
6.5 Conclusion and Outlook	
6.6 Acknowledgements	
6.7 Supporting Information	
6.8 References	

## **Chapter 7 General Discussion** 199

Abstract	
7.1 Main Insights and Conclusions	
7.2 Lessons from Ultra-high Magnetic Field Strength	
7.3 Perspectives for Applications	
7.4 Perspectives for 22.3 T and Beyond	
7.5 References	

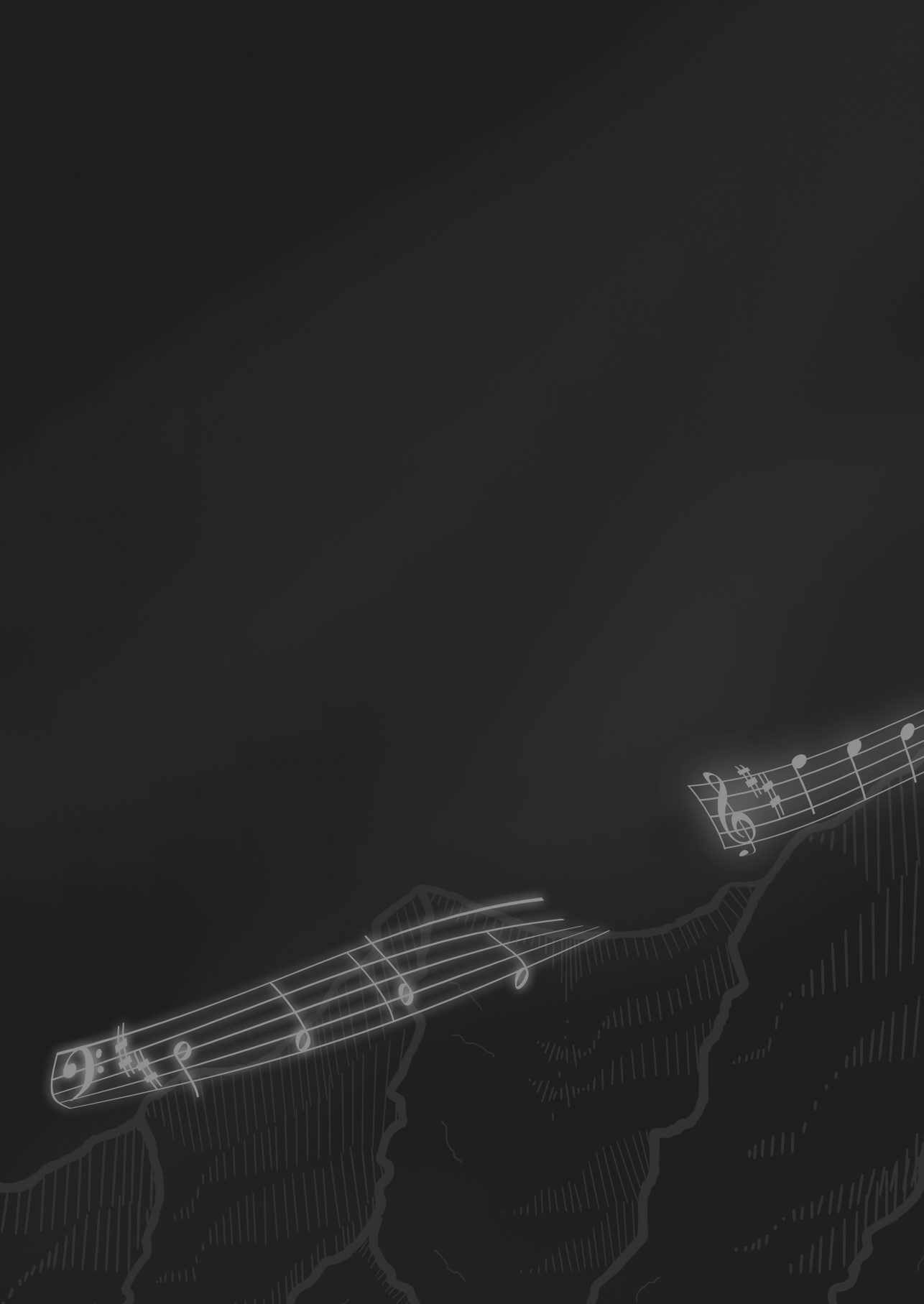
## **Summary/ Samenvatting/ Zusammenfassung** 225

## **Acknowledgements** 241

## **About the Author** 247

## **List of Publications** 249

## **Completed Training Activities** 251



*Für meine Eltern*

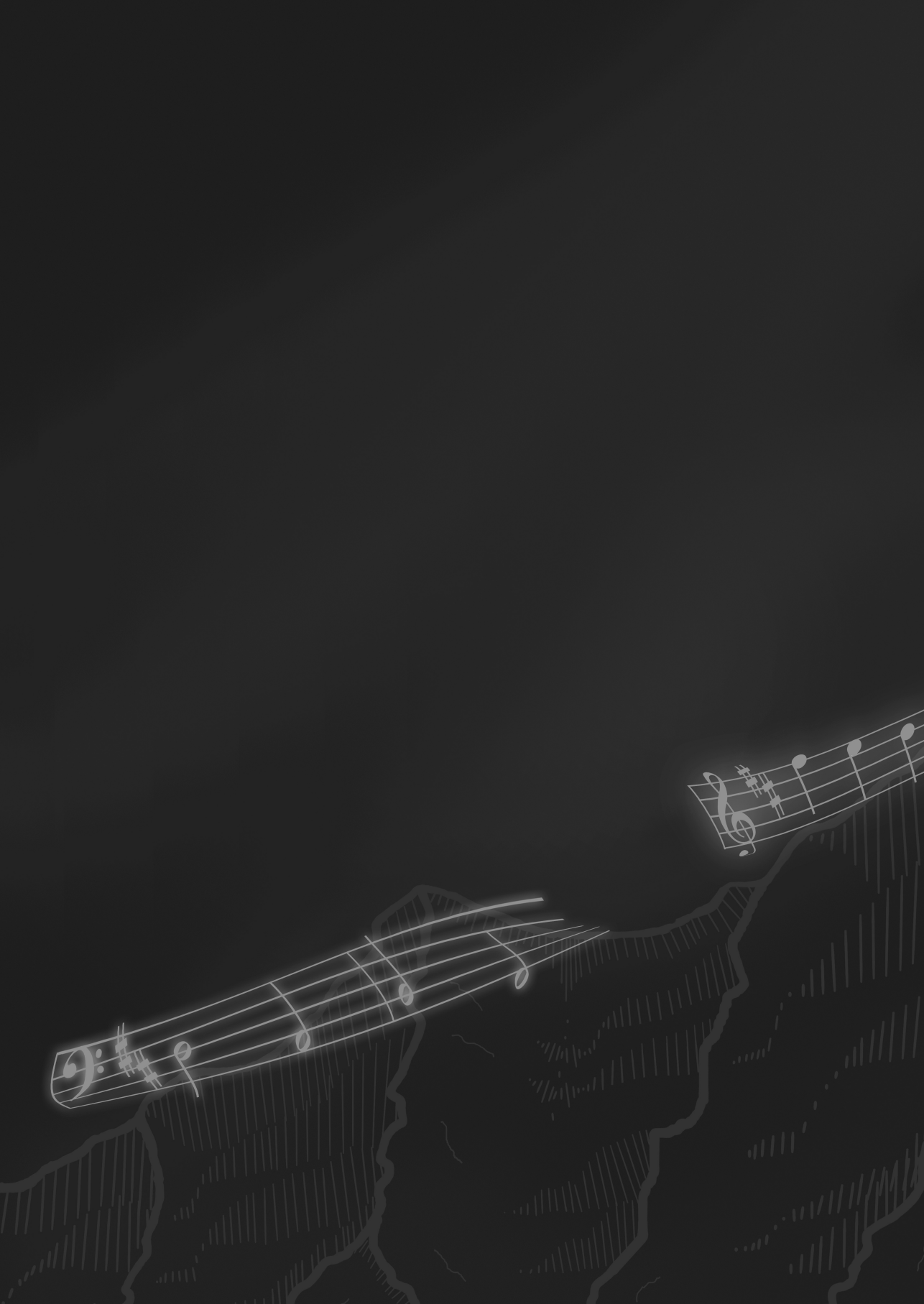






## List of Abbreviations

$B_0$	Main magnetic field strength [T]
$B_1$	Magnetic field induced by the RF pulse [ $\mu$ T]
CEST	Chemical Exchange Saturation Transfer
FA	Flip Angle
FID	Free Induction Decay
FOV	Field-of-view
MRI	Magnetic Resonance Imaging
MRM	Magnetic Resonance Microscopy
MRS	(spatially resolved) Magnetic Resonance Spectroscopy
MX	Matrix size
NA	Number of averages
NMR	Nuclear Magnetic Resonance
Q-factor	Quality factor of a radiofrequency coil
rBW	Receiver bandwidth [kHz]
RF	Radiofrequency
rarefact	RARE-factor
SNR	Signal-to-Noise Ratio
$SNR_i$	Signal-to-Noise Ratio determined from image analysis
$SNR_{i,v}$	Volume normalised Signal-to-Noise Ratio
$SNR_{v,k=1}$	Volume normalised Signal-to-Noise Ratio compared to a single-voxel experiment
ST	Slice thickness
$T_1$	Longitudinal relaxation time
$T_2$	Transverse relaxation time
$t_{acq}$	Acquisition time
$t_p$	Pulse duration [ms]
$T_{Sat}$	Saturation time [s]
TE	Echo time [ms]
TR	Repetition time [s]
UHF	Ultra-high Magnetic Field
$\omega$	Lamor frequency [MHz]



# Chapter 1

## General Introduction



“Dem Anwenden muss das Erkennen vorausgehen“

“Insight must precede application”

Max Planck

### **Abstract**

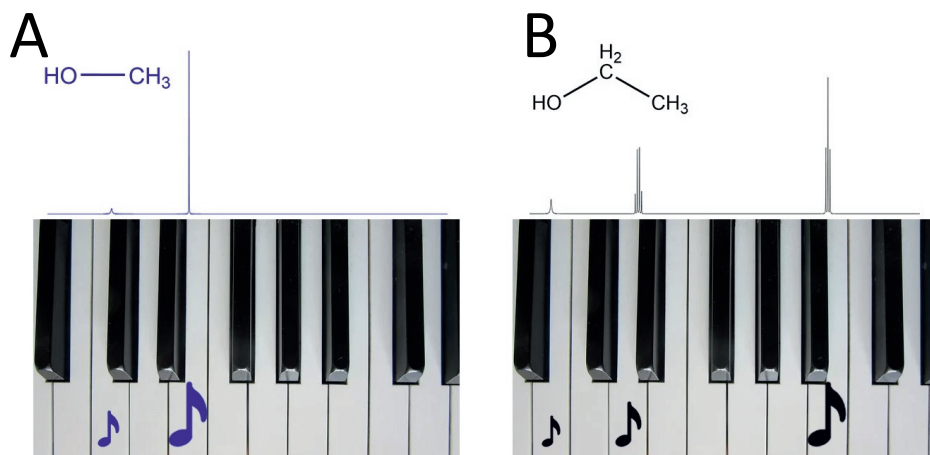
All scientific projects build on previous knowledge often referred to as “standing on the shoulders of giants”(1), this introductory chapter of the thesis highlighting the milestones from the basics to the now widely spread used Nuclear Magnetic Resonance technique. We try to explain the benefits of ultra-high field strength but also challenges associated with high field strength and reflects opportunities and explains the motivation for this thesis.

## 1.1 History of Nuclear Magnetic Resonance, or NMR Explained with a Piano<sup>1</sup>

While nuclear Magnetic Resonance Imaging (MRI) scans have become part of the standard repertoire of modern medicine, their origin remains astonishing. A fundamental discovery in the history of nuclear magnetic resonance (NMR) is the discovery of a property of nuclei called *nuclear spin*, which is often described as a small bar magnet or compass needle to explain it. In 1936, C.J. Gorter postulated an idea and published his negative results on how to measure the nuclear spin (2). The experimental proof was provided by Isidor Isaac Rabi *et al.* in 1937 (3), for which he received the Nobel prize in 1944 (4). This proof meant the potential of a novel method for researchers to observe molecules. The following step transferred the observation in the molecular beam towards practical application (5). Edward Mills Purcell *et al.* and Felix Bloch *et al.* showed the possibility to experimentally use this nuclear spin to detect the spins in paraffin (6) and water (7) respectively, which showed that the NMR method could be used to observe molecules in solids and solution. In the first years, NMR already proved very useful for looking at the “fingerprint” of molecules. Due to the unique magnetic surrounding in which the different nuclei of atoms within a molecule are placed, the nuclei are resonating at different frequencies, similar to that different keys on a piano emit different tunes (Figure 1-1). By knowing which frequency belong to which nuclei, we can deduce the molecule in which they are housed. To continue in this analogy, we can distinguish the different molecules, e.g., ethanol from alcoholic beverages and the toxic compound methanol by their frequencies in the NMR-spectrum, like we can audibly distinguish the trichord (B-D-B) from the dichord (C-E). How loud we hear the different tunes of each chord tells us how much of each nucleus is present in each molecule and also how many molecules we have in the solution. This was already revolutionary as other known spectroscopic methods failed to give a complete and non-destructive analysis of the molecules. NMR methods were further developed (5), and NMR spectroscopy has become a standard tool for organic chemists to verify that they had succeeded in making specific molecules.

---

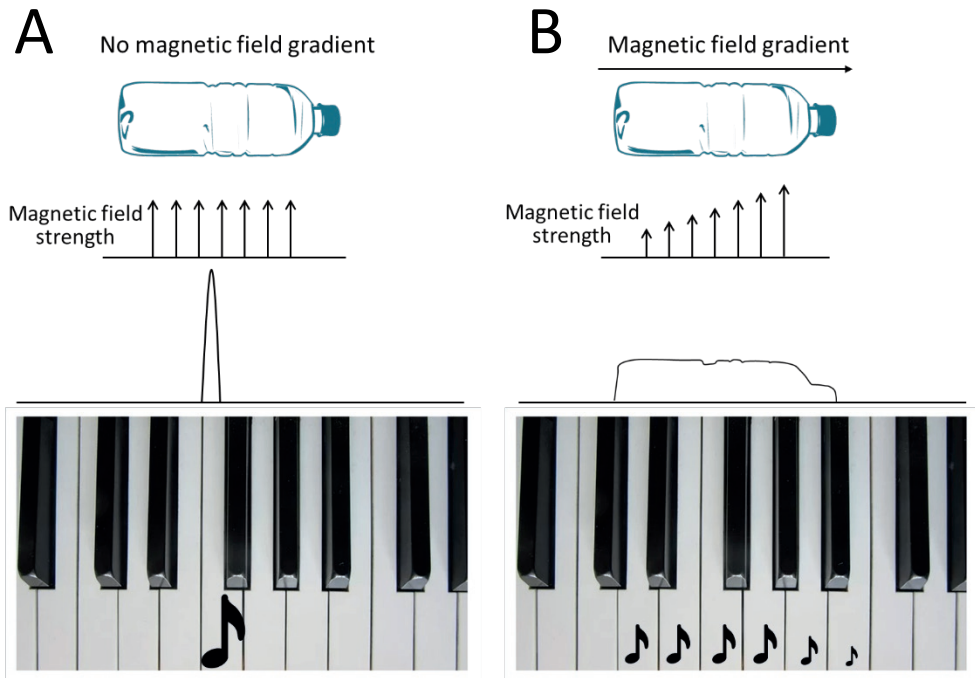
<sup>1</sup> This analogy of the piano is solely intended to explain the basics of NMR and MRI only and like most analogies does not succeed to convey other aspects of NMR theory such as e.g. coherence transfer and relaxation theory.



**Figure 1-1:** The two molecules A.) methanol and B.) ethanol have a different number of hydrogen (-H) atoms and therefore, each proton experiences a different magnetic environment. By their specific frequencies in the NMR-spectrum, they can be distinguished. (NMR spectra were predicted by ChemDraw 18.0)

A different use for the NMR phenomenon was discovered around 1973. Research groups around Paul Lauterbur and Sir Peter Mansfield developed methods on how to use these Magnetic Resonance methods to form an image using magnetic field gradients (8, 9). Other early contributions advanced the initial development of MR, such as the finding that tumours and healthy tissues could be distinguished by the relaxation times, i.e., the signal lifetimes, of water in tissues (10). All these findings contributed to the potential to use of MRI for medical imaging, as besides being non-invasive, it was also a non-ionizing radiation imaging technique.

The spins of water molecules are all at the same frequency when placed in a uniform magnetic field. To stay in the piano analogy, if we would measure a bottle of water with NMR, a single frequency would be observed corresponding to a single F-tone on the piano (Figure 1-2A). For obtaining an MRI image of the water bottle, the spins of water have to be spatially resolved. Magnetic field gradients in three perpendicular directions are applied in an MRI experiment. If a gradient is applied along one direction of the water bottle, the magnetic field strength is different in different positions along the water bottle and the resulted spectrum would show a profile of the water bottle (Figure 1-2B). The sound from the piano would be a bit unusual such as if the piano player is leaning with an arm on the piano on the keys D-A.



**Figure 1-2:** A.) When a water bottle is imaged in an NMR-experiment without a magnetic field gradient a single peak is observed as the hydrogen nuclear spins of water shows only one peak in the NMR-spectrum corresponding to one tone (e.g. F) loudly played (left image). B.) For MRI, a field gradient is applied to change the main magnetic field and therefore the frequency of the spins is spatially resolved (right image).

After the initial discovery on MRI of an object based on the water distribution non-invasively and to distinguish anatomical features, soon other methods were developed. Diffusion, flow, and transport of water could be detected. Different chemical compounds could be spatially resolved; a research field now termed *in vivo* NMR spectroscopy (11) or Magnetic Resonance Spectroscopy (MRS), but in this thesis we refer to it as spatially resolved spectroscopy. This wide variety of information that can be retrieved from this technique makes it more versatile than other imaging techniques, where usually a single type of tissue property (e.g., tissue density with computer tomography (CT)) can be distinguished.

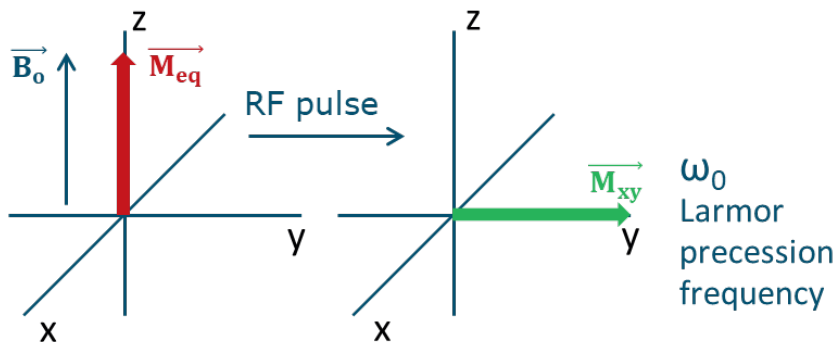
Nowadays, NMR is a versatile tool with applications of NMR Spectroscopy in analytical research (12), used in chemistry and food science, unravelling structures of proteins (13) or battery research. MR relaxometry unravels secrets of art (14) and spatially resolved



applications using MRI (15, 16). The constant challenge for opening this field to novel applications, however, remains in improving the sensitivity of the technique, as magnetic resonance techniques suffer from an unfavourable high limit of detection compared to other analytical techniques.

## 1.2 Basics of MRI and Spatially Resolved Spectroscopy

As discussed in section 1.1, all nuclear magnetic resonance phenomena are based on the property of nuclear spin. When a sample containing a nucleus with a nuclear spin is placed in an external magnetic field  $B_0$ , the net magnetisation from all spins in the sample aligns along the direction of the external magnetic field  $B_0$ . The resonance frequency  $\omega$  of the spins is proportional to the magnetic field strength  $B_0$  and the type of nucleus (i.e. its gyromagnetic ratio  $\gamma$ ) with  $\omega_0 = -\gamma B_0$  (17).

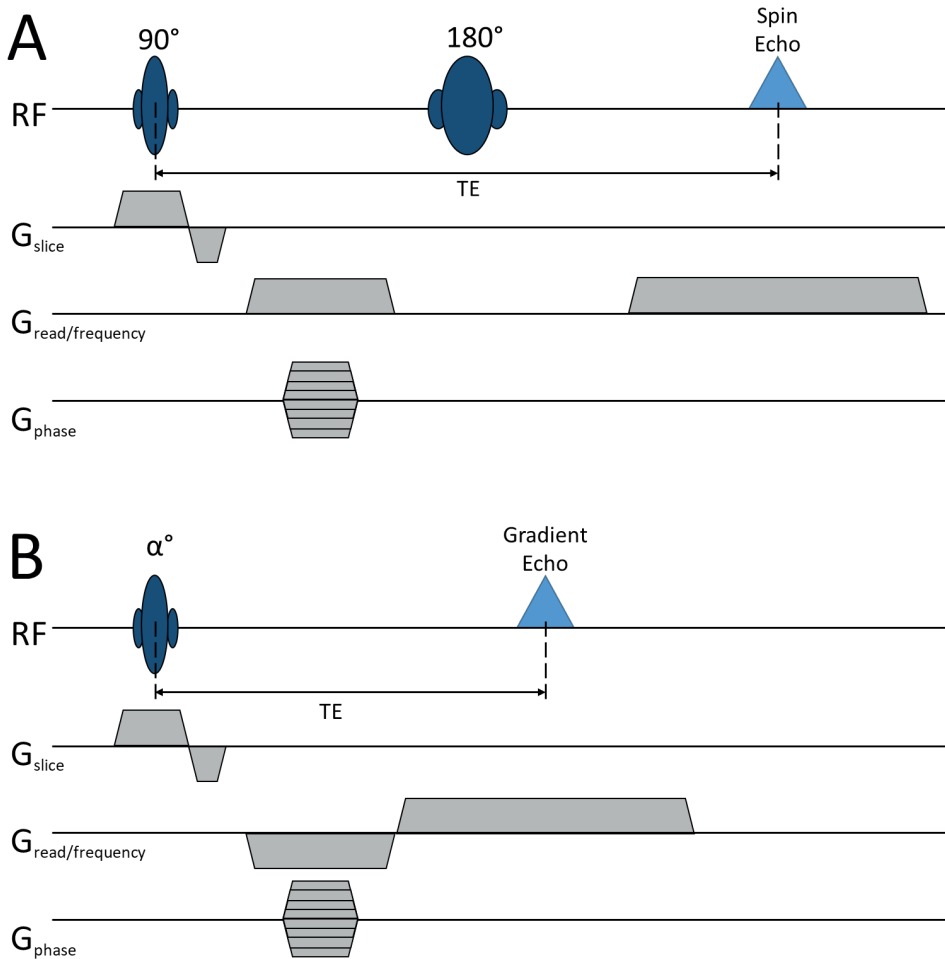


**Figure 1-3:** The vector model is showing the net magnetisation  $M_{eq}$  of a spin ensemble when it is placed in a magnetic field. The magnetisation in the transverse plane (here denoted by the x-y plane) can be detected by a radiofrequency (RF) coil.

Thus, for hydrogen nuclei in a 22.3 T magnet, the resonance frequency is 950 MHz. As the net magnetisation in equilibrium is not observable and thus cannot be used for probing the sample, the net magnetisation  $M_{eq}$  has to be perturbed from equilibrium by applying a second magnetic field called  $B_1$  field which is perpendicular to  $B_0$  and generated by a radiofrequency (RF) pulse (Figure 1-3). The net magnetisation can be manipulated by RF pulses and encoded by magnetic field gradients to yield a variety of information from 1. spatial distribution of matter, e.g. the water proton density, 2. the chemical composition by (spatially resolved) spectroscopy and 3. information on translational motion e.g. diffusion. By varying the timings of the pulses in an MR

sequence, the physical and chemical environment of molecules can be detected. This can be done using the relaxation times  $T_1$  (longitudinal relaxation time constant),  $T_2$  (transverse relaxation time constant) and  $T_2^*$  (transverse relaxation time + contribution of static  $B_0$ -field inhomogeneities). MR offers a large variety of information by varying the experimental sequence and timing of RF pulses and gradient pulses.

How is an MRI image acquired? For a 2D-MRI image, the RF pulses are given in the presence of a magnetic field gradient along the direction of  $G_{\text{slice}}$  (Figure 1-4). The magnetic field strength is thus varying along the direction of the gradient and spins resonate with  $\omega(\vec{r}) = \gamma B_0 + \gamma \vec{G} \cdot \vec{r}$  (18). Only spins along the gradient axis which resonate at the same frequency as the frequency of the applied RF pulse are flipped by the RF pulse. This process is called slice-selection and already restricts the image to a relatively thin slice of 0.05-1 mm (values used in this thesis). For the first dimension in the 2D image, a readout gradient is applied along a different direction  $G_{\text{read/frequency}}$ . The effect is that the spins are resonating at different frequencies. The contribution of spins at the different frequencies can be related to their location in the sample and retraced by a Fourier transform. In the second direction of a 2D image, a phase encoding step is employed along  $G_{\text{phase}}$ . With every repetition step (or echo in case of accelerated sequences such as EPI or RARE), a gradient is switched on for a very short period of time before the echo formation. At the end of this gradient, spins in different locations have acquired a different phase shift and are thereby encoded for the location along  $G_{\text{phase}}$ . This is the most time-consuming step as the step has to be repeated a number of times, corresponding to the final matrix size of the image  $M_y$ . To accelerate this sequence, the refocussing step can be repeated after the first echo and an echo train can be recorded. Here, the gradient strength can be varied for each echo to achieve a different phase-encoding step. For a 3D image, the gradient pulses along  $G_{\text{slice}}$  are replaced by an additional phase encoding step.

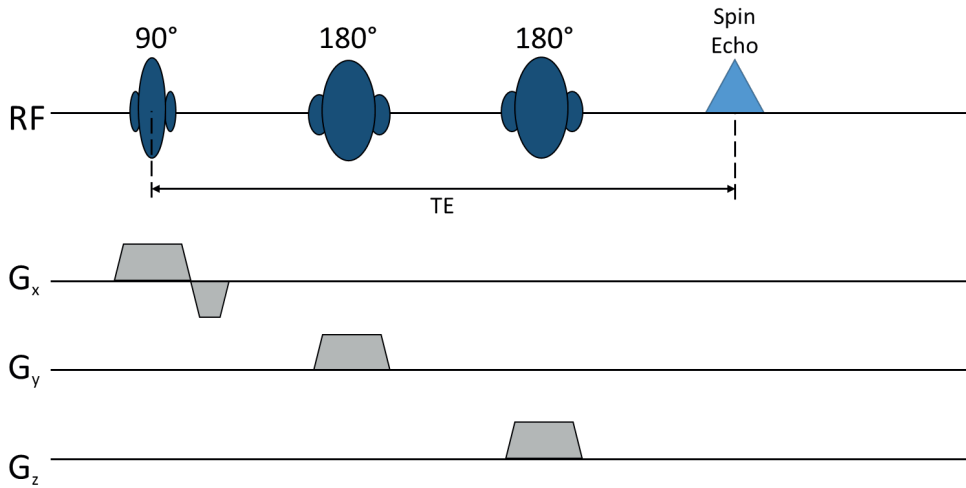


**Figure 1-4:** Two common MRI sequences A.) Spin-echo sequence (18, 19) and B.) gradient-echo sequence (18) with selective RF pulses, slice-selection gradients  $G_{\text{slice}}$ , frequency or readout gradient  $G_{\text{read/frequency}}$  and a phase encoding gradient  $G_{\text{phase}}$ , which is varied in different repetitions of the pulse sequence. The echo time ( $TE$ ) between first excitation pulse and echo is indicated.

Two of the most commonly used experimental sequences (called pulse sequences) for MRI are spin-echo and gradient-echo sequences (Figure 1-4). The spin-echo sequence consists of a  $90^\circ$  pulse followed by a  $180^\circ$  pulse. After the echo time ( $TE$ ), which is twice the interval between the  $90^\circ$  and the  $180^\circ$  pulse, the magnetisation is refocused and produces an echo. The gradient echo sequence consists of a pulse  $\alpha$  between  $5$ - $90^\circ$ .

The echo is produced by reversing the gradient direction in the  $G_{\text{read/frequency}}$ . Gradient echoes are useful for achieving shorter echo times. In spin-echo sequences, the signal decays with  $T_2$ -relaxation time, while in gradient-echo sequences it decays with the  $T_2^*$ -relaxation time. The latter also means that gradient-echo sequences are more prone to  $B_0$  inhomogeneities, as the spins experiencing static inhomogeneities are not refocussed. Examples of spin-echo methods used in this thesis are multi-slice multi-echo (MSME), rapid acquisition with relaxation enhancement (RARE) (20). Gradient-echo sequences are fast low angle shot (FLASH) (21) and multi-gradient echo (MGE).

Spatially resolved spectroscopy is a broad term, which is comprised of several different methods. These methods are used for retrieving spatially resolved information about the chemical compound or metabolite contribution in a sample (11). Single-voxel spectroscopy sequences (e.g. point-resolved spectroscopy (PRESS) (22) or localisation by adiabatic selective refocusing (LASER)) selects a region of interest by applying an RF pulse ( $90^\circ$ ) in the presence of a gradient  $G_x$ , to achieve a selection of a slice (Figure 1-5). By repeating the RF pulse with a  $180^\circ$  pulse in combination with an applied gradient  $G_y$  and a second  $180^\circ$  pulse in combination with the applied gradient  $G_z$ , only the spins in the voxel are refocussed and contribute to an echo, where the spectral information on the chemical compound is encoded. The gradient directions can be arbitrarily chosen as long as the set of directions is orthogonal.



**Figure 1-5:** A single voxel spectroscopy technique with spin-echo formation, called point-resolved spectroscopy (PRESS) (22).

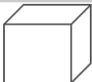


A more thorough description of the basic principles of MRI and spatially resolved spectroscopy can be found e.g. in references (18, 19, 23–25), which also offer a more detailed overview of the basic principles and shows a larger variety of sequences used.

### 1.3 What is Magnetic Resonance Microscopy?

Magnetic Resonance Imaging has several applications roughly divided into three main research fields, namely medical imaging, preclinical imaging and MR Microscopy. The first two definitions are based on the subjects used; clinical imaging develops diagnostic or research methods for humans, while pre-clinical imaging usually investigates rodents for medical or neuroscience research. MR Microscopy, however, is defined by the spatial resolutions (sub-hundredth micrometre resolutions) rather than by type of specimen (23, 26). The wide variety of applications in MR Microscopy range from biofilms (27), plants (28), biological cells (29), rock sediments, histology of animal tissues (30), food (31), electrochemical cells (32).

As previously mentioned, the spatial resolutions of the MR image in each research field can differ. Voxels are in the dimensions of millimetres for clinical images, sub-millimetres for preclinical imaging and sub-hundred micrometres sized for NMR Microscopy applications. A difference that is linked to the spatial resolutions between these applications is that typically the magnetic field strengths are higher to achieve higher spatial resolutions. For clinical studies, it ranges typically between 1.5 and 3 T with a record currently at 10.5 T. For pre-clinical studies, magnetic field strengths are commonly 7 T/ 9.4 T with the ultra-high-field being 21 T (Figure 1-6).

However, the term “ultra-high field” (UHF) is misleading and can only be used in the context of state-of-the-art and the respective research field. For the medical field ultra-high is already 9.4 T while for MR microscopy, ultra-high means at the moment 22.3 T but might soon be outdated when the 28.2 T systems become available. The difference in the record field strength stems from the challenge to obtain a homogeneous field strength over the entire sample area which is more difficult for the diameter of the entire human body than for the 5 mm used for the NMR tube in the 22.3 T system. Therefore, in the remaining of this thesis, we use ultra-high field MRI for the state-of-the-art highest field strength for MR Microscopy at the time of writing of this thesis which is 22.3 T.

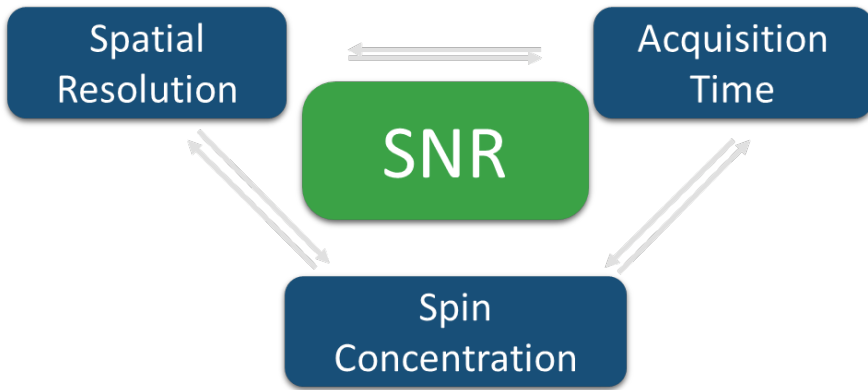
	Clinical imaging	Pre-clinical imaging	NMR Microscopy
Standard $B_0$	1.5 – 3.0 T	7.0 – 11.7 T	7.0 – 14.1 T
State-of-the-art $B_0$	10 T 11.7 T*	21.3 T	22.3 T 28.2 T*
Typical voxel sizes	 (1 mm) <sup>3</sup>	 (75 μm) <sup>3</sup>	 (10 μm) <sup>3</sup>
Sample diameter	< 50 cm	< 10 cm	< 5 mm - 25 mm
Gradient strenghts	~ 40 mT /m	~ 300 mT /m	~ 1.5 – 3 T/m

\*Not yet operational

**Figure 1-6:** Comparison of different fields within MRI research and commonly used specifications of the hardware.

NMR microscopy applications are very diverse, ranging from pre-clinical studies to plants, food and porous media. Next to the higher magnetic field strengths which can (but do not need to) be used in NMR Microscopy, combined with high gradient field strengths allow for higher spatial resolutions. Recently, ultra-high field strengths of up to 21.1 T have proven useful for dynamic and functional imaging for rodent MRI (*e.g.* (33–35) with 18 x 18 x 35 μm<sup>3</sup> resolutions in 29 h using a 3D gradient echo sequence (33). The usage of microcoils for micrometre resolutions was proven on well-defined phantoms (36–38) and biological specimens (39–41). For MRS, the detection limits on phantom solutions (42) and cells (43, 44) were reported.

A significant limitation in most MR applications is the inherent signal-to-noise ratio (SNR) or limit of detection. NMR spectroscopy is already quite insensitive compared to other analytical techniques like *e.g.* mass spectroscopy (45). Using MRI the MR signal is spatially resolved which leads to a relatively low number of spins detected from a voxel.



**Figure 1-7:** Interdependence of a spatial resolution, spin concentration, and acquisition time at a given SNR.

Therefore for a given MR system with a certain RF-coil and a defined object size, at a given SNR, spatial resolution, acquisition time, and detectable spin concentration need to be in balance (Figure 1-7). For instance, at a given SNR, when reducing the resolution by a factor 2 in all three dimensions, the acquisition time has to be increased by a factor 8. Efforts to double the SNR lead to gain of a factor 4 acquisition time.

#### 1.4 How to increase the Signal-to-Noise-Ratio in MR Microscopy?

Several factors contribute to the Signal-to-Noise Ratio (Figure 1-8).

$$SNR \propto [\overset{1}{\gamma B_0}] \left[ \overset{2}{\frac{\gamma^2 h^2 B_0 N_s}{16\pi^2 kT}} \right] \left[ \overset{3}{\frac{B_1}{I}} \right] \left[ \overset{4}{\frac{1}{V_{noise}}} \right]$$

Induced Voltage	Magnetic Polarization	Detector Sensitivity	Random Thermal Noise
-----------------	-----------------------	----------------------	----------------------

**Figure 1-8:** The simplified SNR- equation (46) shows that the SNR is proportional to the 1.) induced voltage containing the gyromagnetic ratio  $\gamma$  and the main magnetic field strengths  $B_0$ , 2.) the magnetic polarisation depending on the gyromagnetic ratio  $\gamma$ , the Planck's constant  $h$  the main magnetic field strengths  $B_0$ , the number of spins  $N_s$ , the Boltzmann constant  $k$  and absolute temperature  $T$ , 3.) the detector sensitivity depending on the magnetic field  $B_1$  generated by the RF-coil with the current  $I$ , and 4.) the random thermal noise given by the noise voltage  $V_{noise}$ .



A significant SNR increase can be achieved by increasing the main magnetic field strength  $B_0$ , which affects both the induced voltage (1.) and the net magnetic polarisation (2.). The magnetic polarisation is equal to the Boltzmann distribution when no additional hyperpolarisation methods are used. Increasing the detector sensitivity (3.) is another option, by optimising the detector towards the sample geometry and size. Other possibilities for improvement include hyperpolarisation techniques that can be used to increase SNR by increasing the net magnetic polarisation (2). Cryo-probe hardware can reduce the thermal noise within the coil (4.); however, these are not yet available for all high-field ( $> 14.1$  T) MRI systems.

### Main Magnetic Field Strength

As an increase in main magnetic field strengths represents one of the main methods to increase the signal-to-noise ratio, traditionally there has been steady developments in magnet technology ranging from electromagnets ( $<100$  MHz) to low-temperature superconducting magnets (200-950 MHz) with development of the alloy material used for the superconducting wires consisting of niobium and zirconium (NbZr) and niobium and tin (Nb<sub>3</sub>Sn) for magnetic fields  $\sim 20$  T (47). For higher magnetic field strength beyond 22 T, one approach is to combine new materials called high-temperature superconducting materials with the conventional superconductors to reach the required field strengths (47), which makes it technically more difficult to upscale the field strength, as it is not simply a matter of extrapolation of existing technology.

### Detector Sensitivity

Besides  $B_0$ , it is worthwhile to look at the detector sensitivity to obtain an SNR increase. The more  $B_1$ -field strength is created per unit current, the more sensitive a transceiver MRI-coil is for signal reception, due to the principle of reciprocity (48). Factors contributing to SNR are the quality factor  $Q$ , the coil temperature  $T_{\text{eff}}$ , the volume of the sample ( $V_{\text{sample}}$ ) the fill factor  $\eta$ , which in turn depends on the coil diameter and its geometry (18) (Equation 1-1). The coil diameter is crucial for the sensitivity of the detector, as a decreasing coil diameter leads to an increase of SNR per unit volume (49). In terms of geometry, a solenoid coil is 3 times more sensitive than a saddle coil (48). SNR can also be increased by decreasing coil losses, which contribute to the noise level. The quality factor, defined as  $Q = \omega L/R$ , is widely used to quantify coil losses (50), and the higher the quality factor, the lower the losses the coil suffers. Losses which are caused by the conductivity in the sample can be quantified by comparing the  $Q$ -factor of the coil loaded with the sample  $Q_{\text{loaded}}$  with the unloaded coil  $Q_{\text{unloaded}}$  (50). Furthermore,

it is crucial to adjust the dimensions of the RF coil to that of the sample, as the higher the ratio of sample volume to coil volume, the larger the filling factor will be (18, 51).

**Equation 1-1:** A simplified equation for the dependence of the image signal-to-noise ratio (SNR<sub>i</sub>) on detector parameters, such as the filling factor  $\eta$ , the coil quality factor  $Q$  and the coil temperature  $T_{eff}$  and the volume of the sample  $V_{sample}$  (adapted from Equation 3.21 in Ref (18)).

$$SNR_i \sim \sqrt{\frac{\eta \times Q}{T_{eff} \times V_{sample}}}$$

## Comparison of SNR across Different MR Systems

For MRI-applications the SNR per unit volume has to be considered, contrary to NMR spectroscopy applications where performance has to be compared based on total spin sensitivity since the NMR measurement is performed on the entire sample volume. Therefore, image SNR (SNR<sub>i</sub>) which is additionally normalised to volume (SNR<sub>i,v</sub>) is most suitable for comparison across different hardware and systems to account for differences in voxel volumes. If the systems cannot be compared using an MR-experiment with the same parameters, such as number of averages, matrix size, bandwidth, these factors should be additionally accounted for (19). Another indicator is the length of the 90° pulse at equal power, which is useful when comparing between different transceiver coils but only at the same field strength. The shorter the 90° pulse, the more sensitive the coil is (48, 50). Additionally, it is crucial that the reference solution which is used for comparison composed of the same compounds, to ensure the same proton density.

## 1.5 Other Benefits and Challenges at Ultra-high Field MRI

### 1.5.1. Susceptibility Effect

SNR increase is the most significant advantage of UHF on one side, but on the other side, other factors can influence the quality of an MR image. Image artefacts, homogeneity and contrast, are important factors in MR imaging and spatially resolved spectroscopy.

A common source of image artefacts in MRM stems from susceptibility mismatches. Especially in specimens where matter with different magnetic susceptibilities can be present, these differences can lead to enhanced contrast in the best case and image artefacts in the worst case.

When two different materials such as water and air have different magnetic susceptibility  $\chi$ , the magnetic field at the interface will be disturbed (local magnetic field variation  $\Delta B_0$ ). Due to these field variations, spins experience a different magnetic field at these interfaces, which leads to inhomogeneous broadening of the MR signal (52). When a standard MRI pulse sequence using frequency encoding is applied for an MRI image, the frequency of the spins is shifted with respect to the “expected” frequency of the spin at its position in the gradient. As the frequency of a spin is directly related to its location in the magnetic field gradient, a shift in frequency manifests itself in a distorted image if the shift is larger than the frequency difference within the voxel due to the macroscopic field inhomogeneities.

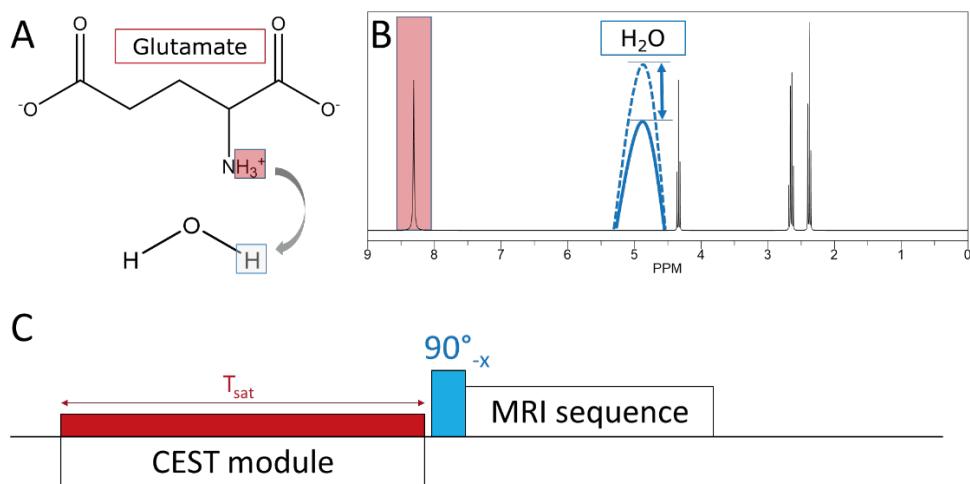
The most common sources of susceptibility mismatches leading to macroscopic field homogeneities in biological specimens can be large air bubbles (53) or metals with a high magnetic susceptibility (32). Contrary to “macroscopic” field inhomogeneities leading to artefacts in the MRI image, microscopic and mesoscopic magnetic field inhomogeneities can also have a beneficial effect and lead to increased image contrast (53). Contrast between two tissue types is essential for distinction and can be challenging as this depends mostly on the relaxation times ( $T_1$ ,  $T_2$  and  $T_2^*$ ) of water within the tissue in standard MRI sequences. However, susceptibility differences ( $T_2^*$  contrast) have a larger effect at increasing field strength (54). A spin-echo technique is more robust to mesoscopic inhomogeneities leading to static dephasing of the signal, however not to the dephasing due to the diffusion of spins through this static field inhomogeneities (53, 54). Thus the choice of pulse sequence is crucial for avoiding image artefacts. Additionally, a reduction in echo times can be beneficial for reducing artefacts.

An additional source of susceptibility mismatches can be the material of the RF-detector. When coils are close to the samples, the differences in magnetic susceptibility between the wire and the air can cause artefacts (45), due to local distortions of the magnetic field.

### 1.5.2 Using the SNR increase for Spatially Resolved Spectroscopy of Low Concentrated Metabolites

One of the opportunities for using high SNR is for chemical compounds other than water. This gives useful information on the chemical or metabolic status of biological specimens. A challenge here is that the commonly sought after metabolites are  $\sim 10$  mM and therefore a factor of  $10^4$  less concentrated than water protons, which are present with  $\sim 110$  M in biological specimens. One common workhorse of metabolite imaging is direct detection methods, where we can spatially localize the region of interest from which we want to have chemical information, i.e. an NMR Spectrum or chemically-selective signal intensity information. For spatially resolved spectroscopic imaging, a distinction is generally made between single-voxel localized spectroscopy (e.g., PRESS or STEAM), multi-voxel spectroscopic imaging (e.g. CHESS/CSSI (55) or CSI (11)). However, the direct spectroscopic imaging methods, where the spins of the metabolites are directly detected are quite time-intensive when low-concentrated compounds need to be detected with a high spatial resolution.

An alternative proposed method is Chemical Exchange Saturation Transfer (CEST) (56–59). CEST detects metabolites indirectly, by exchangeable protons of a metabolite with water (Figure 1-9A). A selective pulse is applied at the chemical shift offset of the exchangeable proton of the metabolite to saturate the magnetisation (Figure 1-9B and C). Subsequently, the metabolite protons exchange with water protons which are available in the phantom or tissue. The net magnetization of water is reduced this process (Figure 1-9B). As this process repeats several times, more proton spins than due to the original metabolite concentration are saturated and therefore, signal enhancement is achieved compared to the measurement of the protons of the metabolite directly. The gain in SNR can be used to either achieve higher spatial resolutions or detection of lower concentrated compounds.



**Figure 1-9:** A.) Chemical structure of glutamate with the exchangeable protons indicated in red which can exchange with the water protons (blue). B.) When the exchangeable proton of glutamate are selectively saturated by a narrow bandwidth pulse (red box), their subsequent exchange with water protons causes a decrease in the water peak. (Spectrum of glutamate predicted in ChemDraw 18.0) C.) The CEST saturation pulse is applied at a certain saturation offset  $\Delta\omega$  and followed by a non-frequency selective  $90^\circ$  pulse followed by an MRI or spatially resolved spectroscopy sequence.

However, the drawback of this method is that it is not uniquely selective to a certain metabolite of interest, and thus CEST contrast caused by application of a narrow bandwidth saturation pulse cannot be uniquely attributed to that metabolite, which has an exchangeable proton at this saturation offset. Here, an advantage of ultra-high magnetic field strength, namely the larger chemical shift dispersion helps not only in the SNR increase but also in an increased selectivity towards certain metabolites.

## 1.6 Motivation and Outline of this Thesis

This thesis is an exploration of Magnetic Resonance Microscopy at ultra-high field strength at the examples of different applications. In each chapter, we are covering a combination of different aspects of ultra-high field MR microscopy: SNR, acquisition time, image contrast, artefacts, sample handling, use of dedicated hardware and possibilities for detecting low-concentrated metabolites. A graphical overview of these aspects related to the chapters can be found in Figure 1-10.

In **chapter 2**, we explored the advantages and feasibility for performing MRI at 22 T at one of the highest magnetic field strengths worldwide. We compared systematically the Signal-Noise Ratio of three different systems 14.1 T, 17.6 T and 22.3 T with notably different hardware. Also, we made an attempt to see which resolutions for a phantom could be achieved and which concentrations were feasible for localized spectroscopy.

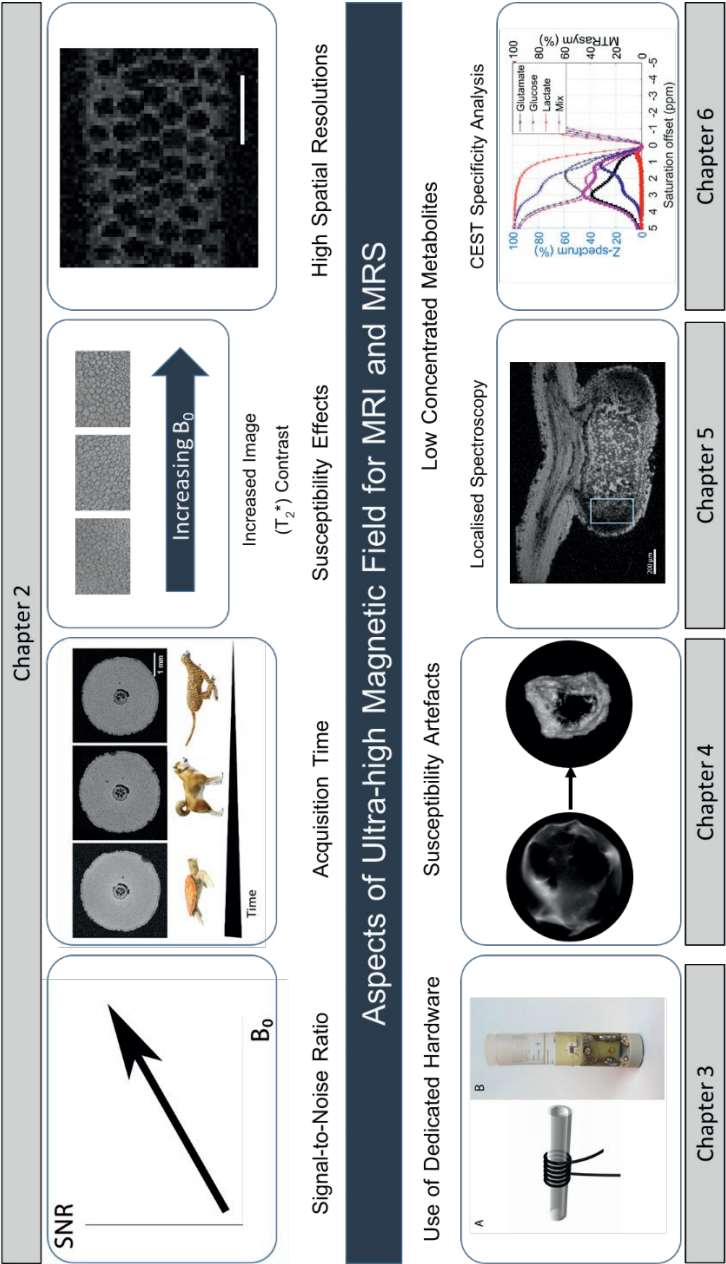
**Chapter 3** gives a practical approach on how to use calibrate and use (micro) coils at ultra-high field strengths and which calibrations are needed. Together with the video protocol, it should provide a new user a starting point to use the microimaging equipment but also the necessary parameters to implement home-build or non-standard coils

**Chapter 4** is a case study of the limits of ultra-high field strength, but it shows that high-resolution 3D MRI can be used complementary to electrical performance measurements. The important aspect for this thesis on UHF is the aim of quantifying biofilms on an electrode material (activated carbon granules). The preamble to this chapter describes the work which had to be done prior to obtaining the first successful images which were presented in the second part of the chapter.

**Chapter 5** is an exploration of the limits at 22.3 T for high spatial resolution imaging and spatially resolved spectroscopy on a plant specimen. More specifically, high-resolution images are shown at 22.3 T on vacuum-infiltrated root nodules of *Medicago truncatula*. Additionally, spatially resolved spectroscopy is demonstrated in *in situ* (i.e. not vacuum-infiltrated) root nodules.

In **chapter 6** we investigated the use of metabolic imaging at ultra-high field strength and more specifically, if higher field strength can help in the selectivity towards specific metabolites in CEST-imaging.

The general discussion in **chapter 7** reflects on the chapters and summarises the main conclusion. The lessons from ultra-high magnetic field strength are discussed in terms of experimental methods and hardware. Initial results and an outlook for ultra-high field MRI and spatially resolved spectroscopy in clinical research, environmental sciences and wastewater treatment, and plant science are provided. Finally, we conclude with an outlook for the future of ultra-high field MRI and MRS beyond 22.3 T.



**Figure 1-10:** Graphical overview of aspects of ultra-high magnetic field for MRI and spatially resolved spectroscopy is given and the respective thesis chapters which are covering the respective aspects. Some images within this graphical overview were adapted from refs (60, 61).



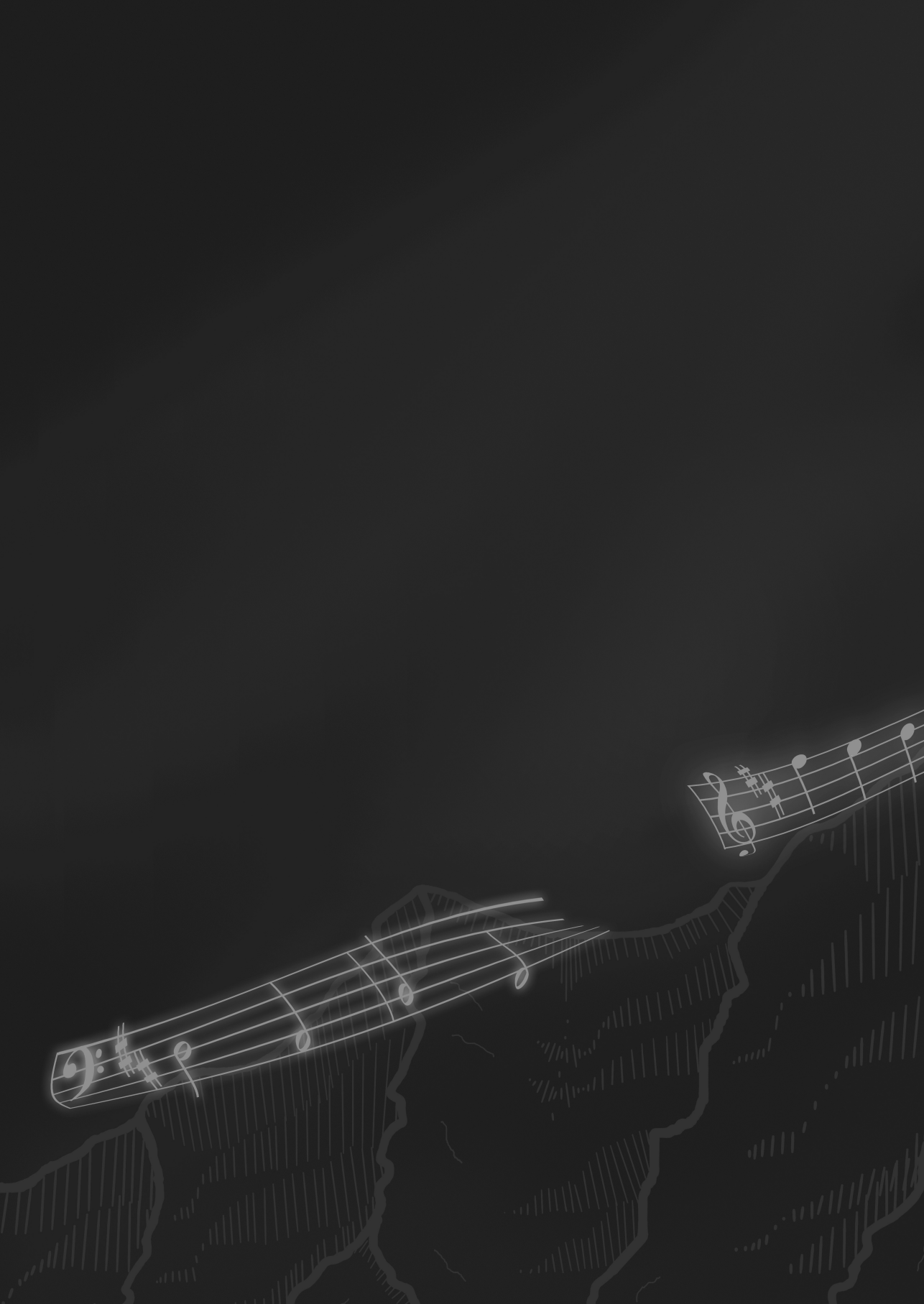
## 1.7 References

1. I. Newton, R. Hooke, “Isaac Newton Letter to Robert Hooke” (1675).
2. C. J. Gorter, Negative result of an attempt to detect nuclear magnetic spins. *Physica*. **3**, 995–998 (1936).
3. I. I. Rabi, J. R. Zacharias, S. Millman, P. Kusch, A New Method of Measuring Nuclear Magnetic Moment. *Phys. Rev.* **53**, 318 (1938).
4. M. A. Shampo, R. A. Kyle, D. P. Steensma, Isidor Rabi - 1944 Nobel Laureate in Physics. *Mayo Clin. Proc.* **87**, e11 (2012).
5. C. Boesch, Nobel Prizes for Nuclear Magnetic Resonance: 2003 and Historical Perspectives. *J. Magn. Reson. Imaging*. **20**, 177–179 (2004).
6. E. M. Purcell, H. C. Torrey, R. V Pound, Resonance absorption by nuclear magnetic moments in a solid. *Phys. Rev.* **69**, 37 (1946).
7. F. Bloch, Nuclear induction. *Phys. Rev.* **70**, 460 (1946).
8. P. C. Lauterbur, Image formation by induced local interactions - Examples employing nuclear magnetic resonance. *Nature* **242**, 190–191 (1973).
9. P. Mansfield, P. K. Grannell, NMR ‘diffraction’ in solids? *J. Phys. C Solid State Phys.* **6**, L422–L426 (1973).
10. R. Damadian, Tumor detection by nuclear magnetic resonance. *Science* **171**, 1151–1153 (1971).
11. R. A. De Graaf, *In vivo NMR spectroscopy: principles and techniques* (John Wiley & Sons, 2019).
12. R. R. Ernst, Nuclear magnetic resonance Fourier transform spectroscopy (Nobel lecture). *Angew. Chemie Int. Ed.* **31**, 805–823 (1992).
13. K. Wüthrich, NMR studies of structure and function of biological macromolecules (Nobel Lecture). *Angew. Chemie Int. Ed.* **42**, 3340–3363 (2003).
14. B. Blümich, F. Casanova, J. Perlo, F. Presciutti, C. Anselmi, B. Doherty, Noninvasive Testing of Art and Cultural Heritage by Mobile NMR. *Acc. Chem. Res.* **43**, 761–770 (2010).
15. P. C. Lauterbur, All science is interdisciplinary—from magnetic moments to molecules to men (Nobel lecture). *Angew. Chemie Int. Ed.* **44**, 1004–1011 (2005).
16. P. Mansfield, Snapshot magnetic resonance imaging (Nobel lecture). *Angew. Chemie Int. Ed.* **43**, 5456–5464 (2004).
17. M. H. Levitt, *Spin dynamics: basics of nuclear magnetic resonance* (John Wiley & Sons, 2001).

18. L. Ciobanu, *Microscopic Magnetic Resonance Imaging: A Practical Perspective*. (Pan Stanford Publishing Pte. Ltd., 2017).
19. M. T. Vlaardingerbroek, J. A. Boer, *Magnetic resonance imaging: theory and practice* (Springer Science & Business Media, 2013).
20. J. Hennig, A. Nauerth, H. Friedburg, RARE imaging: a fast imaging method for clinical MR. *Magn. Reson. Med.* **3**, 823–833 (1986).
21. A. Haase, J. Frahm, D. Matthaei, W. Hanicke, K.-D. Merboldt, FLASH imaging. Rapid NMR imaging using low flip-angle pulses. *J. Magn. Reson.* **67**, 258–266 (1986).
22. P. A. Bottomley, Spatial Localization in NMR Spectroscopy in Vivo. *Ann. N. Y. Acad. Sci.* **508**, 333–348 (1987).
23. P. T. Callaghan, *Principles of nuclear magnetic resonance microscopy* (Oxford University Press on Demand, 1993).
24. M. A. Bernstein, K. F. King, X. J. Zhou, *Handbook of MRI pulse sequences* (Elsevier, 2004).
25. M. A. Brown, R. C. Semelka, MR imaging abbreviations, definitions, and descriptions: a review. *Radiology.* **213**, 647–662 (1999).
26. W. Kuhn, NMR Microscopy—Fundamentals, Limits and Possible Applications. *Angew. Chemie Int. Ed.* **29**, 1–19 (1990).
27. M. P. Herrling, S. Lackner, H. Nirschl, H. Horn, G. Guthausen, "Recent NMR/MRI studies of biofilm structures and dynamics" in *Annu. Reports NMR Spectrosc.* (Elsevier, 2019), vol. 97, chap.4.
28. W. Köckenberger, C. De Panfilis, D. Santoro, P. Dahiya, S. Rawsthorne, High resolution NMR microscopy of plants and fungi. *J. Microsc.* **214**, 182–189 (2004).
29. L. Ciobanu, C. H. Pennington, 3D micron-scale MRI of single biological cells. *Solid State Nucl. Magn. Reson.* **25**, 138–141 (2004).
30. G. A. Johnson, G. P. Cofer, B. Fubara, S. L. Gewalt, L. W. Hedlund, R. R. Maronpot, Magnetic resonance histology for morphologic phenotyping. *J. Magn. Reson. Imaging.* **16**, 423–429 (2002).
31. H. Van As, J. Van Duynhoven, MRI of plants and foods. *J. Magn. Reson.* **229**, 25–34 (2013).
32. M. M. Britton, Magnetic resonance imaging of electrochemical cells containing bulk metal. *ChemPhysChem.* **15**, 1731–1736 (2014).
33. R. Fu, W. W. Brey, K. Shetty, P. Gor'kov, S. Saha, J. R. Long, S. C. Grant, E. Y. Chekmenev, J. Hu, Z. Gan, Ultra-wide bore 900 MHz high-resolution NMR at the national high magnetic field laboratory. *J. Magn. Reson.* **177**, 1–8 (2005).

34. V. D. Schepkin, W. W. Brey, P. L. Gor'kov, S. C. Grant, Initial in vivo rodent sodium and proton MR imaging at 21.1 T. *Magn. Reson. Imaging*. **28**, 400–407 (2010).
35. A. Leftin, J. T. Rosenberg, E. Solomon, F. C. Bejarano, S. C. Grant, L. Frydman, Ultrafast in vivo diffusion imaging of stroke at 21.1 T by spatiotemporal encoding. *Magn. Reson. Med.* **73**, 1483–1489 (2015).
36. S. C. Lee, K. Kim, J. Kim, S. Lee, H. Y. Jeong, W. K. Sung, K. S. Ha, C. Cheong, One micrometer resolution NMR microscopy. *J. Magn. Reson.* **150**, 207–213 (2001).
37. L. Ciobanu, D. Seeber, C. Pennington, 3D MR microscopy with resolution 3.7  $\mu\text{m}$  by 3.3  $\mu\text{m}$  by 3.3  $\mu\text{m}$ . *J. Magn. Reson.* **158**, 178–182 (2002).
38. E. Moore, R. Tycko, Micron-scale magnetic resonance imaging of both liquids and solids. *J. Magn. Reson.* **260**, 1–9 (2015).
39. L. Ciobanu, A. G. Webb, C. H. Pennington, Magnetic resonance imaging of biological cells. *Prog. Nucl. Magn. Reson. Spectrosc.* **42**, 69–93 (2003).
40. J. J. Flint, B. Hansen, S. Portnoy, C.-H. Lee, M. A. King, M. Fey, F. Vincent, G. J. Stanis, P. Vestergaard-Poulsen, S. J. Blackband, Magnetic resonance microscopy of human and porcine neurons and cellular processes. *Neuroimage*. **60**, 1404–1411 (2012).
41. J. J. Flint, C. H. Lee, B. Hansen, M. Fey, D. Schmidig, J. D. Bui, M. A. King, P. Vestergaard-Poulsen, S. J. Blackband, Magnetic resonance microscopy of mammalian neurons. *Neuroimage*. **46**, 1037–1040 (2009).
42. K. R. Minard, R. A. Wind, Picoliter  $^1\text{H}$  NMR Spectroscopy. *J. Magn. Reson.* **154**, 336–343 (2002).
43. J. B. Aguayo, S. J. Blackband, J. Schoeniger, M. A. Mattingly, M. Hintermann, Nuclear magnetic resonance imaging of a single cell. *Nature*. **322**, 190–191 (1986).
44. S. C. Grant, N. R. Aiken, H. D. Plant, S. Gibbs, T. H. Mareci, A. G. Webb, S. J. Blackband, NMR spectroscopy of single neurons. *Magn. Reson. Med.* **44**, 19–22 (2000).
45. A. G. Webb, Radiofrequency microcoils in magnetic resonance. *Prog. Nucl. Magn. Reson. Spectrosc.* **31**, 1–42 (1997).
46. A. Webb, Increasing the sensitivity of magnetic resonance spectroscopy and imaging. *Anal. Chem.* **84**, 9–16 (2012).
47. H. Maeda, Y. Yanagisawa, Future prospects for NMR magnets: A perspective. *J. Magn. Reson.* **306**, 80–85 (2019).
48. D. I. Hoult, R. E. Richards, The signal-to-noise ratio of the nuclear magnetic resonance experiment. *J. Magn. Reson.* **24**, 71–85 (1976).
49. T. L. Peck, R. L. Magin, P. C. Lauterbur, Design and Analysis of Microcoils for NMR Microscopy. *J. Magn. Reson. Ser. B.* **108** (1995), pp. 114–124.

50. A. Haase, F. Odoj, M. Von Kienlin, J. Warnking, F. Fidler, A. Weisser, M. Nittka, E. Rommel, T. Lanz, B. Kalusche, M. Griswold, NMR probeheads for in vivo applications. *Concepts Magn. Reson.* **12**, 361–388 (2000).
51. A. G. Webb, S. C. Grant, Signal-to-noise and magnetic susceptibility trade-offs in solenoidal microcoils for NMR. *J. Magn. Reson. Ser. B.* **1**, 83–87 (1996).
52. P. T. Callaghan, Susceptibility and Diffusion Effects in NMR Microscopy in *Encycl. Magn. Reson. eds-in-chief R. K. Harris R. Wasylishen, John Wiley: Chichester*. doi:10.1002/9780470034590.emrstm0549.
53. M. Musse, H. Van As, NMR imaging of air spaces and metabolites in fruit and vegetables. *Mod. Magn. Reson.*, 1765–1779 (2018).
54. D. A. Yablonskiy, E. M. Haacke, Theory of NMR signal behavior in magnetically inhomogeneous tissues: the static dephasing regime. *Magn. Reson. Med.* **32**, 749–763 (1994).
55. A. Haase, J. Frahm, W. Hanicke, D. Matthaei, <sup>1</sup>H NMR chemical shift selective (CHESS) imaging. *Phys. Med. Biol.* **30**, 341 (1985).
56. M. T. McMahon, A. A. Gilad, J. W. M. Bulte, P. C. M. Van Zijl, *Chemical Exchange Saturation Transfer Imaging: Advances and Applications* (CRC Press, 2017).
57. J. Zhou, P. C. M. Van Zijl, Chemical exchange saturation transfer imaging and spectroscopy. **48**, 109–136 (2006).
58. B. Wu, G. Warnock, M. Zaiss, C. Lin, M. Chen, Z. Zhou, L. Mu, D. Nanz, R. Tuura, G. Delso, An overview of CEST MRI for non-MR physicists. *EJNMMI Phys.* **3** (2016).
59. P. C. M. van Zijl, N. N. Yadav, Chemical exchange saturation transfer (CEST): What is in a name and what isn't? *Magn. Reson. Med.* **65**, 927–948 (2011).
60. L. Caizán-Juanarena, J. R. Krug, F. J. Vergeldt, J. M. Kleijn, A. H. Velders, H. Van As, A. Ter Heijne, 3D biofilm visualization and quantification on granular bioanodes with magnetic resonance imaging. *Water Res.* **167** (2019).
61. R. van Schadewijk, J. R. Krug, D. Shen, K. B. S. S. Gupta, F. J. Vergeldt, T. Bisseling, A. G. Webb, H. Van As, A. H. Velders, H. J. M. de Groot, Magnetic Resonance Microscopy at Cellular Resolution and Localised Spectroscopy of *Medicago truncatula* at 22.3 Tesla. *Sci. Rep.* **10**, 1–11 (2020).



## Chapter 2

### **Assessing Spatial Resolution, Acquisition Times and Signal-to-Noise Ratios for Commercial Microimaging Systems at 14.1, 17.6 and 22.3 T**

This chapter is based on:

Julia R. Krug, Remco van Schadewijk, Frank J. Vergeldt, Andrew G. Webb, Huub J.M. de Groot, A Alia, Henk Van As, Aldrik H. Velders

Assessing spatial resolution, acquisition times and signal-to-noise ratios for commercial microimaging systems at 14.1, 17.6 and 22.3 T (manuscript submitted)

### **Abstract**

This work provides a systematic comparison of the signal-to-noise ratio (SNR), spatial resolution, and metabolite limits-of-detection for magnetic resonance microscopy and spectroscopy at three different magnetic field strengths of 14.1 T, 17.6 T and 22.3 T (the highest currently available), utilising commercially available hardware. We find an SNR increase of a factor 5.9 going from 14.1 T to 22.3 T using 5 mm radiofrequency (saddle and birdcage) coils, which results in a 24-fold acceleration in acquisition time and deviates from the theoretically expected increase of factor 2.2 due to differences in hardware. This underlines the importance of not only the magnetic field strengths but also hardware optimisation. In addition, using a home-built 1.5 mm solenoid coil, we reach an isotropic resolution of  $(5\text{ }\mu\text{m})^3$  in a field-of-view of 1.58 mm x 1.05 mm x 1.05 mm with an SNR of 12:1 using 44 signal averages in 58 hours acquisition time at 22.3 T. In light of these results, we discuss future perspectives for ultra-high field Magnetic Resonance Microscopy and Spectroscopy.

## 2.1 Introduction

Magnetic Resonance Microscopy (MRM) is typically defined as acquiring images with at least one of the dimensions with sub-100  $\mu\text{m}$  resolution (1–3). Many MRM applications use high field vertical bore NMR spectrometers with strong gradients to achieve these high resolutions. In addition to providing highly resolved structural information based on the water signal in biological specimens, the spatial distribution of chemical compounds can be obtained using spatially resolved Magnetic Resonance Spectroscopy (MRS). Due to the inherently low spin polarization, MRM and very high resolution MRS suffer from a low signal-to-noise ratio (SNR) compared to other techniques (4) such as microCT (5), fluorescence microscopy and polarized light microscopy (6), and this limits the maximum attainable spatial resolutions. Improvements in spatial resolution are possible by signal averaging at the expense of long experiment times. For MRS, high concentrations (typically in the mM range) of the compound of interest are required due to the low sensitivity.

The SNR can be expressed in terms of  $B_0$ , the detector sensitivity given by the  $B_1$  field per unit current  $I$ , the number of spins  $N_s$ ,  $T$  the sample temperature  $T$ , and  $V_{\text{noise}}$  the noise from coil and sample (7) (Equation 2-1).

$$SNR \propto [\gamma B_0] \left[ \frac{\gamma^2 h^2 B_0 N_s}{16\pi^2 kT} \right] \left[ \frac{B_1}{I} \right] \left[ \frac{1}{V_{\text{noise}}} \right] \quad (2-1)$$

I                  II                  III                  IV

For MRM cryoprobe technology which reduces the contribution of  $V_{\text{noise}}$  (III) is not widely available and unavailable above 500 MHz (11.7 T). The most common way to improve the SNR is to move to higher magnetic fields. For example, by going from 14.1 T to 22.3 T, the SNR theoretically increases by a factor of 2.2 due to the relation  $SNR \sim B_0^{7/4}$ , taking into account the  $B_0$ -dependence of the detector sensitivity (III) (8). However, improvements of the theoretical SNR are challenging to measure experimentally as the hardware, RF-coil quality and technical capabilities of the used NMR systems differ (cf Table 2-1). Several SNR-formulations for comparing coil performances are readily available in the field of Magnetic Resonance to quantify SNR improvements. These include localised time-domain SNR ( $SNR_t$ ) (9), spectral SNR ( $SNR_f$ ) (9), and image SNR ( $SNR_i$ ) (10). For MRI applications, spin sensitivity per unit



volume ( $SNR_{i,v}$ ) is the most relevant measure (11). Other MRI parameters such as bandwidth, matrix size, number of signal averages, acquisition time, and repetition time (notably in its ratio to the  $T_1$ -relaxation time) should either be kept constant or taken into account when comparing different experiments (10, 12). In this paper, we took a practical approach of comparing SNR using the same MRI parameters on the same samples and using similar coils ( $d = 5$  mm) at three different magnetic field strengths. Besides using the increase in sensitivity at the higher magnetic field strength of 22.3 T for higher spatial resolutions, it is well-known that one can also use the increased sensitivity for higher temporal resolution, i.e., faster image acquisition, and therefore to image dynamic systems. The acquisition time ( $t_{acq}$ ) depends on the desired signal-to-noise ratio SNR, coil diameter  $d$ , spin-lattice  $T_1$  and spin-spin relaxation times ( $T_2$  or  $T_2^*$ ), voxel volume  $(\Delta x)^3$  (3, 13) (Equation 2-2).

$$t_{acq} \sim (SNR)^2 d^2 \left( \frac{T_1}{T_2} \right) \frac{1.418 \times 10^{-15}}{(\gamma B_0)^2 c} \left( \frac{1}{\Delta x} \right)^6 \quad (2-2)$$

In this research, we investigate the effect of high to ultra-high magnetic field strengths  $B_0$  on SNR, by comparing volume coils at different field strengths (14.1 T; 17.6 T and 22.3 T) using standard gradient sets of 2-3 T/m and room temperature conditions for coils and sample. At the highest field strength of 22.3 T ( $^1H$  Larmor frequency = 950 MHz), we additionally studied detector sensitivity by comparing a home-built 1.5 mm solenoid coil with a commercial 5 mm birdcage coil. The improved SNR is quantified for all coils and systems and can be used for optimising acquisition time, spatial resolution and pushing limits for target sample concentrations. In addition, we determine the detection limits of a metabolite at different field strengths. We show that the higher SNR obtained at a  $B_0$ -field of 22.3 T, combined with an increase in detector sensitivity using our home-built solenoid coil, allows a measurement with a voxel size of  $(5.5 \mu m)^3$  and a field-of-view of 1.58 mm x 1.05 mm x 1.05 mm in 58 h of  $t_{acq}$  with an  $SNR_i$  of 12 using a FLASH-sequence. We place our results which are obtained on the highest field strength currently available for MRI including a commercial gradient system of 3 T/m and room temperature coil and sample temperature in perspective with respect to the values achieved by other research groups with highly optimised components such as gradient fields up to 65 T/m and coil temperatures ( $T_{eff}$ ) down to 28 K. Finally, we discuss possibilities and challenges for ultra-high field MRM and provide an outlook for the next milestone in future magnetic field strengths for MRI.

## 2.2 Experimental Methods

### 2.2.1 Spectrometer Specifications and Hardware

The NMR spectrometers used were a 14.1 T system at Wageningen University & Research, a 17.6 T system at Leiden University and the 22.3 T system of the national Dutch NMR facility (uNMR-nl) located at Utrecht University. All systems are equipped with a Micro 5 probe and ParaVision 5 (17.6 T) or ParaVision 6.0.1 (14.1 T and 22.3 T). Other relevant specifications can be found in Table 2-1.

On the 17.6 T and 22.3 T systems commercial 5 mm  $^1\text{H}$  birdcage coils were used in this research, while on the 14.1 T system we used a dual coil ( $^1\text{H}/^2\text{H}$ ) saddle coil, where the  $^1\text{H}$  is the 5 mm inner saddle coil (all Bruker, Ettlingen).

Additionally, we built a customised solenoid coil for the 22.3 T spectrometer for  $^1\text{H}$ -imaging by hand-winding enamelled copper wire of 0.4 mm diameter around a 1.5 mm capillary (6 turns). A fixed tuning capacitor (2.5 pF) and a variable matching capacitor (1.5-6 pF) were added to the resonance circuit mounted on a printed circuit board PCB and attached to a support, compatible with the Micro5 probe socket, which utilises its own in-built RF circuitry.

### 2.2.2 SNR tests, calculations and Q-factor measurements

To compare the radiofrequency-coils of different systems, a solution of 20 (v/v) %  $\text{H}_2\text{O}$ , 80 (v/v) %  $\text{D}_2\text{O}$  and 6.3 mM  $\text{CuSO}_4$  was used ( $T_1 = 265$  ms;  $T_{2,\text{apparent}} = 75$  ms @ 22.3 T (S 2-1)). For the commercial 5 mm coils (saddle and solenoid), the solution was inserted in a 5 mm NMR tube (inner diameter (ID) 4 mm), while for the 1.5 mm solenoid coil, we used a 1.5 mm capillary (ID 1.0 mm) (Hilgenberg, Germany) sealed with capillary wax (Hampton Research, USA). The gradients of a Micro5 gradient coil system were used for all experiments.

For SNR-tests, a spin-echo sequence (MSME) was used with a repetition time (TR) of 1 s, an echo time (TE) of 7 ms and 1 average (NA). The matrix size was set to 256 x 256 with a field-of-view (FOV) of 6 mm x 6 mm, resulting in an in-plane resolution of 23.4  $\mu\text{m}$  x 23.4  $\mu\text{m}$ . The receiver bandwidth was set to 100 kHz. The slice thickness was adjusted to 0.5 mm to achieve an identical receiver gain of 101 to avoid signal clipping on all three spectrometers and thus allow for comparison while maintaining sufficient SNR for quantification at the lowest field strength (see Manual from Bruker (14)).

To calculate the  $SNR_{i,v}$ , regions of interest were chosen in the signal area of the image S and the noise area of the image and the mean and standard deviations were determined in FIJI/ImageJ (15). For the noise area, four regions of interest in the corners of the image were selected and the mean and standard deviations were averaged. We calculated the Signal-to-Noise ratios by determining the SNR of the (magnitude data) image and normalising by the volume of a voxel (Equation 2-3)

$$SNR_{i,v} = \frac{\mu_S - \mu_N}{\sigma_N} \times \frac{1}{d_r \times d_p \times d_s} \quad (2-3)$$

with mean of the signal ( $\mu_S$ ), mean of the noise ( $\mu_N$ ), the standard deviation of the noise ( $\sigma_N$ ) and the voxel dimensions in read ( $d_r$ ), phase ( $d_p$ ) and slice directions ( $d_s$ ). The average  $SNR_{i,v}$  of three slices is reported for each 5 mm RF coils. For the value of  $SNR_{i,v}$  of the 1.5 mm solenoid coil only two slices are used due to the small homogenous  $B_1$  region of the coil.

Q- factor measurement on all coils on their respective probe base were performed using the  $S_{11}$ -measurement on a network analyser (Agilent Technologies). Each coil and probe combination was tuned and matched prior to each Q-factor measurement. The resulting Q-factor was calculated according to Equation 2-4:

$$Q = \frac{\omega_0}{\Delta\omega_{0(@-7dB)}} \quad (2-4)$$

where the bandwidth  $\Delta\omega_0$  is measured at the -7 dB level. The values of  $Q_{loaded}$  deviate by 7% from  $Q_{unloaded}$ , showing that for the relatively low-conductivity samples used in this study the loss is coil-dominated.

### 2.2.3 Metabolite Detection Limit Using Localised Spectroscopy

As a reference solution for the detection limit measurements, we used 5 mm tubes filled with 1.) 100 mM and 2.) 10 mM of sodium acetate in de-ionised water. The temperature during the measurements was kept on 298 K. The 5 mm birdcage (@22.3 T) coil was used.

A localised spectroscopy sequence (PRESS) was used to record a spectrum on a voxel of 125 nL (500 x 500 x 500)  $\mu\text{m}^3$  volume, with TR 1 s, TE 7.2 ms, spectral bandwidth 9.5 kHz and (1) NA 16,  $t_{\text{acq}}$  16 s for 100 mM and 10 mM of acetate or (2) NA 512 and  $t_{\text{acq}}$  8 min 32 s for 10 mM of acetate. The VAPOR-scheme was used for water suppression, and VAPOR pulse powers were calibrated prior to the PRESS-measurements. The voxel of interest was centred on the acetate concentration by setting the working chemical shift to -2.9 ppm with respect to the water resonance. For shim adjustments, the MAPSHIM shim calculation based on a  $B_0$  map was used, followed by (automatic) iterative shimming. A line-broadening factor of 5 was applied during processing.

### 2.2.4 Temporal Resolution

A piece of Lily root (*Nymphaea odorata*) was fixated in 4% (v/v) formaldehyde to ensure that the same sample could be imaged on all three spectrometers. It was then transferred to fomblin, which does not give  $^1\text{H}$ -MR signal and to avoid susceptibility artefacts at the air-tissue interface (16, 17).

A FLASH-3D experiment was recorded at the three spectrometers (14.1 T, 17.6 T and 22.3 T) with a matrix size of 256 x 256 and a field-of-view of 4 mm x 4 mm, resulting in an isotropic spatial resolution of (15.6  $\mu\text{m}$ )<sup>2</sup> with a slice thickness of 100  $\mu\text{m}$ . Other imaging parameters were TR 60 ms, echo time TE 4.03 ms, flip angle 30° and a receiver bandwidth of 50 kHz. The number of averages was 768, 128, 32, and  $t_{\text{acq}}$  was 3 h 17 min, 32 min 44 s, 8 min 11 s for 14.1 T, 17.6 T and 22.3 T, respectively. Furthermore, the 5 mm volume RF coils, namely a saddle on the 14.1 T and birdcage coils on the 17.6 T and 22.3 T were used for these experiments. The  $\text{SNR}_i$  from the magnitude images was determined using the following formula (Equation 2-5)

$$\text{SNR}_i = \frac{\mu_S - \mu_N}{\sigma_N} \quad (2-5)$$

with mean of the signal ( $\mu_S$ ), mean of the noise ( $\mu_N$ ), the standard deviation of the noise ( $\sigma_N$ ).

### 2.2.5 Spatial Resolution

The spatial resolution phantom was prepared using spherical polymer (PMMA) beads called Spheromers® CA40 (Microbeads, Skedsmokorset, Norway) and doped water (6.3 mM  $\text{CuSO}_4$ ). The capillary was approximately half-filled with beads, as trapped air bubbles could still be removed during sample preparation when the capillary was not completely filled with beads.

To test a very high spatial resolution, the 1.5 mm solenoid coil was used on the 22.3 T system. A 3D-FLASH sequence was used to obtain a spatial resolution of  $5.5 \mu\text{m} \times 5.5 \mu\text{m} \times 5.5 \mu\text{m}$  with  $t_{\text{acq}}$  of 58 h 34 min. Other imaging parameters were TE 5.5 ms, TR 130 ms, NA 44, matrix size  $288 \times 192 \times 192$ , field-of-view  $1.575 \text{ mm} \times 1.050 \text{ mm} \times 1.050 \text{ mm}$  and receiver bandwidth 40.760 kHz. The intensity of the (magnitude) image data was plotted using ImageJ (15).

## 2.3 Results

### 2.3.1 Hardware

Since the available hardware, such as the consoles, available coils and maximum gradient strengths differ between the systems (Table 2-1) we kept the experimental parameters constant, wherever feasible.

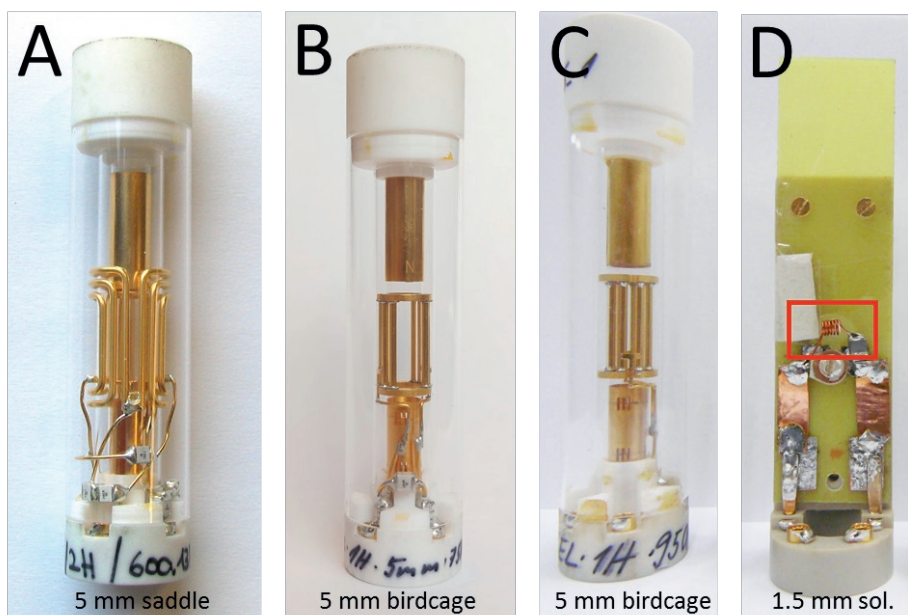
**Table 2-1:** Hardware overview the 14.1 T, 17.6 T and 22.3 T spectrometers and imaging equipment.

	14.1 T	17.6 T	22.3 T
Magnet bore size	Standard bore (52 mm)	Wide bore (89 mm)	Standard bore (52 mm)
Manufacturer	Bruker		
Instrument type	Avance III	Avance I	Avance III HD
Commercial RF coil	5 mm dual saddle $^1\text{H}$ inside $^2\text{H}$ outside	5 mm birdcage	5 mm birdcage

Home-built RF coil	-	-	1.5 mm solenoid
Gradient system	Micro5	Micro5	Micro5
Gradient power supply	GREAT 60	BAFPA 40	GREAT 60
$G_{\text{max, achievable}}$	3 T/m	2 T/m*	3 T/m

\* Due to the gradient amplifiers, this gradient set is limited to 2 T/m.

As mentioned earlier, a commercial saddle coil was used on the 14.1 T (Figure 2-1A) and a commercial birdcage coil at the 17.6 T (Figure 2-1B) and the 22.3 T (Figure 2-1C-left). Additionally, we built a solenoid coil with a coil diameter of 1.5 mm to accommodate smaller samples (Figure 2-1C – right).



**Figure 2-1:** The exchangeable coil inserts of the different spectrometers are shown. A.) On the 14.1 T spectrometer, a 5 mm  $^1\text{H}/^2\text{H}$  dual insert was used with the inner coil being the  $^1\text{H}$ - saddle coil. B.) The 17.6 T spectrometer was equipped with a 5 mm birdcage coil and C.) for the 22.3 T spectrometer a 5 mm birdcage and a home-built 1.5 mm solenoid coil (red highlight) was used.

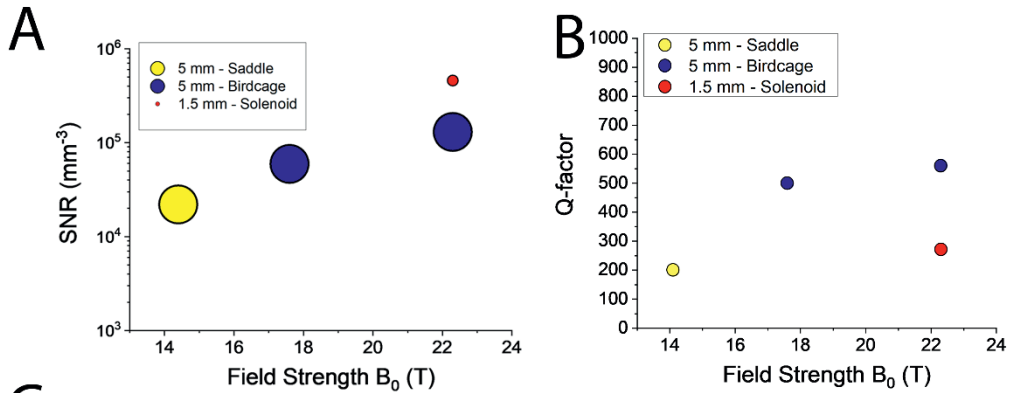
### 2.3.2 SNR and Q-factor Measurements

The experimental  $\text{SNR}_{i,v}$  increased with increasing field strengths from  $2.2 \times 10^4 \text{ mm}^{-3}$  at 14.1 T, to  $5.9 \times 10^4 \text{ mm}^{-3}$  at 17.6 T and  $1.3 \times 10^6 \text{ mm}^{-3}$  at 22.3 T using the 5 mm RF volume coils on all three spectrometers (Figure 2-2A). This corresponds to a factor of 5.9 from 14.1 T to 22.3 T using 5 mm RF volume coils.

When increasing the detector sensitivity by using a home-built solenoid coil ( $d = 1.5 \text{ mm}$ ), the  $\text{SNR}_{i,v}$  increased further by a factor of 3.5 with respect to the 5 mm birdcage coil at 22.3 T (Figure 2-2A). The same image could thus theoretically be recorded 12 times faster if the sample geometry allows the same FOV (13).

Furthermore, a comparison of the Q-factors showed that both birdcage coils (@ 17.6 T and 22.3 T) had the highest Q-factors with 500 and 561 respectively, while the solenoid and the saddle coil had lower Q-factors, with 271 and 200 respectively (Figure 2-2B and C). This difference in Q-factor indicates that the coil losses of the 5 mm saddle (@14.1 T) and the 1.5 mm solenoid (@ 22.3 T) are higher than in the two 5 mm birdcage coils. The afore-mentioned difference between experimental  $\text{SNR}_{i,v}$  increase of a factor 5.9 and theoretical value 2.2 can be explained by this difference in Q-factor.

Theoretically, a 10-fold increase of  $\text{SNR}_{i,v}$  is expected when going from a 5 mm birdcage (@22.3T) coil to a 1.5 mm solenoid (@ 22.3T) coil at the same field strength, due to the decrease in coil diameter (factor 3.3) (10) and changing the geometry from birdcage to solenoid (factor 3) (18). However, the thinner wire diameter of the solenoid coil which leads to higher coil losses. The Q-factor of the solenoid coil is decreased by a factor 2 with respect to the birdcage coil (@ 22.3 T). This difference in Q-factor explains partially the discrepancy between experimentally determined  $\text{SNR}_{v,i}$  increase (factor 3.5) and theoretical increase (factor 10). The discrepancy in the  $\text{SNR}_{v,i}$ -values between the birdcage and the solenoid coil cannot be fully explained by the difference in Q-factor, so there must be other factors like e.g. imperfect shimming of the sample in the solenoid which could lead to a lower  $\text{SNR}_{v,i}$  than the difference in Q-factor alone.

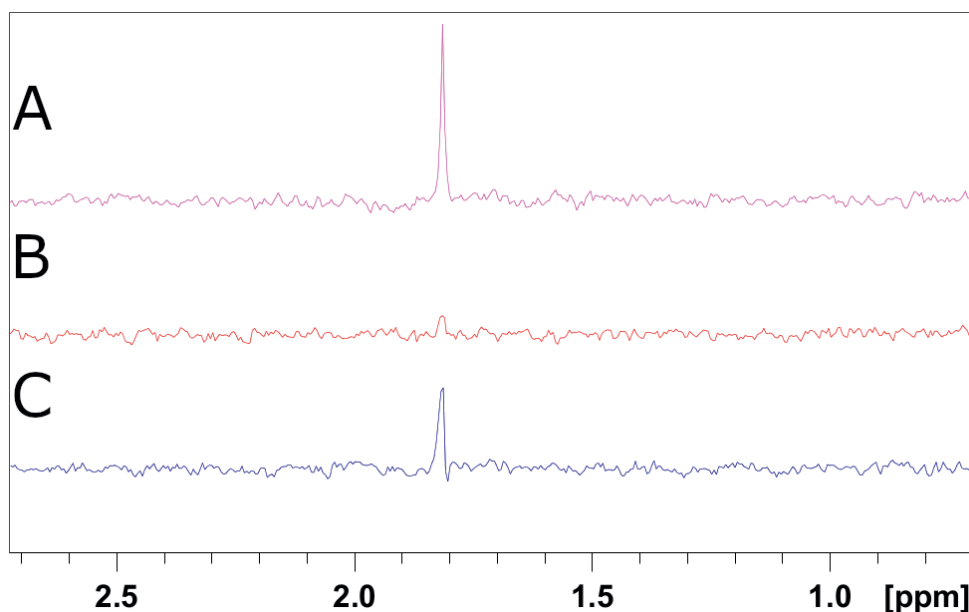


**Figure 2-2:** A) Signal-to-Noise Ratio for different coils at 14.1 T, 17.6 T and 22.3 T shows an SNR<sub>i,v</sub> increase for the 5 mm volume coils with an increase of B<sub>0</sub> field and an SNR<sub>i,v</sub> increase for the 1.5 mm solenoid compared to the 5 mm birdcage(@22.3T). B) The Q-factor of all available coils of the different spectrometers were determined. C) All numerical quantities as depicted in A and B are listed.



### 2.3.3 Determining the Detection Limits for Metabolites at 22.3 Tesla Using 5 mm RF Coils

To determine the detection limit of potential metabolites, a localised spectroscopy experiment was performed on the 5 mm birdcage(@22.3T) using a voxel volume of  $(500\text{ }\mu\text{m})^3$ , corresponding to 125 nL (Figure 2-3). 100 mM of acetate could be detected with 16 averages over a 16 s acquisition time with an SNR of 25:1 (Figure 2-3A), while the SNR of 10 mM acetate was slightly above 2:1 using the same parameters (Figure 2-3B). When measuring 10 mM acetate with 512 averages for 8 min and 32 s acquisition time, the peak was visible with an SNR of 12:1 (Figure 2-3C).



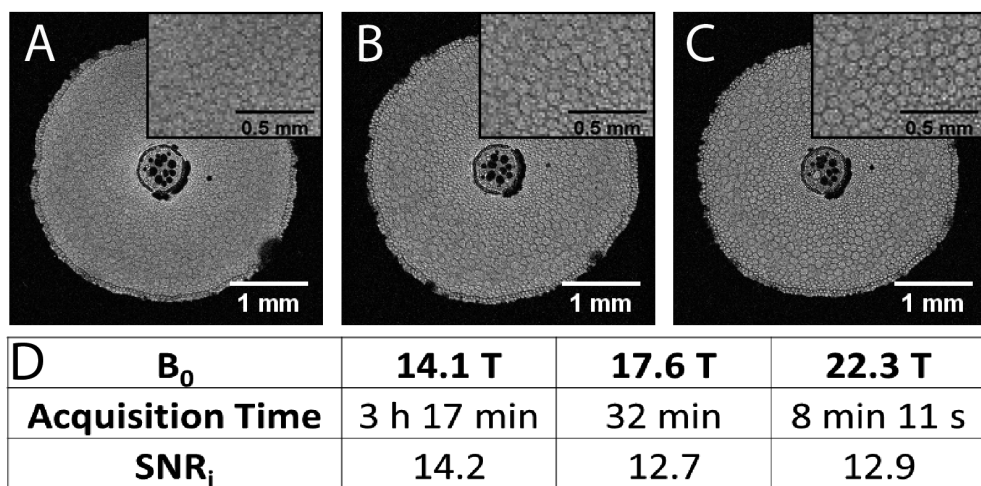
**Figure 2-3:** Localized Spectroscopy (PRESS) on different acetate concentrations at 22.3 T A.) 100 mM acetate and B.) 10 mM acetate on 125 nL in 16 s C.) 10 mM acetate 125 nL in 8 min and 32 seconds.

The ability to detect these low-concentrated metabolites in small volumes enables high spatial resolutions for biological specimen  $<4\text{ mm}$ .

### 2.3.4 Temporal Resolution at Constant Spatial Resolution

The increased  $\text{SNR}_{i,v}$  at higher  $B_0$  can also be used to minimise the  $t_{acq}$  of the MRI experiment. To enable the direct comparison a piece of Lily root was fixated and a 2D-FLASH experiment as a cross-section through the root was recorded on all three systems using approximately the same slice location in the same sample (Figure 2-4). We first recorded the 2D-FLASH on the 22.3 T and obtained an  $\text{SNR}$  of 12.9 in 8 minutes and 11 s (Figure 2-4C). To obtain a similar  $\text{SNR}_i$  at identical spatial resolution, we adapted the number of signal averages which resulted in 32 min at 17.6 T (Figure 2-4B,D) and 3 h and 17 min at 14.1 T (Figure 2-4A, D). Thus, at 22.3 T, we can accelerate the same imaging experiment 4 times with respect to 17.6 T and 24 times with respect to the 14.1 T.

Image contrast differs with the contrast between cell walls and cell cytoplasm increasing from 14.1 T to 22.3 T (Figure 2-4A-C). The signal is decreased in the cell walls due to shorter  $T_2^*$  most likely caused by magnetic susceptibility mismatches in the cell walls, which have a stronger effect at higher the magnetic field strengths (19, 20). While this  $T_2^*$  decrease at high field strengths can be a disadvantage for imaging at ultra-high field, in this case, it is favourable for increased contrast and Figure 2-4C shows that especially the smaller cells around the xylem bundles are distinguishable at 22.3 T, while they are less apparent in the 14.1 T. Surprisingly, susceptibility artefacts which are expected at high-field strength seem not to increase towards 22.3 T. The small artefact at the 14.1 T stems most likely from an air bubble as the slice might have been shifted slightly with respect to the slice at 22.3 T or appeared during sample storage between measurements.

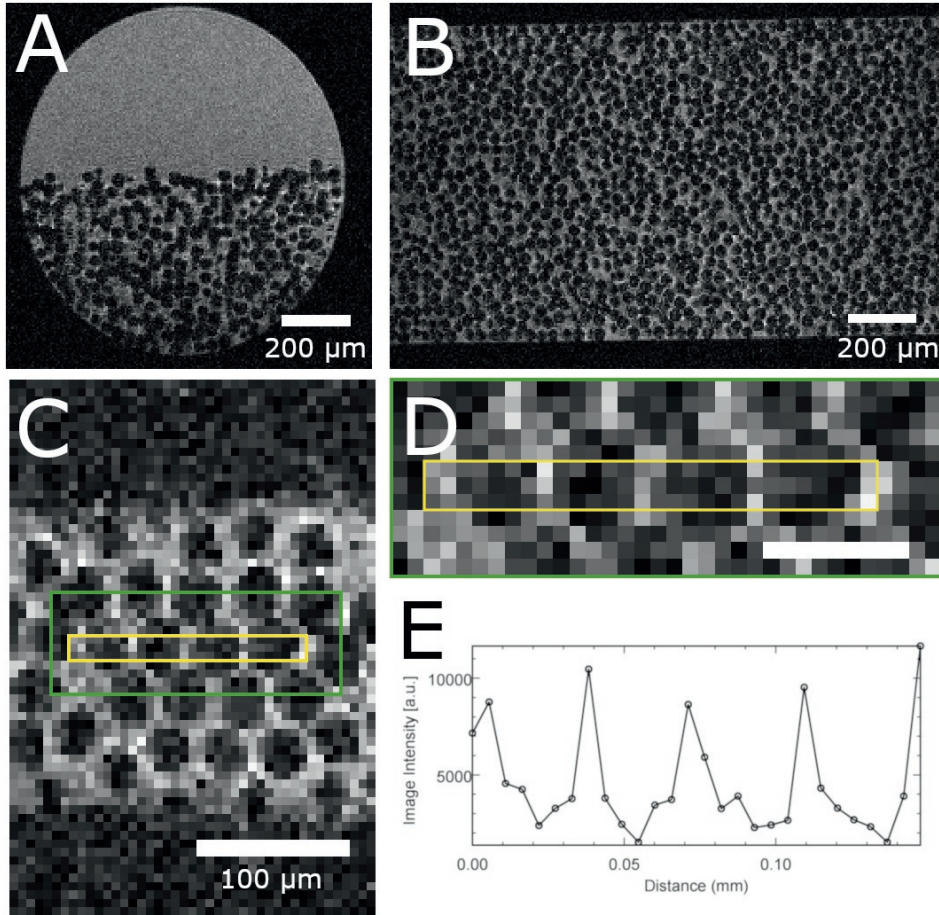


**Figure 2-4:** 2D-FLASH experiments of the same fixed Lily root section at A) 14.1 T B) 17.6 T and C) 22.3 T. The slice position was slightly shifted between the three experiments. The image inserts show an enlarged region of the image. D) The  $SNR_i$  and the measurement times demonstrate the much shorter experiment times possible at 22.3 T.

### 2.3.5 Spatial Resolution Achievable Using 1.5 mm Coil with $t_{acq}$ of 58 h

To estimate the spatial resolution achievable at 22.3 T with using a geometrically well-defined sample, we used a phantom consisting of polymer (PMMA) beads with a diameter of 40  $\mu\text{m}$  (Figure S 2-2) in doped water and the 1.5 mm solenoid coil. The PMMA beads are densely packed at the bottom of the capillary and less ordered towards the middle of the sample (Figure 2-5A). The capillary was not completely filled with beads. An  $SNR_i$  of 12 was measured in the top part where only doped water was present (Figure S 2-3). Figure 2-5B shows a plane of this 3D-dataset with a nominal resolution  $(5.5 \mu\text{m})^3$ , corresponding to 164 fL. A video of this full 3D-experiment is available on request (S 2-3). Enhanced image intensity around the beads is observed likely due to diffusion edge enhancement. Small air spaces in the sample in combination with the gradient echo sequence used caused susceptibility effects in the form of a lower image intensity. An image plane located at the bottom of the phantom (Figure 2-5C) shows that the PMMA beads are ordered due to dense packing and enables the identification of the individual beads. If the intensity across individual beads (Figure 2-5D) is plotted, the separation of individual beads can be confirmed (Figure 2-5E). However, significant

intensity differences over the bead at the right side of the image show that for rigorous data analysis a higher SNR might be needed.



**Figure 2-5** All images were acquired with a 3D-FLASH experiment with  $(5 \mu\text{m})^3$  isotropic resolution A) One plane of the 3D-FLASH showing the cross-section of the capillary half-filled with PMMA beads B) One plane orthogonal on A) through the centre of the capillary is shown; C) From the same 3D dataset a plane with packed beads at the bottom of the capillary; D) Close-up image of 4 beads (indicated with a green frame in image C; E) Intensity profile of the cross-section through the beads across the area indicated in C and D (yellow rectangle).

## 2.4 Discussion

### 2.4.1 Spatial and Temporal Resolution

At the advent of the field of Magnetic Resonance Microscopy, predictions concerning the limits of resolutions stated a ‘brick wall’ around  $10\ \mu\text{m}$  (*1*) due to sensitivity limitations. To push the limit of resolution, numerous researches have successfully increased SNR by moving to higher  $B_0$  and used highly-sensitive RF microcoils (*21–26*). However, these studies have in common that in addition to microcoils, dedicated hardware such as extremely high gradient field strengths up to  $65\ \text{T/m}$  (*21*) or low temperatures (*27*) were utilised, which mitigate resolution limiting factors such as  $T_2$ -line broadening and diffusion limitations (*10, 28*). In this research (Section 3.4), we have demonstrated that a 3D-scan at high resolutions is possible when using a  $1.5\ \text{mm}$  solenoid coil in combination with a high field strength and standard gradient set of  $3\ \text{T/m}$ . Our solenoid coil had a larger diameter than those used in previous research and we were able to obtain larger FOVs ( $1.58\ \text{mm} \times 1.05\ \text{mm} \times 1.05\ \text{mm}$ ). The key difference is therefore that our setup enables high-resolution 3D MRI measurements at larger FOV and object sizes than previous research (*21–26*) using standard gradients of  $3\ \text{T/m}$  for this experiment.

However, the SNR increase by  $B_0$  and detector sensitivity increases will not be sufficient to increase the spatial resolution using our current  $22.3\ \text{T}$  system. Linewidth-affecting factors, such as diffusion,  $T_2$ -broadening and susceptibility are known to limit the achievable spatial resolution (*1, 29*). Higher magnetic field gradient strengths mitigate these effects and lead to a lower contribution of these effects to the broadening of the point-spread function (*28, 30*). Using our current system with a gradient field strength of  $3\ \text{T/m}$ , the resolution limit is predicted to be around  $4\ \mu\text{m}$  (*28, 30*). Gradient development is an essential component to increase the achievable spatial resolution also at ultra-high field strength  $B_0$ . At higher resolution, the true resolution becomes diffusion-limited and  $T_2$  limited (*29*). Susceptibility artefacts due to for instance air spaces are a problem at the presented ultra-high field strength of  $22.3\text{T}$ . To this end, pure-phase encoding approaches are promising firstly to overcome the resolution limit arising from diffusion and secondly as they suffer less from susceptibility artefacts (*31–33*). To approach the optimal resolution close to the resolution limit, additionally multiple echo summation should be considered (*1*).

## 2.4.2 Opportunities and Challenges of MRM at Ultra-high Field Strength

The most obvious advantage of reaching higher field strength is the SNR increase for a given measurement time. This can be conveniently used for a higher temporal resolution, so shortening of the acquisition time with respect to lower-field spectrometers. Furthermore, as the detection limit is lowered by the increased SNR, it can be used for imaging metabolites at tens of mM concentrations in small volumes of interest of 125 nL. In contrast to localized spectroscopy in smaller sample volumes within biological cells has readily been shown on microcoils (34, 35), our results show the possibilities of spatially resolved metabolite detection in a commercial 5 mm coil and therefore its application to larger sample sizes, where the high-field can provide sufficient SNR for metabolite MRM in plant tissues (36, 37).

At higher field strength, the  $T_2$  decreases while the  $T_1$  increases. Therefore, MR parameters for acquisition need to be optimised to allow for a short echo time and a longer repetition time for maximum signal acquisition, in case of quantitative measurements.  $T_2$ -quantification below 100  $\mu\text{m}$  resolution is dependent on the image resolution (38). The resolution dependence impedes the quantitative interpretation of high-resolution  $T_2$  maps, and a distinction based on  $T_2$ -maps is getting more difficult due to the convergence of apparent  $T_2$  values. An alternative workaround for high-resolution  $T_2$ -experiments at high  $B_0$ ,  $T_2$ -prepared sequences could be used for high resolution. However, these come with increased measurement time, as only one echo time point could be measured in each repetition time.

Susceptibility effects increase with increasing field strengths, which can lead to positive as well as negative effects. On the one hand, it can decrease  $T_2^*$ -values of certain tissue types and therefore enhance image contrast, which is beneficial. The  $T_2^*$  decrease towards higher magnetic field strengths caused by mesoscopic magnetic field inhomogeneities in i.e. cell walls can manifest as an advantage due to an increased contrast in the (inevitably)  $T_2^*$ -weighted images (see section 3.4) (37). On the other hand, macroscopic inhomogeneities caused (e.g. air bubbles) can cause severe image artefacts, and therefore, not all samples are suitable for MRM for frequency-encoded sequences at ultra-high field. Spin-echo sequences are more robust than gradient-echo sequences but are used at the expense of longer  $t_{\text{acq}}$ . Examples of factors causing susceptibility artefacts are the presence of air spaces in the phantoms or tissues (10) and materials containing paramagnetic ions. Air spaces which cause image artefacts in

biological tissues can be resolved by infiltrating the tissue by perfluorodecalin (39). When imaging an activated carbon granule (40), we also observed strong image artefacts, which are suspected to be due to the paramagnetic ions which are present in the activated carbon granule. Efforts to reduce the amounts of paramagnetic ions have paid off; we could complete this study on 14.1 T but not yet obtained artefact-free images on 22.3 T. To enlarge the applicability of ultra-high field, susceptibility free imaging approaches could be used such as SPEN (41) which is more robust to sample susceptibility or pure phase encoding approaches such as SE SPI, SPRITE or BLIPPED (31–33).

### 2.5. Outlook and Conclusion

Using the SNR-increase for shorter  $t_{acq}$  at 22.3 T offers opportunities for imaging systems in a shorter time and potentially dynamic systems. To improve acquisition times further, combining the ultra-high field with acceleration techniques (e.g. compressed sensing) (42) techniques would be very promising.

To further increase SNR for MRI and MRS at ultra-high field strength, additional methods for sensitivity enhancement could be used. Chemical Exchange Saturation Transfer (CEST) can detect lower concentrations of metabolites as saturation of the exchangeable metabolite protons and the subsequent exchange with water protons lead to a signal amplification over direct localized spectroscopy methods (43). Higher field strengths are postulated to be advantageous for CEST as the chemical shift dispersion is higher and allows for more selective saturation. Additionally, hyperpolarization techniques such as SABRE (44) and DNP (45) are being developed for *in vivo* MRI application and can lead to promising applications in MRS in the future.

Where will the developments go with ultra-high field MRI when the first magnets above 23.5 T are becoming available? With the current 5 mm diameter coils, we do not expect  $B_1$ -inhomogeneity problems due to interference, which is a challenge at high-field MRI for medical applications. The SNR increase expected at this field strength will certainly enable to image with a higher spatial and temporal resolution which will be advantageous for numerous applications. However, we do not expect to breach the resolution limit of  $(5\text{ }\mu\text{m})^3$  considerably as this resolution limit is the regime where it is limited by the maximum gradient strength of the currently commercially available

gradient strengths on NMR spectrometer systems (28). Furthermore, coil development and dedicated setups are highly recommended for smaller samples ( $d < 3$  mm).

Using a 22.3 T magnetic field strengths we have shown that a 4.8-fold increase of the volumetric SNR can be achieved compared to the 14.1 T using 5 mm commercial volume coils at the respective systems. When using a home-built 1.5 mm solenoid coil, this further increases with a factor 3.5 with respect to the 5 mm volume coil at the 22.3 T. This  $\text{SNR}_{i,v}$  increase can be used for faster imaging, lower spin concentrations in localised spectroscopy or increasing the spatial resolution until the resolution limit. Spatial resolution of down to  $(5.5 \mu\text{m})^3$  using a standard gradient set and a large FOV demonstrate the opportunities for high-resolution MRI with larger specimens. The detection limits on localised spectroscopy in a 5 mm birdcage show the potential of using ultra-high field MRI for metabolite detection. In future, a combination with additional sensitivity enhancement techniques could open the field of MRM to a wider range of spatially resolved metabolite imaging applications.

## 2.6 Acknowledgments

J.R.K. was supported by the NWO-funded Netherlands' Magnetic Resonance Research School (NMARRS) graduate school [022.005.029]. R.v.S. was supported through BioSolarCells [Project U 2.3]. Experiments at the 950MHz instrument were supported by uNMR-NL, an NWO-funded National Roadmap Large-Scale Facility of the Netherlands [184.032.207]. We thank Klaartje Houben, Johan van der Zwan and Marie Renault for technical support at the uNMR-NL facility, Pieter de Waard and John Philippi for technical support at the MAGNEFY center and Karthick B. Sai Sankar Gupta for technical support at Leiden University.



## 2.7 Supporting Information

### S 2-1: $T_1$ and $T_2$ maps of the reference solution used for SNR tests

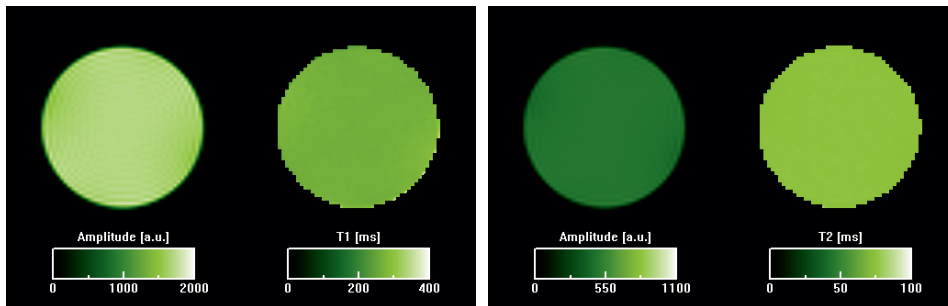


Figure S 2-1: Amplitude and  $T_1$  map corresponding to the  $T_1$ -experiments RAREVTR are shown on the left and amplitude and  $T_2$ -map corresponding to the  $T_2$ -experiment (MSME) are shown on the right.

The reference solution used was 20 (v/v) %  $H_2O$ , 80 (v/v) %  $D_2O$  and 6.3 mM  $CuSO_4$  to determine the  $T_1$  and  $T_2$  values of the reference solution. The  $T_1$ -experiment (RAREVTR-sequence) was recorded with the following MR-parameters: TE 2.8 ms, 6 TR steps varying from 100, 149, 211, 298, 445 and 1100 ms, NA 8,  $t_{acq}$  19 min 39 s, FOV 6 mm x 6 mm, MX 64 x 64, rBW 50 kHz. The  $T_2$ -experiment (MSME-sequence) was recorded with the following MR-parameters: echo spacing 3.2 ms, number of echoes 128, TR 2000 ms, NA 4,  $t_{acq}$  8 min 32 s, FOV 6 mm x 6 mm, MX 64 x 64, rBW 100 kHz. It has to be noted that at high spatial resolutions, the measured  $T_2$ -values dependent on the chosen spatial resolution (46).

## S 2-2: Microscope image of PMMA beads

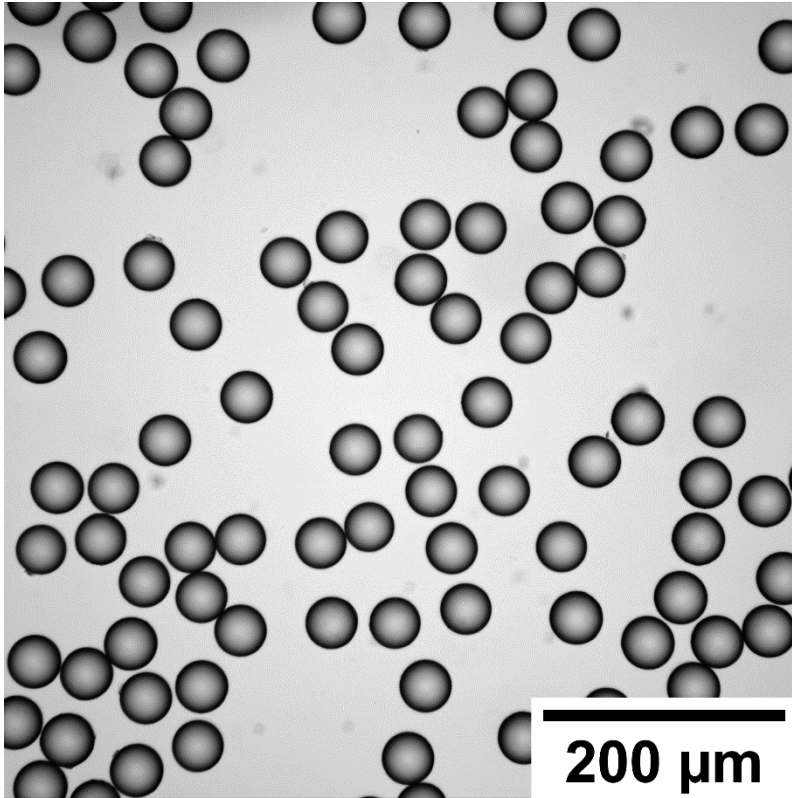


Figure S 2-2: The light microscopy image shows the monodispersity of the PMMA beads ( $d = 40 \mu\text{m}$ )

**S 2-3: SNR<sub>i</sub> of the (5.5 μm)<sup>3</sup> experiment**

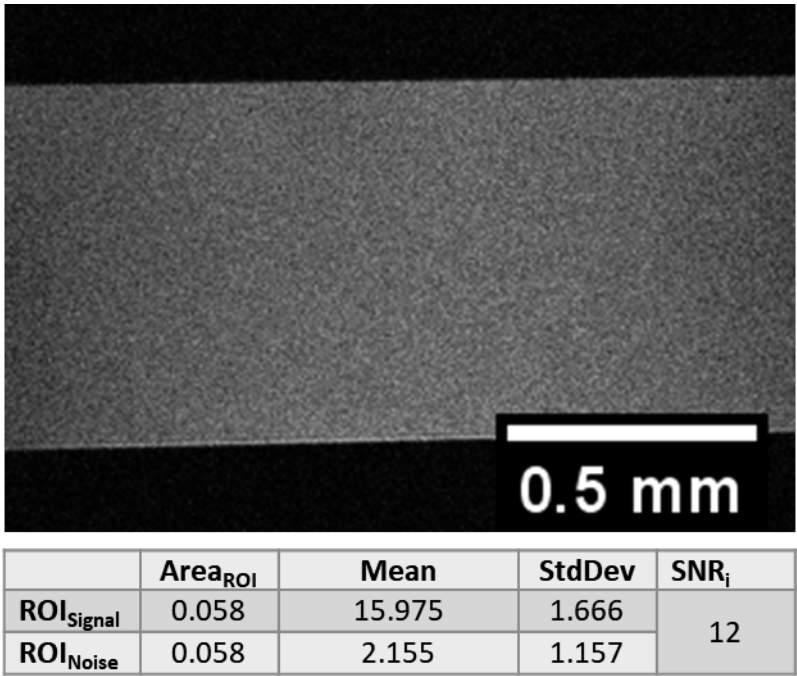


Figure S 2-3: One plane of the 3D-FLASH dataset with (5.5 μm)<sup>3</sup> isotropic resolution through the top part of the capillary is shown. Here, only doped water was present and the SNR<sub>i</sub> was determined on this slice.

**S 2-4: Video of 3D experiment of phantom**

This video is only available upon request.

## 2.8 References

1. P. T. Callaghan, *Principles of nuclear magnetic resonance microscopy* (Oxford University Press, 1993).
2. W. Kuhn, NMR Microscopy—Fundamentals, Limits and Possible Applications. *Angew. Chemie Int. Ed.* **29**, 1–19 (1990).
3. S. J. Blackband, D. L. Buckley, J. D. Bui, M. I. Phillips, NMR microscopy---beginnings and new directions. *Magn. Reson. Mater. Physics, Biol. Med.* **9**, 112–116 (1999).
4. A. R. Kherlopian, T. Song, Q. Duan, M. A. Neimark, M. J. Po, J. K. Gohagan, A. F. Laine, A review of imaging techniques for systems biology. *BMC Syst. Biol.* **2**, 74 (2008).
5. B. Driehuys, J. Nouis, A. Badea, E. Bucholz, K. Ghaghada, A. Petiet, L. W. Hedlund, Small Animal Imaging with Magnetic Resonance Microscopy. *ILARJ.* **49**, 35–53 (2008).
6. Y. Xia, J. B. Moody, N. Burton-Wurster, G. Lust, Quantitative in situ correlation between microscopic MRI and polarized light microscopy studies of articular cartilage. *Osteoarthr. Cartil.* **9**, 393–406 (2001).
7. A. Webb, Increasing the sensitivity of magnetic resonance spectroscopy and imaging. *Anal. Chem.* **84**, 9–16 (2012).
8. D. I. Hoult, R. E. Richards, The signal-to-noise ratio of the nuclear magnetic resonance experiment. *J. Magn. Reson.* **24**, 71–85 (1976).
9. K. R. Minard, R. A. Wind, Picoliter <sup>1</sup>H NMR Spectroscopy. *J. Magn. Reson.* **154**, 336–343 (2002).
10. L. Ciobanu, *Microscopic Magnetic Resonance Imaging: A Practical Perspective* (Pan Stanford Publishing Pte. Ltd., 2017).
11. A. G. Webb, Radiofrequency microcoils in magnetic resonance. *Prog. Nucl. Magn. Reson. Spectrosc.* **31**, 1–42 (1997).
12. M. T. Vlaardingerbroek, J. A. Boer, *Magnetic resonance imaging: theory and practice* (Springer Science & Business Media, 2013).
13. P. G. Morris, P. Mansfield, *NMR Imaging in Biomedicine* (Academic Press, 1986).
14. T. Oerther, “Manual - Micro Imaging for AVANCE III Systems User Guide Version 001” (2012).
15. J. Schindelin, I. Arganda-Carreras, E. Frise, V. Kaynig, M. Longair, T. Pietzsch, S. Preibisch, C. Rueden, S. Saalfeld, B. Schmid, Fiji: an open-source platform for biological-image analysis. *Nat. Methods.* **9**, 676 (2012).

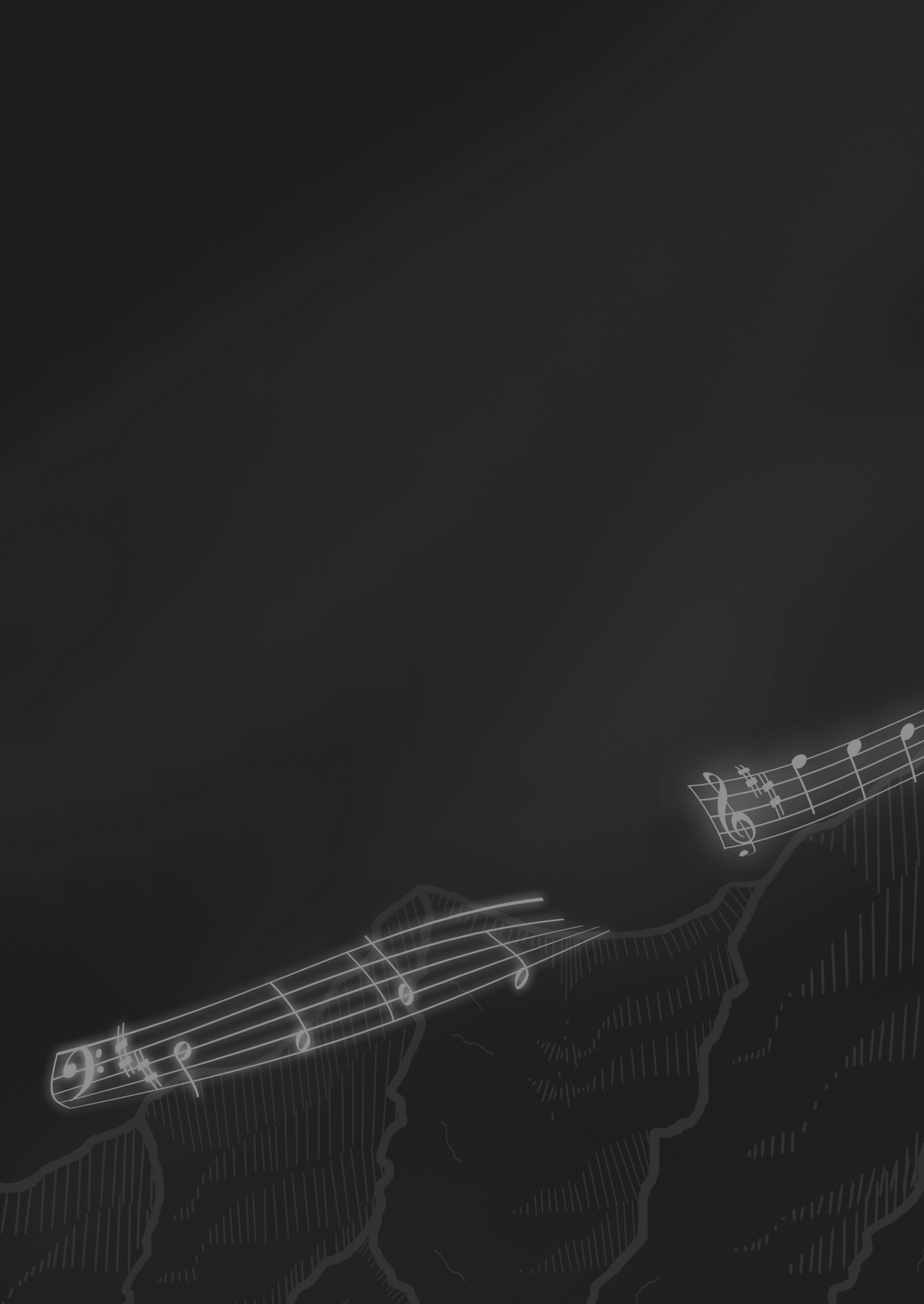
16. H. Benveniste, G. Einstein, K. R. Kim, C. Hulette, G. A. Johnson, Detection of neuritic plaques in Alzheimer's disease by magnetic resonance microscopy. *Proc. Natl. Acad. Sci.* **96**, 14079–14084 (1999).
17. H. Benveniste, S. Blackband, MR microscopy and high resolution small animal MRI: Applications in neuroscience research. *Prog. Neurobiol.* **67**, 393–420 (2002).
18. J. Mispelter, M. Lupu, A. Briguët, *NMR probeheads for biophysical and biomedical experiments: theoretical principles & practical guidelines* (Imperial College Press, 2006).
19. R. W. Brown, E. M. Haacke, Y.-C. N. Cheng, M. R. Thompson, R. Venkatesan, *Magnetic resonance imaging: physical principles and sequence design* (John Wiley & Sons, 2014).
20. D. A. Yablonskiy, E. M. Haacke, Theory of NMR signal behavior in magnetically inhomogeneous tissues: the static dephasing regime. *Magn. Reson. Med.* **32**, 749–763 (1994).
21. M. Weiger, D. Schmidig, S. Denoth, C. Massin, F. Vincent, M. Schenkel, M. Fey, NMR microscopy with isotropic resolution of 3.0  $\mu\text{m}$  using dedicated hardware and optimized methods. *Concepts Magn. Reson. Part B Magn. Reson. Eng.* **33B**, 84–93 (2008).
22. H. Y. Chen, R. Tycko, Low-temperature magnetic resonance imaging with 2.8  $\mu\text{m}$  isotropic resolution. *J. Magn. Reson.* **287**, 47–55 (2018).
23. E. Moore, R. Tycko, Micron-scale magnetic resonance imaging of both liquids and solids. *J. Magn. Reson.* **260**, 1–9 (2015).
24. S. C. Lee, K. Kim, J. Kim, J. H. Yi, S. Lee, C. Cheong, MR microscopy of micron scale structures. *Magn. Reson. Imaging.* **27**, 828–833 (2009).
25. S. C. Lee, K. Kim, J. Kim, S. Lee, H. Y. Jeong, W. K. Sung, K. S. Ha, C. Cheong, One micrometer resolution NMR microscopy. *J. Magn. Reson.* **150**, 207–213 (2001).
26. L. Ciobanu, D. Seeber, C. Pennington, 3D MR microscopy with resolution 3.7  $\mu\text{m}$  by 3.3  $\mu\text{m}$  by 3.3  $\mu\text{m}$ . *J. Magn. Reson.* **158**, 178–182 (2002).
27. H.-Y. Chen, R. Tycko, Low-temperature magnetic resonance imaging with 2.8  $\mu\text{m}$  isotropic resolution. *J. Magn. Reson.* **287**, 47–55 (2018).
28. A. G. Webb, Optimizing the point spread function in phase-encoded magnetic resonance microscopy. *Concepts Magn. Reson.* **22A**, 25–36 (2004).
29. P. T. Callaghan, C. D. Eccles, Diffusion-limited resolution in nuclear magnetic resonance microscopy. *J. Magn. Reson.* **78**, 1–8 (1988).
30. T. Neuberger, A. Webb, Radiofrequency coils for magnetic resonance microscopy. *NMR Biomed.* **22**, 975–981 (2009).

31. I. V. Mastikhin, B. J. Balcom, Centric SPRITE MRI of Biomaterials with Short  $T_2^*$ . *Encycl. Magn. Reson.* **1**, 783–788 (2012).
32. D. Xiao, B. J. Balcom, Restricted k-space sampling in pure phase encode MRI of rock core plugs. *J. Magn. Reson.* **231**, 126–132 (2013).
33. D. Xiao, B. J. Balcom, BLIPPED (BLipped Pure Phase EncoDing) high resolution MRI with low amplitude gradients. *J. Magn. Reson.* **285**, 61–67 (2017).
34. S. C. Grant, N. R. Aiken, H. D. Plant, S. Gibbs, T. H. Mareci, A. G. Webb, S. J. Blackband, NMR spectroscopy of single neurons. *Magn. Reson. Med.* **44**, 19–22 (2000).
35. S.-C. Lee, J.-H. Cho, D. Mietchen, Y.-S. Kim, K. S. Hong, C. Lee, D. Kang, K. D. Park, B.-S. Choi, C. Cheong, Subcellular in vivo  $^1\text{H}$  MR spectroscopy of *Xenopus laevis* oocytes. *Biophys. J.* **90**, 1797–1803 (2006).
36. W. Köckenberger, Nuclear magnetic resonance micro-imaging in the investigation of plant cell metabolism. *J. Exp. Bot.* **52**, 641–652 (2001).
37. M. Musse, H. Van As, NMR imaging of air spaces and metabolites in fruit and vegetables. *Mod. Magn. Reson.*, 1765–1779 (2018).
38. H. T. Edzes, D. van Dusschoten, H. Van As, Quantitative T2 Imaging of Plant Tissues By Means Of Multi-Echo MRI Microscopy. *Magn. Reson. Imaging.* **16**, 185–196 (1998).
39. R. van Schadewijk, J. R. Krug, D. Shen, K. B. S. S. Gupta, F. J. Vergeldt, T. Bisseling, A. G. Webb, H. Van As, A. H. Velders, H. J. M. de Groot, Magnetic Resonance Microscopy at Cellular Resolution and Localised Spectroscopy of *Medicago truncatula* at 22.3 Tesla. *Sci. Rep.* **10**, 1–11 (2020).
40. L. Caizán-Juanarena, J. R. Krug, F. J. Vergeldt, J. M. Kleijn, A. H. Velders, H. Van As, A. ter Heijne, 3D biofilm visualization and quantification on granular bioanodes with magnetic resonance imaging. *Water Res.*, 115059 (2019).
41. A. Leftin, J. T. Rosenberg, E. Solomon, F. C. Bejarano, S. C. Grant, L. Frydman, Ultrafast in vivo diffusion imaging of stroke at 21.1 T by spatiotemporal encoding. *Magn. Reson. Med.* **73**, 1483–1489 (2015).
42. J. Tsao, S. Kozerke, MRI temporal acceleration techniques. *J. Magn. Reson. Imaging.* **36**, 543–560 (2012).
43. P. C. M. van Zijl, N. N. Yadav, Chemical exchange saturation transfer (CEST): What is in a name and what isn't? *Magn. Reson. Med.* **65**, 927–948 (2011).
44. J.-B. Hövener, N. Schwaderlapp, T. Lickert, S. B. Duckett, R. E. Mewis, L. A. R. Highton, S. M. Kenny, G. G. R. Green, D. Leibfritz, J. G. Korvink, A hyperpolarized equilibrium for magnetic resonance. *Nat. Commun.* **4**, 2946 (2013).

45. M. S. Vinding, C. Laustsen, I. I. Maximov, L. V. Søgaard, J. H. Ardenkjær-Larsen, N. C. Nielsen, Dynamic nuclear polarization and optimal control spatial-selective  $^{13}\text{C}$  MRI and MRS. *J. Magn. Reson.* **227**, 57–61 (2013).
46. H. T. Edzes, D. Van Dusschoten, H. Van As, Quantitative T2 imaging of plant tissues by means of multi-echo MRI microscopy. *Magn. Reson. Imaging.* **16**, 185–196 (1998).



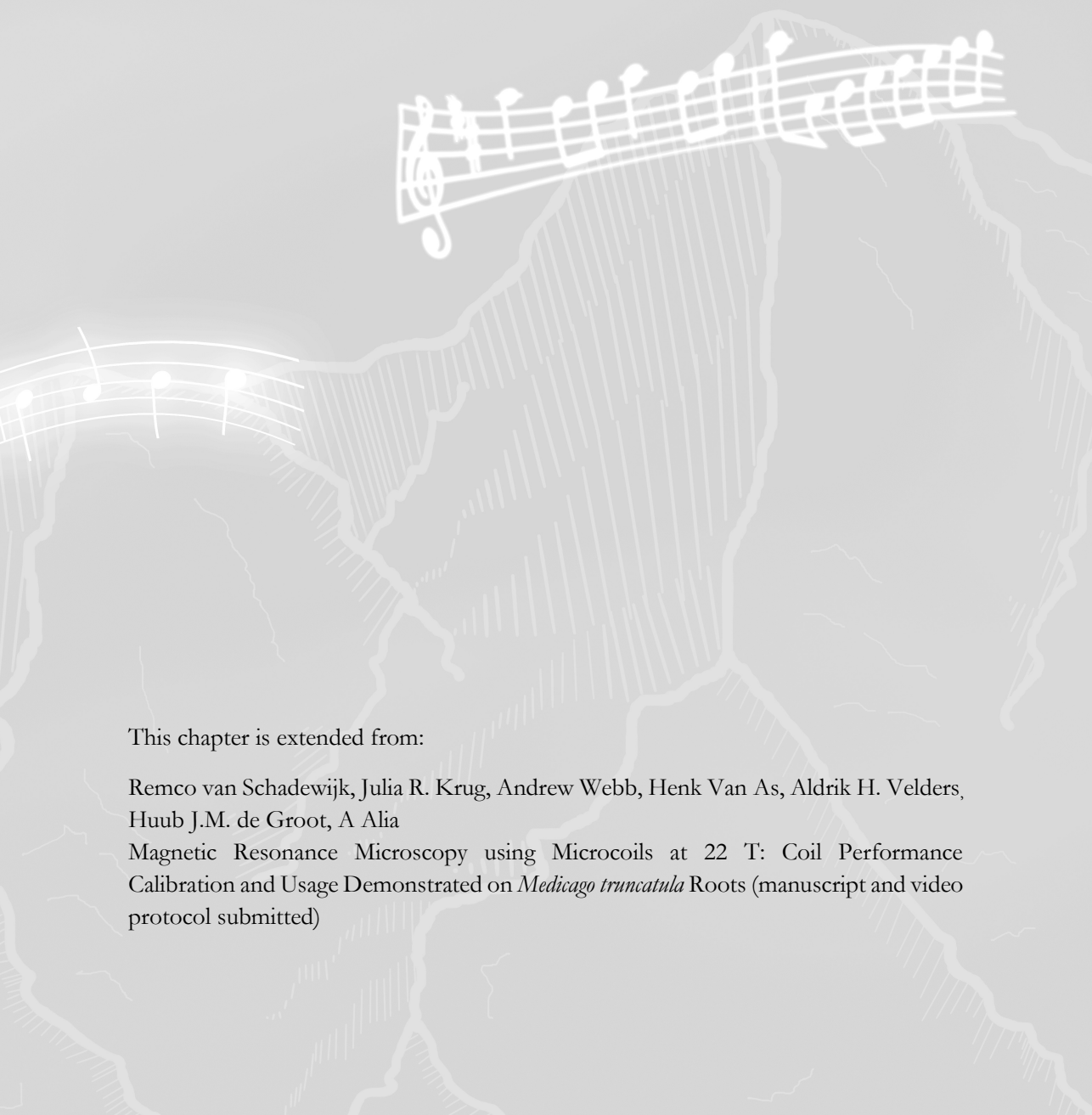




## Chapter 3

### Magnetic Resonance Microscopy using Microcoils at 22.3 T:

#### A Method Protocol for Sample Preparation and Coil Calibration



This chapter is extended from:

Remco van Schadewijk, Julia R. Krug, Andrew Webb, Henk Van As, Aldrik H. Velders, Huub J.M. de Groot, A Alia

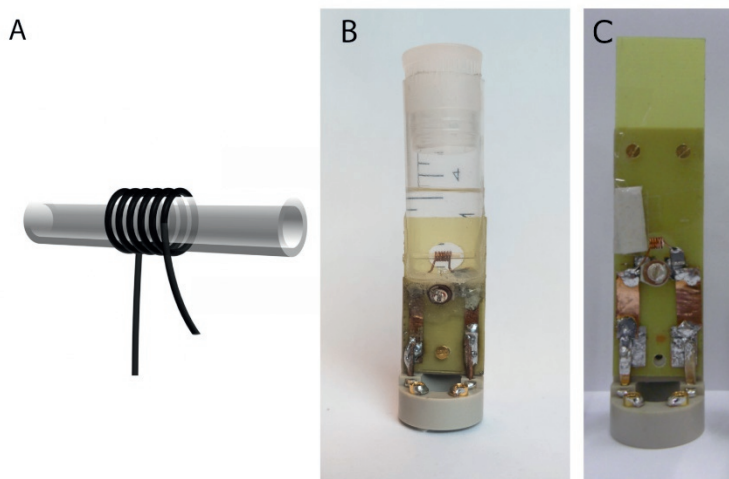
Magnetic Resonance Microscopy using Microcoils at 22 T: Coil Performance Calibration and Usage Demonstrated on *Medicago truncatula* Roots (manuscript and video protocol submitted)

### Abstract

This chapter describes a method to calibrate and use microcoils designed for ultra-high field (UHF) magnetic resonance imaging (MRI), also referred to as MR microscopy (MRM). At UHF, the Signal-to-Noise Ratio (SNR) increases. Microcoils further increase SNR by matching the size of the radiofrequency (RF) resonator to the size of the sample of interest, thereby enabling higher image resolutions in a given data acquisition time. Due to the relatively simple design, solenoid microcoils are straightforward and cheap to construct and can be easily adapted to the sample requirements. Systematically, we explain how to calibrate new or home-built microcoils, using a reference solution. The calibration steps include: 1. pulse power determination using a nutation curve, 2. estimation of RF-field homogeneity, and 3. calculating a volume-normalised SNR using standard pulse sequences. Essential steps in sample preparation for small biological samples are discussed, as well as possible mitigating factors such as magnetic susceptibility differences within biological specimens and the RF-coil. The potential of an optimised home-built solenoid coil at 22.3 T is demonstrated by high-resolution ( $13 \times 13 \times 13 \mu\text{m}^3$ , 2.2 fL) 3D imaging of a *Medicago truncatula* root sample for 20 h and 23 min with a matrix of  $128 \times 64 \times 64$  and a field-of-view of  $1.6 \times 0.8 \times 0.8 \text{ mm}^3$ . The presented protocol is written for a Bruker NMR Avance III system with a Micro5 probe and ParaVision 6.0.1/ Topspin 3.5 software. For other systems, the protocol may be used, however the approach might differ in terms of terminology and available functionalities.

### 3.1 Introduction

Magnetic Resonance Imaging (MRI) is a versatile tool to non-invasively image a wide variety of biological specimens, ranging from humans to single cells (1–3). While MRI-scanners for medical imaging applications typically use magnets with a field strength of 1.5 T to 3 T, single-cell applications are imaged at much higher field strengths (1, 3, 4). The study of specimens at resolutions below a hundred micrometres is referred to as Magnetic Resonance Microscopy (MRM) (5). MRM suffers from a low Signal-to-Noise Ratio (SNR) compared to other available microscopy or imaging techniques (*e.g.*, optical microscopy or Computer Tomography). To optimise the SNR, several approaches can be pursued (6). One approach is to use a higher magnetic field strength, while a complementary approach is to optimise the signal detector for individual samples. For the first approach, namely UHF-MRI, 22.3 T (Proton Larmor Frequency 950 MHz) is one of the highest commercially available magnetic field strengths. For the latter, the dimensions of the detector should be adjusted to match the dimensions of the sample of interest. For small samples ( $\approx 0.5$ -2 mm in diameter), *e.g.*, root tissues, solenoidal microcoils are useful as the SNR is inversely proportional to the coil diameter (6, 7). Resolutions as high as  $7.8 \times 7.8 \times 15 \mu\text{m}^3$  have been attained on animal cells using dedicated microcoils (8). A variety of microcoil geometry types exist, with planar and solenoid coils most commonly used depending on application and tissue geometry (9). For example, a method designed specifically for imaging perfused tissue has been described for planar microcoils (10). Here, we describe the characteristics of the solenoid coil, a protocol to prepare samples for microcoil MRI, as well as the calibration of a solenoid microcoil (Figure 3-1A).



**Figure 3-1:** A solenoid microcoil A.) The solenoid coil design consists of wire looped helically, typically wrapped around a capillary. The geometry and specifications of the wire, such as its thickness, coil diameter, number of windings and wire spacing, influence the coil characteristics. B.) A home-built solenoid microcoil with a reservoir for susceptibility matching fluid (Fomblin) consists of a 0.4 mm thick coated copper wire wound six times around a capillary with an outer diameter of 1.5 mm. The coil is submerged in a reservoir which is made from a syringe. Sample capillaries up to an outer diameter of 1 mm can be inserted. Two capacitors are used, a 1.5 pF capacitor in series with the inductor, and a second variable 1.5-6 pF capacitor is placed in parallel to the inductor. All components are soldered to copper tape which is supported by a fibreglass board (yellow). It is mounted on a commercial holder (grey polymer) that is modified to support the reservoir. C.) A home-built 1.5 mm not susceptibility matched microcoil (as described in Chapter 2) as reference.

The solenoid coil consists of a conducting wire looped, like a corkscrew, around a capillary holding the sample. Used in combination with the specific MR system (Materials and Methods), microcoils can be constructed using only enamelled copper wire, an assortment of capacitors, and a suitable base for soldering the components (Figure 3-1B). The major advantages are the simplicity and low cost, combined with good performance characteristics in terms of SNR per unit volume and  $B_1$  field homogeneity. The relative ease of construction enables fast iteration of coil designs and geometries. The specific requirements of solenoid microcoil design and probehead characterisation, *i.e.*, the theory of electronics, workbench measurements, and spectrometer measurements for a variety of coil geometries, have been described extensively elsewhere(7, 11–14). In the case of the system used in this chapter, the coil

is mounted on a socket of the Micro5 probe which has an own tuning and matching circuit.

Basic experimental MR parameters are highly dependent on the hardware of the system used, including gradient system, field strength, and console. Several parameters can be used to describe the system performance, of which  $90^\circ$  pulse power,  $B_1$ -homogeneity and SNR per unit volume ( $\text{SNR}/\text{mm}^3$ ), are the most practically relevant.  $\text{SNR}/\text{mm}^3$  is useful to compare the performance of different coils on the same system (15). While hardware differences across systems may exist, the uniform application of a benchmarking protocol also facilitates the comparison of system performance.

This protocol focuses on calibration and sample preparation. The stepwise characterisation of the performance of solenoid microcoils is shown: 1. calibrating the  $90^\circ$  pulse length and power 2. assessing the RF-field homogeneity and 3. calculating SNR per unit volume ( $\text{SNR}/\text{mm}^3$ ). RF-field homogeneity is essential to uniformly excite the entire region of interest with the experimentally required nutation angle (16). A standardised spin-echo measurement using a phantom is described to facilitate comparison of coil designs, which allows for optimisation of distinct applications. Phantom and biological specimen sample preparation, specific for microcoils, are described. The protocol may be implemented on any suitable narrow-bore ( $\leq 60$  mm) vertical spectrometer equipped with a microimaging system. For other systems, it can serve as a guideline and can be used with some adjustments.

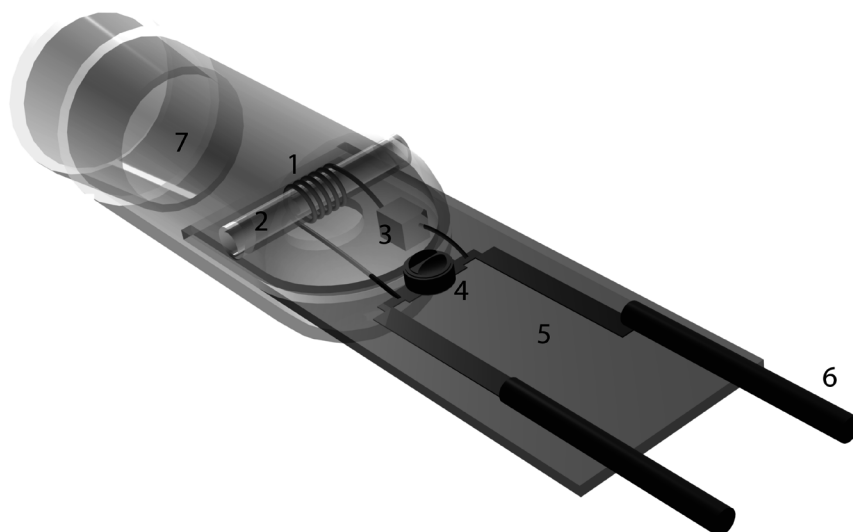
Biological sample preparation for MRI measurements is usually not very extensive since the specimen is imaged as intact as possible. However, air cavities in biological tissue can cause image artefacts due to differences in magnetic susceptibility (17). The effect increases with increasing magnetic field strength (18). Thus, air cavities should be avoided at high-field strengths, if possible, and this might require the immersion of the sample in a fluid to avoid air around the tissue and the removal of air cavities within the tissue structures. If the chosen fluid does not dissolve air cavities, vacuum infiltration might be needed (19). Specifically, when microcoils are employed, excision of the desired sample tissue might be required, followed by submerging it in a suitable fluid. This is followed by insertion of the sample into a pre-cut capillary, and finally sealing the capillary with capillary wax. Using wax as a sealant instead of glue, flame-sealing or alternatives, means that the sample may be easily extracted. This procedure is demonstrated on the root of *Medicago truncatula* a small leguminous plant. The advantage

of correlation of MRI data with optical microscopy is highlighted since MRI is non-destructive and can be followed by a destructive technique.

### **3.2 Protocol for Microcoil and Sample Preparation**

This protocol describes procedures for microcoil usage and evaluation of coil characteristics of a 1.5 mm inner diameter (ID) solenoid coil (Fig 1B). The coil used to demonstrate the protocol is housed in a susceptibility-matched reservoir, but the protocol is equally applicable to non-susceptibility-matched coils. The protocol may be adapted to other sizes and different spectrometer setups.

A solenoid coil can be built by keeping in mind design rules for the desired dimensions according to the guidelines described elsewhere (7, 20). In this specific case, a coil was used with an inner diameter of 1.5 mm, made from 0.4 mm enamelled copper wire looped around a capillary of 1.5 mm outer diameter. This solenoid is held on a base plate on which a circuit is made, consisting of a tuning capacitor (2.5 pF), a matching capacitor (1.5-6 pF) as well as copper connecting wires (Figure 3-2). The exact values of the capacitors are determined by the designated resonance frequency and the probe base circuit.



**Figure 3-2:** Solenoid coil components: 1. solenoid coil, 2. sample capillary, 3. 1.5 pF tuning capacitor, 4. variable matching capacitor, 5. fibreglass base plate, 6. copper wire leads, 7. reservoir for susceptibility-matching fluid.

The susceptibility-matched design of the coil includes a reservoir with perfluorinated liquid to reduce susceptibility mismatches between the coil material and the surrounding air, arising from the copper coil being close to the sample (21). A reservoir was made out of a plastic syringe to enclose the coil and filled with Fomblin. As the perfluorinated liquid needs to enclose the coil, the available diameter for a sample is reduced to an outer diameter of 1 mm. For ease of sample changing, the sample was prepared in smaller sample capillary with an outer diameter of 1 mm and an inner diameter of 0.7 mm. By using a smaller inner capillary, the sample can be easily prepared separate from the microcoil and easily exchanges.

The coil can be mounted on a holder which fits the Bruker Micro5 probe. In this case, we used a modified support insert equipped with the necessary connections to connect to the  $^1\text{H}$  channel of the Micro5 probe.



### 3.2.1 Reference Sample Preparation

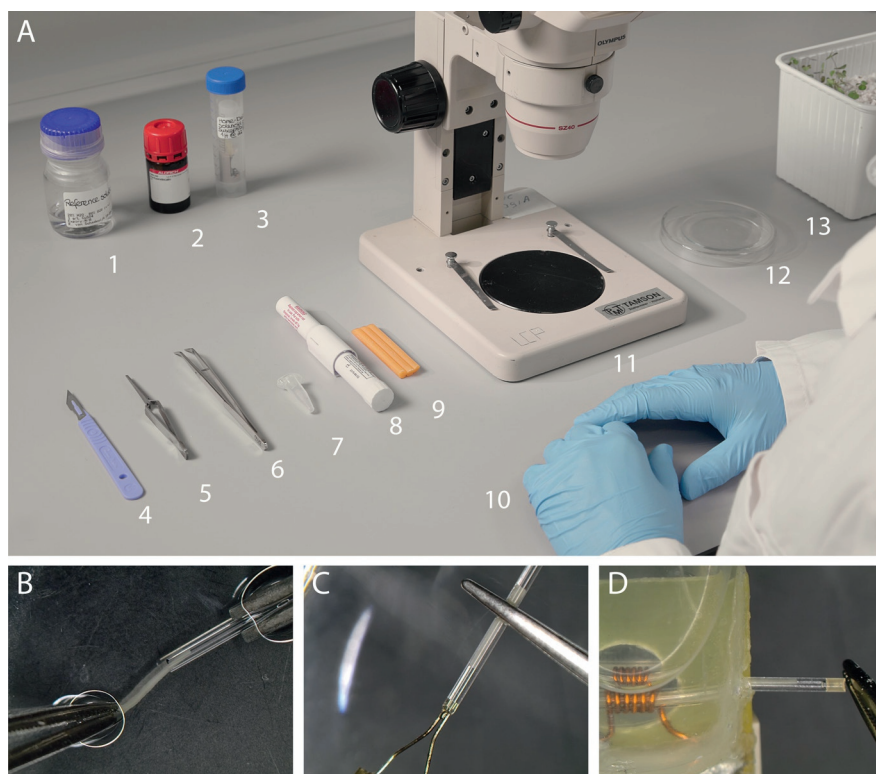
- To prepare 100 ml of the sensitivity reference solution, dissolve 156.4 mg of  $\text{CuSO}_4 \cdot 5 \text{H}_2\text{O}$  into 80 mL of  $\text{D}_2\text{O}$  contained in a 100 mL GL45 flask. Manually stir until solids are completely dissolved.
- Adjust volume to 100 ml using de-ionised water for a final concentration of  $1 \text{ g L}^{-1}$   $\text{CuSO}_4$  (anhydrous).

NOTE: The reference sample should be sealed to prevent changing the ratio of  $\text{H}_2\text{O}$ :  $\text{D}_2\text{O}$ .

- To test if the coil resonates at the desired resonance frequency, the probe base can be connected to a network analyser (i.e., <https://pocketvna.com>). An  $S_{11}$  test can be performed to test the frequency range achieved by tuning and for Q- factor measurements as described in Haase *et al.* (14).

### 3.2.2 Sample Preparation

- The necessary tools for sample preparation are shown in **Figure 3-3**.
- Capillaries of suitable outer diameter need to be cut to size, to fit inside the diameter of the microcoil holder (18 mm), and allow for repositioning (Figure 3-1B). Use a ceramic cutter to make an incision every 10-12 mm and break carefully on the incision point.



**Figure 3-3:** Sample preparation under a stereomicroscope A.) Items needed for the preparation of microcoils. From left to right: 1.  $\text{CuSO}_4$  reference solution, 2. perfluorodecalin, 3. microcoil, 4. scalpel, 5. positive tension tweezers, 6. tweezers, 7. capillaries outer diameter = 1000  $\mu\text{m}$ , 8. wax pen, 9. capillary wax, 10. nitrile gloves, 11. stereomicroscope, 12. watch glass with petri dish cover, 13. plant material in growth substrate. Not shown: 2 mL syringe with  $\phi$  0.8 x 40 mm needle and fine tissue paper. B.) Close up of sample insertion into a capillary using tweezers, while both are kept submerged. C.) Sealing of the capillary using molten wax. D.) Insertion of the prepared capillary into the microcoil.

### **Reference Sample**

- Add 1 ml  $\text{CuSO}_4$  solution to a watch dish under a stereomicroscope.
- Use tweezers and the stereo microscope to bring a pre-cut capillary in contact with the surface of the  $\text{CuSO}_4$  solution inside the watch glass, allowing capillary action to fill the capillary.
- Remove circa 1 mm of liquid from both ends of the capillary using fine tissue paper.
- Melt a small volume of capillary wax using a wax pen. Apply wax on either side while taking care to eliminate any possible air pockets with the capillary (Figure 3-3C). When the wax has hardened, it will become opaque.
- NOTE: Avoid overheating wax or capillary as this may cause explosive boil off as well as cavitation pockets when the finished sample cools.
- Remove excess wax from the exterior of the capillary with a scalpel and wipe clean with fine tissue paper.

### **Biological Sample**

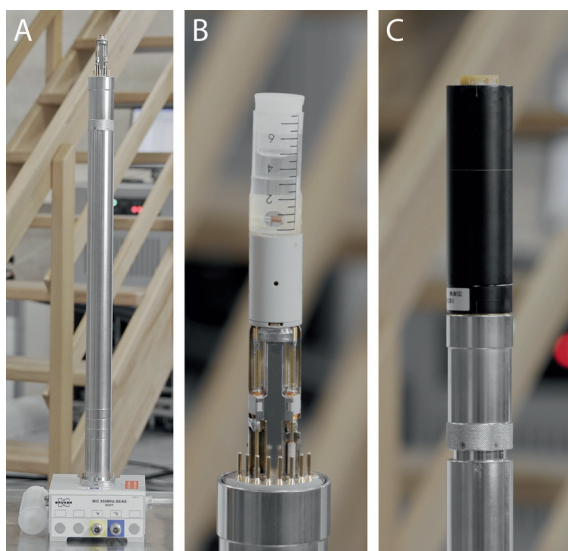
- Place 1 ml of perfluorodecalin (PFD) inside a watch glass under a stereomicroscope. PFD will infiltrate a biological specimen without entering the intact cells and thereby reduce the number of air cavities. Immediately cover the watch glass with a petri dish lid to prevent evaporative loss, until the PFD is needed. NOTE: PFD is highly volatile and a potent long-term greenhouse gas(22). When its oxygen-dissolving properties and its low viscosity are not required, it may be substituted with Fomblin, a perfluoroether which also gives no observable  $^1\text{H}$  signal, but which does not evaporate as quickly(21).
- Use tweezers and a stereo microscope, to bring a pre-cut capillary in contact with the surface of the PFD inside the watch glass, allowing capillary action to fill the capillary fully. Release the capillary into the watch glass so that it becomes fully submerged.
- Next, carefully extract a whole root system from its soil or soil replacement. Clean the root sample meticulously. Photograph if needed for future reference. Select and excise a root section using a scalpel.
- To reduce the presence of air pockets within biological samples:

- Place the sample into a 1.5 ml Eppendorf tube containing a suitable buffer solution. Leave the tube cap off, then apply parafilm to seal the opening of the tube. Then, punch a hole in the with a sharp tool to allow for ventilation of the tube.
- Place the sample tube in a vacuum chamber, seal the chamber, connect a vacuum pump to the chamber, and apply vacuum for 30 minutes. Air bubbles may be seen escaping the sample.
- Using tweezers and stereomicroscope, submerge the sample in infiltration medium prepared previously. Wash the sample of potential debris.
- Next, insert the sample into the capillary using tweezers, while both capillary and sample are fully submerged in order to avoid the inclusion of air bubbles. A smaller capillary or syringe may serve as a pushing rod (Figure 3-3B).
- Take the sample capillary from the medium watch glass, using tweezers. In the case of PFD, cover the petri-dish lid.
- Remove circa 1 mm of liquid from both ends of the capillary using fine tissue paper.
- Melt a small volume of capillary wax using a wax pen. Apply wax on either side while taking care to eliminate any possible air pockets with the capillary (Figure 3-3C). When the wax has hardened, it will become opaque.
- NOTE: Avoid overheating wax or capillary as this may cause explosive boil off as well as cavitation pockets when the finished sample cools.
- Remove excess wax from the exterior of the capillary with a scalpel and wipe clean with fine tissue paper.

### 3.2.3 Mounting Sample

- Place a microcoil underneath the stereo microscope and insert the sample using tweezers while immobilising the microcoil (Figure 3-3D).
- Position the sample in the centre of the coil by sliding the capillary inside the solenoid coil.
- Optionally, apply scotch tape to fix the position of the capillary.
- Inspect the capillary to ensure no air bubbles are visible inside the solenoid coil, to avoid MR signal destruction caused by susceptibility differences.

- Place the microcoil on the socket of the probe base (Figure 3-4A & B).



**Figure 3-4:** The component of a micro-imaging probe. A) Micro5 probe base, containing all necessary connections for water cooling, heating, temperature sensors, gradient power, RF (co-axial connector visible) and optionally probe identification (PICS). Underneath the probe base are knobs that allow for adjusting the variable tuning and matching capacitors, as well as retaining screws to hold the probe in place inside the spectrometer. B) The home-built microcoil mounting atop the probe-base. Note the variable capacitors (white ceramic) integrated in the probe-base that allow for tuning and matching. C) Integrated 3-axial gradient mounted on the probe base with water-cooling receptacles and gold-plated contacts for grounding the gradient.

- Carefully slide gradient coils over the microcoil while matching the water-cooling connectors of the gradient to that of the probe base (Figure 3-4C). (Note: This step applies for a Micro5 probe only. In the case of a Micro2.5 or a Biospect system, the gradients are on a separate socket from the coil)

### 3.3 Determining Coil Characteristics

- If the coil is tested for the first time, we recommend using the reference sample solution to create a homogeneous sample, which is useful for power calibration and  $B_1$  homogeneity tests. Also, potential susceptibility problems due to the coil wires may be tested easily with this reference sample.

- Insert the probe into the magnet and connect all cables.
- Set desired water-cooling temperature (recommended 298 K) for the water-cooling unit (BCU20).
- Set the target temperature (298 K) and the target gas flow (300 L h<sup>-1</sup>). The gas flow might be different for a different coil design or sample volume. This instruction applies only to systems with a temperature control system.

NOTE: The next steps outside of the magnet are only necessary when testing novel (home-built) coils.

- Connect the probe using a 50  $\Omega$  coaxial cable to a network analyser with a suitably wide sweep width (400 MHz), centred on the designated resonance frequency.
- Observe the resonant modes by adjusting the matching and tuning capacitors of the probe base.
- Tune and match the resonant mode to the desired frequency.
- Optionally, determine the coil quality factor (Q-factor) on a network analyser. One method to obtain the quality factor is to use a coupling network and dividing the centre frequency by the width of the resonance peak at -3 dB (*i.e.*,)(14). Some network analysers have Q-factor determination built-in.

NOTE: For the next steps, the coil has to be inserted into the magnet, and the steps apply to all coils.

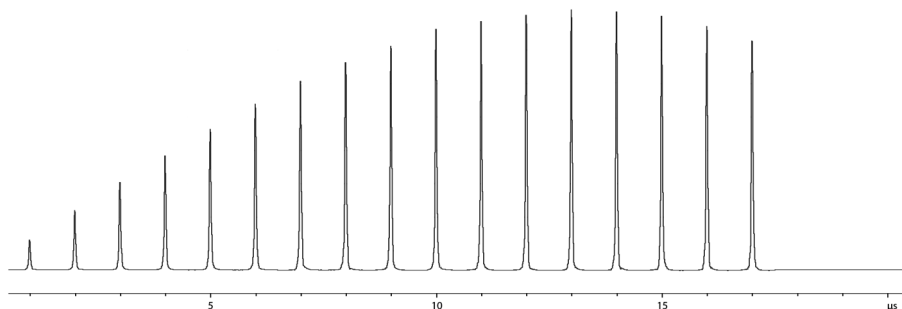
- Initiate a wobble curve and adjust the tuning and matching as necessary. It is recommended to set any tuning and matching capacitors to the midpoint of their range for new coils. Therefore, using a high spectral sweep width is recommended. In some cases, it might be more convenient to tune and match the coil outside the magnet on a network analyser.
- Select appropriate coil configuration if it is available in the imaging software (*i.e.*, ParaVision). Else, create a new coil configuration matching the specifications of the coil, *e.g.*, single tuned or double-tuned, according to the manual of your system. Estimations for the safe limits for this solenoid microcoil used in this research with 1.5 mm inner diameter in size is 1 ms at 1 W peak power and 1 mW continuous power.

CAUTION: the small capacitors (typically 1 mm in size) needed for microcoils are highly sensitive and easily damaged by high voltages. Automated pulse power determination might not function with non-standard coils, and too high powers could

cause damage to the coil or other parts of the spectrometer. Therefore, manual adjustments are recommended.

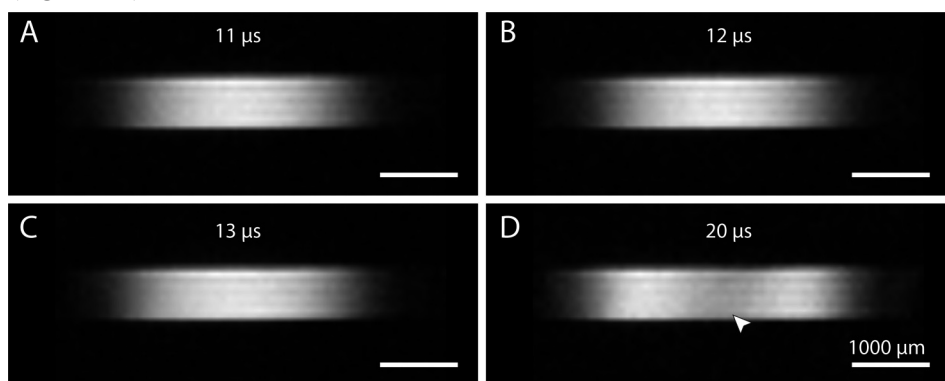
### 3.3.1 90°-pulse Length and Power Determination and RF-field Homogeneity

- A nutation curve should be recorded in Topspin for a new coil to obtain an indication of the correct RF-power for the coil (Figure 3-5). Using an FID-experiment in the absence of gradient encoding, the RF-pulse length is varied systematically while the pulse power is kept constant. The ideal pulse length is the pulse length, where the signal intensity reaches the maximum. If testing a new coil, use a 10  $\mu\text{s}$  pulse with a very low power compared to the expected order of magnitude first and start increasing the pulse power gradually. In case the power is much higher than expected for the combination of coil characteristics and spectrometer, this is already an indication that the wrong resonant mode has been selected. For a coil with a homogeneous  $B_1$ -field, like a solenoid coil, the 180° pulse can also be determined where the signal intensity decreases to zero (23).



**Figure 3-5:** Nutation curve A nutation curve is acquired to determine the reference pulse power. The reference pulse power (90° pulse) is defined as the combination of power and pulse length needed to generate a  $B_1$  field that flips all available magnetisation in the z-direction to the transverse plane. A series of spectra is recorded in the absence of gradient encoding. With each pulse, either pulse length or pulse power is incremented. Here the pulse power is set to 0.6 W, while the pulse length is incremented by 1  $\mu\text{s}$  each time. The maximum signal intensity indicates the 90° pulse, around 12-13  $\mu\text{s}$ . The 180° pulse may also be determined in this way using the minimum intensity.

- Set the determined  $90^\circ$  pulse power into the adjustment card of the created study (In ParaVision, the reference power adjustment card may be used to enter the hard pulse power).
- Use a Localiser scan with 3 slices, one slice in each of the three primary axes, to locate the position of the coil within the magnet. Starting with a large field-of-view is recommended. If the sample is precisely in the centre of the gradient system, the Localizer scan will show the sample. If the coil or sample is not centred in the image slices or missing, the localiser scan might need to be adjusted.
- NOTE: If multiple resonant modes are observed in the resonance (wobble) curve, repeat the above steps for each resonant mode to determine the most sensitive one.
- A complementary way to find the correct  $90^\circ$  pulse is based on image evaluation: Once an approximate pulse power is determined, one could vary the pulse powers gradually to check the image for  $B_1$ -field homogeneity. For some coils, the  $90^\circ$  pulse power determined using the nutation curve could be overestimated, which leads to over-tipping in the homogeneous region of the  $B_1$  field. The pulse reference pulse may then be reduced, and the new images can be checked against the previous images (Figure 3-6).



**Figure 3-6:** Visual determination of the  $90^\circ$  pulse length. Once an approximate reference pulse power has been found using a nutation curve, it may be checked visually by varying the pulse length. Depending on the coil, the  $B_1$  field may be more or less sensitive to changes A)  $11\ \mu\text{s}$  pulse length B)  $12\ \mu\text{s}$  pulse length, optimal for this coil. C)  $13\ \mu\text{s}$  pulse length. D)  $20\ \mu\text{s}$  pulse length. If the pulse power is set too high, over-tipping may occur, thereby reducing image intensity in the centre of the coil (arrowhead). The increased  $B_1$  field also increases the range of the coil, as can be observed in the width of the image.



### 3.3.2 $B_0$ -field Homogeneity

- Select a shim file for the largest volume coil of the imaging probe if it is available. If starting from a coil that has been used previously, use an available shim file. If both options are not available, start with all shim values set to 0.
- Manually shim the magnetic field based on the FID signal. A recommended order for initial shimming is Z-Z2-Z-X-Y-Z-Z2-Z-XY-XZ-YZ-Z. In the case of a solenoid, the main symmetry-axis is in the XY-plane. Therefore, shims in different directions might be more sensitive for this coil configuration. Higher-order shims have a small effect and may be ignored.
- A more detailed overview of shimming strategies for each experiment can be found in section 3.4.2.

### 3.3.3 Calculation of Volume-normalised SNR

- Next, a volume-normalised SNR must be calculated to allow for comparison of microcoil characteristics across different systems, adapted from the manufacturer's protocol (15). For our microcoils we used a spin-echo sequence with the following parameters: field-of-view (FOV) 6 mm x 6 mm, repetition time (TR) 1000 ms, echo time (TE) 7 ms, matrix size 256 x 256 and slice thickness 0.5 mm. To compare the SNR with an identical experiment on a different coil, the receiver gain should be identical in both experiments. To this end, we adjusted the slice thickness so that the receiver gain was 101 in all experiments. Next, adjust the number of slices so that slices extend beyond the region of B<sub>1</sub>-field homogeneity. Record the images without signal averaging if possible.
- The volume-normalised SNR (SNR/mm<sup>3</sup>) can be determined in two steps.
- First, the voxel volume ( $V_{\text{voxel}}$ ) is calculated (Eq. 3-1):

**Equation 3-1:** Formula to calculate the voxel volume ( $V_{\text{voxel}}$ ) by multiplying the dimensions of the voxel in-plane ( $D_x$  and  $D_y$ ) with the dimension in the slice direction ( $D_{\text{slice}}$ ) for a 2D experiment, for a 3D experiment  $D_{\text{slice}}$  can be replaced by  $D_z$

$$V_{\text{Voxel}} = D_x \times D_y \times D_{\text{slice}}$$

- Second, by selecting regions of interest, determine the signal intensity ( $\mu$ ) and standard deviation ( $\sigma_{\text{noise}}$ ) of the sample (i.e. the signal) and a region outside the sample (i.e. the noise). Either the spectrometer control software or general-purpose image processing software may be used for these calculations (i.e. MATLAB or ImageJ). The values may then be used to calculate a volume-normalised SNR (Eq. 3-2):

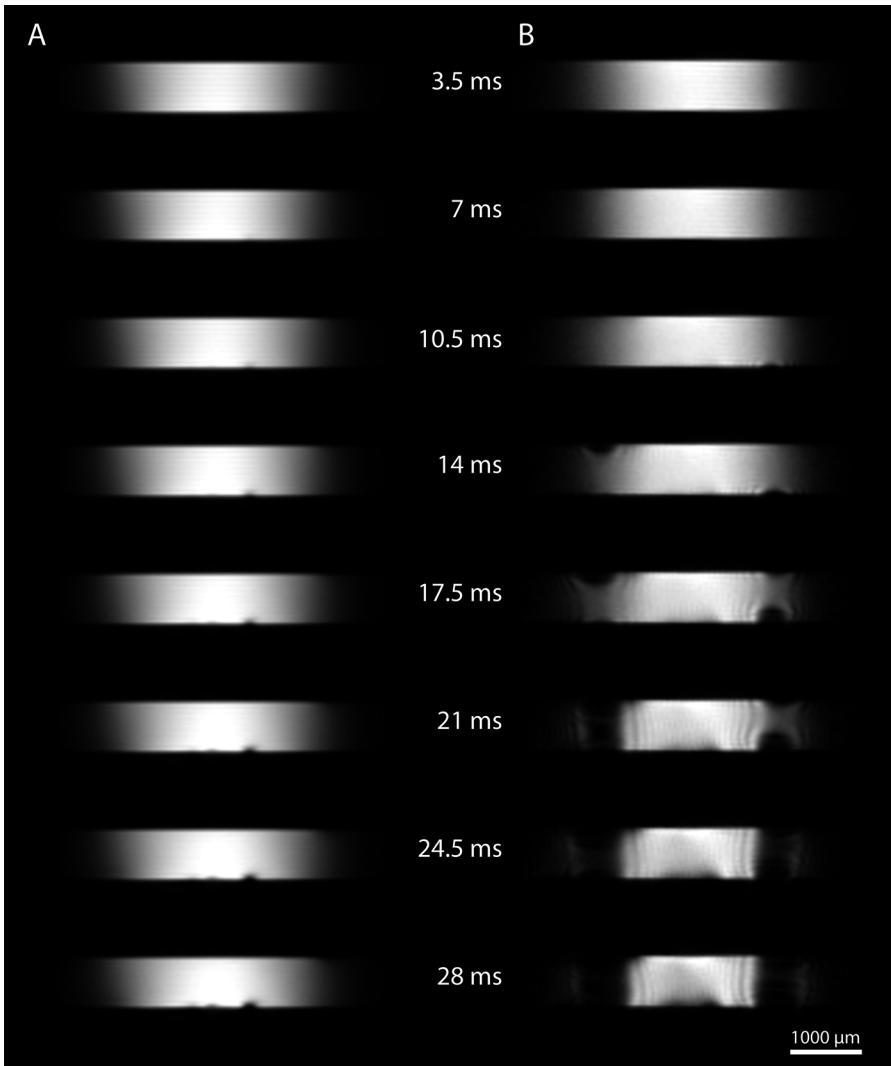
**Equation 3-2:** The volume-normalized SNR ( $\text{SNR}_v$ ) can be calculated by subtracting the mean value of the noise  $\mu_{\text{noise}}$  from the mean value of the region of interest (ROI) of the signal  $\mu_{\text{ROI}}$  divided by the standard deviation  $\sigma_{\text{noise}}$  times the voxel volume  $V_{\text{voxel}}$

$$\text{SNR}_v = \frac{\mu_{\text{ROI}} - \mu_{\text{noise}}}{\sigma_{\text{noise}} \times V_{\text{voxel}}}$$

- When comparing the SNR of coils at different magnetic field strengths, the relaxation properties of the phantom would need to be measured (24), unless a very long repetition time (TR) and very short echo time (TE) are used.

NOTE: The units for  $D_x$ ,  $D_y$  and  $D_{\text{slice}}$  are in mm. This calculation can likewise be performed for a series of slices.

- Check for susceptibility problems due to magnetic field inhomogeneities: load and run a multiple gradient-echo (MGE) sequence (Figure 3-7). Magnetic field inhomogeneities due to susceptibility differences are visible in the images with higher echo times as the gradient echo does not refocus spins which dephase due to static field inhomogeneities. This way inhomogeneities in the sample may be visualised (due to, *e.g.*, air cavities in the sample), as well as  $B_0$ -field inhomogeneities introduced by the coil material. The following parameters are suggested, to be adjusted depending on the specifications of the spectrometer and coil used: repetition time 200 ms, echo time 3.5 ms with 48 echoes, echo spacing 3.5 ms, flip angle  $30^\circ$  and matrix size 128 x 128.



**Figure 3-7:** RF homogeneity evaluated by gradient-echo imaging: A Multiple Gradient Echo (MGE) sequence is used to evaluate RF ( $B_1$ -Field) homogeneity using a series of gradient echoes. Basic parameters were: repetition time 200 ms, echo time 3.5 ms with the number of echoes 48, echo spacing 3.5 ms, 64 averages, acquisition time 27 m 18 s, flip angle  $30^\circ$ . Field-of-view was  $5 \times 5$  mm, matrix  $128 \times 128$ , resolution  $39 \times 39 \times 200 \mu\text{m}$  A) Susceptibility-matched coil. The susceptibility matching fluid (Fomblin) surrounding the RF coil reduces susceptibility effects due to the coil wire. Small air bubbles cause loss of signal as the echo time increases, B) An RF-coil (not susceptibility matched) with equal coil diameter. At longer echo times, increasing artefacts caused by  $B_0$  field inhomogeneity are observed.

### 3.4 Magnetic Resonance Imaging: A Comprehensive Overview for Starting with a Readily Calibrated System

The protocol as mentioned above should be followed when starting to measure a new sample at ultra-high field and using a previously shimmed and calibrated coil. The following steps should be taken into account when inserting a new sample and are applicable to a Bruker system.

#### 3.4.1. Preparing for the Localizer Scan

- Tuning and matching of the RF-coil
- Load in the most optimized shim file in ParaVision
- Basic frequency adjustment can be done in the adjustment platform in ParaVision. This adjusts the spectrometer reference frequency to the frequency of the dominant resonance, which is the proton resonance frequency of water protons for most biological specimens (25).
- Shimming – Optimizing the static magnetic field homogeneity
  - For a microcoil, this should be done manually, as described above (in step 3.3.2). The automatic shimming procedure may be tried, but likely fails due to shim overpowering. When the coil or sample has a z-symmetry the automatic shim is usually a good starting point.
- Basic frequency adjustment should be repeated after each shim optimization.
- Reference power – Determine the correct 90° pulse

**Using ParaVision:** For larger volumes, the automatic reference pulse power might be sufficient, but for samples with a smaller volume or a complex geometry, the selected volume on which the reference calibration might be adjusted in the Adjustment platform.

**Using Topspin:** In Topspin, the 90° pulse can be adjusted using a non-localized zg-sequence. The nutation curve can be recorded with the macro 'popt' to determine the exact value of the 90° pulse, which should be relatively close to the previously determined value during the coil calibration. This value can then manually be added in the adjustment platform in ParaVision. For coils with an inhomogeneous B<sub>1</sub>-field, the 90°-pulse value should be checked visually with a spin-echo sequence. To this end, the pulse power should be varied in different experiments and the resulting images can be evaluated (see Figure 3-

6) to estimate whether the most intense region coincides with the region of interest.

- Receiver gain adjustment - Caution: When cloning an existing scan, the receiver gain is not maintained but reinitialized to 64.

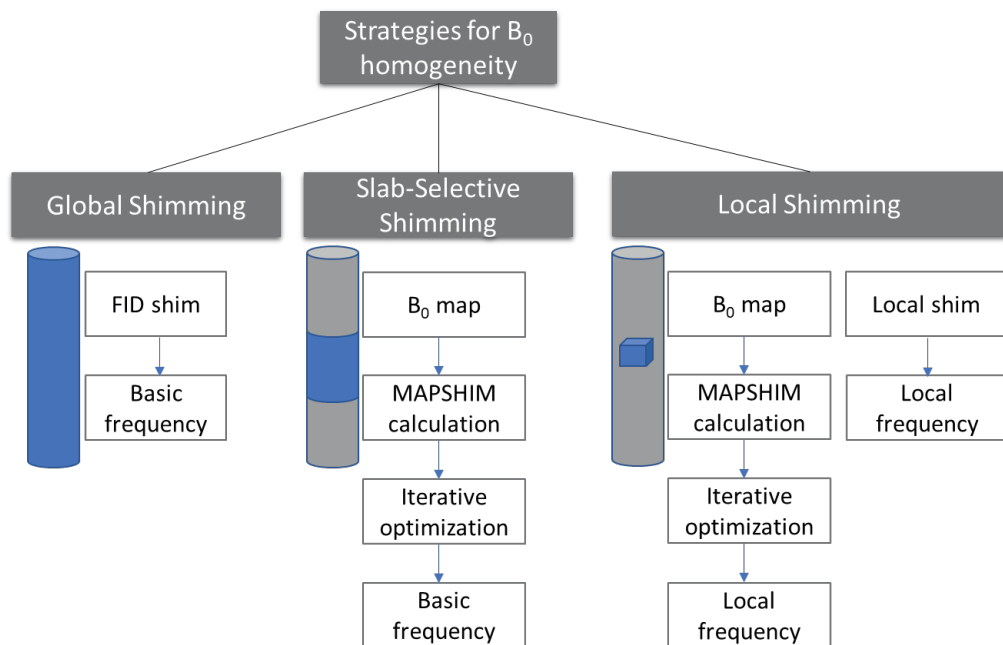
- Start measuring with 'GOP'

In the localizer-image, which usually consists of three orthogonal slices that intersect in the centre of the rf-coil, some factors can be investigated, namely the  $B_0$ -field,  $B_1$ -field homogeneity and the area where the coil is most sensitive.

### 3.4.2 Shim Adjustments for Different Scans

For different MR sequences, the adjustments depend on the method, e.g. global shim for multi-slice imaging or voxel-specific shimming for single-voxel localized spectroscopy. In Figure 3-8, the different shim adjustment strategies for different purposes are depicted.

For global shimming, an automatic FID-shim procedure can be used and adjusted to include different shimming steps. The first iteration should be with a large shim range, to prevent to enter a local optimum. Alternatively, a manual shimming can be employed using 'gs' in Topspin. Manual shimming is especially useful when the automatic Paravision procedure fails due to the overpowering of the shim channels. The slab-selective shimming is very useful when the magnetic field in a particular slice needs to be more homogeneous. This is very important for high-field spectroscopic imaging experiments. The MAPSHIM calculation on a larger area, followed by an iterative correction, has proved to be useful. For Localized Spectroscopy applications, MAPSHIM can be used as well. In this case, a two-step strategy has proven useful by first starting from a significantly large voxel size and then decreasing in a second shim adjustment round. Alternatively, local shimming on the voxel can be used.



**Figure 3-8:** Scheme of adjustment strategies for different MR experiments.

### 3.4.3 High-resolution Imaging

- Run a 3D-FLASH experiment with the following suggested parameters: repetition time 70 ms, echo time 2.5 ms, matrix size of 128 x 64 x 64, field-of-view 1.6 x 0.8 x 0.8 mm, and receiver bandwidth 50 kHz. Adjust the FOV if necessary, covering the whole object in both phase-encoding directions to avoid aliasing, which manifests as a wrap-around artefact (26).

## 3.5 Representative Results

### Coil Characterisation

Upon successful tuning and matching of a coil, its performance may be characterised by the coil quality factor (Q-factor calculated by  $Q = \omega L/R$  (14)), 90° reference pulse, and the volume-normalised SNR/mm<sup>3</sup>. For the 1.5 mm ID susceptibility-matched solenoid coil demonstrated here, the Q-factor (not loaded with a sample) was 244, compared to 561 for a 5 mm birdcage coil.

The reference 90° pulse was 11 μs at a power level of 0.6 W; cf. 5 μs at 45 W for a 5 mm birdcage coil. See also Figure 3-5. This 90° pulse length equates to an RF field strength ( $B_1$ ), using ( $B_1 = \pi/2\gamma\tau$ ), of 0.53 mT for the microcoil and 1.17 mT for the birdcage coil (14). Since the pulse power levels (P) differ, coils may be compared in terms of transmit efficiency ( $B_1/\sqrt{P}$ ): 0.69 mT/W<sup>1/2</sup> and 0.18 mT/W<sup>1/2</sup> for the microcoil and birdcage, respectively (14). Comparing using the 90° pulse, the microcoil is found to be a factor  $\approx 4$  times more sensitive than the birdcage coil.

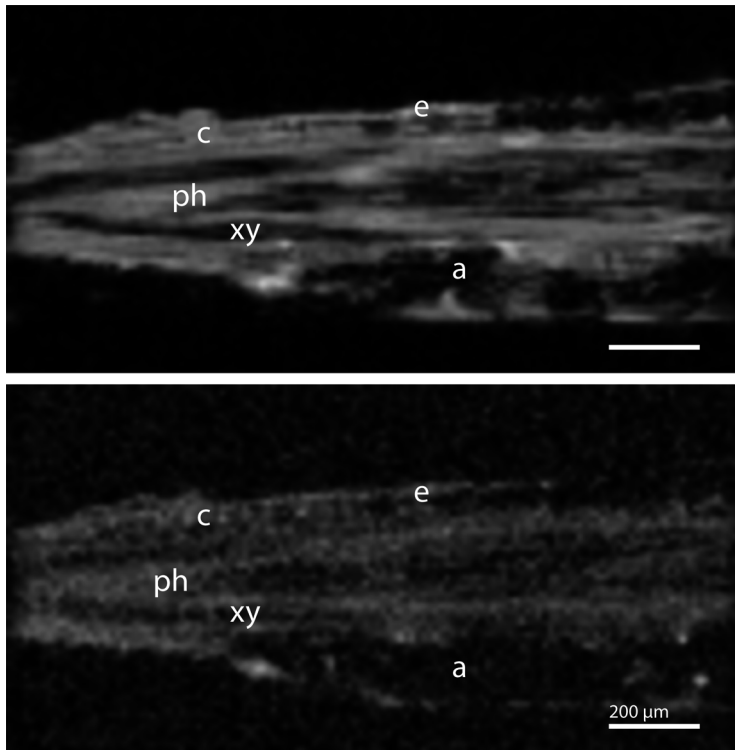
### Effect of Susceptibility Matching

At ultra-high field strengths, sample and coil susceptibility become a dominant factor for image quality, as seen in Figure 3-7. Compared to a coil lacking a susceptibility matching fluid reservoir, the signal is retained longer and more homogeneously in a reference sample. However, due to the susceptibility reservoir, the maximum sample dimensions decrease with respect to the coil without the reservoir.

### High-resolution Imaging

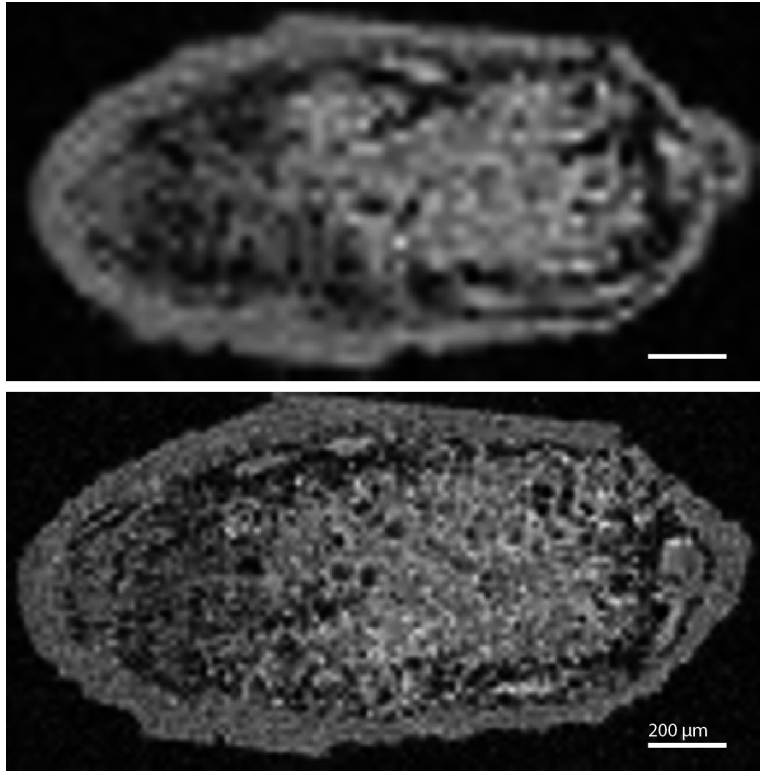
A high resolution of 13 x 13 x 13 μm<sup>3</sup> of a *Medicago truncatula* root specimen was attained in 20 hours and 23 minutes (Figure 3-9). Starting from the surface of the root, the root cortex is seen, along with some residual water on the outside of the root. Furthermore, the xylem is observed as a dark band enclosing the phloem. Some air pockets are observed as dark spots with complete signal loss.





**Figure 3-9:** 3D imaging of a *Medicago truncatula* root section. A.) FLASH image. Several features of the root section can be distinguished, including the epidermis (e), cortex (c), phloem (ph) and xylem (xy). Air pockets (a) in the root cause complete signal loss. Basic parameters were as follows: Repetition time 70 ms, echo time 2.5 ms, 256 averages, acquisition time 20 h 23 m. Resolution  $13 \times 13 \times 13 \mu\text{m}^3$ . Matrix size was  $128 \times 64 \times 64$  and field of view  $1.6 \times 0.8 \times 0.8 \text{ mm}$ . Receiver bandwidth 50 kHz. B.) MSME image. Basic parameters were as follows: Repetition time 500 ms, echo time 5.2 ms, 28 averages, acquisition time 15 h 55 m. Resolution  $13 \times 13 \times 13 \mu\text{m}^3$ . Matrix size was  $128 \times 64 \times 64$  and field of view  $1.6 \times 0.8 \times 0.8 \text{ mm}$ . Receiver bandwidth 70 kHz.

Symbiotic root nodules of *M. truncatula* may also be imaged using this protocol (Figure 3-10). Using a slightly larger, non-susceptibility matched coil (inner diameter  $1500 \mu\text{m}$ ), images with a resolution of up to  $16 \times 16 \times 16 \mu\text{m}^3$  were obtained in 33 minutes.



**Figure 3-10:** 3D imaging of a *Medicago truncatula* root nodule. A.) A plane is shown of a low-resolution 3D-experiment. Basic parameters were as follows: Repetition time 60 ms, echo time 2.3 ms, 4 averages, acquisition time 4 m. Resolution  $31 \times 31 \times 31 \mu\text{m}^3$ . Matrix size was  $64 \times 32 \times 32$  and field of view  $2 \times 1 \times 1 \text{ mm}$ . Receiver bandwidth 50 kHz. B.) A plane is shown of a high-resolution 3D-experiment. Basic parameters were as follows: Repetition time 60 ms, echo time 2.3 ms, 8 averages, acquisition time 33 m. Resolution  $16 \times 16 \times 16 \mu\text{m}^3$ . Matrix size was  $128 \times 64 \times 64$  and field of view  $2 \times 1 \times 1 \text{ mm}$ . Receiver bandwidth 50 kHz.

### 3.6 Discussion

While solenoid microcoils are relatively easy to fabricate, the sample preparation is more complicated than for 5 mm birdcage coils. In addition to submerging and sealing of the capillary containing the specimen, any movement of the specimen must be avoided inside the horizontal coil. Customizing the capillary diameter or using agar gel to confine the specimen might be necessary.

As microcoils are ideally very close to the sample, the magnetic susceptibility differences between the surrounding medium (e.g., air) and the wire can cause additional signal loss. For this reason, we presented a susceptibility-matched coil, by submerging the wire in fluorinated liquid (Fomblin or FC-43). An alternative approach for constructing a susceptibility matched coil is to use susceptibility-matched wire (27). Furthermore, only susceptibility issues due to the coil are addressed with this approach.

Susceptibility mismatches inside the sample (e.g., due to air cavities) remain challenging. Air pockets or bubbles pose an experimental challenge that causes extensive signal loss, caused by susceptibility differences at the interface of the air and the fluid or specimen (17) (Figure 3-7B). An important aspect for successful sample preparation is submersion of both sample and capillary. However, even small bubbles can cause signal losses, especially for gradient echo type sequences. Mobile air bubbles can migrate through the capillary until they are in contact with the sample. Some of these effects can be alleviated by slightly tilting the capillary so that one end is higher than the other. Tilting ensures potential air bubbles are held in place at the higher end, without disturbing the sample. For the air cavities inside the sample, PFD was used to fill up the intercellular air cavities (28) while not penetrating the cell membranes. However, even with this approach, we were not able to remove all air cavities. Additionally, this approach means that we need an additional agent, which is usually not preferred due to the desire to study a system as non-invasive as possible.

The cylindrical shape of capillaries means that perfusion setups should be viable, especially for tissues vulnerable to decay such as biopsies or studying processes in living root material. A perfusion setup could be realised in two steps. First, by connecting and a medium feed tube and drain tube at either side of the capillary would be sufficient to create a chemostat. Second, the addition of an indentation in the sample capillary could hold the sample in place against the direction of flow. This analogous to a protocol published for planar microcoils (10).

### 3.7 Conclusion and Outlook

We have demonstrated a method for imaging plant material using dedicated microcoils on an ultra-high field NMR spectrometer. Relatively large sample volumes can be studied at high resolution with a good RF homogeneity. Adapting microcoil design to samples is facilitated by an efficient method to determine coil performance characteristics. The solenoid coil approach may also be readily applied to other samples than plants, including animal tissue.

The non-invasive nature of MR imaging, combined with the inert liquid used in this protocol (PFD for Fomblin), means after completion of experiments samples may be removed from their capillaries for further study. Combinations include optical or electron microscopy and other destructive imaging techniques. We have recently demonstrated a combination with optical microscopy on *Medicago truncatula* root nodules (29).

The presented protocol is suitable for high spatial resolution *in situ* measurements, and more elaborate designs could allow for imaging *in vivo* samples, where challenges related to life support systems would need to be addressed.

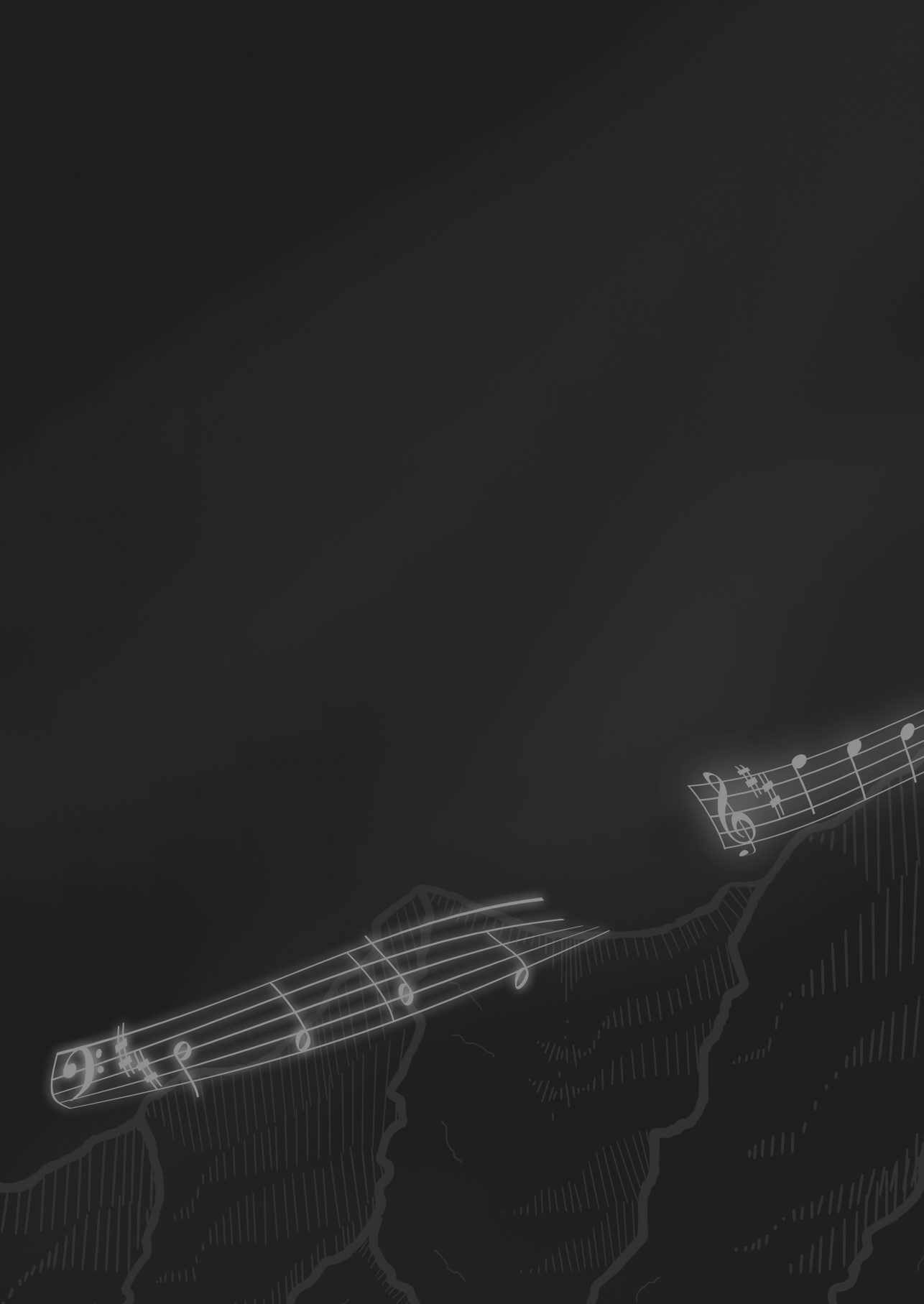
### 3.8 Acknowledgements

Experiments at the 950MHz instrument were supported by uNMR-NL, an NWO-funded National Roadmap Large-Scale Facility of the Netherlands (project 184.032.207). R.S. was supported by the BioSolarCells consortium project U2.3. J.R.K. was supported by the NWO-funded Netherlands' Magnetic Resonance Research School (NMARRS) graduate school [022.005.029]. We thank Klaartje Houben, Marie Renault and Johan van der Zwan for technical support at the uNMR-NL facility. We would further like to thank Volker Lehmann, Henny Janssen and Pieter de Waard for technical help. Lastly, we express our gratitude to Frank Vergeldt, John Philippi and Karthick B. Sai Sankar Gupta for their advice.

### 3.9 References

1. L. Ciobanu, C. H. Pennington, 3D micron-scale MRI of single biological cells. *Solid State Nucl. Magn. Reson.* **25**, 138–141 (2004).
2. J. B. Aguayo, S. J. Blackband, J. Schoeniger, M. A. Mattingly, M. Hintermann, Nuclear magnetic resonance imaging of a single cell. *Nature* **322**, 190–1 (1986).
3. G. Radecki, R. Nargeot, I. O. Jelescu, D. Le Bihan, L. Ciobanu, Functional magnetic resonance microscopy at single-cell resolution in *Aplysia californica*. *Proc. Natl. Acad. Sci. U. S. A.* **111**, 8667–72 (2014).
4. C. H. Lee, N. Bengtsson, S. M. Chrzanowski, J. J. Flint, G. A. Walter, S. J. Blackband, Magnetic Resonance Microscopy (MRM) of Single Mammalian Myofibers and Myonuclei. *Nat. Publ. Gr.*, 1–9 (2016).
5. P. T. Callaghan, *Principles of nuclear magnetic resonance microscopy* (Oxford University Press, 1993).
6. P. Glover, S. P. Mansfield, Limits to magnetic resonance microscopy. *Reports Prog. Phys.* **65**, 1489–1511 (2002).
7. T. L. Peck, R. L. Magin, P. C. Lauterbur, Design and analysis of microcoils for NMR microscopy. *J. Magn. Reson. B.* **108**, 114–124 (1995).
8. C. H. Lee, J. J. Flint, B. Hansen, S. J. Blackband, Investigation of the subcellular architecture of L7 neurons of *Aplysia californica* using magnetic resonance microscopy (MRM) at 7.8 microns. *Sci. Rep.* **5**, 11147 (2015).
9. R. M. Fratila, A. H. Velders, Small-volume nuclear magnetic resonance spectroscopy. *Annu. Rev. Anal. Chem.* **4**, 227–49 (2011).
10. J. J. Flint, K. Menon, B. Hansen, J. Forder, S. J. Blackband, Metabolic support of excised, living brain tissues during magnetic resonance microscopy acquisition. *J. Vis. Exp.* **2017**, 1–10 (2017).
11. K. R. Minard, R. A. Wind, Solenoidal microcoil design. Part I: Optimizing RF homogeneity and coil dimensions. *Concepts Magn. Reson.* **13**, 128–142 (2001).
12. V. Vegh, P. Gläser, D. Maillet, G. J. Cowin, D. C. Reutens, High-field magnetic resonance imaging using solenoid radiofrequency coils. *Magn. Reson. Imaging.* **30**, 1177–85 (2012).
13. K. R. Minard, R. A. Wind, Solenoidal microcoil design - Part II: Optimizing winding parameters for maximum signal-to-noise performance. *Concepts Magn. Reson.* **13**, 190–210 (2001).
14. A. Haase, F. Odoj, M. Von Kienlin, J. Warnking, F. Fidler, A. Weisser, M. Nittka, E. Rommel, T. Lanz, B. Kalusche, M. Griswold, NMR probeheads for in vivo applications. *Concepts Magn. Reson.* **12**, 361–388 (2000).
15. T. Oerther, *Micro Imaging Manual for AV3 Systems* (Bruker Biospin GmbH, Rheinstetten, Germany, Rev. 32., 2012).
16. W. A. Edelstein, Radiofrequency Systems and Coils for MRI and MRS in *Encycl. Magn. Reson.* eds-in-chief R. K. Harris R. Wasylishen, John Wiley Chichester., doi:10.1002/9780470034590.emrstm0444.

17. P. T. Callaghan, Susceptibility and Diffusion Effects in NMR Microscopy in *Encycl. Magn. Reson. eds-in-chief R. K. Harris R. Wasylishen, John Wiley Chichester*. doi:10.1002/9780470034590.emrstm0549.
18. H. C. W. Donker, H. Van As, H. J. Snijder, H. T. Edzes, Quantitative <sup>1</sup>H-NMR imaging of water in white button mushrooms (*Agaricus bisporus*). *Magn. Reson. Imaging*, **15**, 113–121 (1997).
19. H. C. W. Donker, H. Van As, H. T. Edzes, A. W. H. Jans, NMR imaging of white button mushroom (*Agaricus bisporis*) at various magnetic fields. *Magn. Reson. Imaging*, **14**, 1205–1215 (1996).
20. A. G. Webb, Radiofrequency microcoils for magnetic resonance imaging and spectroscopy. *J. Magn. Reson.* **229**, 55–66 (2013).
21. D. L. Olson, T. L. Peck, A. G. Webb, R. L. Magin, J. V Sweedler, High-Resolution Microcoil <sup>1</sup>H-NMR for Mass-Limited, Nanoliter-Volume Samples. *Science* **270**, 1967–1970 (1995).
22. W. T. Tsai, Environmental property modelling of perfluorodecalin and its implications for environmental fate and hazards. *Aerosol Air Qual. Res.* **11**, 903–907 (2011).
23. P. A. Keifer, 90° pulse width calibrations: How to read a pulse width array. *Concepts Magn. Reson.* **11**, 165–180 (1999).
24. M. T. Vlaardingerbroek, J. A. Boer, *Magnetic resonance imaging: theory and practice* (Springer Science & Business Media, 2013).
25. Bruker BioSpin MRI GmbH, “ParaVision 6.0.1 Operating Manual Version 001” (Ettlingen, 2015).
26. S. Heiland, From A as in Aliasing to Z as in Zipper: Artifacts in MRI. *Clin. Neuroradiol.* **18**, 25–36 (2008).
27. R. Kc, I. D. Henry, G. H. J. Park, A. Aghdasi, D. Raftery, New solenoidal microcoil NMR probe using zero-susceptibility wire. *Concepts Magn. Reson. Part B Magn. Reson. Eng.* **37B**, 13–19 (2010).
28. G. R. Littlejohn, J. D. Gouveia, C. Edner, N. Smirnov, J. Love, Perfluorodecalin enhances in vivo confocal microscopy resolution of *Arabidopsis thaliana* mesophyll. *New Phytol.* **186**, 1018–1025 (2010).
29. R. van Schadewijk, J. R. Krug, D. Shen, K. B. S. S. Gupta, F. J. Vergeldt, T. Bisseling, A. G. Webb, H. Van As, A. H. Velders, H. J. M. de Groot, Magnetic Resonance Microscopy at Cellular Resolution and Localised Spectroscopy of *Medicago truncatula* at 22.3 Tesla. *Sci. Rep.* **10**, 1–11 (2020).



## Chapter 4

### 3D Biofilm Visualisation and Quantification on Granular Bioanodes with Magnetic Resonance Imaging

The second part of this chapter is published as:

Leire Caizán-Juanarena<sup>‡</sup>, Julia R. Krug<sup>‡</sup>, Frank J. Vergeldt, J. Mieke Kleijn, Aldrik H. Velders, Henk Van As, Annemiek Ter Heijne

3D biofilm visualization and quantification on granular bioanodes with magnetic resonance imaging. *Water Res.*, 115059 (2019)

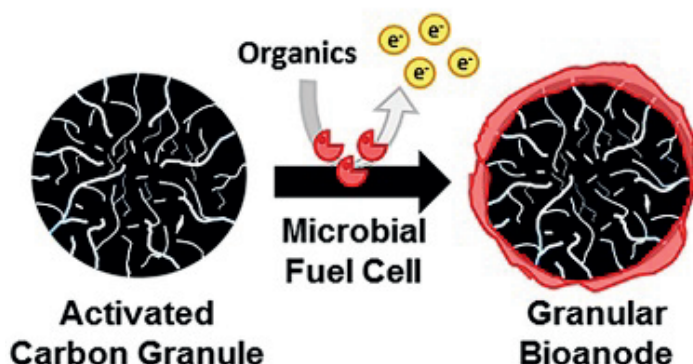


#### **4.0 Preamble, or How to Deal with Artefacts**

In this chapter, 3D biofilm visualisation and quantification on an irregular-shaped support (specifically an electrode material) and its correlation with electrochemical performance are discussed. The published paper (Section 4.1-4.5) focuses on correlating non-invasive and non-destructive visualisation and quantification of biofilm on these activated carbon granules with electrochemical performance and total nitrogen analysis on the same single bioanode. As this thesis is entitled ultra-high field (UHF) MRI and MRS, we aim to explain a caveat of UHF MRI, namely susceptibility effects, at the example of this specific specimen. The first part (Section 4.0) focusses on the need for ultra-high magnetic field strength for the research question and background on the arising susceptibility artefacts. In Section 4.0.1, the need for MRI accompanied by a high signal-to-noise ratio (SNR) is explained, followed by a screening for different granule types (4.0.2), treatment for paramagnetic ion reduction (4.0.3), magnetic field strengths (4.0.4). Efforts for accelerating the MRI-experiment are described in section 4.0.5. We conclude by discussing the possibilities for ultra-high field MRI of bioanodes beyond 14.1 T in section 4.6.

#### 4.0.1 Need for MRI and a High SNR for Biofilm Visualization

The system studied in this chapter consists of a single activated carbon granules on which an electroactive biofilm is growing (Figure 4-1). For more details on the growth and the operation of this capacitive microbial fuel cell system, the reader is referred to the thesis of Leire Caizán-Juanarena(1) and Section 4.1 (2).



**Figure 4-1:** Scheme of an activated carbon granule on which an electroactive biofilm is growing (Modified from Caizán-Juanarena et al. (2)). The activated carbon granules in this research were irregularly-shaped and 1-2 mm in diameter, while the average biofilm thickness varied between 28 and 116  $\mu\text{m}$ .

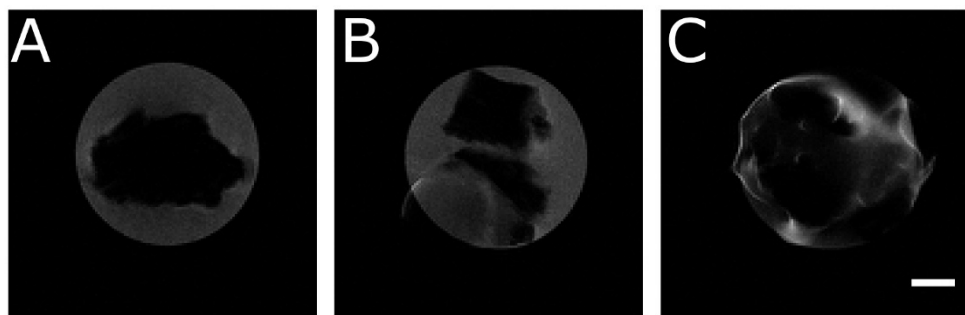
During the characterisation of the bioanode system, it proved to be crucial to determine the biofilm volume and distribution on the activated carbon granule (1). However, the non- invasive and non-destructive visualisation of the electroactive biofilm posed a challenge during the characterisation of the single-granule anode system. While CLSM was invasive and not suitable for these irregular-shaped and opaque granules, SEM was destructive. MRI was proposed as an alternative as it is a non-invasive and non-destructive imaging technique.

In contrast, MRI is one of the most insensitive techniques among the above-mentioned imaging techniques. The requirement for spatial resolutions of at least sub-50  $\mu\text{m}$  in three dimensions is rather challenging for MRI. The higher the magnetic field strength, the better is the signal-to-noise ratio (SNR) per unit volume for comparable performing hardware, as shown in chapter 2. As a consequence, the required high spatial resolutions can be obtained at higher magnetic field strength. Therefore, the method of choice was to use an MRI-setup with a higher magnetic field strength. For this research, high field

spectrometers with magnetic field strengths of 7.0 T, 14.1 T and 22.3 T were system available.

### 4.0.2 Screening for Type of AC Granules

Within the materials tested as support for the biofilm, there were three options, namely the activated carbon materials PK from a peat precursor, GAC from a coal precursor and a non-activated carbon material, namely GG from a graphite precursor (1). When evaluating the feasibility of using high-field MRI for visualisation of biofilms on a bioanode in a Microbial Fuel Cell (MFC), we found that the different types of activated carbon material, i.e. PK, GAC and GG were contributing to artefacts in different degrees of severity even with a spin-echo sequence at the chosen experimental parameters and 7 T (Figure 4-2). These artefacts were attributed to a difference in magnetic susceptibility between the support and the surrounding water, which causes magnetic field inhomogeneities and subsequently distortion in the MRI images. MRI images of PK granules showed no severe image distortions (Figure 4-2A) while for GAC (Figure 4-2B) we observed image artefacts in the form of high intensities even outside the region where signal is expected (i.e. outside the NMR- tube). MRI images of GG were completely distorted (Figure 4-2C). These distortions in images of the GG and GAC type can be an effect of an inhomogeneous excitation slice profile and/or frequency encoding gradient profile (3) resulting from severe magnetic field inhomogeneities due to the susceptibility differences or presence of ferromagnetic ions. From these preliminary tests, it became clear that high-field MRI would only permit to study the PK granules, but not the GG and GAC type. A spin-echo sequence for frequency-encoding sequences with a short echo time was used, as the spin-echo sequences includes a 180° pulse which refocusses the dephasing due to static field inhomogeneities. In contrast, gradient-echo sequences, in which the echo is formed by gradient reversal, are more prone to static field inhomogeneities.



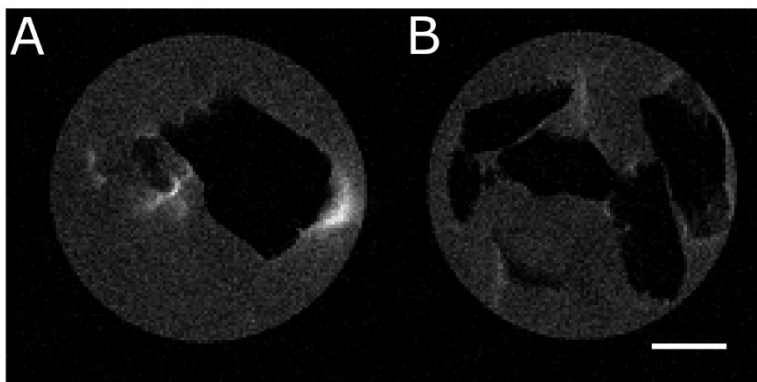
**Figure 4-2:** Comparison of different abiotic AC granules at 7.0 T using a multi-slice spin-echo (mic\_msme, repetition time (TR) 5 s, echo time (TE) 4.2 ms, acquisition time ( $t_{acq}$ ) 2 h 50 min, number of averages (NA) 16, receiver bandwidth (rBW) 100 kHz, slice thickness (ST) 0.5 mm, matrix size (MX) 128 x 128, field-of-view (FOV) 7 mm x 7 mm, 10 slices). MRI images of one slice of A.) a PK granule in water B.) a GAC granule in water and C.) a GG granule in water. The scalebar in all images is 2 mm and the images were extrapolated bilinear to an image matrix of 256 x 256 pixels.

Combining the occurrence of artefacts already with the requirement of needing sub-50  $\mu\text{m}$  resolution in all three dimensions, the choice for material fell on PK, and the choice of spectrometer would be at least 14 T. Additionally, frequency-encoded 3D-MRI sequences suffer slightly less from susceptibility artefacts than slice-selective, and frequency encoded 2D sequences, due to the phase-encoding steps in two dimensions.

### 4.0.3 Reducing Paramagnetic Ions

The PK type proved to be the best granule type; however, the GAC type was also of interest for the study of the growth of electroactive biofilm. Therefore, we investigated whether an acid pre-treatment might alleviate the image artefacts. Due to the assumption that the image artefacts originate from the presence of paramagnetic ions (i.e. iron ions), we tested a pre-treatment with acid, which conveniently also is a standard method in MFC research. 22% HCl acid treatment reduced the MRI-image artefacts in treated GAC granules (Figure 4-3A) compared to the untreated (Figure 4-3B) was, therefore subsequently used in all experiments. The image artefacts were less severe in the treated GAC granules, but not completely absent. However, we want to note explicitly that the MRI images do not compare the same granule before and after acid pretreatment, which would have been the most desirable comparison. Even within the granule types, a variation between the susceptibility artefacts could be observed between individual granules. As the acid pretreatment is a conventional pre-treatment for

electrodes, we included it in our protocol before inserting the carbon granule into the reactor and starting the biofilm growth (2).



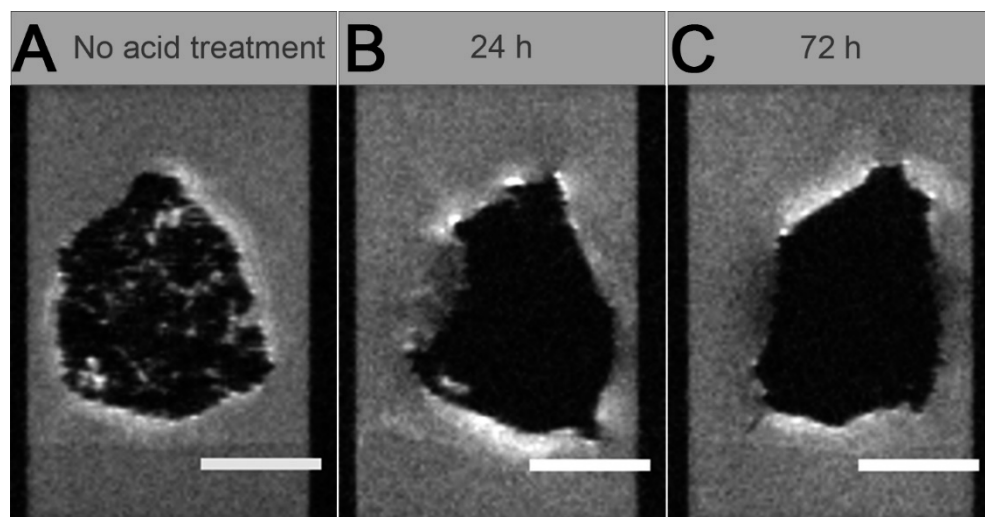
**Figure 4-3:** A.) Not acid-pretreated GAC granule and B.) acid pre-treated GAC granule in water imaged on a 7.0 T (mic\_msme, TR 5 s, TE 5.3 ms,  $T_{acq}$  2 h 50 min, NA 16, rBW 50 kHz, ST 0.2 mm, MX 128 x 128, FOV 5 x 5 mm<sup>2</sup>, 5 slices). The scale bar indicates 1 mm and the images were extrapolated bilinear. Note that these MR parameters (notably rBW and TE) differ from the parameters in figure 4-2 and therefore, the susceptibility effects in the MR images are directly not comparable with figure 4-2.

Elemental analysis (Inductively coupled plasma analysis- IPS) confirmed that the acid treatment reduced the amount of iron ion in the PK granule type (S 4-2).

#### 4.0.4 MRI Images at 14.1 T and 22.3 T

Using the acid pre-treated PK activated carbon granules, MRI images were acquired successfully at 14.1 T. The choice for the sequence was a RARE sequence as it is a spin-echo sequence and thus more robust to static field inhomogeneities than a gradient-echo sequence. We chose  $T_1$ -weighted contrast ( $TR = 700$  ms) and centric k-space encoding to reduce  $T_2$ -weighting by minimising the echo time ( $TE = 2.92$  ms). Additionally, a 3 mm NMR-tube was chosen to minimise the field-of-view as the bioanodes were 1-2 mm in diameter. The  $T_1$ -weighted 3D-RARE images (Figure 4-8A) were thresholded (Figure 4-8B) and the 3D distribution of biofilm was visualised (Figure 4-8C) and used to quantify biofilm volume for different durations of biofilm growth (Figure 4-9A). Information on biofilm distribution and volume was correlated to the electrochemical performance. The details can be found in sections 4.1-4.5 and the supporting information S 4-4)

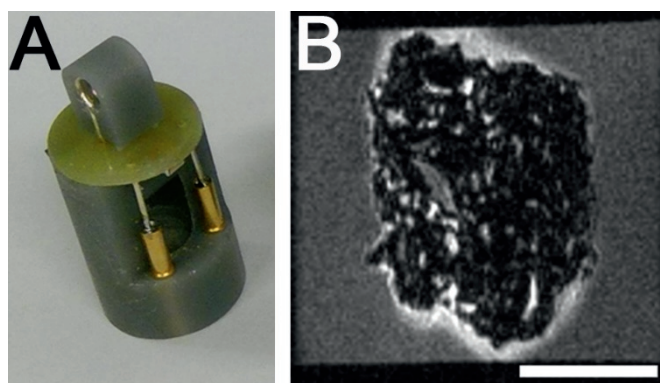
To explore if we could reduce measurement time by using a higher magnetic field strength, we acquired 3D-MRI images biofilm on activated carbon granules of the PK type at 22.3 T with an optimized MRI-protocol and different pre-treatment options of the carbon granule, namely without pre-treatment (Figure 4-4A), with acid pre-treatment of 24 h (Figure 4-4B) and with acid pre-treatment of 72 h (Figure 4-4C) prior to the insertion into the MFC reactor. Interestingly, the MRI image of the bioanode without pre-treatment suffered less severe from MRI image artefacts (Figure 4-4A) than the MRI-images of the bioanodes with pre-treatment (Figure 4-4B and C). Additionally, signal intensity can be observed inside the activated carbon granule in Figure 4-4A, which is not observed in Figure 4-4B and C. As we also clearly observed artefacts in previous tests and several MR experiments during these trials, we concluded to continue the experiments on 14.1 T. Additional tests with the same granule before and after pre-treatment would be desirable to quantify the effects of the pre-treatment at ultra-high field strength and exclude the uncertainty by a variation of paramagnetic ions among different granules of the same type.



**Figure 4-4:** Biotic bioanodes (i.e. activated carbon granules with biofilm) where the activated carbon granule (type PK) was A.) not pre-treated, B.) pre-treated with 22% HCl for 24 hours and C.) pre-treated with 22% HCl for 72 hours. A 3D-RARE at 22.3 T was used (rarefact 8,  $TE_{eff}$  3.27 ms, TR 0.7 s,  $T_{acq}$  27 min, MX 128 x 96 x 96, FOV 3.6 x 2.7 x 2.7 mm<sup>3</sup>, rBW 100 kHz). The scale bar indicates 1 mm and magnitude image data is shown.

#### 4.0.5 Efforts to Accelerate MRI-Experiment at 14.1 T

When 14.1 T became evident as the “compromise” field strengths between the ultra-high-field 22.3 T for high SNR and lower field strength 7.0 T for less susceptibility effects, we did some efforts to accelerate the 3D-MRI acquisition. In theory (4) and chapter 2, increasing the field strengths is not the only factor which can increase image SNR. Optimising the detector to our specific samples will in many cases, increase the image SNR of our 3D-MRI experiment. To this end we designed a 3 mm solenoid coil, as changing the geometry from birdcage to saddle should already increase the SNR by a factor 3. Additionally, reducing the coil diameter from 5 mm to 3 mm which is the requirement of our sample, should give us an additional gain of a factor 1.6.



**Figure 4-5:** A.) The 3 mm  $^1\text{H}$  solenoid coil was used to acquire a 3D-MRI experiment on the 14.1 T spectrometer in B.) one plane of a 3D-RARE (TR 0.5 s, TE 3.3 ms; FOV (2.7 mm) $^3$ , Resolution (21  $\mu\text{m}$ ) $^3$ ;  $t_{\text{acq}}$  9 h 6 min, rBW 100kHz, RAREfactor 2; 8 averages). The granule was an acid pre-treated biotic granule of the PK type. The scale bar indicates 1 mm and magnitude image data is shown.

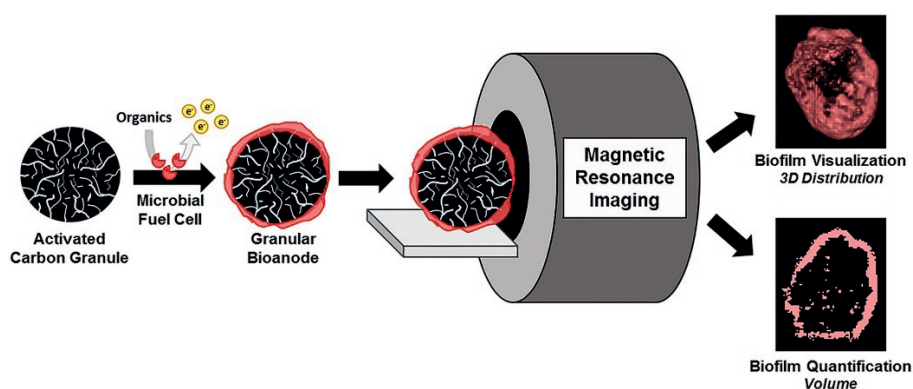
The SNR gain by using the solenoid was considerable. A 3D-RARE experiment with an isotropic resolution of (21  $\mu\text{m}$ ) $^3$  took 9 h and 22 min with an SNR<sub>i</sub> ratio of signal in the biofilm area to noise area of 22. While this proved the potential of using an optimised detector, our trial experiments with the coil failed. The horizontal orientation of the solenoid caused some granules to move in the glass capillary. Approaches to include an agar block at either side were dismissed due to the requirement that the imaging needs to be as non-invasive as possible. Additionally, with a solenoid coil, a probe change for the sample insertion is required, and manual adjustments might be needed (see chapter 3). Hence, the 5 mm saddle coil in which the granule was positioned



on an agar block in a vertical NMR-tube was preferred for the remainder of the experiment. However, if a solution for the sample fixation could be found without biofilm destruction, the 3 mm solenoid coil offers the advantage of increased SNR.

## 4.1 Abstract

The use of microbial fuel cells (MFCs) for wastewater treatment fits in a circular economy context, as they can produce electricity by the removal of organic matter in the wastewater. Activated carbon (AC) granules are an attractive electrode material for bioanodes in MFCs, as they are cheap and provide electroactive bacteria with a large surface area for attachment. The characterisation of biofilm growth on AC granules, however, is challenging due to their high roughness and three-dimensional structure. In this research, we show that 3D magnetic resonance imaging (MRI) can be used to visualise biofilm distribution and determine its volume on irregular-shaped single AC granules in a non-destructive way while being combined with electrochemical and biomass analyses. Ten AC granules with electroactive biofilm (i.e. granular bioanodes) were collected at different growth stages (3 to 21 days after microbial inoculation) from a multi-anode MFC and  $T_1$ -weighted 3D-MRI experiments were performed for three-dimensional biofilm visualisation. With time, a more homogeneous biofilm distribution and an increased biofilm thickness could be observed in the 3D-MRI images. Biofilm volumes varied from 0.4  $\mu\text{L}$  (day 4) to 2  $\mu\text{L}$  (day 21) and were linearly correlated ( $R^2=0.9$ ) to the total produced electric charge and total nitrogen content of the granular bioanodes, with values of 66.4 C  $\mu\text{L}^{-1}$  and 17  $\mu\text{g N } \mu\text{L}^{-1}$ , respectively. In future, *in situ* MRI measurements could be used to monitor biofilm growth and distribution on AC granules.



## 4.2 Introduction

Recovery of resources from waste streams is necessary to transit towards renewable forms of energy and a circular economy. Wastewater streams from industries, agriculture and households are known to be a valuable source of organics and nutrients that can be recovered and used for energy production (5–7). The microbial fuel cell (MFC) is a technology that uses bacteria to clean wastewater by oxidising the organics while simultaneously producing electricity (8–11). This oxidation reaction occurs at the anode, where bacteria grow by forming a biofilm on the surface of the electrode, known as bioanode. However, the application of MFCs on up-scaled wastewater treatment processes remains challenging due to the expected non-favourable conditions such as complex substrates, changes in temperature or increased internal resistances of the system. For these reasons, and the stagnating power production trend MFCs have shown in the last decade even at laboratory scale (up to  $\sim 5 \text{ W m}^{-2}$  cathode surface area) (12), the ability of MFCs to compete with other wastewater treatment technologies such as anaerobic digestion has been hindered (13, 14). Electrode material properties (e.g. biocompatibility, electrical conductivity and surface area) are of importance for the performance of MFCs and hence the power density (15, 16). Carbonaceous materials are widely used, as they are cheap and hold most of the desired electrode properties. Among them, activated carbon (AC) granules have a three-dimensional structure and a large specific surface area (even larger than  $2000 \text{ m}^2 \text{ g}^{-1}$ ) (17) that allows for good biofilm attachment, hence leading to high volumetric power density. In this research, we use single AC granules as previously described by Caizán-Juanarena and co-workers (18), where up to 24 granular bioanodes of different sizes and types were electrochemically and microbiologically studied under the same conditions (i.e. same reactor system).

Many studies focus on electrochemical (19–21) and physical properties (22–24) of AC, while quantification and distribution of biofilm on such electrode material are less extensively addressed. These are important parameters to determine as biofilm growth plays a crucial role on the performance of MFCs. Moreover, when using rough, three-dimensional and porous materials such as AC granules, it is of particular interest to get more information about biofilm development on the electrode surface. A wide variety of techniques is available for biofilm characterisation (25–27). Biofilm quantification can be done by using well-established methods, such as protein analysis (28) and total nitrogen (TN) (29) content analysis, which relate to the total amount of biomass.

However, these techniques are destructive and cannot give any information about biofilm distribution on electrode surfaces, which is an important parameter to better understand the growing behaviour and limitations of biofilms and determine features such as the biofilm thickness. To this aim, the spatial distribution of a biofilm is commonly obtained by microscopy techniques such as scanning electron microscopy (SEM) (30–32) or confocal laser scanning microscopy (CLSM) (30, 33). However, they are destructive (e.g. SEM), need the addition of chemicals (e.g. CLSM) and can only scan small areas of an electrode as shown by Tejedor-Sanz and co-workers on activated carbon granules (34). Optical coherence tomography (OCT) has been used to visualise the structure of biofilms growing on glass slides (35) and carriers (36). A recent study has demonstrated accurate measurements of biofilm volume and thickness of an active bioanode growing on an electrode surface, both in situ and non-invasively (29). However, the three-dimensional nature of AC granules impedes the application of OCT on these specific electrodes, unlike the more or less flat surfaces used in other studies (37–39). Therefore, other techniques need to be used to visualise and quantify biofilm growth on AC granules and, in this way, add to the information obtained about these granular bioanodes in previous studies (18, 19). In this context, magnetic resonance imaging (MRI) is a technique that has already been used to visualise biofilms in different applications and that is attractive to characterise biofilms growing on our electrodes.

Magnetic resonance imaging (MRI), a technique well-known from medical diagnostics, is suitable for visualisation and characterisation of biofilms (25, 40–44). For an overview on recent studies in biofilm research using MRI, a book chapter is available (45). Existing MRI research studies on biofilms have mainly focused on biofilm structure, transport of water (i.e. diffusion and flow) and metal ions in and around biofilms (40, 46–53), localised spectroscopic measurements on metabolites present in biofilm (53), and biofilm growth on carriers (even with complex geometry) (51, 53–56) (57) and in porous media e.g. (58). Furthermore, 3D MRI has also been used to visualise biofilm growth on a flat carrier (53, 59, 60), in a tube reactor (61) and on complex geometries in porous media applications (62, 63). Specifically, MRI research of biofilm growth on electrodes as a carrier, has revealed information about diffusion coefficients (64) and metabolic activity (i.e. electron transfer) (65) within the biofilm growing on flat electrodes.

In this study, we generalise this previous approach of imaging a biofilm on a 2D flat electrode geometry (64–66) to 3D biofilm visualisation and also quantification on an electrode material (AC granules) with a rather irregular 3D shape and surface, where the main challenge is to make a clear distinction between biofilm and both the electrode material and surrounding water (as opposed to a flat 2D electrode surface where the support shape is well-defined). Because of the irregular features of AC granules and the thin biofilm layer, high-resolution 3D images are needed, i.e. at sub-hundred micrometre resolution. These resolutions are usually difficult to obtain with MRI due to the low sensitivity of the technique, and would require long experimental times of days to weeks. To shorten experimental times while obtaining such high-resolution images, high magnetic field strengths are needed, as the sensitivity of the MRI technique increases with increasing magnetic field strength (4). To obtain high-resolution 3D images in reasonable experimental times this study was therefore conducted at a magnetic field strength of 14.1 T (56), which is much stronger than the 1.5 and 3 T MRI scanners used for conventional medical imaging. Magnetic field strengths used in biofilm MRI research are commonly ranging between 4.7 T (e.g. (51)) and 11.7 T (e.g. (64)) to achieve higher spatial resolutions in view of the smaller dimensions of biofilms, but biofilm studies have also been performed at very low field strengths of 0.7 T (e.g. (67)).

Since MRI is an imaging modality based on the detection of the magnetic moments (spins) of hydrogen nuclei in a magnetic field after excitation (with an appropriate pulse sequence) (68), it allows to visualise the distribution of hydrogen nuclei in e.g. biological samples. As water is the most abundant component containing hydrogen in biological samples, the main application is to image water distribution. To distinguish different tissues within a biological sample, we can make use of the differences in magnetic resonance (MR) signal lifetimes of water in those tissues compared to the surrounding bulk water, called relaxation times ( $T_1$  and/or  $T_2$ ). As the bulk water signal has a different relaxation time than the biofilm water signal, (50), MRI signal acquisition timings such as repetition time (TR) and echo time (TE) can be selected to maximise the contrast between biofilm and bulk water, which will lead to different signal intensities. An optimised TR leads to a contrast based on  $T_1$ -relaxation time, while an optimised TE leads to a contrast based on  $T_2$ -relaxation time. To select one of these contrast types, the other has to be minimised; thus while for  $T_1$  contrast we minimise

TE to avoid  $T_2$ -weighting, while for  $T_2$  contrast we maximise TR to avoid  $T_1$  weighting (68). Based on this image contrast, the biofilm region can be selected, and the distribution can be visualized.

The aim of this research was to develop an MRI protocol to non-destructively visualise and quantify the three-dimensional biofilm distribution on single AC granules, which were grown as bioanodes in a multi-anode MFC. To this end, we investigated whether biofilm water could be distinguished from bulk water by  $T_1$ -relaxation time at a high magnetic field strength (14.1 T). 3D-MRI images of granular bioanodes, collected at different growth stages, were acquired and biofilm distribution and volume were determined. Biofilm quantification with MRI was complemented with measurements of total nitrogen content and total produced electric charge of the same granular bioanodes.

## 4.3 Experimental Methods

### Preparation of AC Granules

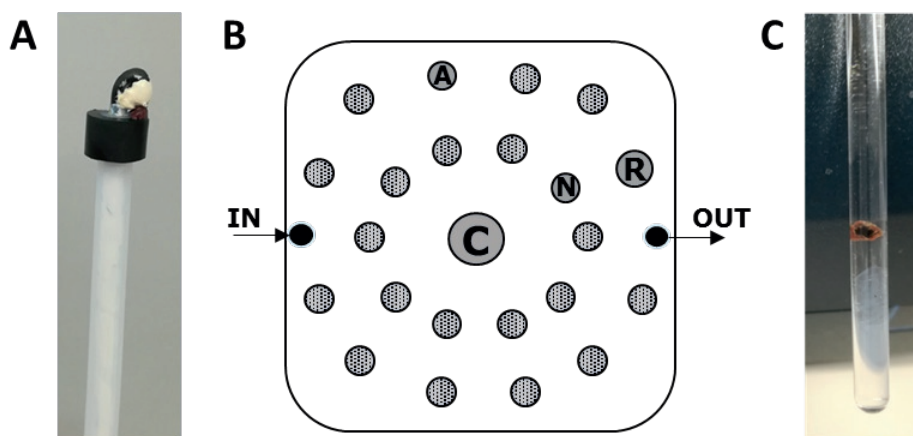
The type of AC granules used are commercially known as PK 1-3 (Cabot Norit Nederland B.V., Amersfoort, the Netherlands). They were prepared as explained in a previous publication, i.e. by Caizan-Juanarena and co-workers (18): first, sieved using an aperture size between 1 and 2 mm (Retsch®, Germany); then individually selected for an approximate spherical shape, and finally weighted. Their volume was estimated by using the apparent density provided by the manufacturer, i.e.  $0.3 \text{ g mL}^{-1}$ . Their radius was approximated from the volume by assuming a spherical shape of the granule. Their outer surface area was also estimated assuming a spherical shape, without considering the possible roughness or pores where bacteria could have access to. The measured values of weight and the estimated values of volume and surface area can be seen in the Supplementary Information (S 4-1).

After selection, granules were treated with 22% hydrochloric acid (HCl) for 24 hours to remove surface organic contamination and metal impurities and washed three times with demi water (69). This cleaning procedure is common practice and useful for comparative experiments. Additionally, for MRI experiments, it was a crucial step as the AC granules should contain as little concentration of iron ions as possible in order to avoid image artefacts. In the Supplementary Information (S 4-2) the composition of AC granules before and after the acid treatment can be seen, measured with Inductive-Coupled Plasma Mass Spectrometry (ICP-MS).

### Preparation and Operation of the MFC

A custom-made MFC reactor was built (see the schematic top view in Fig. 1B), consisting of a 2.3 L container as the anode chamber and a glass tube in the middle as the cathode chamber. The anode chamber had 2 L of anolyte (10 mM  $\text{NaCH}_3\text{COO} \cdot 3\text{H}_2\text{O}$ ;  $1 \text{ mL L}^{-1}$  Wolfe's Vitamin solution;  $1 \text{ mL L}^{-1}$  Wolfe's modified mineral solution; 3.7 mM  $\text{NH}_4\text{Cl}$ , 1.6 mM  $\text{KCl}$ ; 30 mM  $\text{Na}_2\text{HPO}_4 \cdot 2\text{H}_2\text{O}$ ; 19 mM  $\text{KH}_2\text{PO}_4$ ), of which 0.2 L was an inoculum from another active MFC ran on acetate. The cathode chamber had an approximate volume of 0.13 L (100 mM  $\text{K}_3\text{FeCN}_6$ ; 30 mM  $\text{Na}_2\text{HPO}_4 \cdot 2\text{H}_2\text{O}$ ; 19 mM  $\text{KH}_2\text{PO}_4$ ) where a  $24 \text{ cm}^2$  graphite felt was used as electrode material, attached to a titanium wire (1 mm diameter, 36 cm long) as current collector. A cation exchange membrane (Fumasep FKB, FuMa-Tech GmbH, St.

Ingbert, Germany) of  $1.76 \text{ cm}^2$  was placed on the bottom of the cathode chamber, in contact with the anode chamber. The lid of the container had several holes: one for the cathode chamber ( $\phi = 2.5 \text{ cm}$ ), one for the inflow of substrate ( $\phi = 1.5 \text{ cm}$ ), one for the reference electrode (3M KCl Ag/AgCl,  $+0.199 \text{ V}$  vs NHE) ( $\phi = 1.5 \text{ cm}$ ) and 29 for the working electrodes ( $\phi = 1 \text{ cm}$ ). Additionally, a hole on the side of the container was made for the outflow ( $\phi = 1.5 \text{ cm}$ ). The effect of the distance between working and the reference electrodes on current production was neglected as the latter one was placed outside of the electric field.



**Figure 4-6:** A) A clamped activated carbon (AC) granule with biofilm (i.e. granular bioanode) collected from the reactor; B) Schematic top view of the reactor ( $18 \times 18 \text{ cm}$ ), where C stands for cathode ( $\phi = 2.5 \text{ cm}$ ), R for reference electrode ( $\phi = 1.5 \text{ cm}$ ), N for nitrogen inflow ( $\phi = 1 \text{ cm}$ ) and A for abiotic granule ( $\phi = 1 \text{ cm}$ ). The rest of circles ( $\phi = 1 \text{ cm}$ ) with no name indicate the place where clamps with AC granules were placed; C) An AC granule with biofilm inside a 3 mm diameter magnetic resonance (MR)-tube, filled with a buffer solution (no nitrogen) and with an agar block at the bottom.

Single granules were held separately with clamps made of titanium wire ( $\phi = 1 \text{ mm}$ ) (see Figure 4-6). One side of the clamp had the shape of a hook, where the granule could be fixated. The contact area with the granule was minimised using (yellow) non-conductive resin (Revlon® Colorstay™) that served to limit bacterial growth on the clamp. The other side of the titanium wire was passed through a rubber that fitted the size of the holes on the lid for the working electrodes. The average resistance of the clamps was  $0.8$  to  $1 \ \Omega$  between the two ends. Each clamp was connected to a channel from a



MultiWE32 module (Ivium Technologies, Eindhoven, The Netherlands), which can operate up to 32 working electrodes that share common reference and counter electrodes. All working electrodes (one abiotic and 10 biotic) were operated at -0.35 V vs Ag/AgCl with continuous anolyte inflow. As the anode potential was controlled versus the reference electrode, the counter electrode was of no influence to the current production and biofilm growth. This would not be the case if, instead, the cell voltage was controlled. The abiotic granule consisted of a 2 mm diameter glass bead (B Braun biotech international, Schwarzenberg, Germany) covered with PTFE tape. Acetate concentration was maintained above 5 mM. Anaerobic conditions were ensured with N<sub>2</sub> flushing and the stirring velocity was fixed at 100 rpm.

Electric current was monitored, with a sampling time of 600 seconds, until granular bioanodes were collected from the reactor (see S 4-1 for the exact days). Total produced electric charge by each bioanode was calculated according to Equation (4-1):

$$Q_T = \int_0^t I dt \quad (4-1)$$

where  $Q_T$  is the total produced electric charge (C),  $I$  is the current (A) and  $t$  is the overall time (s) during which the current was measured.

After collecting each granular bioanode, the rubber stopper was replaced with a new stopper to avoid oxygen leakage into the reactor. Prior to MRI measurements, clamped granular bioanodes were submerged 2 to 3 times in a buffer solution without nitrogen (1.6 mM KCl; 30 mM Na<sub>2</sub>HPO<sub>4</sub>·2H<sub>2</sub>O; 19 mM KH<sub>2</sub>PO<sub>4</sub>) to avoid accounting for additional nitrogen content from the anolyte in the total nitrogen analysis. Each granular bioanode was then transferred to a 3 mm diameter MR-tube (Hilgenberg, Malsfeld, Germany) containing the same buffer solution and an agar block (2% w/w) of approximately 8 mm placed at the bottom (see Figure 4-6C).

### MRI Measurements

MRI measurements experiment as on a 14.1 T Bruker Avance-III-600 spectrometer (Bruker, Karlsruhe, Germany) controlled by ParaVision 5 or 6. The Micro5 imaging probe was equipped with a Micro5 gradient set driven by Great60 amplifiers, located at MAGNEFY (MAGNETic resonance research FacilitY, Wageningen, The Netherlands). The radiofrequency (RF)-coil used was a <sup>1</sup>H/<sup>2</sup>H saddle coil insert with the inner coil

being the  $^1\text{H}$ -coil with a diameter of 5 mm and the outer coil being a  $^2\text{H}$ -coil (not used in this study). All MRI measurements were performed at room temperature ( $\sim 293\text{ K}$ ) with no extra temperature control.

### ***T<sub>1</sub> Map***

A 2D spin-echo RAREVTR sequence (echo time= 2.93 ms, 5 different repetition time (TR) steps (TR= 0.10 s, 0.39 s, 0.79 s, 1.46 s, and 5.0 s), 64 averages, receiver bandwidth 50 kHz, field-of-view  $3 \times 3\text{ mm}^2$ , matrix size  $64 \times 64$ , slice thickness 0.2 mm) was used for  $T_1$  measurements. The raw data were Fourier-transformed and phase-corrected. Per-pixel the signal intensity as a function of the repetition time TR was mono-exponentially fitted with in-house developed IDL scripts using IDL Version 6.4 (ITT, Visual Information Solutions, Boulder, CO, USA) to obtain quantitative  $T_1$  maps according to Equation (4-2):

$$I(TR) = I_0 \left(1 - e^{-\frac{TR}{T_1}}\right) \quad (4-2)$$

where  $I(TR)$  (a.u) is the image intensity as function of repetition time TR (s),  $I_0$  the proton density (a.u.), and the  $T_1$  is the  $T_1$  relaxation time (s).

### ***3D-RARE***

A 3D turbo spin-echo (RARE) sequence (echo time= 2.92 ms, turbo factor 4 with centric encoding, isotropic voxel resolution  $(28\text{ }\mu\text{m})^3$ , acquisition time 19 h 42 min, field-of-view  $3.6 \times 2.7 \times 2.7\text{ mm}^3$ , matrix size  $128 \times 96 \times 96$ , receiver bandwidth 100 kHz) was recorded. TR was chosen to be 0.7 s to obtain a  $T_1$ -weighted image with high contrast. Before and after this scan, a control localiser scan was performed to confirm that the sample did not move during the experiment.

### **Image Processing for 3D Reconstruction**

To process the 3D dataset, a script was written in IDL Version 6.4 (ITT, Visual Information Solutions, Boulder, CO, USA). A threshold was set above the noise intensity level to mask areas with no signal intensity. Furthermore, we corrected for the inhomogeneous intensity of the bulk water signal as function of position due to the inhomogeneity of the  $B_1$ -field, which is caused by the geometry of the detection coil, namely the saddle geometry. After this correction, a threshold was set above the image

intensity corresponding to bulk water to distinguish volume elements (voxels) containing biofilm from those containing bulk water. The dataset containing the threshold images was then loaded into ImageJ/FIJI (70) and a 3D-volume reconstruction was done using the Image J 3D viewer (71) applying a resampling factor of 2. Voxels with a signal intensity higher than the threshold attributed to biofilm were summed up and multiplied by the volume of a single voxel ( $28\text{ }\mu\text{m}^3$ ), resulting in the biofilm volume. Based on biofilm volumes and the estimation of the outer surface area of AC granules, the average biofilm thickness was calculated at each growth stage, as reported in the Supplementary Information (S 4-1).

### **Total Nitrogen (TN) Analysis**

After MRI measurements, granular bioanodes were processed with the Laton Total Nitrogen (LCK) cuvette test with a concentration range of 20-100  $\text{mg L}^{-1}$  TNb (HACH®, Manchester, United Kingdom). This method measures organic and inorganic bound nitrogen, excluding elemental nitrogen ( $\text{N}_2$ ). 0.2 mL of miliQ water was added to the reaction vessel together with the granular bioanode, which was directly transferred from the MR-tube. Direct contact between the liquids in the reaction vessel (water) and the MR-tube (buffer) ensured that the granular bioanode could move with little interference. The digestion step in the reaction vessel consisted of 30 minutes at 120 °C. The digested sample (0.5 mL) was transferred from the reaction vessel to the LCK cuvette, from which the nitrogen concentration ( $\text{mg N L}^{-1}$ ) was read after 15 minutes. This concentration was converted to  $\text{mg N}$  by correcting for the initial added volume of miliQ water (i.e. 0.2 mL).

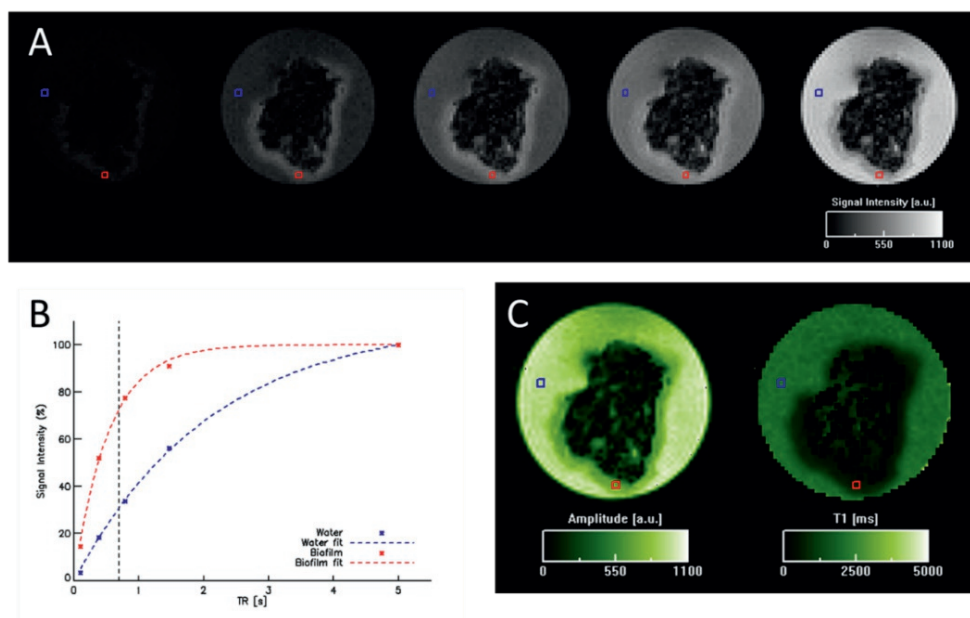
The nitrogen content of AC granules without biofilm (i.e. not placed in the reactor) and treated with 22% HCl, was found to be around  $1\text{ mg L}^{-1}$ , which is more than 10 times lower than for granules with biofilm. This residual nitrogen in abiotic granules could originate from the AC that contains some nitrogen. However, the exact value is difficult to specify, as it will depend on the dry weight of each granule.

## 4.4 Results and Discussion

In this section, we present and discuss i) the MRI method used to visualise the biofilm growing on AC granules, ii) the 3D-MRI images obtained at different biofilm growth stages of different granular bioanodes, iii) the image processing and determination of biofilm volume, and iv) the correlation between biofilm volume and both the total produced electric charge and total nitrogen content of single granular bioanodes.

### 4.4.1 Distinguishing biofilm water from bulk water using MRI

Differences in  $T_1$ -relaxation times provide the means to control contrast in MRI experiments. Therefore, it is important to quantify this parameter for both biofilm water and bulk water (consisting of a buffer solution without nitrogen, see Experimental Section). Figure 4-7A shows the resulting 2D images for the repetition time (TR) varying from 0.1 s (left) to 5 s (right). The absolute image intensity increases with increasing TR, as the magnetisation is given more time to recover. The signal intensity of each pixel was fitted as a function of TR with a mono-exponential recovery curve. In Figure 4-7B, we plotted the curve fitted for two pixels, corresponding to biofilm water (red) and bulk water (blue) (marked in Figure 4-7A as example). With this analysis, a proton density map (known as signal amplitude map; Fig. 2C, left) and a  $T_1$ -parameter map (Fig. Figure 4-7C, right) were obtained. The amplitude map shows that the proton density (a.u.) is lower inside the biofilm than in the bulk water, while the AC granule has a very low proton density due to absence of mobile protons in the AC and a too short signal relaxation time ( $T_2$ ) for the water in the pores to be observable by MRI. The  $T_1$  map shows that  $T_1$  values of biofilm water ( $\sim 0.4$ - $0.7$  s) and bulk water ( $\sim 2$  s) can indeed be distinguished, a trend which was also seen by Hoskin and co-workers (72). The  $T_1$  value of the biofilm water was lower than the bulk water value as the  $T_1$ -relaxation time of water spins is affected by the different local (physical and chemical) environment in the biofilm (73). A  $T_1$  value of the AC granule could not be established due to the low intensity of the signal. Having established that biofilm and bulk water signal could be distinguished by their difference in  $T_1$ -relaxation time, the TR for maximum image contrast was determined. Using the recovery curves, we used the value of TR at which the difference in signal intensity (i.e. the contrast) between bulk water and biofilm was the largest. In this case, we chose to use a TR of 0.7 s as indicated by the black dotted line (Figure 4-7B) for all subsequent 3D-MRI experiments on the bioanodes.



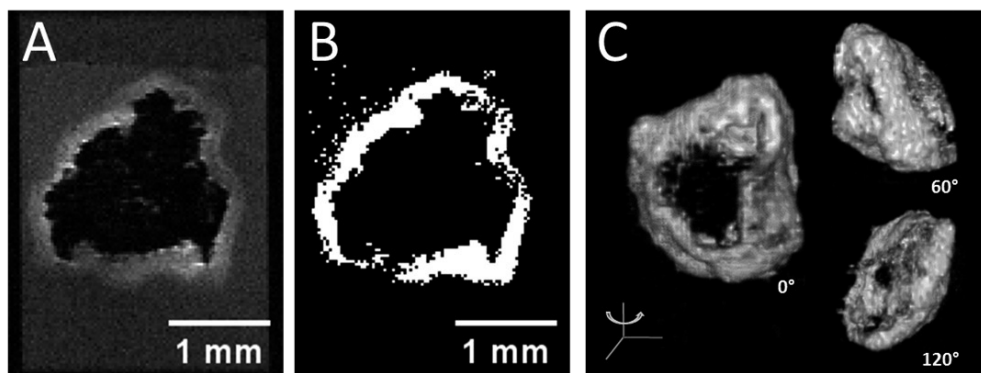
**Figure 4-7:**  $T_1$ -contrast experiments AC granule with biofilm collected after a growth period of 15 days. A) 2D spin-echo MRI images with different repetition times (TR): 0.10 s, 0.39 s, 0.79 s, 1.46 s and 5 s from left to right show an increase in signal intensity with increasing TR. B) Signal intensity values of (A) for one biofilm pixel (red) and bulk water pixel (blue) plotted against TR show the increase in signal intensity due to  $T_1$ -relaxation. The respective mono-exponential fits are shown by the dotted lines. The black dotted line indicates the TR chosen for maximum contrast between the biofilm and bulk water. C) Amplitude (i.e. proton density) map and  $T_1$  map from the fit of the signal intensities in (A) are depicted. The images in C) were re-sampled using bilinear interpolation.

As an alternative method to generate image contrast, we proved on the same AC granule as used for the  $T_1$ -experiments in Figure 4-7 that  $T_2$  weighting could be used as well to distinguish biofilm water ( $T_{2,\text{apparent}} = \sim 15\text{--}30$  ms) from bulk water ( $T_{2,\text{apparent}} = \sim 40$  ms). The reported (apparent)  $T_2$  values are specific for the resolution ( $47 \times 47 \times 200 \mu\text{m}^3$ ) and magnetic field strength (14.1 T) used in this  $T_2$  experiment (74). However, the low contrast we found between biofilm and the AC granule with  $T_2$ -weighted images (Supplementary Information, S 4-3) would impede the distinction and subsequent quantification of biofilm. The contrast between biofilm water and bulk water in  $T_2$  experiments was also lower than in  $T_1$  experiments due to the smaller difference in  $T_2$ -relaxation times at the required high resolutions (74). Additionally, performing full  $T_2$ -weighted 3D experiments would take longer experimental time than  $T_1$ -weighted

experiments, in fact, it would require a TR of  $5 \cdot T_{1,\max}$ , with  $T_{1,\max}$  being the highest  $T_1$ -relaxation time among the components, in this case of bulk water ( $T_1 = \sim 2$  s). Therefore,  $T_1$ -weighted MRI images were preferred for the present study.

#### 4.4.2 Biofilm Distribution Using 3D MRI

Figure 4-8A shows a cross-section of the 3D dataset of a granular bioanode where the biofilm was grown for 11 days. The signal intensity of biofilm was higher than both the AC granule and the bulk water and could thus be used to determine biofilm growth. As a cross-section is not representative for the biofilm distribution on the whole granule surface, a 3D reconstruction of the biofilm was made. After selecting the voxels containing biofilm in each cross-section by applying a threshold on the signal intensity (Figure 4-8B), a 3D reconstruction of the biofilm showed the biofilm distribution and coverage (Figure 4-8C, reconstruction depicted from three different angles turned around the vertical axis). Cross-sections, threshold images and images of the 3D volume reconstruction of every granular bioanode can be found in the Supplementary Information (S 4-4). Additionally, videos of the 3D reconstruction of each studied granule can also be found in the online supplementary information of the publication on which this chapter is based (2). The whole surface of the AC granule at day 11 was covered with biofilm, except for an area that corresponds to the position of the clamp used as current collector. This partly covered the surface of the AC granules, hence preventing biofilm growth on this area. Therefore, this served as an internal control within the 3D images indicating that bulk water at the granular surface was not falsely attributed to biofilm volume, which is the case when a surface acts as a relaxation sink (75). This internal control served thus as proof that MRI image artefacts were not interfering in our study.



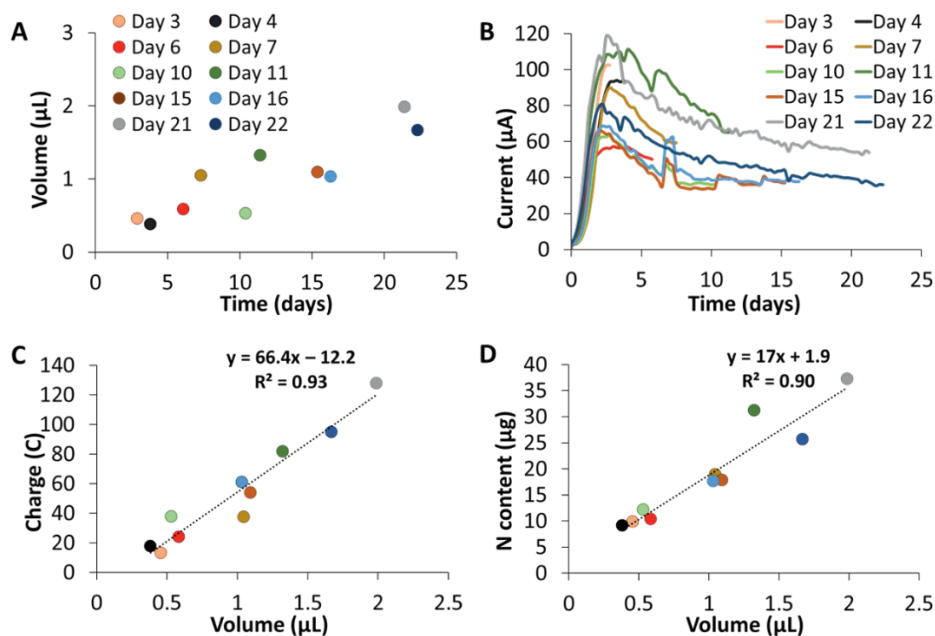
**Figure 4-8:** One cross-sectional plane through the  $T_1$ -weighted 3D dataset of an 11-day-old granular bioanode. B) The same plane is depicted after thresholding analysis. C) 3D volume reconstruction, depicted from 3 angles (turned around in the vertical axis), based on the threshold image stack.

Using the 3D reconstructions of all different granular bioanodes (see Supplementary Information, S 4-4), we assessed biofilm growth at different days. At early stages (days 3 and 4), there were large surface areas of the AC granules that were not covered, and the biofilm distribution was not homogeneous over the surface. At later stages (days 6 and 7), the biofilm was more equally distributed over the granule surface, but it was still not very thick. More mature granular bioanodes, grown for 11 days or more, had thicker biofilms that allowed for a clearer view of the biofilm distribution on the AC granule. It is important to highlight that the area of the clamp was visible in every granular bioanode, which served as an internal control as previously explained. At the early growth stages, when the biofilm was not much developed, the area covered by the clamp was not as distinct as for more mature biofilms. However, when compared to an abiotic granule (see also Supplementary Information, S 4-4), this latter did not show a hole and the whole granule surface was instead covered by an equidistant signal originating from the surface of the AC granule acting as a relaxation sink (75).

#### 4.4.3 Biofilm Volume Determination using 3D MRI

Figure 4-9A shows the biofilm volume of 10 granular bioanodes, each with different AC granule weight, collected from the reactor at different days. Values ranged from 0.4  $\mu\text{L}$  on day 4 to 2  $\mu\text{L}$  on day 21. An increased biofilm volume is observed with longer growth periods for the time range studied here. As biofilm thickness is known to be a

crucial parameter for the electrochemical activity of bioanodes (33), the average biofilm thickness was calculated assuming that the whole outer surface area of the granules was completely covered by biofilm (see Supplementary Information, S 4-1). The lowest average thickness estimated was at day 4 with a value of 27.8  $\mu\text{m}$ , while the highest average thickness was 165.9  $\mu\text{m}$  for the granular bioanode collected at day 21. This biofilm thickness is in the same range as reported for electroactive biofilms on macroscopically flat anodes (29, 76). The increasing thickness may be a contributing factor to the decrease of electric current production by the bioanodes over time, as shown in Figure 4-9B. In fact, some studies (77, 78) have revealed that diffusion limitations increase with thicker biofilms, which may hinder current production of the system.



**Figure 4-9:** A) Biofilm volume obtained with 3D-MRI images at different growth stages, distinguished by colours. B) Current production of granular bioanodes at different growth stages (see end of the growth curves). C) Total produced electric charge by granular bioanodes as a function of the biofilm volume. D) Total nitrogen content of granular bioanodes as a function of biofilm volume. The colours in (C) and (D) represent the granular bioanodes at the same biofilm growth stages as in (A) and (B).



#### 4.4.4 Comparison of biofilm volume with total produced electric charge and total nitrogen content

Electric current production was recorded for each granular bioanode during the biofilm growth period (see Figure 4-9B). Most of them reached the maximum current (ranging from 57 to 119  $\mu\text{A}$ ) approximately 3-4 days after inoculation. After those days, the current decreased to values between 87% (in day 6) and 44% (in day 22) of the maximum current value. In fact, three weeks after inoculation, current values seemed to approach a steady-state. This current curve appears to be characteristic for bioanodes that are continuously fed and controlled at a certain potential (29). The variability of current values among granular bioanodes might relate to the granular material itself, due to its irregularities in shape, surface and porosity, even when the raw material, the activation process and the selected granule size is the same. This variability was already found in a previous research study (18) where the reproducibility of single AC granules was proven for different granule sizes and types.

We expect current production to be related to biofilm volume, as electroactive bacteria gain energy from transporting electrons from the substrate to the electrode. To prove this, we correlated the biofilm volume with the total produced electric charge (i.e. current integrated over time, see Experimental Section). Figure 4-9C revealed a linear relation of  $66.4 \text{ C } \mu\text{L}^{-1}$  ( $R^2 = 0.9$ ). This value is in the same order of magnitude but 1.6-fold higher than the linear relation found for bioanodes by OCT measurements (29). Similarly, total nitrogen content can be used as an indication of biofilm growth, as both the bacteria and extracellular polymeric substances (EPS) that are part of the biofilm contribute to the nitrogen content. In fact, the biofilm volume determined from 3D-MRI images was linearly related to total the total nitrogen content of granular bioanodes (Figure 4-9D); the relation found was  $17 \text{ } \mu\text{g N } \mu\text{L}^{-1}$  ( $R^2 = 0.9$ ).

By characterising the biofilm on the same granule using three different approaches, in fact by recording the current production electrochemically, determining the biofilm volume with MRI and indirectly quantifying the biomass with total nitrogen content analysis, makes this study complete. Especially correlating the total produced electric charge and the biofilm volume is valuable information which is difficult to obtain non-destructively with other methods. Nevertheless, we believe MRI should be seen as a complementary technique to other quantitative methods like protein and nitrogen analyses, and particularly be used in studies where biofilm distribution or volume might

give extra relevant information about the electrode-biofilm interface or the MFC performance in general.

In this study, we did not continuously monitor the same bioanode at different growth stages in terms of volume, as the bioanode was permanently removed from the reactor on the day of the MRI measurement. However, we showed that the correlation between electric charge, nitrogen content and volume of the 10 measured bioanodes was independent of their growth stage and electrical performance, meaning a larger number of samples would not give any extra information on this matter. To make sure that these linear correlations did not deviate from the actual values due to a possible biofilm stability issue as a consequence of long MRI experimental times with no substrate, additional total nitrogen analyses were done with fresh granular bioanodes, directly collected from the reactor (i.e. without any MRI measurements). The relation between nitrogen content and total produced electric charge was found to be similar (see Supplementary Information, S 4-5), indicating that sample handling and the duration of MRI measurement time had little effect on the amount of biofilm grown on AC granules and confirming the non-destructive nature of MRI. Even though biofilm detachment proved to be negligible based on these data, the effect of the long experimental times and substrate absence during MRI measurements on the biofilm morphology was not addressed. To this aim, *in situ* measurements are needed, where bioanodes do not deviate from their original state and growth curve and where thus a non-invasive nature is also achieved.

#### 4.4.5 Challenges and Outlook

Regarding the resolution used to visualize the biofilm distribution on AC granules, MRI images with a resolution of  $(28\text{ }\mu\text{m})^3$  were sufficient to elucidate biofilm distribution but not to discriminate individual bacterial cells ( $\sim 1\text{ }\mu\text{m}$ ) (79) or clusters below  $28\text{ }\mu\text{m}$  potentially present in surface cavities or inner pores of the AC granules. In fact, by using SEM to visualize the cross-section of AC granules, we found that bacterial growth occurred in their inner pores (see Supplementary Information, S 4-6). Therefore, this might have caused an underestimation of biofilm growth on AC granules. However,  $(28\text{ }\mu\text{m})^3$  was the optimum resolution with acceptable measurement times ( $< 24\text{ h}$ ). Nevertheless, previous research on single AC granules (18) showed a positive linear relation between nitrogen content (as quantification of biomass) and the outer surface area of granular electrodes, strongly indicating a big contribution of biofilm growth on

the surface. This means 3D MRI measurements in this study were able to cover, to a large extent, the total biofilm volume of granular bioanodes. If we consider that MRI can additionally show the distribution of biofilm over the electrode surface, unlike other (indirect) quantitative measurements of biomass, such as nitrogen or protein analyses, it can be considered a valuable technique to study biofilms on flat but also porous electrodes.

Higher resolutions than  $(28\text{ }\mu\text{m})^3$  would allow to image the biofilm distribution more accurately but would require longer measurement times that might damage the integrity of the biofilm. To achieve higher resolutions, more sensitive detection coils or accelerated measurement techniques (80) are recommended for the future. Another approach to achieve higher resolutions is to use an MRI scanner with a higher magnetic field strength. In fact, within this research we also imaged granular bioanodes at 22 T, but the paramagnetic ions present in AC granules (see Supplementary Information, S 4-2) had a stronger effect on the MR signal at this field strength and the resulting image artefacts made biofilm quantification infeasible (images not shown). At 14.1 T the paramagnetic ions did not cause severe artefacts and therefore did not disturb biofilm visualization and quantification as this effect decreases with decreasing magnetic field strength.

High-resolution 3D-MRI measurements on electrode materials as presented in this study can be easily applied to other complex geometry biofilms with complex geometries of support structures. The limiting factor to the smallest resolvable features is the maximum resolution attainable at a given magnetic field strength with the desired measurement time. If the biofilm is not attached to an electrode support, this could be even easier as measurements might suffer less from susceptibility artefacts.

As for the determination of biofilm volume, it depends on several steps that can introduce errors that are not exactly quantifiable. The choice of the threshold value in the image processing step is therefore crucial. If this value is too high, biofilm will not be counted, while if the threshold is too low, voxels containing bulk water will be attributed to biofilm. In fact, in the threshold images (Fig. 3B and Supplementary Information, S 4-4), several voxels in the bulk water region and the pore water of granules are accounted as biofilm, while in the biofilm region certain areas are instead not counted as such. The signal intensity encountered within AC granules could mean

that protons originating from either water or biofilm water were present in the internal pore structure of the granules. This is difficult to resolve using MRI, due to the resolution of the 3D-MRI images  $(28\text{ }\mu\text{m})^3$  and the presence of e.g. iron ions (see Supplementary Information, S 4-2) that can cause MRI image artefacts inside the granule. Furthermore, even though we corrected for image intensity differences caused by inhomogeneity in the detector of the MRI-equipment (see Experimental Section), small differences in image intensity remain and can cause local over- or underestimation of the biofilm volume. Another inaccuracy results from partial volume effects (81). This means that, if the voxel of  $(28\text{ }\mu\text{m})^3$  is partly filled with biofilm and partly filled with bulk water, it might not be accounted as biofilm volume. The estimation of the partial volume effect has not been done in this study. Additionally, to obtain a more accurate biofilm thickness from the 3D-MRI volume data, determining the exact interfacial area between the biofilm and the AC granule would also be needed. However, this requires more sophisticated image processing procedures. In any case, MRI image artefacts should always be carefully considered for biofilm visualisation purposes, as the signal identified as biofilm could originate from a different source (e.g. relaxation sinks at the surface of the AC granule).

A next step in biofilm characterisation of granular bioanodes with MRI would be to perform *in situ* measurements (66) so that biofilm development can be followed in time for the same AC granules with no change in the growth conditions. To this end, the clamp containing the single bioanode could be inserted into the magnet in a flow-cell, which would allow flow of influent and effluent. In that case, efforts to reduce acquisition time (i.e. more sensitive detector, accelerated techniques (80)) in 3D-MRI measurements would be highly recommended, as it would be preferable to stop the flow during MRI measurements to minimise artefacts. The material of the clamp (i.e. current collector) would need to be carefully selected to minimise susceptibility artefacts originating from the setup. In the same way, when working with real wastewater, special attention should be paid to artefacts that might occur due to the complex composition of wastewater that contains e.g. more soluble metals than the lab electrolyte. In case granular bioanodes (with no attached current collector) are collected from up-scaled reactors treating wastewater as done in reference (82), developing a specific protocol for it could provide information about biofilm growth over time on these electrodes, but again not for the same AC granule as in this study.

Furthermore, MRI presents opportunities for biofilm research not only regarding structural information but also related to the study of its chemical composition. By combining MRI for localisation with NMR spectroscopy for chemical compound identification, localised detection of chemical compounds is already feasible in 20-30  $\mu\text{m}$  thick 2D-plane (53, 66). However, currently, the resolution is still too low to detect relevant (low) metabolite concentrations at the high spatial resolutions which would be required for the thin biofilm on the bioanodes of this study. By translating recent sensitivity enhancement methods from the field of biomedical MRI such as chemical exchange saturation transfer (CEST) (83), or spin hyperpolarisation techniques (84), the metabolite concentrations could be detected with a higher spatial resolution in the future.

With the further improvements of this study as well as the other possibilities of biofilm characterisation that MRI offers (i.e. diffusion and detection of chemical compounds), this technique would not only serve to quantify and visualise biofilms in three-dimensional electrode materials but also could provide strategies to improve the power output as well as to potentially elucidate on the degradation of complex organics during bioelectrochemical wastewater treatment processes.

### 4.5 Conclusions

Determining the distribution and morphology of electroactive biofilms, as well as quantifying them, is of utmost importance since biofilm growth ultimately determines the performance of microbial fuel cells (MFCs). In the case of activated carbon (AC) granules, this is of particular interest in order to better understand the interaction between the biofilm and such highly porous electrode material. In this study, we have shown that high-field (14.1 T) magnetic resonance imaging (MRI) can be used for high-resolution ( $(28\ \mu\text{m})^3$ ) imaging of thin biofilms ( $\sim 28\text{-}116\ \mu\text{m}$ ) growing on granular electrodes in a multi-anode MFC. By using 3D MRI, we could visualise the electroactive biofilm on single AC granule surfaces with a high contrast between biofilm and bulk water, and subsequently determine the biofilm volume as well as estimate its thickness at different growth stages (from day 3 to day 22). For AC granules, this would have not been possible to obtain with electrochemical, chemical or (other) microscopy techniques. Moreover, as it is a non-destructive technique, biofilm quantification was combined with another analytical technique, i.e. total nitrogen content analysis, to yield complementary information. Therefore, the innovation of this study relies on the

combination of using MRI on granular electrodes complementary with other quantification techniques. Additionally, high-resolution 3D MRI enabled the quantification of arbitrarily shaped thin biofilms growing on arbitrarily shaped electrodes for the first time. In the future, *in situ* experiments can be used to monitor biofilm growth and distribution on the same single AC granule in time, as well as to implement this technique on electrode materials within other bioelectrochemical systems.

#### 4.6 MRI of bioanodes beyond 14.1 T – A mission impossible?

Connecting this research back to ultra-high field, suggestions for future research include the use of pure phase encoding techniques (85), as pure phase encoding techniques are less prone to image artefacts arising from susceptibility. The combination of SPI with acceleration techniques such as a turbo-spin-echo (turboSPI)(86) and SPRITE (87) compensate for the disadvantageous long acquisition times of pure phase encoding techniques in comparison to the more standardly used frequency/phase encoding techniques. Higher gradient strength or higher readout bandwidth in frequency encoding is also a means to reduce the image artefacts (88). Recently, a fast 3D-PEPI sequence with  $T_2$  weighting was published by Xiao and Balcom (89), who demonstrated that the sequence performed well for porous media applications at a favourable acquisition time.

However, all these suggestions would have required additional method programming or optimisation which in this case was not needed for the research question by choosing the 14.1 T. While using ultra-high field and developments in detector sensitivity certainly offers advantages for future research, it was not obligatory to answer this particular research question and might not guarantee the optimal results in future. In a broader perspective, it might also not be strictly necessary to use an ultra-high field system with all its advantages of increased SNR. For the research question of the subsequent paper, 14.1 T was sufficient, but for faster high-resolution MRI measurements, a different approach would be needed. While ultra-high magnetic fields are a straightforward means to increase SNR, other approaches such as detector optimisation, cryoprobe to decrease the noise contribution or hyperpolarisation to increase the difference in spin population can be used to increase the signal-to-noise ratio for either high resolution or faster acquisition times (see Chapter 7-General Discussion).

#### **4.7 Acknowledgements**

This research is supported by the Netherlands Organization for Scientific Research (NWO), Domain Applied and Engineering Science (ITW) (VENI grant no 13631) and which is partly funded by the Ministry of Economic Affairs. This research was performed in the cooperation framework of Wetsus, the European Centre of Excellence for Sustainable Water Technology ([www.wetsus.eu](http://www.wetsus.eu)). Wetsus is co-funded by the Dutch Ministry of Economic Affairs and Ministry of Infrastructure and Environment, the European Union Regional Fund, the Province of Fryslân, and the Northern Netherlands Provinces. J.R.K. received funding from the NWO-funded graduate school Netherlands Magnetic Resonance Research School [022.005.029]. The authors would like to thank the participants of the research theme Resource Recovery of Wetsus for the fruitful discussions and their financial support. Furthermore, the authors would like to thank Agnieszka Tomaszewska for the SEM images and Roos Goedhart for her help with preliminary experiments. We also thank John Philippi and Pieter de Waard for their technical assistance at the MAGNetic resonance research FacilitY (MAGNEFY) at Wageningen University & Research.

## 4.8 Supporting Information

**S 4-1** Information about each of the AC granules used in this study: harvest day, weight, estimated granule volume and surface area, and estimated biofilm thickness.

Harvest day	Weight (mg)	Estimated volume (μL)	Estimated surface area (mm <sup>2</sup> )	Estimated biofilm thickness (μm)
3	1.02	3.52	11.18	40.9
4	1.39	4.79	13.75	27.8
6	1.46	5.03	14.20	41.2
7	1.16	4.00	12.19	85.8
10	0.97	3.34	10.82	49.2
11	1.75	6.03	16.03	82.6
15	0.80	2.76	9.51	115.0
16	1.05	3.62	11.40	90.5
21	1.13	3.90	11.97	166.0
22	1.16	4.00	12.19	136.9

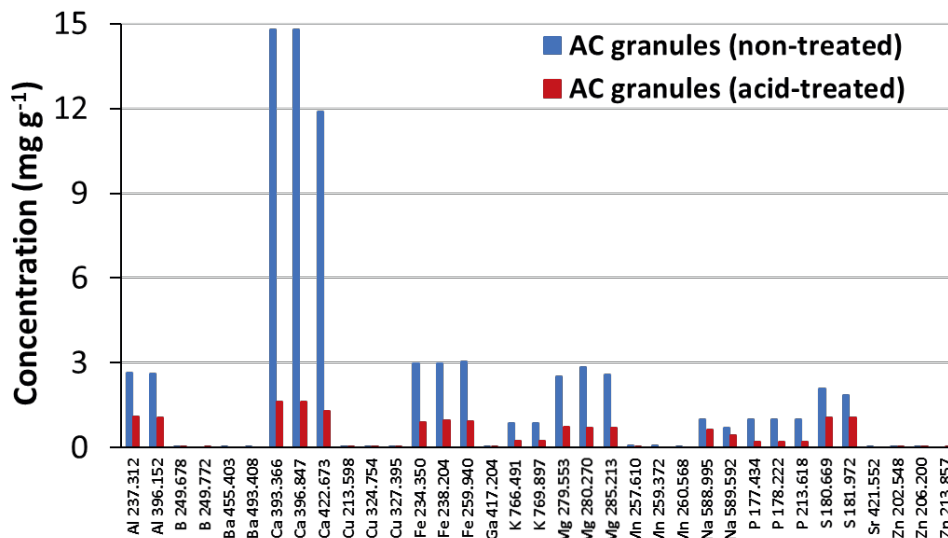
Density of PK granules used: 1.03 g mL<sup>-1</sup>

Volume of a sphere:  $V = \frac{4}{3} \pi r^3$

Surface area of a sphere:  $A = 4 \pi r^2$



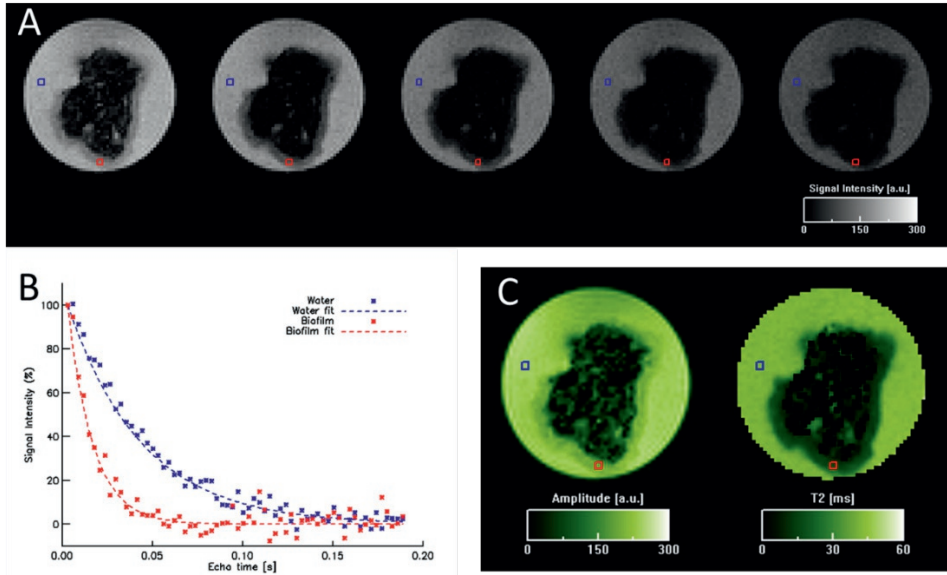
**S 4-2** Elemental composition of AC granules (PK 1-3) with no treatment (in blue) and with 22% HCl acid-treatment (in red). Results were obtained with ICP-MS.



The elemental composition of AC granules was analysed with an inductively coupled plasma analyser (ICP-OES, Varian Vista MPX). 0.209 g of PK granules with no treatment and 0.203 g of PK granules with acid treatment (22% HCl for 24h) were used for the analysis. Multi- and single-element standard solutions were prepared (with aqua regia as dissolvent) to cover a concentration range from 0.2 to 5 mg L<sup>-1</sup>. These standards contained the following elements: Ag, Al, B, Ba, Bi, Ca, Cd, Co, Cr, Cu, Fe, Ga, In, K, Li, Mg, Mn, Na Ni, P, Pb, S, Sr, Tl and Zn.

Prior to measurements, granules were mixed with 4 mL HNO<sub>3</sub>, 1mL HClO<sub>4</sub>, 1 mL H<sub>2</sub>O<sub>2</sub> and 1 mL H<sub>2</sub>O in a vessel with vent-and-reseal technology, and digested in a microwave (ETHOS 1, Milestone S.r.l.). The overall digestion program took 1 hour with a maximum temperature of 220 °C. After samples were cooled down, the resulting liquid was diluted in a 100 mL volumetric flask with milli-Q water. Results were normalised to the initial weight of the samples.

**S 4-3**  $T_2$  measurements of an AC granule with biofilm that was collected after a growth period of 15 days. A) 2D spin echo MRI images at echo times  $t = 2.9, 11.8, 20.6, 29.5, 38.3$  ms are shown. B) Signal intensity values of all recorded echo images of one biofilm pixel (red) and bulk water pixel (blue) (positions indicated in (A)) are plotted against the echo time. C) Amplitude map and  $T_2$  map from the mono-exponential fit of the image intensities in (A) are depicted. The images in C) were resampled with the bilinear interpolation method.



### $T_2$ map – Methods

A 2D spin-echo MSME sequence (Echo time (TE) = 2.9 ms, number of echoes 64, Repetition time TR = 12500 ms), 24 averages, receiver bandwidth 100 kHz, Field-of-View  $3 \times 3$  mm<sup>2</sup>, matrix size  $64 \times 64$ , slice thickness 0.2 mm) was used. The raw data were phase-corrected and Fourier-transformed. The signal intensity within a pixel as a function of actual echo time ( $t = n \cdot TE$ ) was fitted mono-exponentially using home-built software in IDL Version 6.4 (ITT, Visual Information Solutions, Boulder, CO, USA) to obtain quantitative  $T_2$  maps according to the function:

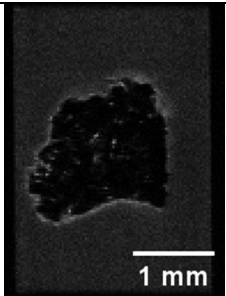

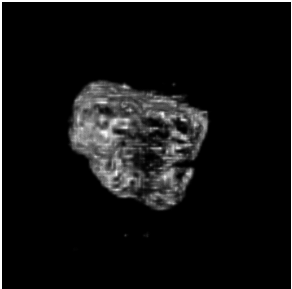
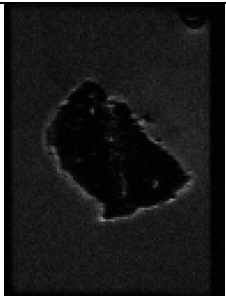

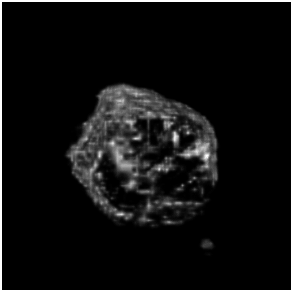
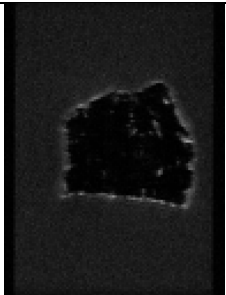
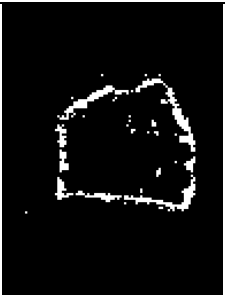
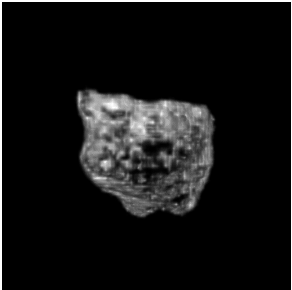
$$I(t) = I_0 e^{-\frac{t}{T_2}} \quad (1)$$

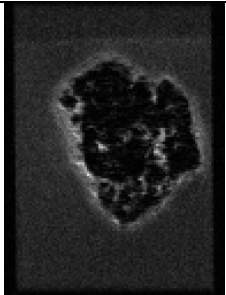

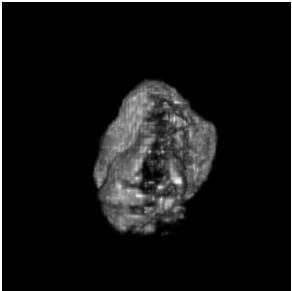
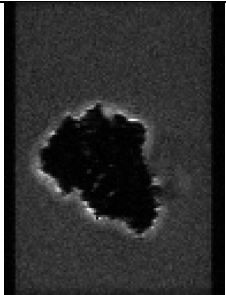

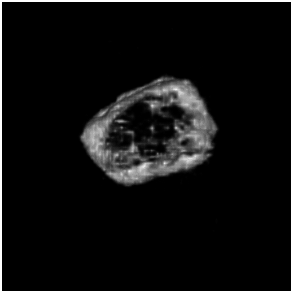
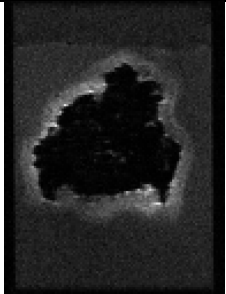

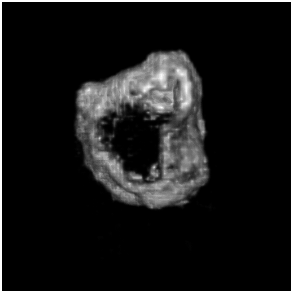
where  $I(t)$  is the image intensity as function of echo time  $t = n \cdot TE$ , the proton density  $I_0$ , and the  $T_2$ -relaxation time.

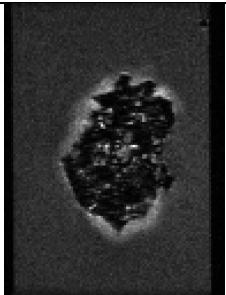

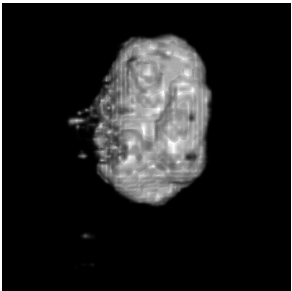
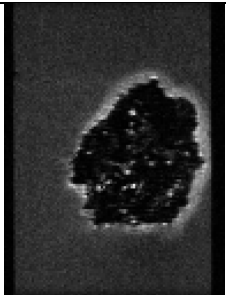
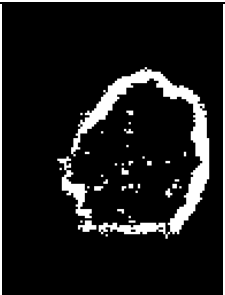
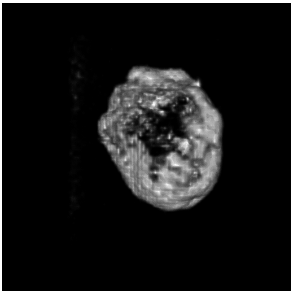
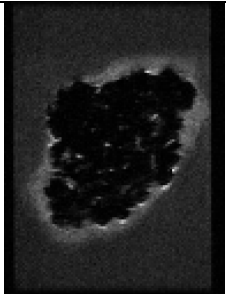

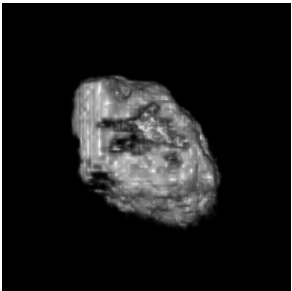
### **$T_2$ map – Results**

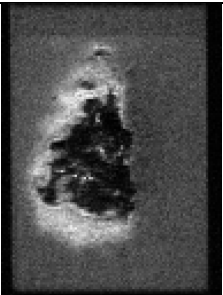

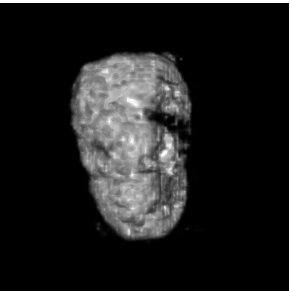
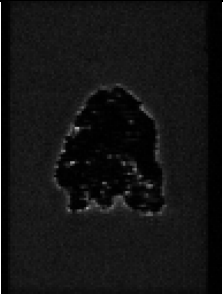

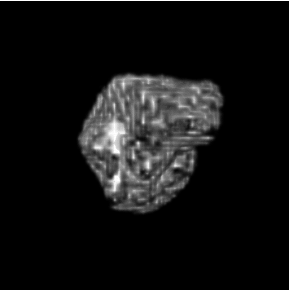
The spin-echo images at different echo times show that biofilm and bulk water can be distinguished based on  $T_2$  contrast (Figure S 4-3A). However, the contrast between biofilm water and AC granule is lower than in the  $T_1$ -weighted images. Therefore, the distinction between these two regions is easier based on  $T_1$  contrast than on  $T_2$  contrast.

**S 4-4:** This table shows one cross-section of the MRI-data (left), the corresponding image after the threshold procedure has been applied (middle) and the 3D-volume reconstruction (right). The scale bars shown in the picture of day 3 can be used for the rest of figures as well, which have the exact same dimensions.

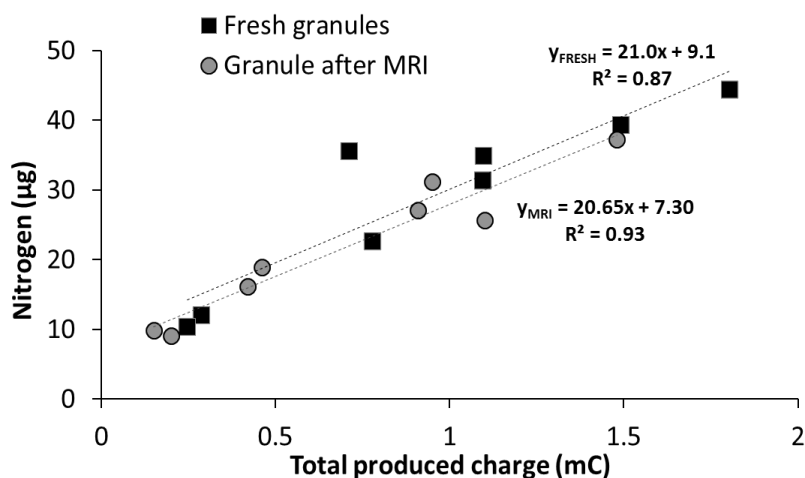
Biofilm growth period [d]	MRI data	Theshold image	3D- reconstruction
3			 See Video “Day_3.avi”
4			 See Video “Day_4.avi”
6			

			See Video “Day_6.avi”
7			 See Video “Day_7.avi”
10			 See Video “Day_10.avi”
11			 See Video “Day_11.avi”

15			 See Video “Day_15.avi”
16			 See Video “Day_16.avi”
22			 See Video “Day_22.avi”

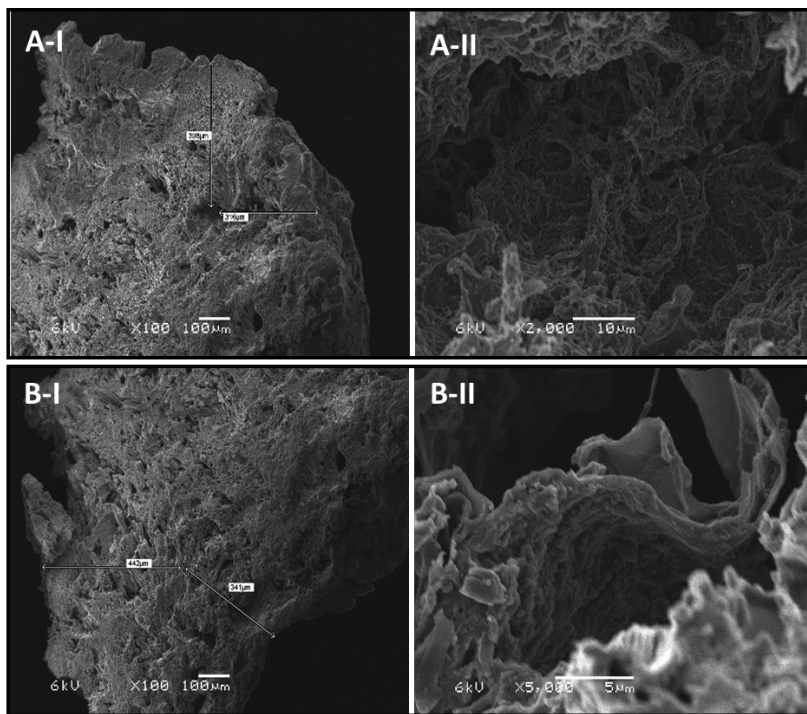
23			 See Video “Day_23.avi”
Abiotic			 See Video “Abiotic.avi”

**S 4-5** Nitrogen content of granular bioanodes that were i) previously used for MRI images (in grey); and ii) fresh, directly taken from the MFC reactor (in black). The correlation of the nitrogen content and the total produced electric charge was linear in both cases, meaning that no damage was caused to the biofilm during MRI measurements.





**S 4-6** Two cross-section images of AC granules taken with SEM. On the left (A-I and B-I), the granule inner surface can be seen (100x), and cavities that were further checked for bacterial growth are marked with arrows, at a distance of approximately 300 to 400  $\mu\text{m}$  from the granule surface. On the right (A-II and B-II), a closer view of the cavities can be seen (2000x and 5000x), where bacterial growth is visible.



In order to take SEM images of the granules, these were individually collected from the reactor and fixated with 2.5% glutaraldehyde for 2 h at room temperature. Afterwards, they were rinsed 3 times with a phosphate buffer solution (30.5 mM  $\text{Na}_2\text{HPO}_4$  and 19.5 mM  $\text{KH}_2\text{PO}_4$ ) and dehydrated with a sequence of ethanol solutions (30%, 50%, 70%, 90% and 100%) for 30 min each. Finally, granules were dried at 105  $^\circ\text{C}$  for 1 h.

Prior to imaging, granules were embedded in optimal cutting temperature (OCT) compound to do the frozen sectioning on a microtome-cryostat. Usually, this process is done to create very thin slides of a sample. However, AC granules were too brittle and the slides broke. Therefore, several cuts were done until the middle of the granule ( $\sim 0.7$  mm) was approximately reached. The remaining sample was then left at room

temperature until the OCT melted, washed with PBS and dried for 1h. For the imaging, single granules were placed in a specimen holder of the scanning electron microscope (SEM) JEOL JSM-6480 LV (JEOL Technics Ltd., Tokyo, Japan). With a magnification of 100x, SEM was operated at an acceleration voltage of 6 kV and an electron beam diameter of 20-30%. Images were analyzed with the software JEOL SEM Control User Interface version 7.07.

## 4.9 References

1. L. Caizán Juanarena, thesis, Wageningen University, Wageningen (2019).
2. L. Caizán-Juanarena, J. R. Krug, F. J. Vergeldt, J. M. Kleijn, A. H. Velders, H. Van As, A. ter Heijne, 3D biofilm visualization and quantification on granular bioanodes with magnetic resonance imaging. *Water Res.*, 115059 (2019).
3. K. M. Koch, B. A. Hargreaves, K. B. Pauly, W. Chen, G. E. Gold, K. F. King, Magnetic resonance imaging near metal implants. *J. Magn. Reson. Imaging*. **32**, 773–787 (2010).
4. A. Webb, Increasing the sensitivity of magnetic resonance spectroscopy and imaging. *Anal. Chem.* **84**, 9–16 (2012).
5. G. Zeeman, K. Kujawa-Roeleveld, Resource recovery from source separated domestic waste(water) streams; full scale results. *Water Sci. Technol.* **64**, 1987–1992 (2011).
6. W. Mo, Q. Zhang, Energy-nutrients-water nexus: Integrated resource recovery in municipal wastewater treatment plants. *J. Environ. Manage.* **127**, 255–267 (2013).
7. O. Nir, R. Sengpiel, M. Wessling, Closing the cycle: Phosphorus removal and recovery from diluted effluents using acid resistive membranes. *Chem. Eng. J.* **346**, 640–648 (2018).
8. R. M. Allen, P. H. Bennetto, Microbial Fuel-Cells Electricity Production from Carbohydrates. *Appl. Biochem. Biotechnol.* **39**, 27–40 (1993).
9. J. Heilmann, B. E. Logan, Production of Electricity from Proteins Using a Microbial Fuel Cell. *Water Environ. Res.* **78**, 531–537 (2006).
10. R. A. Rozendal, H. V. M. Hamelers, K. Rabaey, J. Keller, C. J. N. Buisman, Towards practical implementation of bioelectrochemical wastewater treatment. *Trends Biotechnol.* **26**, 450–459 (2008).
11. T. Shimoyama, S. Komukai, A. Yamazawa, Y. Ueno, B. E. Logan, K. Watanabe, Electricity generation from model organic wastewater in a cassette-electrode microbial fuel cell. *Appl. Microbiol. Biotechnol.* **80**, 325–330 (2008).
12. B. E. Logan, M. J. Wallack, K. Y. Kim, W. He, Y. Feng, P. E. Saikaly, Assessment of Microbial Fuel Cell Configurations and Power Densities. *Environ. Sci. Technol. Lett.* **2**, 206–214 (2015).
13. A. Ter Heijne, F. Liu, L. S. Van Rijnsoever, M. Saakes, V. M. Hamelers, C. J. N. Buisman, Performance of a scaled-up Microbial Fuel Cell with iron reduction as the cathode reaction. *J. Power Sources*. **196**, 7572–7577 (2011).
14. J. B. A. Arends, W. Verstraete, 100 years of microbial electricity production: Three concepts for the future. *Microb. Biotechnol.* **5**, 333–346 (2012).
15. M. Zhou, M. Chi, J. Luo, H. He, T. Jin, An overview of electrode materials in microbial fuel cells. *J. Power Sources*. **196**, 4427–4435 (2011).
16. J. Wei, P. Liang, X. Huang, Recent progress in electrodes for microbial fuel cells. *Bioresour. Technol.* **102**, 9335–9344 (2011).
17. D. Qu, H. Shi, Studies of the activated carbons used in double-layer supercapacitors. *J. Power Sources*. **74**, 99–107 (1998).

18. L. Caizán-Juanarena, I. Servin-Balderas, X. Chen, C. J. N. Buisman, A. ter Heijne, Electrochemical and microbiological characterization of single carbon granules in a multi-anode microbial fuel cell. *J. Power Sources* (2019), doi:10.1016/j.jpowsour.2019.04.042.
19. C. Borsje, D. Liu, C. J. N. Buisman, A. Heijne, Performance of Single Carbon Granules As Perspective for Larger Scale Capacitive Bioanodes. *J. Power Sources*. **325**, 690–696 (2016).
20. A. Deeke, T. H. J. A. Sleutels, H. V. M. Hamelers, C. J. N. Buisman, Capacitive bioanodes enable renewable energy storage in microbial fuel cells. *Environ. Sci. Technol.* **46**, 3554–3560 (2012).
21. J. Rodrigo-Quejigo, L. F. M. Rosa, F. Harnisch, Electrochemical characterization of bed electrodes using voltammetry of single granules. *Electrochem. commun.* **90**, 78–82 (2018).
22. B. Kastening, M. Hahn, B. Rabanus, M. Heins, U. zum Felde, Electronic properties and double layer of activated carbon. *Electrochim. Acta.* **42**, 2789–2799 (1997).
23. E. Frackowiak, F. Béguin, Carbon materials for the electrochemical storage of energy in capacitors. *Carbon N. Y.* **39**, 937–950 (2001).
24. J. Pastor-Villegas, C. J. Durán-Valle, Pore structure of activated carbons prepared by carbon dioxide and steam activation at different temperatures from extracted rockrose. *Carbon N. Y.* **40**, 397–402 (2002).
25. T. R. Neu, B. Manz, F. Volke, J. J. Dynes, A. P. Hitchcock, J. R. Lawrence, Advanced imaging techniques for assessment of structure, composition and function in biofilm systems. *FEMS Microbiol. Ecol.* **72**, 1–21 (2010).
26. R. Valladares Linares, L. Fortunato, N. M. Farhat, S. S. Bucs, M. Staal, E. O. Fridjonsson, M. L. Johns, J. S. Vrouwenvelder, T. Leiknes, Mini-review: novel non-destructive in situ biofilm characterization techniques in membrane systems. *Desalin. Water Treat.* **57**, 22894–22901 (2016).
27. H. Beyenal, Z. Lewandowski, G. Harkin, Quantifying Biofilm Structure: Facts and Fiction. *Biofouling*. **20**, 1–23 (2004).
28. M. C. A. A. Van Eerten-Jansen, A. B. Veldhoen, C. M. Plugge, A. J. M. Stams, C. J. N. Buisman, A. Ter Heijne, Microbial community analysis of a methane-producing biocathode in a bioelectrochemical system. *Archaea*. **2013** (2013), doi:10.1155/2013/481784.
29. S. Molenaar, T. Sleutels, J. Pereira, M. Lorio, C. Borsje, J. A. Zamudio, F. Fabregat-Santiago, C. J. N. Buisman, A. Heijne, In situ biofilm quantification in Bioelectrochemical Systems using Optical Coherence Tomography. *ChemSusChem*. **11**, 1–9 (2018).
30. B. Saba, A. D. Christy, Z. Yu, A. C. Co, R. Islam, O. H. Tuovinen, Characterization and performance of anodic mixed culture biofilms in submersed microbial fuel cells. *Bioelectrochemistry*. **113**, 79–84 (2017).
31. S. Marzorati, A. Goglio, S. Fest-Santini, D. Mombelli, F. Villa, P. Cristiani, A. Schievano, Air-breathing bio-cathodes based on electro-active biochar from pyrolysis of Giant Cane stalks. *Int. J. Hydrogen Energy* (2018), doi:10.1016/j.IJHYDENE.2018.07.167.
32. B. S. Zakaria, S. Barua, A. Sharaf, Y. Liu, B. R. Dhar, Impact of antimicrobial silver nanoparticles on anode respiring bacteria in a microbial electrolysis cell. *Chemosphere*. **213**, 259–267 (2018).

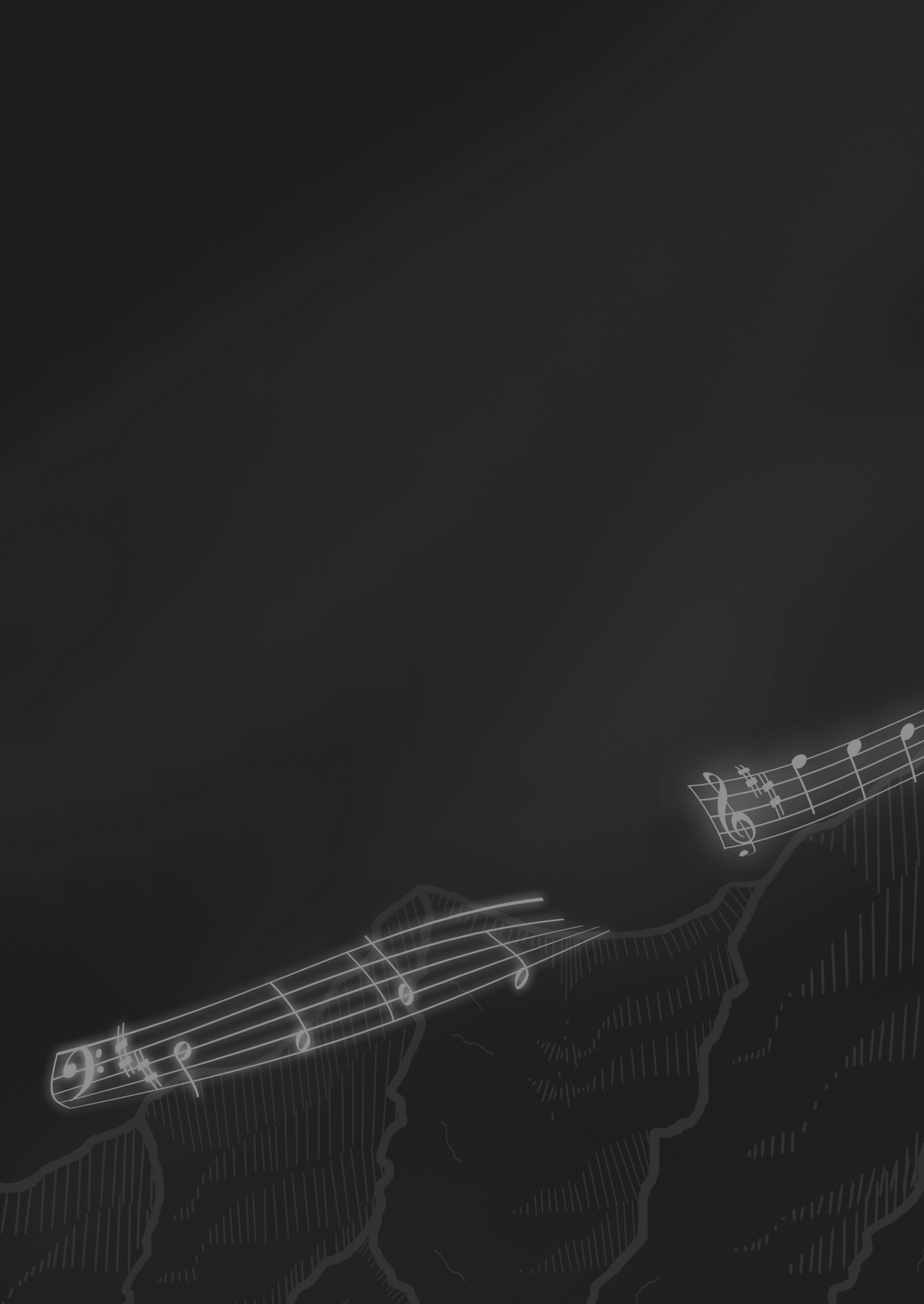
33. D. Sun, J. Chen, H. Huang, W. Liu, Y. Ye, S. Cheng, The effect of biofilm thickness on electrochemical activity of *Geobacter sulfurreducens*. *Int. J. Hydrogen Energy*. **41**, 16523–16528 (2016).
34. S. Tejedor-Sanz, P. Fernández-Labrador, S. Hart, C. I. Torres, A. Esteve-Núñez, *Geobacter* Dominates the Inner Layers of a Stratified Biofilm on a Fluidized Anode During Brewery Wastewater Treatment. *Front. Microbiol.* **9**, 1–12 (2018).
35. M. Wagner, D. Taherzadeh, C. Haisch, H. Horn, Investigation of the mesoscale structure and volumetric features of biofilms using optical coherence tomography. *Biotechnol. Bioeng.* **107**, 844–853 (2010).
36. C. Li, S. Felz, M. Wagner, S. Lackner, H. Horn, Investigating biofilm structure developing on carriers from lab-scale moving bed biofilm reactors based on light microscopy and optical coherence tomography. *Bioresour. Technol.* **200**, 128–136 (2016).
37. C. Xi, D. Marks, S. Schlachter, W. Luo, S. A. Boppart, High-resolution three-dimensional imaging of biofilm development using optical coherence tomography. *J. Biomed. Opt.* **11**, 034001 (2006).
38. C. Haisch, R. Niessner, Visualisation of transient processes in biofilms by optical coherence tomography. *Water Res.* **41**, 2467–2472 (2007).
39. L. Fortunato, T. Leiknes, In-situ biofouling assessment in spacer filled channels using optical coherence tomography (OCT): 3D biofilm thickness mapping. *Bioresour. Technol.* **229**, 231–235 (2017).
40. V. R. Phoenix, W. M. Holmes, Magnetic resonance imaging of structure, diffusivity, and copper immobilization in a phototrophic biofilm. *Appl. Environ. Microbiol.* **74**, 4934–4943 (2008).
41. B. Ramanan, W. M. Holmes, W. T. Sloan, V. R. Phoenix, Magnetic resonance imaging of mass transport and structure inside a phototrophic biofilm. *Curr. Microbiol.* **66**, 456–461 (2013).
42. F. Ranzinger, M. P. Herrling, S. Lackner, V. W. Grande, A. Baniodeh, A. K. Powell, H. Horn, G. Guthausen, Direct surface visualization of biofilms with high spin coordination clusters using Magnetic Resonance Imaging. *Acta Biomater.* **31**, 167–177 (2016).
43. G. Gonzalez-Gil, P. N. L. Lens, A. Van Aelst, H. Van As, A. I. Versprille, G. Lettinga, Cluster Structure of Anaerobic Aggregates of an Expanded Granular Sludge Bed Reactor. *Appl. Environ. Microbiol.* **67**, 3683–3692 (2001).
44. B. Manz, F. Volke, D. Goll, H. Horn, Measuring local flow velocities and biofilm structure in biofilm systems with magnetic resonance imaging (MRI). *Biotechnol. Bioeng.* **84**, 424–432 (2003).
45. M. P. Herrling, S. Lackner, H. Nirschl, H. Horn, G. Guthausen, Recent NMR/MRI studies of biofilm structures and dynamics. *Annu. Reports NMR Spectrosc.* **97**, 163 (2019).
46. J. Bartacek, F. J. Vergeldt, J. Maca, E. Gerkema, H. Van As, P. N. L. Lens, Iron, Cobalt, and Gadolinium Transport in Methanogenic Granules Measured by 3D Magnetic Resonance Imaging. *Front. Environ. Sci.* **4**, 13 (2016).
47. B. Ramanan, W. M. Holmes, W. T. Sloan, V. R. Phoenix, Application of Paramagnetically Tagged Molecules for Magnetic Resonance Imaging of Biofilm Mass Transport Processes . **76**, 4027–4036 (2010).

48. J. D. Seymour, S. L. Codd, E. L. Gjersing, P. S. Stewart, Magnetic resonance microscopy of biofilm structure and impact on transport in a capillary bioreactor. *J. Magn. Reson.* **167**, 322–327 (2004).
49. B. Manz, F. Volke, D. Goll, H. Horn, Investigation of biofilm structure, flow patterns and detachment with magnetic resonance imaging. *Water Sci. Technol.* **52**, 1–6 (2005).
50. H. Van As, P. Lens, Use of <sup>1</sup>H NMR to study transport processes in porous biosystems. *J. Ind. Microbiol. Biotechnol.* **26**, 43–52 (2001).
51. M. P. Herrling, J. Weisbrodt, C. M. Kirkland, N. H. Williamson, S. Lackner, S. L. Codd, J. D. Seymour, G. Guthausen, H. Horn, NMR investigation of water diffusion in different biofilm structures. *Biotechnol. Bioeng.* **114**, 2857–2867 (2017).
52. A. Wieland, D. de Beer, D. van Dusschoten, L. R. Damgaard, M. Kuehl, H. van As, Fine-scale measurement of diffusivity in a microbial mat with NMR imaging. *Limnol. Ocean.* **44**, 248–259 (2001).
53. J. S. McLean, O. N. Ona, P. D. Majors, Correlated biofilm imaging, transport and metabolism measurements via combined nuclear magnetic resonance and confocal microscopy. *ISME J.* **2**, 121–131 (2008).
54. M. P. Herrling, G. Guthausen, M. Wagner, S. Lackner, H. Horn, Determining the flow regime in a biofilm carrier by means of magnetic resonance imaging. *Biotechnol. Bioeng.* **112**, 1023–1032 (2015).
55. D. A. Graf von der Schulenburg, J. S. Vrouwenvelder, S. A. Creber, M. C. M. van Loosdrecht, M. L. Johns, Nuclear magnetic resonance microscopy studies of membrane biofouling. *J. Memb. Sci.* **323**, 37–44 (2008).
56. A. M. Lefterink, R. M. Fratila, M. A. Koenrades, C. A. van Blitterswijk, A. Velders, L. Moroni, An open source image processing method to quantitatively assess tissue growth after non-invasive magnetic resonance imaging in human bone marrow stromal cell seeded 3D polymeric scaffolds. *PLoS One.* **9**, 1–16 (2014).
57. J. S. Vrouwenvelder, D. A. Graf von der Schulenburg, J. C. Kruithof, M. L. Johns, M. C. M. van Loosdrecht, Biofouling of spiral-wound nanofiltration and reverse osmosis membranes: A feed spacer problem. *Water Res.* **43**, 583–594 (2009).
58. J. D. Seymour, J. P. Gage, S. L. Codd, R. Gerlach, Magnetic resonance microscopy of biofouling induced scale dependent transport in porous media. **30**, 1408–1420 (2007).
59. R. S. Renslow, P. D. Majors, J. S. McLean, J. K. Fredrickson, B. Ahmed, H. Beyenal, In situ effective diffusion coefficient profiles in live biofilms using pulsed-field gradient nuclear magnetic resonance. *Biotechnol. Bioeng.* **106**, 928–937 (2010).
60. P. D. Majors, J. S. McLean, G. E. Pinchuk, J. K. Fredrickson, Y. A. Gorby, K. R. Minard, R. A. Wind, NMR methods for in situ biofilm metabolism studies. *J. Microbiol. Methods.* **62**, 337–344 (2005).
61. M. Wagner, B. Manz, F. Volke, T. R. Neu, H. Horn, Online Assessment of Biofilm Development, Sloughing and Forced Detachment in Tube Reactor by Means of Magnetic Resonance Microscopy. **107**, 172–181 (2010).
62. D. A. Graf von der Schulenburg, B. S. Akpa, L. F. Gladden, M. L. Johns, Non-Invasive Mass Transfer Measurements in Complex Biofilm-Coated Structures. *Biotechnol. Bioeng.* **101**, 602–608 (2008).

63. K. P. Nott, F. P. Heese, M. Paterson-Beedle, L. E. Macaskie, L. D. Hall, Visualization of the Function of a Biofilm Reactor by Magnetic Resonance Imaging. *Can. J. Chem. Eng.* **83**, 68–72 (2005).
64. R. S. Renslow, J. T. Babauta, P. D. Majors, H. Beyenal, Diffusion in biofilms respiring on electrodes. *Energy Environ. Sci.* **6**, 595–607 (2013).
65. R. S. Renslow, J. T. Babauta, A. Dohnalkova, M. I. Boyanov, K. M. Kemner, P. D. Majors, J. K. Fredrickson, H. Beyenal, Metabolic spatial variability in electrode-respiring *Geobacter sulfurreducens* biofilms. *Energy Environ. Sci.* **6**, 1827–1836 (2013).
66. R. S. Renslow, J. T. Babauta, P. D. Majors, H. S. Mehta, R. J. Ewing, T. W. Ewing, K. T. Mueller, H. Beyenal, A biofilm microreactor system for simultaneous electrochemical and nuclear magnetic resonance techniques. *Water Sci. Technol.* **69**, 966–973 (2014).
67. J. Bartacek, F. J. Vergeldt, J. Maca, E. Gerkema, H. Van As, P. N. L. Lens, Iron, Cobalt, and Gadolinium Transport in Methanogenic Granules Measured by 3D Magnetic Resonance Imaging. *Front. Environ. Sci.* **4**, 13 (2016).
68. C. Westbrook, J. Talbot, *MRI in Practice* (John Wiley & Sons, 2018).
69. S. Wu, P. Liang, C. Zhang, H. Li, K. Zuo, X. Huang, Enhanced performance of microbial fuel cell at low substrate concentrations by adsorptive anode. *Electrochim. Acta.* **161**, 245–251 (2015).
70. J. Schindelin, I. Arganda-Carreras, E. Frise, V. Kaynig, M. Longair, T. Pietzsch, S. Preibisch, C. Rueden, S. Saalfeld, B. Schmid, Fiji: an open-source platform for biological-image analysis. *Nat. Methods.* **9**, 676 (2012).
71. B. Schmid, J. Schindelin, A. Cardona, M. Longair, M. Heisenberg, A high-level 3D visualization API for Java and ImageJ. *BMC Bioinformatics.* **11**, 274 (2010).
72. B. C. Hoskins, P. D. Majors, M. M. Sharma, G. Georgiou, Non-Invasive Imaging of Biofilms in Porous Media Using NMR Methods. *Explor. Prod. Environ. Conf.* **73**, 67–73 (1999).
73. P. S. Belton, R. G. Ratcliffe, NMR and compartmentation in biological tissues. *Prog. Nucl. Magn. Reson. Spectrosc.* **17**, 241–279 (1985).
74. H. T. Edzes, D. Van Dusschoten, H. Van As, Quantitative T2 imaging of plant tissues by means of multi-echo MRI microscopy. *Magn. Reson. Imaging.* **16**, 185–196 (1998).
75. S. Godefroy, J.-P. Korb, M. Fleury, R. G. Bryant, Surface nuclear magnetic relaxation and dynamics of water and oil in macroporous media. *Phys. Rev. E.* **64**, 021605 (2001).
76. P. S. Jana, K. Katuri, P. Kavanagh, A. Kumar, D. Leech, Charge transport in films of *Geobacter sulfurreducens* on graphite electrodes as a function of film thickness. *Phys. Chem. Chem. Phys.* **16**, 9039–9046 (2014).
77. B. Korth, L. F. M. Rosa, F. Harnisch, C. Picioreanu, A framework for modeling electroactive microbial biofilms performing direct electron transfer. *Bioelectrochemistry.* **106**, 194–206 (2015).
78. J. M. Savéant, Electron hopping between fixed sites- Equivalent diffusion and migration laws. *J. Electroanal. Chem.* **201**, 211–213 (1986).
79. D. R. Bond, D. R. Lovley, Electricity Production by *Geobacter sulfurreducens* Attached to Electrodes. *Appl. Environ. Microbiol.* **69**, 1548–1555 (2003).

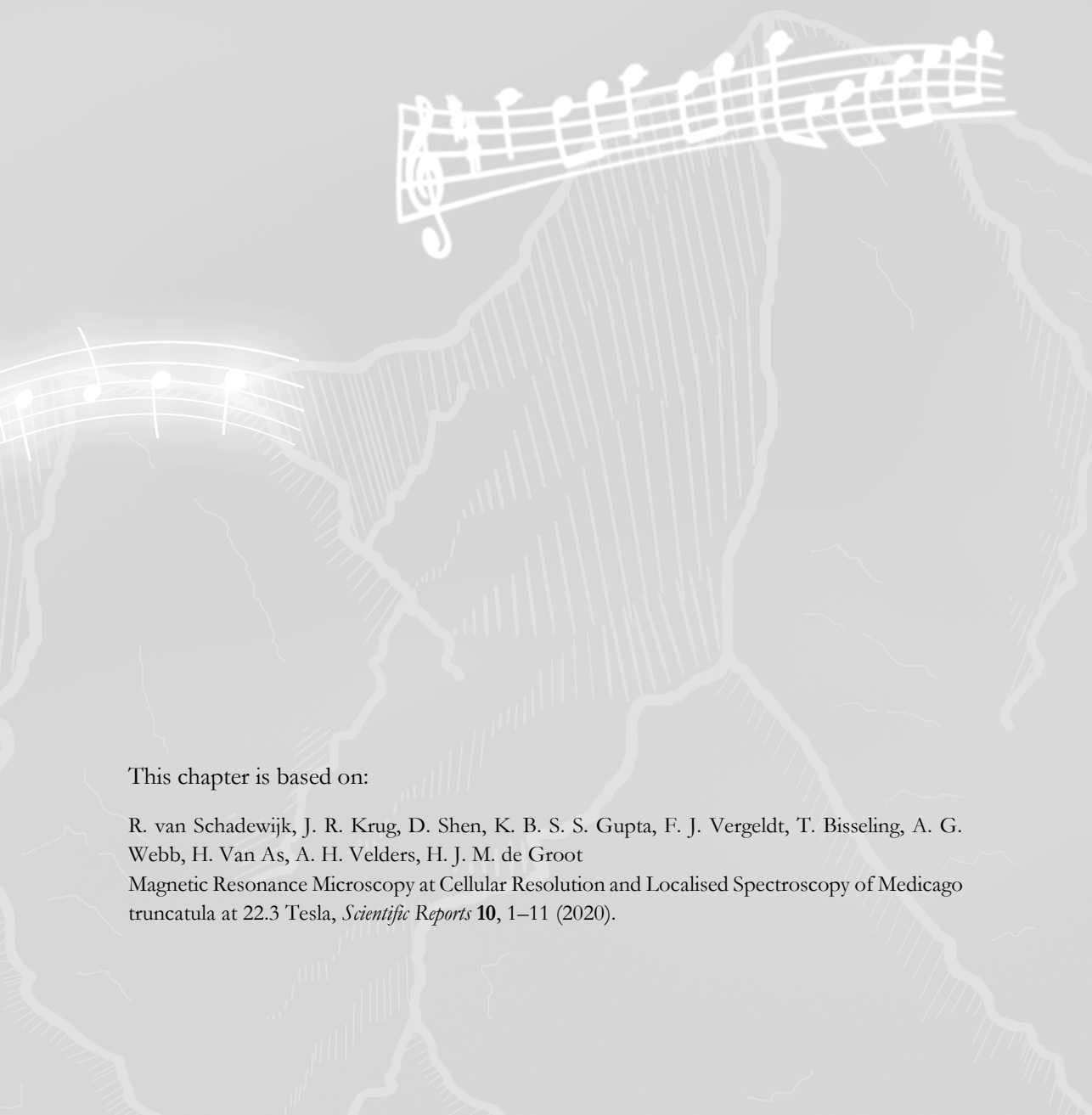
80. J. Tsao, S. Kozerke, MRI temporal acceleration techniques. *J. Magn. Reson. Imaging*, **36**, 543–560 (2012).
81. M. Á. González Ballester, A. P. Zisserman, M. Brady, Estimation of the partial volume effect in MRI. *Med. Image Anal.* **6**, 389–405 (2002).
82. J. Rodrigo Quejigo, L. F. M. Rosa, F. Harnisch, Electrochemical characterization of bed electrodes using voltammetry of single granules. *Electrochem. commun.* **90**, 78–82 (2018).
83. B. Wu, G. Warnock, M. Zaiss, C. Lin, M. Chen, Z. Zhou, L. Mu, D. Nanz, R. Tuura, G. Delso, An overview of CEST MRI for non-MR physicists. *EJNMMI Phys.* **3** (2016), doi:10.1186/s40658-16-0155-2.
84. P. Nikolaou, B. M. Goodson, E. Y. Chekmenev, NMR hyperpolarization techniques for biomedicine. *Chem.-Eur. J.* **21**, 3156–3166 (2015).
85. S. Gravina, D. G. Cory, Sensitivity and Resolution of Constant-Time Imaging. *J. Magn. Reson. Ser. B*, **104**, 53–61 (1994).
86. S. D. Beyea, B. J. Balcom, I. V. Mastikhin, T. W. Bremner, R. L. Armstrong, P. E. Grattan-Bellew, Imaging of Heterogeneous Materials with a Turbo Spin Echo Single-Point Imaging Technique. *J. Magn. Reson.* **144**, 255–265 (2000).
87. D. Xiao, B. J. Balcom, Restricted k-space sampling in pure phase encode MRI of rock core plugs. *J. Magn. Reson.* **231**, 126–132 (2013).
88. M. M. Britton, Magnetic resonance imaging of electrochemical cells containing bulk metal. *ChemPhysChem.* **15**, 1731–1736 (2014).
89. D. Xiao, B. J. Balcom, T2 selective  $\pi$  Echo-Planar Imaging for porous media MRI. *J. Magn. Reson.* **277**, 52–58 (2017).





## Chapter 5

### Magnetic Resonance Microscopy at Cellular Resolution and Localised Spectroscopy of *Medicago truncatula* at 22.3 Tesla



This chapter is based on:

R. van Schadewijk, J. R. Krug, D. Shen, K. B. S. S. Gupta, F. J. Vergeldt, T. Bisseling, A. G. Webb, H. Van As, A. H. Velders, H. J. M. de Groot  
Magnetic Resonance Microscopy at Cellular Resolution and Localised Spectroscopy of *Medicago truncatula* at 22.3 Tesla, *Scientific Reports* **10**, 1–11 (2020).

## Abstract

Interactions between plants and the soil's microbial & fungal flora are crucial for the health of soil ecosystems and food production. Microbe-plant interactions are challenging to investigate *in situ* due to their intertwined relationship involving morphology and metabolism. Here, we describe an approach to overcome this challenge by elucidating morphology and the metabolic profile of *Medicago truncatula* root nodules using Magnetic Resonance (MR) Microscopy, at the highest magnetic field strength (22.3 T) currently available for imaging. A home-built solenoid RF coil with an inner diameter of 1.5 mm was used to study individual root nodules. A 3D imaging sequence with an isotropic resolution of  $(7\ \mu\text{m})^3$  was able to resolve individual cells and distinguish between cells infected with rhizobia and uninfected cells. Furthermore, we studied the metabolic profile of cells in different sections of the root nodule using localised MR spectroscopy and showed that several metabolites, including betaine, asparagine/aspartate and choline, have different concentrations across nodule zones. The metabolite spatial distribution was visualised using chemical shift imaging. Finally, we describe the technical challenges and outlook towards future *in vivo* MR microscopy of nodules and the plant root system.

## 5.1 Introduction

Interactions between plants and microbes are considered to be essential for the health of the soil ecosystem as a whole (1). Understanding the metabolic interactions between plants and microbes, both commensal and parasitic, could help address many of the challenges we face today, related to agriculture and food security. One such interaction is the microbiome-mediated uptake of nitrogen by plants. Availability of biologically-active forms of nitrogen in the soil is an essential factor determining crop yield. Current agricultural practice, therefore, relies strongly on nitrogen fertiliser to supplement soil nitrogen to ensure high crop yield (2). The Haber-Bosch nitrogen fixation process, used to produce the ammonia needed for these fertilisers, currently consumes 1% of the world energy sources; making it the most energy-consuming process in the chemical industry (3). In contrast, alternative processes (*e.g.* symbiotic nitrogen fixation, SNF) achieve the same result of fixing nitrogen without the need for high pressure and temperature required by the Haber-Bosch process.

More precisely, plants have solved the problem of biological nitrogen fixation through commensal processes, involving bacterial infection of plant roots (4). Mutualistic infections are omnipresent in nature, with a wide range of nitrogen-fixing bacteria – such as those that are collectively named rhizobium – invading not just plants but also the phycosphere of green algae (5). The mutualistic symbiosis involves almost all parts of the plant cell machinery, including plastids and mitochondria. Of particular interest are the interactions between rhizobial bacteria and leguminous plants, which form dedicated organs - root nodules - to accommodate the bacteria. *Medicago truncatula* infected with *Sinorhizobium meliloti* (*S. meliloti*) has long since been used as a model plant system to study plant-rhizobia interactions (6). The root nodules facilitate intracellular hosting and nutrient exchange (7). The result is the efficient formation of fixed nitrogen ( $\text{NH}_4^+$ ), which provides considerable growth advantages to leguminous plants (8). Recently, a detailed fate map of root nodule formation at a genetic level has been developed (9). It has also been proposed that rhizobial metabolic activity may confer resistance to drought and salt stress (10–12). More detailed understanding of key metabolites in plant-nodule metabolism and importantly, their localisation within root nodule tissues could, therefore, shed light on the mechanism by which Symbiotic Nitrogen Fixation (SNF) confers advantages to host plants.

Tracking metabolite exchange non-invasively within intact nodule systems is difficult with most imaging modalities since they require a form of sample fixation, for example in the case of Matrix-Assisted Laser Desorption/Ionisation Mass Spectrometry (MALDI-MS) imaging (13). The current knowledge of the metabolic profile in the root nodules is based on analysis with destructive extraction procedures. For example, Gas Chromatography and Liquid Chromatography in combination with Mass Spectrometry (GC/LC-MS) has provided rich metabolic information but required destructive extraction procedures (14). These *in vitro* methods may not faithfully reflect the native structural and molecular information. Examining and mapping the levels of metabolites directly in the intact root nodule would be important to understand the functional framework of metabolism in the native state. Magnetic resonance techniques may offer advantages in terms of spatially resolved spectroscopic information on a single nodule, which is difficult to access with alternative techniques. Magnetic resonance imaging (MRI) has been previously used to visualise belowground root structures (15–17).

Advances in magnetic resonance technology have resulted in a steady increase in sensitivity, making Magnetic Resonance Microscopy (MRM) a research area where resolution below 100  $\mu\text{m}$  can be achieved (18). A combination of advances in gradients strengths, magnetic field strengths and radiofrequency (RF) coil design, have made it possible to attain ever higher resolutions (19). Specifically, microcoils have played an essential role in increasing sensitivity by optimally matching the RF coil to a sample of interest (20–22). The highest possible resolution on phantoms has steadily increased over the years, and thus far maximum nominal resolutions of around 3  $\mu\text{m}$  has been attained on phantoms (23–26). Biological applications have been diverse, including imaging of neuronal tissue, where cellular resolution were obtained on individual neurons (27–31). Moreover, highly resolved Nuclear Magnetic Resonance spectroscopy has also been demonstrated using the same type of hardware (32).

In this work, we applied state-of-the-art magnetic resonance microscopy (MRM) in conjunction with localised spectroscopy at ultra-high magnetic field (22.3 T), using a home-built solenoid RF coil in order to image root nodules of *Medicago truncatula*. We obtained not only cellular level structural information but also mapped some of the metabolic information in localised zones and how they vary across different tissues. Lastly, we describe some of the technical challenges that were encountered and an outlook towards future *in vivo* imaging of nodules and plant root systems.

## 5.2 Experimental Methods

### Growing Conditions *Medicago truncatula*

*Medicago truncatula* accession R108 was grown in perlite saturated with Färhaeus medium without nitrate in a growth chamber at a temperature of 21 °C and 16/8-h light/dark cycle (33). Plants were inoculated with *Sinorhizobium meliloti* Rm41 (OD<sub>600</sub>=0.1, 2 mL per plant) (34). Root nodules were collected for analysis 21 days after inoculation. Perlite was used as a soil replacement to facilitate the extraction of intact root systems.

### Sample Preparation

For MRI measurements, a single *M. truncatula* plant was carefully extracted from the perlite substrate. Healthy nodules that exhibited a light-pinkish colour were selected and used for MRI imaging. For *in situ* MRI and MRS measurements, a nodule was excised and was directly used for measurements without fixation. For *ex vivo* MRI and optical microscopy, root nodules were fixed with paraformaldehyde (4% w/v) and glutaraldehyde (5% v/v) in 50 mM phosphate buffer (pH 7.2) at 4 °C overnight, followed by vacuum treatment for 30 minutes. Samples were then stored at a temperature of 4 °C until use.

Using an SZ40 stereomicroscope (Olympus, Tokyo, Japan), individual nodules were selected that could fit within capillaries with an inner diameter of  $(1050 \pm 50) \mu\text{m}$  (Hilgenberg GmbH, Malsfeld, Germany). To avoid artifacts during MRI acquisition from air bubbles both within and outside the sample, a Perfluorochemical solution (Perfluorodecalin, PFD) was used to submerge the sample. The use of a Perfluorochemical solution not only prevents sample dehydration but also minimises susceptibility artefacts. PFD was chosen because it has several advantageous properties, making it suitable as an infiltration agent. Importantly, it is a non-toxic compound, capable of dissolving both CO<sub>2</sub> and O<sub>2</sub>(35). Furthermore, PFD exhibits a low surface tension ( $1.9 \times 10^{-2} \text{ N m}^{-1}$ ), below the limit for stomatal penetration ( $2.5\text{--}3.5 \times 10^{-2} \text{ N m}^{-1}$ ) in *Arabidopsis thaliana* leaves(35, 36), making it useful for reducing air bubbles within the sample without entering the cells. Care was taken to minimise the required amount of PFD as it is known to function as a potent greenhouse gas(37).

During insertion of the nodule in the centre position of the capillary, both nodule and capillary were kept submerged in PFD. Capillary wax (Hampton Research, California, USA) was then applied to both ends of the open capillary with a MaxWax Pen

(Hampton Research, California, USA). Considerable effort was spent on minimising the inclusion of air bubbles within the capillary.

For solution NMR measurements, metabolites were extracted from root and root nodules as described in detail by Kim *et al.* (2010) (38). Key steps included manual excision of root and root nodule tissue and consequent crushing with mortar and pestle in the presence of liquid nitrogen. Samples were then freeze-dried and lastly extracted with an extraction buffer consisting of 50% (v/v) deuterated methanol and 50% D<sub>2</sub>O phosphate buffer (pH 6) (38).

### **MRI Measurements**

A custom solenoid microcoil was built in order to achieve the necessary sensitivity required for high-resolution imaging. For the microcoil assembly, a glass-fibre circuit board was used as a base to hold all the necessary components in place. The radiofrequency (RF) coil consisted of coated 28 AWG ( $\varnothing$  0.4 mm) copper wire, wound into a solenoid with six windings around a glass capillary with an outer diameter of  $(1500 \pm 50)$   $\mu\text{m}$ . A fixed 1.5 picoFarad (pF) capacitor was placed in series with the RF coil. To complete the resonance circuit, a single 1.5-6 pF variable capacitor was placed parallel to the RF coil and 1.5 pF capacitor, which allowed for fine-tuning the resonant frequency to 950 MHz. The circuit board was then attached to a Micro5 probe (Bruker Biospin, Ettlingen, Germany) compatible circuit holder.

MRI measurements were performed on a Bruker 22.3 T (950 MHz) spectrometer (Bruker Biospin, Ettlingen, Germany), at the uNMR-nl national facility (Utrecht, The Netherlands). The magnet had a vertical bore of 54 mm in diameter and was connected to an Avance III HD console. A Bruker Micro5 probe with exchangeable RF inserts allowed operation of the 1500  $\mu\text{m}$  custom-built solenoid resonator. The Micro5 probe contained a built-in 48 mT/m/A (2.88 T/m at 60 A) triple axial gradient system coupled to GREAT 60 A amplifiers and cooled with a BCU 20 water cooler. Control of spectrometer operations was performed with Paravision 6.0.1 and Topspin 3.1PV running on a CentOS workstation. Sample temperature was maintained at  $(298 \pm 1)$  K using a BCU II cooler.

High-resolution 3D Fast Low Angle Shot (FLASH) images on *ex vivo* and *in situ* root nodules were acquired with the following parameters: matrix size (MX)  $256 \times 192 \times 192$ ; read direction along the largest matrix direction; the field-of-view (FOV) was  $(1.8 \times 1.4 \times 1.4) \text{ mm}^3$ . Resolution  $(7 \times 7 \times 7) \mu\text{m}^3$  isotropic, number of averages (NA) 28, acquisition time ( $t_{\text{acq}}$ ) 34 h 24 m, repetition time (TR) 120 ms, flip angle (FA)  $30^\circ$  and echo time (TE) 2.9 ms. Receiver bandwidth (rBW) was set to 100 kHz. To allow for co-registration with coupes from optical microscopy, the JIVE tool was utilised to generate oblique slices.

### Localised Spectroscopy

Point Resolved Spectroscopy (PRESS) was used for localised magnetic resonance spectroscopy (MRS) on root nodules (39, 40). PRESS employs  $90^\circ$ - $180^\circ$ - $180^\circ$  orthogonal pulses with concurrent slice selective gradients. The PRESS sequence was preceded by a VAPOR (Variable Pulse Power and Optimized Relaxation Delays) sequence for global water suppression, which consists of seven variable power RF pulses with an optimised relaxation delay (41). Prior to MRS, a reference FLASH image was acquired with the following parameters: TE = 3.3 ms, TR = 80 ms, MX =  $192 \times 128$ , FOV =  $1.8 \times 1.2 \text{ mm}$  and rBW = 50 kHz. In-plane resolution =  $9 \times 9 \mu\text{m}$ , slice thickness (ST) =  $52 \mu\text{m}$ , NA = 256 and  $t_{\text{acq}}$  = 43 min. Appropriate volumes of interest (voxel) for PRESS were selected from the reference FLASH image. Correct positioning of the voxel was also verified after all spectroscopic measurements, by high-resolution 2D FLASH using the following parameters: TE = 4.6 ms, TR = 280 ms, MX =  $288 \times 192$ , FOV =  $1.8 \times 1.2 \text{ mm}$  and rBW = 50 kHz. In-plane resolution was  $6.2 \times 6.2 \mu\text{m}$  and ST was  $52 \mu\text{m}$ . A total of NA = 768 were acquired for an  $t_{\text{acq}}$  of 11 h 28 min.

Five individual MRS voxel ( $200 \times 350 \times 350 \mu\text{m}^3$ ) were localised covering various zones in the nodule. The local field homogeneity was optimised over the voxel by MAPSHIM. The field homogeneity was further improved by manual shimming of up to second order shims (Z-Z<sup>2</sup>-Z-X-Y-Z-Z<sup>2</sup>-Z-XY-XZ-YZ-Z). The time needed for shimming varied between 5-10 min. The field homogeneity resulted in a water line width of 10 Hz. For PRESS measurement, TR was set to 1000 ms, TE was 7.2 ms, and NA 2048 were acquired for a total  $t_{\text{acq}}$  of 34 min 8s. Spectra were manually phased and automatically baseline corrected with a 3<sup>rd</sup> or 6<sup>th</sup> order Bernstein-polynomial fit. Chemical shift alignment was adjusted to the largest peak (3.3 ppm).



### **Chemical Shift Imaging**

Chemical Shift Imaging (CSI) was used to acquire a multi-voxel spatial map of metabolic distribution. A large volume of interest was selected using a PRESS approach, consisting of three mutually orthogonal slice selective pulses. Then phase encoding occurred in two directions by applying incremental pulse gradients in each direction, resulting in a matrix of spectroscopic spin echoes.

The following basic parameters were used: TR = 760 ms; TE = 3 ms; MX = 24 x 16; FOV = 1.8 x 1.2 mm<sup>2</sup>; ST = 400  $\mu$ m; resolution = 150 x 150 x 400  $\mu$ m<sup>3</sup>; NA = 1024. Spectra were acquired with 2048 points; dwell time 26.4  $\mu$ s; spectral width 19.93 ppm (18,939 Hz). Magnetic field homogeneity in the selected volume was optimised by shimming the water resonance. A VAPOR suppression scheme was applied for efficient water signal saturation before CSI acquisition.

Reference FLASH images were acquired with the following parameters: matrix size was 96 x 64; Read direction along the largest matrix direction; FOV was 1.8x1.2 mm<sup>2</sup>. ST was 0.1 mm; resolution (19 x 19 x 100)  $\mu$ m<sup>3</sup> isotropic. Number of slices 4; NA 128; t<sub>acq</sub> 28m 40s. TR was 210 ms; FA 30° and TE 3.26ms. The rBW was set to 50 kHz.

For the processing of the CSI data, the integration of selected signal of specific metabolite areas in magnitude mode was overlaid on reference FLASH images using the Bruker CSI Visualisation Tool.

### **NMR Spectroscopy Measurements**

NMR measurements were performed on a Bruker 20.0 T (850 MHz) spectrometer with a vertical bore 54 mm in diameter connected to an Avance III HD console. A triple-tuned broadband cryoprobe was used. Topspin 3.2 was used to control the spectrometer and for processing of the acquired data. The sample temperature was maintained at 298K.

<sup>1</sup>H NMR spectra were collected using a zgpr30 sequence with pre-saturation to suppress water efficiently. Data was acquired into 65k points; dwell time 29.3  $\mu$ s, spectral width 20 ppm or 17,045 Hz; NA, 512; dummy scans 4; pre-scan delay 10  $\mu$ s. 2D homonuclear <sup>1</sup>H-<sup>1</sup>H experiments were performed using chemical shift correlated spectroscopic sequence (COSY). The following parameters were used: 3400 points in the direct dimension, 400 points in the indirect dimension in Digital Quadrature Mode. Both

dimensions zero-filled to 4096 points. NA, 96; dummy scans, 16; Spectral width 12.0 ppm, 10,000 Hz; Temperature 298K.

Assignments were cross-checked against metabolite databases and fitting was performed using Chenomx deconvolution software (Chenomx, Edmonton, Canada) (42, 43). 1D reference spectra were acquired with parameters as follows: data was acquired into 65k points; dwell time 41.6  $\mu$ s, spectral width 20 ppm or 12,019 Hz; NA, 64; dummy scans 4; pre-scan delay 10  $\mu$ s. COSY reference spectra were acquired with the following parameters: 4096 points in the direct dimension, 256 points in the indirect dimension in Digital Quadrature Mode. Indirect dimension zero-filled to 4096 points. NA, 4; dummy scans, 16; Spectral width 12.3 ppm, 7200 Hz; Temperature 298 K.

All experimental data were acquired and processed using ParaVision 6.0.1 (Bruker Biospin, Ettlingen, Germany) and Topspin 3.1 running on Linux. The default bi-cubic interpolation was applied to enhance the details of the image prior to exporting images. Figures were prepared in Adobe Photoshop CC 2019 and Adobe Illustrator CC 2019 (Adobe Systems Incorporated, Mountain View, California, USA). Stacked spectra were produced in MestReNova (MestreLab Research S.L., Santiago de Compostela, Spain).

### Light Microscopy

After MR imaging, the sample material was dehydrated in an ethanol series and subsequently embedded in Technovit 7100 resin (Heraeus Kulzer, Hanau, Germany) according to the manufacturer's protocol. Sections (5  $\mu$ m) were made by using a microtome (Reichert-Jung, Leica Microsystems, Netherlands), stained with 0.05% Toluidine blue O for 1 min and additionally with Lugol's iodine solution for a few seconds (if applicable). Sections were analysed by using a DM5500B microscope equipped with a DFC425C camera (Leica Microsystems, Wetzlar, Germany).

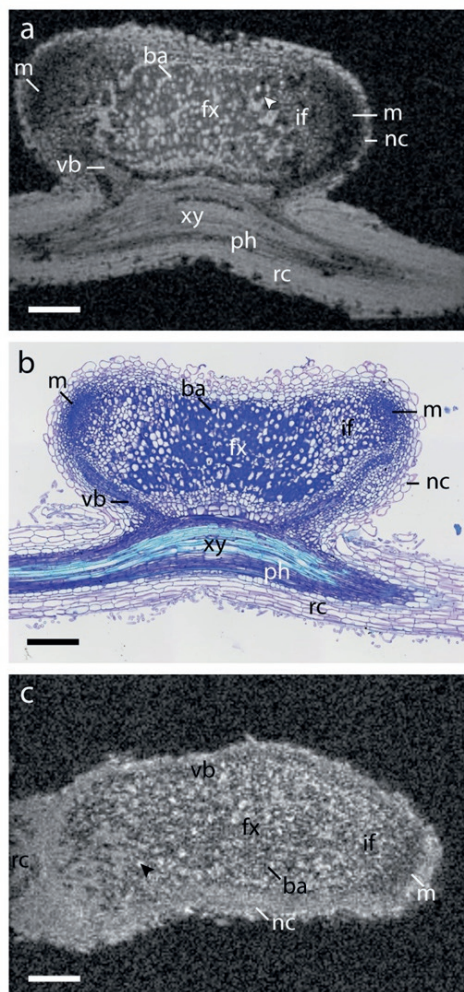
### 5.3 Results

#### Root Nodule Morphology Resolved by MR microscopy in Cellular Detail

A representative *M. truncatula* specimen with a single root nodule shown in Figure 5-1a was imaged using a custom home-built 1.5 mm diameter solenoid coil as depicted in Figure 5-1b.



**Figure 5-1:** Photograph of *M. truncatula* root system and custom-designed home-built microcoil. a.) Photograph of a representative *M. truncatula* plant (five weeks old, three weeks post-inoculation). Typical root nodule indicated with a red square. Some white perlite beads are still visible along the root system. b.) Photograph of a home-built solenoid coil insert mounted on a Bruker insert holder. The solenoid inner diameter is 1.5 mm; further details are described in the materials and methods.



**Figure 5-2:** High-resolution MR imaging and optical microscopy of root nodules. a.) FLASH image of fixed root nodule at  $7 \times 7 \times 7 \mu\text{m}^3$  resolution with a  $t_{\text{acq}}$  of 34 h 24 m. Individual cells containing bacteroids (ba) can be discerned by the dark rings inside the cells, where *S. meliloti* cells accumulate. The nodule exhibits a double meristem (m) on opposed directions with cells becoming smaller towards the meristem until individual cells can no longer be resolved. Air pockets appear as hypo-intense regions marked with an arrowhead. b.) Optical transmission microscopy of nodule section (thickness  $5 \mu\text{m}$ ) stained with Toluidine blue. c.) FLASH image of *in situ* root nodule at  $7 \times 7 \times 7 \mu\text{m}^3$  resolution with a  $t_{\text{acq}}$  of 34 h 24 m. Though lower in signal-to-noise, both uninfected cells (black arrow) and infected cells (ba) can be discerned. Abbreviations: rc, root cortex; xy, xylem; ph, phloem; nc, nodule cortex; vb, vascular bundle; fx, fixation zone; if, infection zone; ba, bacteroid containing cells; m, meristem. Scale bars  $200 \mu\text{m}$ .

Individual cells of a root nodule with two lobes and meristems (m) could be distinguished on the MRI scans. A high-resolution 3D Fast Low Angle SHot (FLASH) image of the root nodule, fixed with formaldehyde and submerged in perfluorodecalin (PFD), is shown in Figure 5-2a. All image slices through the entire root nodule are shown in the supplementary material (Supplementary Video 1- Available on-line). Root nodule morphology in *M. truncatula* nodules are of the indeterminate type, *i.e.*, four distinct regions (zones) occur, from the apex of the root nodule to the root attachment point (4). Nodule tissue - from outward to inward - starting with the nodule cortex (nc), delineated as a high-intensity ring on the surface of the nodule, contrasted with the darker region of the meristem (m). Cells in the meristem, responsible for the growth of the nodule, were significantly smaller than mature bacteroid containing cells. In the next region, the rhizobial infection zone (if), young cells infected by rhizobia bacteria could be seen as a region of alternating high- and low-intensity patches. Not all cells in the rhizobial infection zone were infected, which was apparent due to the presence of variation in image intensities, *i.e.*, non-infected plant cells had a higher image intensity as compared to cells infected with the bacterium. Lastly, in the active nitrogen fixation zone (fx), large cells (40 to 50  $\mu\text{m}$ ) could be distinguished by their grey rings, caused by the presence of bacteroids surrounding the vacuole (44). The fixation zone is where rhizobia make nitrogenase, the enzyme required for nitrogen fixation. In the same area, uninfected interstitial cells were visible, which did not exhibit the rings. These interstitial cells perform an important role in the regulation of nitrogen fixation activity (45). Lastly, connective tissues (vascular bundles) could be seen extending from the root towards the periphery of the nodules, providing a route for nutrient exchange with the rest of the plant.

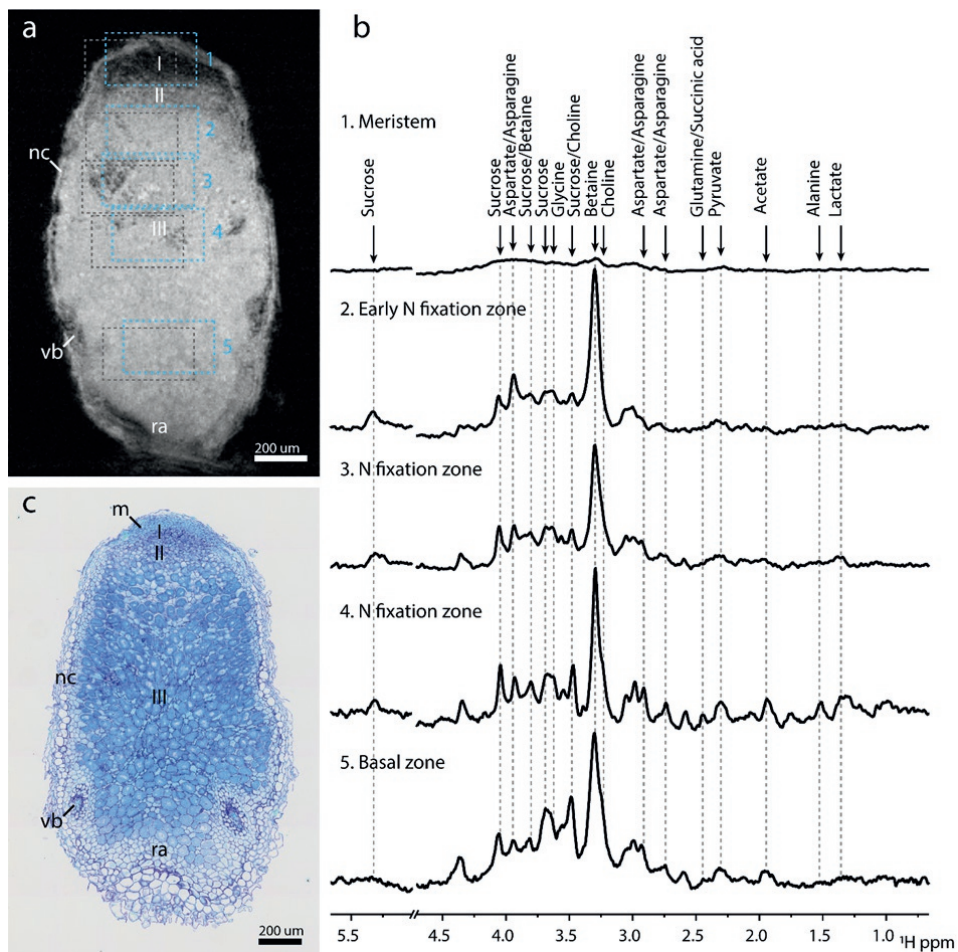
Figure 5-2b shows a light microscopy image of a histological slice stained with Toluidine blue, from the same root nodule at approximately the same plane as the MR image (co-registration). Toluidine blue stained the nuclei and lignin of the cell wall (46). Common features in Figure 5-2a and b are seen, including the bacteroid ring as observed on the MR image, occurring in the staining of cells in the nitrogen fixation zone. Especially visible were the vascular bundles extending from the central root, which due to their smaller cells appeared more densely stained in the optical microscopy image. In addition, air pockets could also be imaged as they appeared as hypo-intense regions in the FLASH image (Figure 5-2a, arrowhead). Air pockets also introduced differences in

magnetic susceptibility within the sample, which influenced image quality. Air pockets of different sizes could be seen within the fixation zone using multiple gradient echo (MGE) imaging with echoes acquired at increasing echo times (S 5-1). Because of the abundance of air pockets in the apical zone, the susceptibility-induced hypointense regions also increased in size in the apical direction.

To evaluate the possibilities of high-resolution MR imaging of root nodule without any fixation or treatment, measurements were performed on freshly excised nodules (Figure 5-2c). While the image contrast and signal-to-noise ratio (SNR) was noticeably reduced, individual cells in the nitrogen fixation zone could still be distinguished. The uninfected cells appeared bright while infected cells appeared dark in the active infection zone. Cells in the meristem appear slightly brighter in freshly excised nodule (*in situ*) than in the fixed nodule, possibly due to the native contrast in freshly excised nodule, while in fixed nodule the contrast was possibly affected by formaldehyde fixation (47, 48).

### **Localised Spectroscopy Revealed the Spatial Distribution of Nodule Metabolites**

Since the root nodule is an active plant organ whose primary function is to fix nitrogen and to facilitate nutrient exchange, SNF-linked metabolite distribution over the various nodule zones is of interest. According to earlier literature, a nodule may be divided into four zones, based on SNF activity: (I) meristem zone, (II) infection zone, (III) nitrogen fixation zone, and (IV) senescence zone, the latter observed mostly in older nodules. In the infection zone, bacteroids accumulate and mature, while in the fixation zone active SNF takes place (49). Localised Magnetic Resonance Spectroscopy (MRS) was utilised to distinguish metabolites in a freshly excised and PFD submerged root nodule, based on their frequency differences (chemical shift) and location. Localised MR spectra were recorded from five different regions of interest (ROI), localised in the four different zones in an intact freshly excised root nodule, *in situ* (Figure 5-3a). The presence of bacteroids was verified with optical microscopy after the MRI measurements (Figure 5-3c). The first ROI was placed on the meristem (ROI 1) in Figure 5-3b, where little MR signal was recorded, possibly due to the small volumes of individual cells which may cause  $T_2$ -shortening, reducing the SNR. The second voxel (ROI 2) was placed in the infection/early fixation zone. The third (ROI 3) and fourth voxels (ROI 4) were placed in the largest zone: the active nitrogen fixation zone. The last voxel (ROI 5) was placed in the basal region of the root nodule.



**Figure 5-3:** Localised spectroscopy in *in-situ* root nodule reveals sugar differences in pre- and post-granule onset regions. (a) FLASH reference with PRESS Region of Interest (ROI), numbered one through five. Roman numerals indicate nodule zones: Meristem (I), Infection zone (II), Nitrogen fixation zone (III). Grey dotted boxes show ROI shift of Betaine due to Chemical Shift Displacement Error (CDSE). Pulse excitation was centred around 4.0 ppm. (b) Co-registration of Optical Microscopy confirms the presence of bacteroids in the active nitrogen fixation region. Toluidine blue staining 10x magnification. (c) PRESS spectra captured from Regions of Interest (ROI) shown in Figure 5-3a, for Nodule Meristem (1.), (early) Nitrogen fixation zone (2.), Nitrogen fixation zone (3. & 4.), Basal region (5.). PRESS voxel sizes were  $200 \times 350 \times 350 \mu\text{m}^3$ . Spectra were aligned to the betaine peak at 3.3 ppm. Water peak region at 4.7 ppm has been omitted for ease of viewing. Intensities of the spectra have not been normalised, reflecting the strength of the signal recorded. This means that for the meristem little information can be discerned. Line broadening 10 Hz. Abbreviations: nc, nodule cortex; vb, vascular bundle; m, meristem; ra, root attachment area. Scale bars 200  $\mu\text{m}$ .

The spectra obtained from ROIs 2-5 showed the presence of several metabolites including various amino acids, sugars, choline and betaine. Betaine was present in a high amount in all four ROIs (Figure 5-3b). The signal from sucrose and asparagine/aspartate was also clearly detected. Assignment of various metabolites was confirmed with solution-state NMR performed on an extract obtained from the root nodules, using two-dimensional  $^1\text{H}$ - $^1\text{H}$  correlation spectroscopy (2D-COSY) (see S 5-2). It should be noted that, due to the chemical shift displacement error, which increases with magnetic field strength, the regions of interest chosen for the localised spectra were shifted slightly for each metabolite, as the spatial selection relied on the frequency of the metabolite relative to the chosen centre frequency of 4.0 ppm (50). This shift meant that the indicated regions of interest in Figure 5-3a were correct for signals at  $\delta = 4$  ppm, while for example the strongest signal (at  $\delta = 3.3$  ppm) originated from an ROI which was shifted by 35  $\mu\text{m}$  along x, 97  $\mu\text{m}$  along y and 97  $\mu\text{m}$  along z (see the dotted region of interest in Figure 5-3a).

The most intense peak observed in all spectra was attributed to a resonance of glycine betaine ( $\delta = 3.3$  ppm) (Figure 5-3b). A complementary spectroscopic imaging method, Chemical shift imaging (CSI) confirmed the presence of betaine throughout the nodule (S 5-3). Betaine serves as an important osmoprotectant produced by *S. meliloti* (51). Furthermore choline – a precursor to glycine betaine in both plants and bacteria, was visible in ROI 3 as a shoulder on the low-frequency side of the betaine peak, and was even more pronounced in ROIs 4 and 5 (52). In uninfected root tissue, choline, but not glycine betaine was detected as seen in solution NMR measurements (S 5-4).

In root nodule, another strong peak from asparagine and aspartate was seen primarily in ROIs 2-5 (Figure 5-3b). Notably, glutamine - though present in ROI 4 - appeared much lower in concentration in all ROIs than asparagine, suggesting a smaller pool or higher turnover rate in the nitrogen assimilation process.

Intermediates from the tricarboxylic acid cycle such as acetate ( $\delta = 1.9$  ppm), pyruvate ( $\delta = 2.3$  ppm) and succinic acid ( $\delta = 2.4$  ppm) were also seen in the nitrogen fixation zone (region 3 & 4). Lactate ( $\delta = 1.3$  ppm) was visible only in the active nitrogen fixation zone (region 3 & 4). Alanine ( $\delta = 1.5$  ppm) has been suggested by metabolic network modelling to be the primary metabolite for the uptake of assimilated nitrogen by plants



(53). However, our results indicated that the pool of alanine was small compared to asparagine.

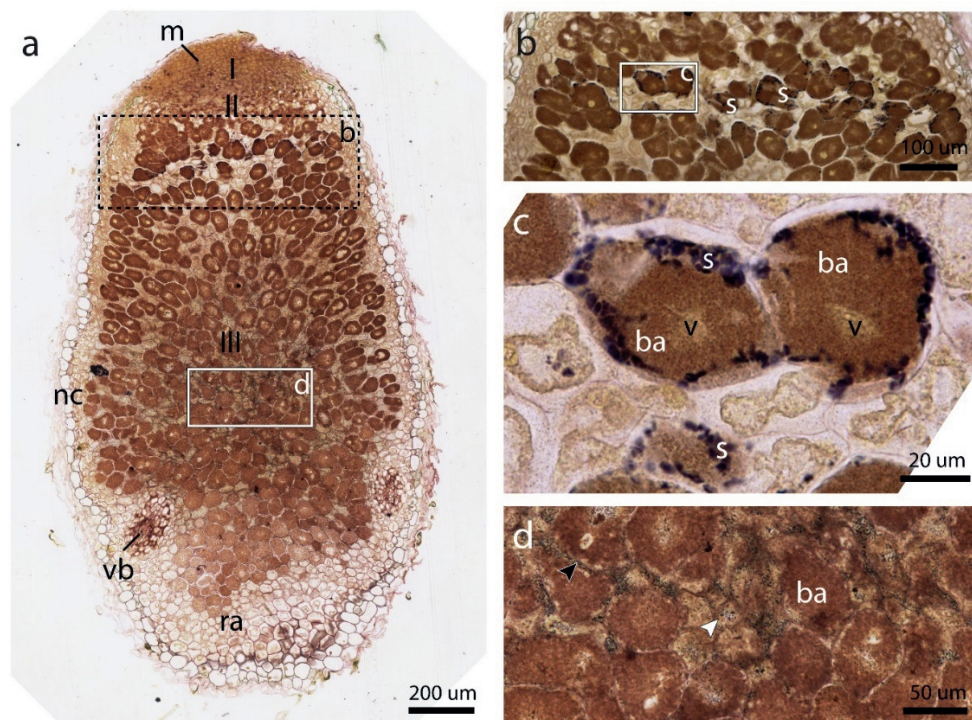
Sucrose, the most important resource for growth and root nodule activity, was present in all regions with a concentration gradient towards the basal area, starting with the early fixation zone (Figure 5-3b, ROI 2). Several peaks were assigned to sucrose (e.g.,  $\delta = 5.3$  ppm), with some overlap with choline ( $\delta = 3.5$  ppm) and fructose ( $\delta = 3.8$  ppm). In the basal region (region 5), the sucrose peak at  $\delta = 5.3$  ppm was hard to distinguish, possibly due to baseline distortions. Overall, the metabolic pattern exhibited in regions 3-4 appeared to be maintained in the basal region (region 5), though attenuated and with a broader linewidth, possibly reflecting a more disorganised structure of the tissue. At the same time active SNF still appeared to take place, indicating this region is not (yet) the senescent zone IV in which the activity would be reduced.

### **Optical Microscopic Detection of Starch Correlates with MR Based Sucrose Profile**

Starch is a carbohydrate storage polymer that is unique to plants. Indeterminate root nodules are known to form amyloplasts in certain cells, detectable by optical microscopy, especially in the youngest cells of the nitrogen-fixation zone of an actively growing nodule (54). Accumulation of amyloplasts has also been found in cells located behind the division zone in shoot meristems (55). Zeeman *et al.* speculated that this might be caused by 'a temporary imbalance between carbon import and utilisation as cells move from division to expansion and differentiation' (56). If correct, this marker for high metabolic activity should be reflected in changes to the metabolic profile of bacteroid containing cells. Therefore, we aimed to detect pre- and post-starch granule formation zones in an intact root nodule, and correlate them with sugar metabolites as measured by localised spectroscopy.

Lugol's solution was used to stain amyloplasts (Figure 5-4a) on an optical section immediately adjacent to that of Figure 5-3b, to relate the distribution of sucrose and other metabolites to starch. Starch distribution was seen as dark spots, concentrated in a band located in the first layer of the nitrogen fixation zone as well as in smaller amyloplasts throughout the fixation zone (Figure 5-4b and d). In the nitrogen fixation zone, amyloplasts were small and dispersed over infected cells (black arrowhead) as well as uninfected interstitial cells (white arrowhead)(Figure 5-4d). In contrast, the cells present in the first layer on the border of the infection zone (II) and fixation zone (III)

exhibited a different distribution of starch (Figure 5-4b). At higher magnification, large amyloplasts were visible at the periphery of the infected cells, which were almost completely filled with bacteroids (Figure 5-4c). Thus, sucrose and starch appear to co-localise with SNF activity. Taken together, starch distribution patterns could provide a possible biomarker for changes in cellular metabolism during nodule development.



**Figure 5-4:** Optical microscopy of root nodules reveals multiple starch distribution patterns. Coupes were stained with both Lugol's solution and Toluidine blue. **a.)** A section immediately adjacent to that of Figure 5-3a reveals starch distribution throughout the nodule. 10x magnification, scale bar 200  $\mu\text{m}$ . A black dotted rectangle indicates the zone shown in (b) on an alternate section. A white rectangle indicates an enlargement seen in (d). 10x magnification, zoomed; scale bar 50  $\mu\text{m}$ . **b.)** At the first layer of cells in zone III, starch is present as a band (s). A white rectangle indicates the area shown in (c). Alternate section, 20x Magnification, scale bar 100  $\mu\text{m}$ . **c.)** Starch granules (s) are located near the periphery of infected cells. The vacuole (v) reappears in the fixation zone after disorganisation in the infection zone. (b). 40x Magnification, scale bar 20  $\mu\text{m}$ . **d.)** A fine distribution of starch granules can be seen in Zone III contained in nitrogen fixing cells (black arrowhead) and uninfected cells (white arrowhead). Abbreviations: ra, root attachment site; nc, nodule cortex; vb, vascular bundles; m, meristem; s, starch granules; v, vacuole; ba, bacteroids.

## 5.4 Discussion

This paper showed the feasibility of attaining cellular resolution ( $7 \times 7 \times 7$ )  $\mu\text{m}^3$  in *M. truncatula* root nodules over a relatively large volume ( $1.8 \times 1.4 \times 1.4$  mm<sup>3</sup>), opening up new applications for MR microscopy in plant studies (Figure 5-2). Individual cells, especially young and mature bacteroids containing cells, were resolved with high contrast in fixed root nodule, exhibiting a unique ‘grey ring’ pattern where *S. meliloti* cells accumulated near the cell walls around a central vacuole. Smaller cells, such as those present in the meristem, could not be resolved individually. A low signal to noise in meristem may be attributed to the shortening of  $T_1$  and  $T_2$  relaxation times as a result of formaldehyde-based fixation. Formaldehyde is known to alter the relaxation properties of tissues by cross-linking proteins, which may lead to a gel-like cytoplasm. This alters the rates of chemical exchange between water protons and proteins, thus leading to a reduced  $T_1$  and  $T_2$  (47, 48, 57). However, vacuoles are less affected by this, potentially contributing to the strong contrast between bacteroids and vacuoles. Looking towards *in situ* imaging in Figure 5-2c, although nodules suffered from lower image contrast and SNR, the meristem appears brighter as compared to fixed nodule (Figure 5-2a). These results also support the notion that lower signal in meristem in fixed nodule could be due to *shortening of relaxation parameters*. A possible reason for the overall lower image quality in freshly excised nodule may be due to the abundance of air cavities since no vacuum treatment was applied for *in situ* imaging. More quantitative measurements are required to determine the causes of reduced SNR and contrast.

Although the hypo-intense regions caused by small and large air pockets can be detrimental to overall image quality (S 5-1), they also contain useful information. Air pockets in root nodules of *M. truncatula* are of particular interest, because of the delicate balance of oxygen levels required for the proper functioning of the nitrogen fixation. The pockets may thus have a regulatory role, as nitrogenase is paradoxically both dependent on oxygen for carrying out its function but can also be poisoned by oxygen under high concentrations (58). Previous MR investigations into root nodules of soybean (*Glycine max*) have focused on investigating the oxygen diffusion barrier, believed to regulate nodule functioning (59, 60). Furthermore, *Glycine max* root nodules are known to be sensitive to changes in gas perfusion (61). Thus, MRM could be a useful tool to study oxygen regulation mechanisms, due to its ability to detect air spaces through enhanced signal loss.

PRESS localised spectroscopy results show that betaine was distributed throughout the nodule (Figure 5-3c). The relatively high concentration of betaine could be due to maintaining a high degree of osmoregulation, an indicator of stress, or both (52). High asparagine levels seen especially in the nitrogen fixation zone indicate significant SNF activity. The presence of asparagine, as well as betaine, was also confirmed by high-resolution 2D correlation spectroscopy on extracts prepared from nodules (S 5-2). Asparagine, together with glutamine, is known to be a major export product of assimilated nitrogen (62). Our results show that asparagine accumulates mostly in active SNF areas (regions 3-5). As such, asparagine was absent in normal root tissue (S 5-4).

Metabolite levels of betaine and asparagine might therefore potentially provide useful markers for stress and SNF activity, respectively. The sucrose concentration gradient, decreasing from the basal to the apical end of the nodule, may reflect either consumption rates or limitations in transport through the nodule. In conjunction, starch granules appeared to be localised to two specific regions, a band in the transition from infection to fixation zone, and the fixation zone (III) itself (Figure 5-4). The band seemed to provide support for Zeeman's prediction of amyloplast formation due to a 'temporary metabolic imbalance', though it is located at some distance from the meristem (Figure 5-4b) (56). As for the fixation zone, it has been observed in the literature that starch amyloplast accumulation in uninfected cells is related to the expression of SNF-related (*nif*) genes (Figure 5-4d) (63, 64). Considering that sucrose was present throughout the nodule, albeit in a diminishing concentration gradient, it is likely that cell-specific metabolism and environmental conditions determine whether and in what quantity starch amyloplasts are formed (49, 65). For instance, sucrose must be metabolised by the host cell in order to provide carboxylic acids that are preferentially taken up by the bacteroids (66, 67). The observed distribution in size and location of amyloplasts could be affected in this way as well.

As an explorative study of ultra-high field MRM for plant imaging, several recommendations might be of interest to the reader. Sample handling and preparation are essential for high-resolution imaging. More generally, special attention needs to be given to managing sample susceptibility at ultra-high fields, since the inclusion of even small air bubbles in the vicinity of samples can distort image quality significantly, as well as cause line broadening in localised spectroscopic experiments. Perfluorodecalin (PFD) was useful as a submerging fluid as its magnetic susceptibility is close to that of tissues

and it gives no observable  $^1\text{H}$  signal. It is also efficient in displacing and dissolving air pockets, which are present in root nodule tissue. The absence of extraneous signal allowed for a manual shimming strategy that was sufficient for imaging and provided a good starting point for shimming voxels of interest for localized spectroscopy. Still, maximum shim currents on a particular system may prove to be a limiting factor for microimaging applications. Another source of sample susceptibility could be the presence of iron in the form of leghemoglobin which regulates oxygen levels. In bacteroids of mature nodules, up to 25% of the total soluble protein consists of leghemoglobin (7). The high concentrations of this iron-heme containing protein might have implications for the values of longitudinal relaxation ( $T_1$ ) and transverse relaxation ( $T_2$ ) and their interpretation, as these properties may depend strongly on the physiological state of the root nodule when measured. Thus, with further characterisation, susceptibility-weighted imaging may provide a useful method for evaluating the physiological state of root nodules.

Although MRS was done on freshly excised root nodules, the use of PFD as a submerging fluid may have some influence on the vitality of the nodule, since PFD displaces air pockets thus, altering oxygen diffusion to the cells within the nodule.

Rather than a higher resolution per se, the future applications for MRM at ultrahigh field for – *in vivo* – imaging are also enticing, yet challenging. To achieve *in vivo* imaging, novel coil-insert designs with the necessary life support systems would be required. The solenoid coil type used here could be modified to allow for a relatively simple setup that would support whole plants. Vertical-bore MRI systems allow top access to supply light and fresh medium. Additionally, controlled nutrient supply would be desirable, e.g. a continuous medium perfusion setup (68). Overall, an imaging setup optimised for longitudinal studies would allow testing of stress conditions for host-symbionts, non-destructively.

## 5.5 Conclusion

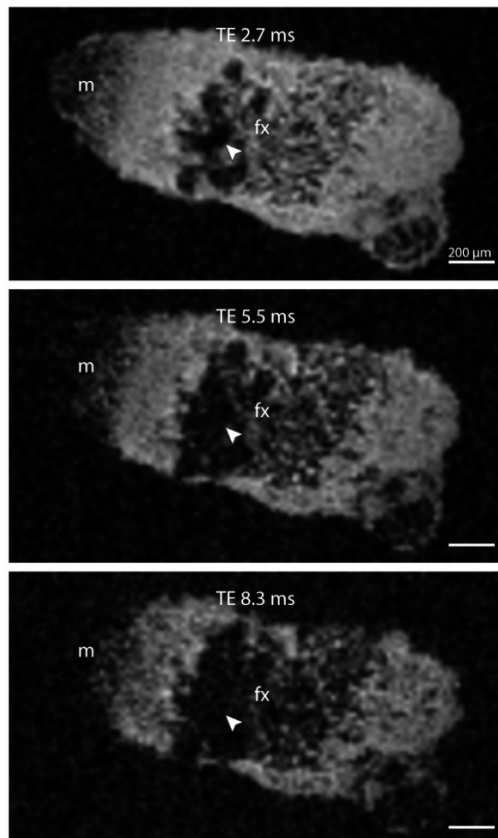
In conclusion, our results demonstrate that MRM at ultra-high fields in conjunction with microcoils provides a promising technique to determine physiology and metabolic profiling non-invasively in plant root nodules. Further research and development on coil design are required to exploit this application to its full potential.

## 5.6 Acknowledgements

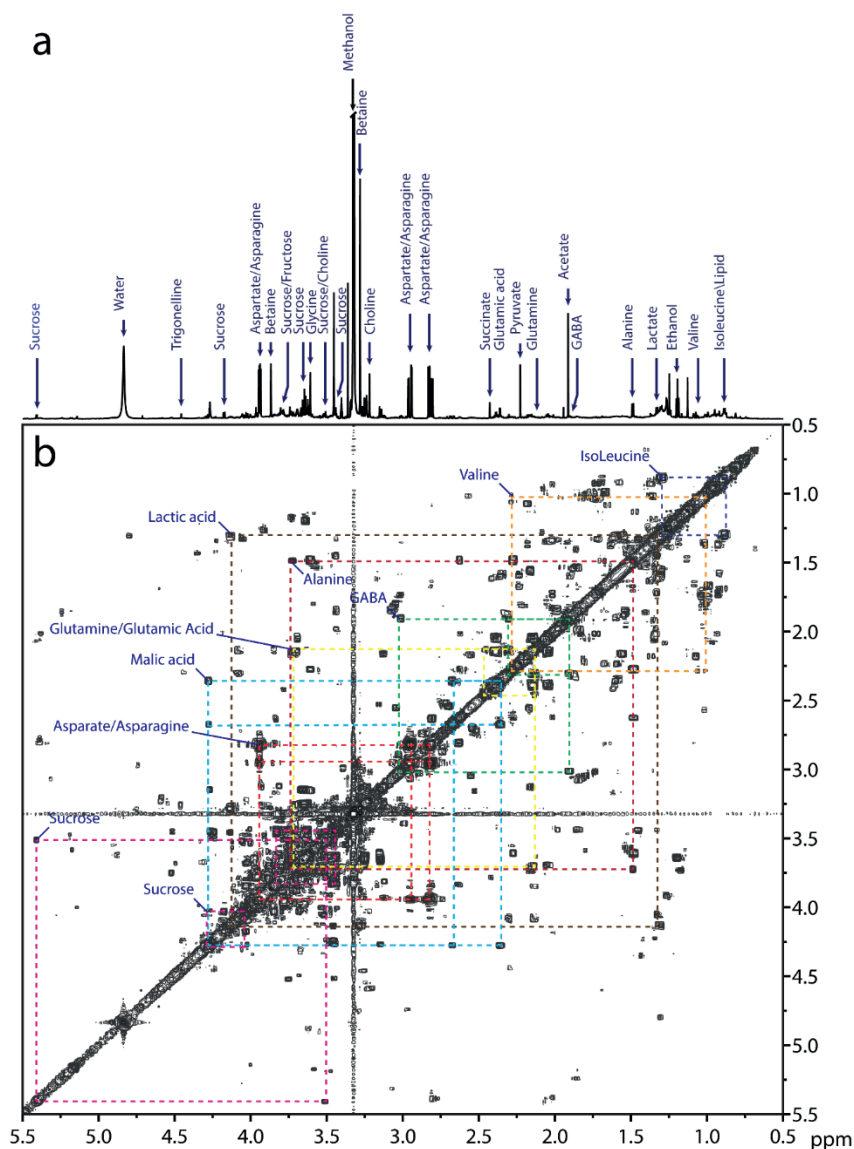
Experiments at the 950 MHz instrument were supported by uNMR-NL, an NWO-funded National Roadmap Large-Scale Facility of the Netherlands (project 184.032.207). R.S. was supported by the BioSolarCells consortium project U2.3. J.R.K. was supported by the NWO-funded graduate school Netherlands' Magnetic Resonance Research School (NMARRS) graduate school [022.005.029]. D.S was supported by China Scholarship Council (201306040120). A.G.W. was partially supported by European Research Grant 670629 NOMA MRI. We thank Klaartje Houben, Marie Renault and Johan van der Zwan for technical support at the uNMR-NL facility. We would further like to thank Volker Lehmann, Henny Janssen and Pieter de Waard for help in troubleshooting.

## 5.7 Supporting Information

**S 5-1:** T<sub>2</sub>-weighted images reveals susceptibility artefacts caused by air pockets. An MGE sequence was used to acquire scans with increasing echo times on a fixed but not vacuum treated nodule, showing a progressive loss of signal as a function of echo time. Nodule Apical-Basal orientation is left-to-right. Dark areas are indicative of air pockets that dephase signal through increased local magnetic susceptibility differences (arrow). Notably, air pockets are variable in size with smaller pockets seen in the basal direction. The meristem and nitrogen fixation area are particularly affected by the signal loss, though the meristem signal loss is likely due to short T<sub>2</sub>, not susceptibility. A total of 32 gradient recalled echoes were acquired; initial echo was TE 2.7 ms, further echoes were spaced 2.8 ms apart resulting in echo times of 2.7, 5.5, 8.3, ..., 89.5 ms. MX was 128×64×64; Read direction along the largest matrix direction; FOV was (1.8×1.4) mm<sup>2</sup>. ST was 1.4 mm; resolution (19×19×19) μm<sup>3</sup>. NA was 24; t<sub>acq</sub> 3 h 16 m. TR was 120 ms; FA 5°. Abbreviations: fx, fixation zone; m, meristem. Scale bar 200 μm.

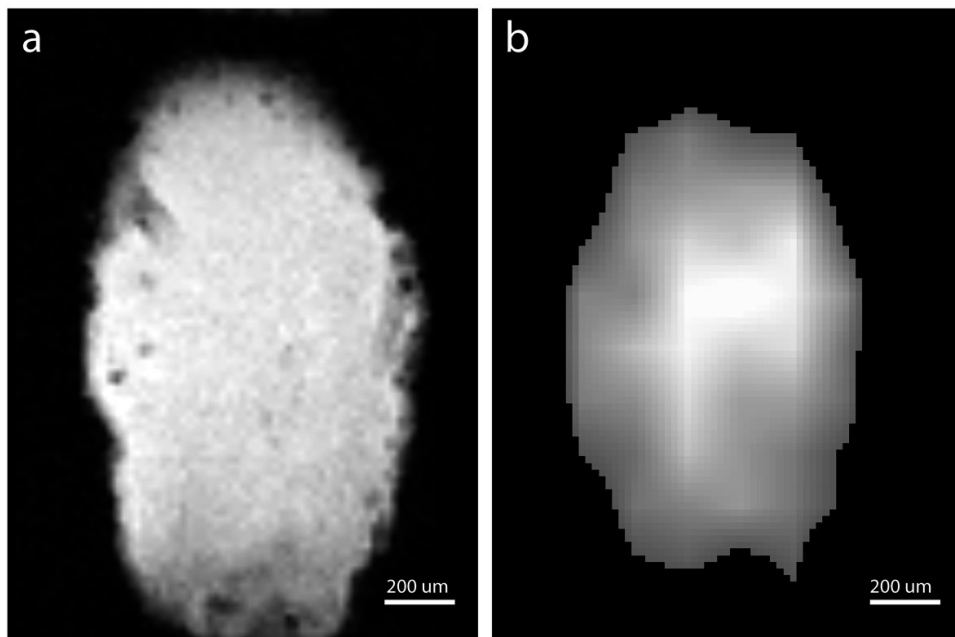


**S 5-2:** Homo-nuclear  $^1\text{H}$  correlation spectroscopy (COSY) of root nodule. **a.)** 1D NMR from 0.5 to 5.5 ppm with the most abundant metabolites assigned. Solvent Methanol/ $\text{D}_2\text{O}$ , water suppressed. GABA =  $\gamma$ -aminobutyric acid. **b.)** COSY was used to verify assignments of in situ PRESS results. COSY assignments for the most relevant metabolites are indicated with coloured boxes. Range 0.5 to 5.5 ppm, water suppressed.

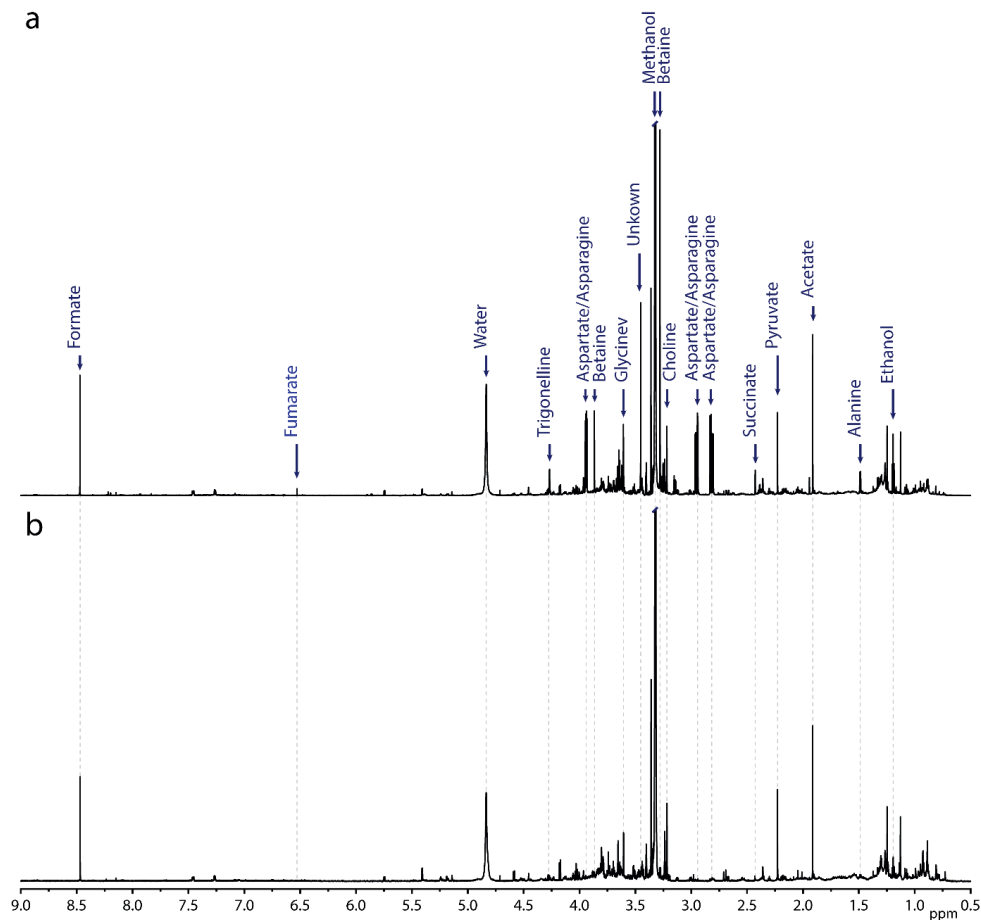




**S 5-3:** Chemical Shift imaging showing betaine localisation. Nodule Apical-Basal orientation is top to bottom. **a.)** MSME reference image. Note that the CSI volume of interest is larger than the nodule itself. Thus, the distribution of metabolites may be skewed. **b.)** Heat map generated from betaine peak (integration bandwidth 300 Hz).



**S 5-4:** A representative solution state  $^1\text{H}$  NMR spectrum of root and nodule tissue, revealing differences in several major metabolites. Spectra acquired at 850 MHz. **a.)** Nodule tissue **b.)** Root tissue.



## 5.8 References

1. J. W. Doran, M. R. Zeiss, Soil health and sustainability: managing the biotic component of soil quality. *Appl. Soil Ecol.* **15**, 3–11 (2000).
2. V. Smil, Nitrogen cycle and world food production. *World Agric.* 9–13 (2001).
3. B. E. Smith, Nitrogenase reveals its inner secrets. *Science* **297**, 1654–1655 (2002).
4. T. Suzaki, E. Yoro, M. Kawaguchi, *Leguminous Plants: Inventors of Root Nodules to Accommodate Symbiotic Bacteria* (Elsevier Ltd, 2015), vol. 316.
5. B. H. Kim, R. Ramanan, D. H. Cho, H. M. Oh, H. S. Kim, Role of Rhizobium, a plant growth promoting bacterium, in enhancing algal biomass through mutualistic interaction. *Biomass and Bioenergy*. **69**, 95–105 (2014).
6. D. G. Barker, S. Bianchi, F. Blondon, Y. Dattée, G. Duc, S. Essad, P. Flament, P. Gallusci, G. Génier, P. Guy, X. Muel, J. Tourneur, J. Dénarié, T. Huguet, Medicago truncatula, a model plant for studying the molecular genetics of the Rhizobium-legume symbiosis. *Plant Mol. Biol. Report.* **8**, 40–49 (1990).
7. J. P. Nap, T. Bisseling, Developmental biology of a plant-prokaryote symbiosis: The legume root nodule. *Science* **250**, 948–954 (1990).
8. M. K. Udvardi, D. A. Day, Metabolite transport across symbiotic membranes of legume nodules. *Annu. Rev. Plant Physiol. Plant Mol. Biol.* **48**, 493–523 (1997).
9. T. T. Xiao, S. Schilderink, S. Moling, E. E. Deinum, E. Kondorosi, H. Franssen, O. Kulikova, A. Niebel, T. Bisseling, Fate map of Medicago truncatula root nodules. *Development*. **141**, 3517–3528 (2014).
10. K. J. Kunert, B. J. Vorster, B. A. Fenta, T. Kibido, G. Dionisio, C. H. Foyer, Drought Stress Responses in Soybean Roots and Nodules. *Front. Plant Sci.* **7**, 1–7 (2016).
11. C. Staudinger, V. Mehmeti-Tershani, E. Gil-Quintana, E. M. Gonzalez, F. Hofhansl, G. Bachmann, S. Wienkoop, Evidence for a rhizobia-induced drought stress response strategy in Medicago truncatula. *J. Proteomics* **136**, 202–213 (2016).
12. M. López, N. A. Tejera, C. Lluch, Validamycin A improves the response of Medicago truncatula plants to salt stress by inducing trehalose accumulation in the root nodules. *J. Plant Physiol.* **166**, 1218–1222 (2009).
13. H. Ye, E. Gemperline, M. Venkateshwaran, R. Chen, P.-M. Delaux, M. Howes-Podoll, J.-M. Ané, L. Li, MALDI mass spectrometry-assisted molecular imaging of metabolites during nitrogen fixation in the Medicago truncatula-Sinorhizobium meliloti symbiosis. *Plant J.* **75**, 130–145 (2013).

14. A. J. Ogden, M. Gargouri, J. J. Park, D. R. Gang, M. L. Kahn, Integrated analysis of zone-specific protein and metabolite profiles within nitrogen-fixing *Medicago truncatula*-*Sinorhizobium medicae* nodules. *PLoS One*. **12**, 1–17 (2017).
15. S. Schmittgen, R. Metzner, D. Van Dusschoten, M. Jansen, F. Fiorani, S. Jahnke, U. Rascher, U. Schurr, Magnetic resonance imaging of sugar beet taproots in soil reveals growth reduction and morphological changes during foliar *Cercospora beticola* infestation. *J. Exp. Bot.* **66**, 5543–5553 (2015).
16. D. van Dusschoten, R. Metzner, J. Kochs, J. A. Postma, D. Pflugfelder, J. Buehler, U. Schurr, S. Jahnke, *Plant Physiol.* **170**, 01388.2015 (2016).
17. R. Metzner, D. van Dusschoten, J. Bühler, U. Schurr, S. Jahnke, Belowground plant development measured with magnetic resonance imaging (MRI): exploiting the potential for non-invasive trait quantification using sugar beet as a proxy. *Front. Plant Sci.* **5**, 469 (2014).
18. P. Glover, S. P. Mansfield, Limits to magnetic resonance microscopy. *Reports Prog. Phys.* **65**, 1489–1511 (2002).
19. V. Vegh, P. Gläser, D. Maillet, G. J. Cowin, D. C. Reutens, High-field magnetic resonance imaging using solenoid radiofrequency coils. *Magn. Reson. Imaging*. **30**, 1177–85 (2012).
20. T. L. Peck, R. L. Magin, P. C. Lauterbur, Design and analysis of microcoils for NMR microscopy. *J. Magn. Reson. Ser. B*. **108** (1995), pp. 114–124.
21. K. R. Minard, R. A. Wind, Solenoidal microcoil design. Part I: Optimizing RF homogeneity and coil dimensions. *Concepts Magn. Reson.* **13**, 128–142 (2001).
22. K. R. Minard, R. A. Wind, Solenoidal microcoil design Part II: Optimizing winding parameters for maximum signal-to-noise performance. *Concepts Magn. Reson.* **13**, 190–210 (2001).
23. H.-Y. Chen, R. Tycko, Low-temperature magnetic resonance imaging with 2.8  $\mu\text{m}$  isotropic resolution. *J. Magn. Reson.* **287**, 47–55 (2018).
24. M. Weiger, D. Schmidig, S. Denoth, C. Massin, F. Vincent, M. Schenkel, M. Fey, NMR microscopy with isotropic resolution of 3.0  $\mu\text{m}$  using dedicated hardware and optimized methods. *Concepts Magn. Reson. Part B Magn. Reson. Eng.* **33B**, 84–93 (2008).
25. E. Mattle, M. Weiger, D. Schmidig, P. Boesiger, M. Fey, MRI of human hair. *Magn. Reson. Mater. Physics, Biol. Med.* **22**, 181–186 (2009).
26. L. Ciobanu, D. Seeber, C. Pennington, 3D MR microscopy with resolution 3.7  $\mu\text{m}$  by 3.3  $\mu\text{m}$  by 3.3  $\mu\text{m}$ . *J. Magn. Reson.* **158**, 178–182 (2002).

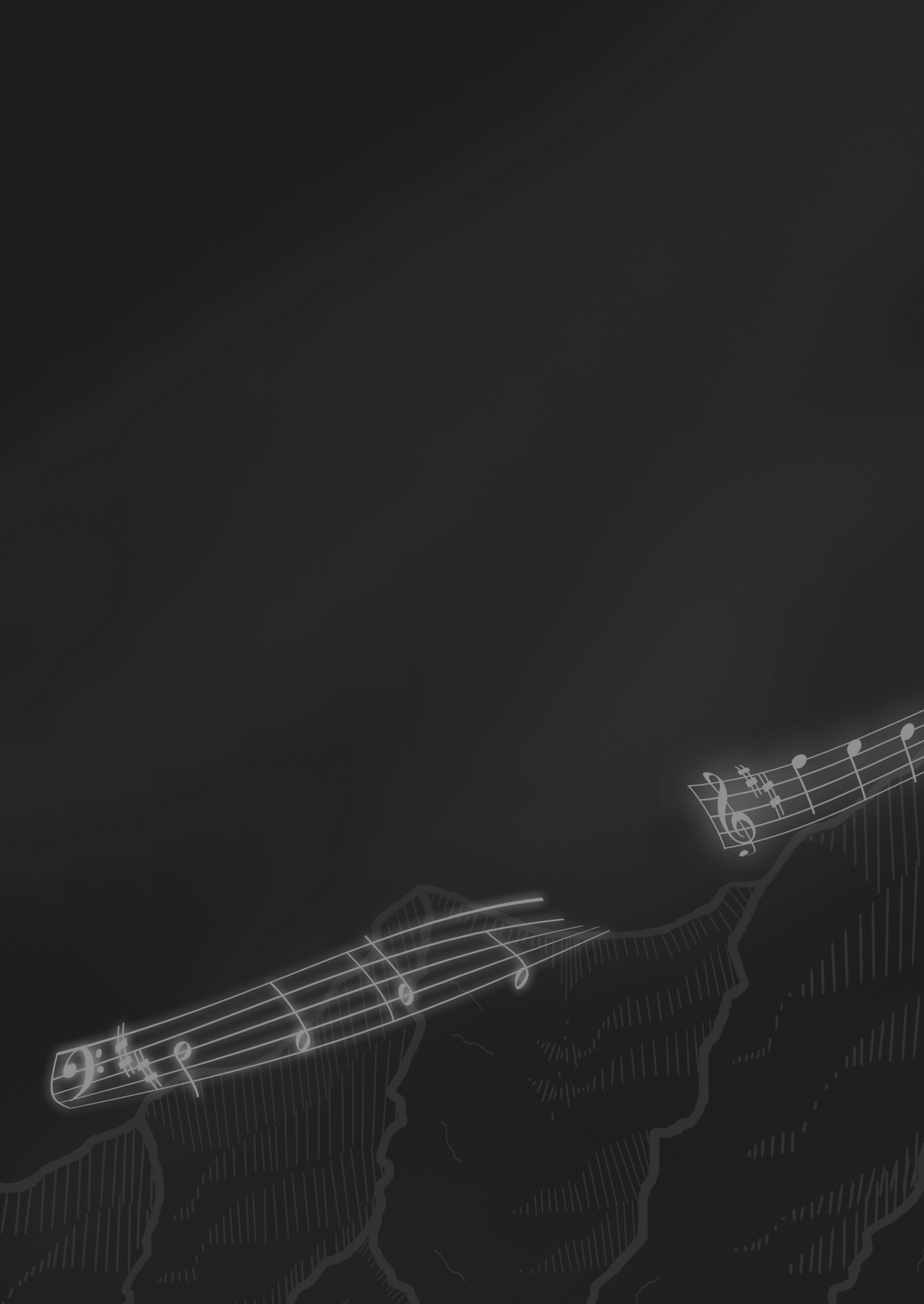
27. C. H. Lee, J. J. Flint, B. Hansen, S. J. Blackband, Investigation of the subcellular architecture of L7 neurons of *Aplysia californica* using magnetic resonance microscopy (MRM) at 7.8 microns. *Sci. Rep.* **5**, 11147 (2015).
28. J. J. Flint, C. H. Lee, B. Hansen, M. Fey, D. Schmidig, J. D. Bui, M. a King, P. Vestergaard-Poulsen, S. J. Blackband, Magnetic resonance microscopy of mammalian neurons. *Neuroimage*. **46**, 1037–40 (2009).
29. C. H. Lee, N. Bengtsson, S. M. Chrzanowski, J. J. Flint, G. A. Walter, S. J. Blackband, Magnetic Resonance Microscopy (MRM) of Single Mammalian Myofibers and Myonuclei. *Nat. Publ. Gr.*, 1–9 (2016).
30. S. C. Grant, D. L. Buckley, S. Gibbs, A. G. Webb, S. J. Blackband, MR microscopy of multicomponent diffusion in single neurons. *Magn. Reson. Med.* **46**, 1107–1112 (2001).
31. L. Ciobanu, C. H. Pennington, 3D micron-scale MRI of single biological cells. *Solid State Nucl. Magn. Reson.* **25**, 138–141 (2004).
32. D. L. Olson, T. L. Peck, A. G. Webb, R. L. Magin, J. V Sweedler, High-Resolution Microcoil 1H-NMR for Mass-Limited, Nanoliter-Volume Samples. *Science* **270**, 1967–1970 (1995).
33. E. Limpens, J. Ramos, C. Franken, V. Raz, B. Compaan, H. Franssen, T. Bisseling, R. Geurts, RNA interference in *Agrobacterium rhizogenes*-transformed roots of *Arabidopsis* and *Medicago truncatula*. *J. Exp. Bot.* **55**, 983–992 (2004).
34. S. Weidner, B. Baumgarth, M. Gottfert, S. Jaenicke, A. Puhler, S. Schneiker-Bekel, J. Serrania, R. Szczepanowski, A. Becker, Genome Sequence of *Sinorhizobium meliloti* Rm41. *Genome Announc.* **1**, 12–13 (2013).
35. G. R. Littlejohn, J. Love, A simple method for imaging *Arabidopsis* leaves using perfluorodecalin as an infiltrative imaging medium. *J. Vis. Exp.* **2**, 3–6 (2012).
36. J. Schönherr, M. J. Bukovac, Penetration of Stomata by Liquids. *Plant Physiol.* **49**, 813–819 (1972).
37. W. T. Tsai, Environmental property modelling of perfluorodecalin and its implications for environmental fate and hazards. *Aerosol Air Qual. Res.* **11**, 903–907 (2011).
38. H. K. Kim, Y. H. Choi, R. Verpoorte, NMR-based metabolomic analysis of plants. *Nat. Protoc.* **5**, 536–549 (2010).
39. P. A. Bottomley, Spatial Localization in NMR Spectroscopy in Vivo. *Ann. N. Y. Acad. Sci.* **508**, 333–348 (1987).
40. P. A. Bottomley, Point resolved spectroscopy (PRESS). *US Pat.* **4**, 228 (1984).

41. I. Tkáč, Z. Starcuk, I. Y. Choi, R. Gruetter, In vivo <sup>1</sup>H NMR spectroscopy of rat brain at 1 ms echo time. *Magn. Reson. Med.* **41**, 649–56 (1999).
42. D. S. Wishart, C. Knox, A. C. Guo, R. Eisner, N. Young, B. Gautam, D. D. Hau, N. Psychogios, E. Dong, S. Bouatra, R. Mandal, I. Sinelnikov, J. Xia, L. Jia, J. A. Cruz, E. Lim, C. A. Sobsey, S. Shrivastava, P. Huang, P. Liu, L. Fang, J. Peng, R. Fradette, D. Cheng, D. Tzur, M. Clements, A. Lewis, A. De Souza, A. Zuniga, M. Dawe, Y. Xiong, D. Clive, R. Greiner, A. Nazyrova, R. Shaykhutdinov, L. Li, H. J. Vogel, I. Forsythe, HMDB: a knowledgebase for the human metabolome. *Nucleic Acids Res.* **37**, D603-10 (2009).
43. Q. Cui, I. A. Lewis, A. D. Hegeman, M. E. Anderson, J. Li, C. F. Schulte, W. M. Westler, H. R. Eghbalnia, M. R. Sussman, J. L. Markley, Metabolite identification via the Madison Metabolomics Consortium Database. *Nat. Biotechnol.* **26**, 162–4 (2008).
44. A. Gavrin, B. N. Kaiser, D. Geiger, S. D. Tyerman, Z. Wen, T. Bisseling, E. E. Fedorova, Adjustment of Host Cells for Accommodation of Symbiotic Bacteria: Vacuole Defunctionalization, HOPS Suppression, and TIP1g Retargeting in *Medicago*. *Plant Cell.* **26**, 3809–3822 (2014).
45. F. D. Dakora, C. A. Atkins, Adaptation of Nodulated Soybean (*Glycine max* L. Merr.) to Growth in Rhizospheres Containing Nonambient pO<sub>2</sub>. *Plant Physiol.* **96**, 728–736 (1991).
46. T. P. O'Brien, N. Feder, M. E. McCully, Polychromatic staining of plant cell walls by toluidine blue O. *Protoplasma.* **59**, 368–373 (1964).
47. M. Rivlin, U. Eliav, G. Navon, NMR studies of proton exchange kinetics in aqueous formaldehyde solutions. *J. Magn. Reson.* **242**, 107–112 (2014).
48. M. Rivlin, U. Eliav, G. Navon, NMR studies of the equilibria and reaction rates in aqueous solutions of formaldehyde. *J. Phys. Chem. B.* **119**, 4479–4487 (2015).
49. L. Dupont, G. Alloing, O. Pierre, S. El, J. Hopkins, D. Hrouart, P. Frendo, in *Senescence* (InTech, 2012), vol. 2, p. 64.
50. M. van der Graaf, In vivo magnetic resonance spectroscopy: basic methodology and clinical applications. *Eur. Biophys. J.* **39**, 527–40 (2010).
51. L. T. Smith, J. A. Pocard, T. Bernard, D. Le Rudulier, Osmotic control of glycine betaine biosynthesis and degradation in *Rhizobium meliloti*. *J. Bacteriol.* **170**, 3142–9 (1988).
52. M. Ashraf, M. R. Foolad, Roles of glycine betaine and proline in improving plant abiotic stress resistance. *Environ. Exp. Bot.* **59**, 206–216 (2007).

53. T. Pfau, N. Christian, S. K. Masakapalli, L. J. Sweetlove, M. G. Poolman, O. Ebenhoeh, The intertwined metabolism of *Medicago truncatula* and its nitrogen fixing symbiont *Sinorhizobium meliloti* elucidated by genome-scale metabolic models. *bioRxiv* (2016), doi:10.1101/067348.
54. M. López, J. A. Herrera-Cervera, C. Iribarne, N. A. Tejera, C. Lluch, Growth and nitrogen fixation in *Lotus japonicus* and *Medicago truncatula* under NaCl stress: Nodule carbon metabolism. *J. Plant Physiol.* **165**, 641–650 (2008).
55. M. N. Jordy, Seasonal variation of organogenetic activity and reserves allocation in the shoot apex of *Pinus pinaster* ait. *Ann. Bot.* **93**, 25–37 (2004).
56. S. C. Zeeman, J. Kossmann, A. M. Smith, Starch: Its Metabolism, Evolution, and Biotechnological Modification in Plants. *Annu. Rev. Plant Biol.* **61**, 209–234 (2010).
57. R. Thavarajah, V. Mudimbaimannar, U. Rao, K. Ranganathan, J. Elizabeth, Chemical and physical basics of routine formaldehyde fixation. *J. Oral Maxillofac. Pathol.* **16**, 400 (2012).
58. P. O. Lundquist, Nitrogenase activity in *Alnus incana* root nodules. Responses to O(2) and short-term N(2) deprivation. *Plant Physiol.* **122**, 553–562 (2000).
59. J. A. Chudek, G. Hunter, J. I. Sprent, G. Wurz, An application of NMR microimaging to investigate nitrogen fixing root nodules. *Magn. Reson. Imaging.* **15**, 361–368 (1997).
60. S. M. Brown, J. A. Chudek, G. Hunter, J. I. Sprent, K. B. Walsh, G. Wurtz, Proton density and apoplastic domains within soybean nodules in relation to the oxygen diffusion barrier. *Plant Cell Environ.* **20**, 1019–1029 (1997).
61. J. S. Macfall, P. E. Pfeffer, D. B. Rolin, J. R. Macfall, G. A. Johnson, Observation of the Oxygen Diffusion Barrier in Soybean (*Glycine Max*) Nodules with Magnetic-Resonance Microscopy. *Plant Physiol.* **100**, 1691–1697 (1992).
62. S. Sulieman, L. S. P. Tran, Asparagine: An amide of particular distinction in the regulation of symbiotic nitrogen fixation of legumes. *Crit. Rev. Biotechnol.* **33**, 309–327 (2013).
63. A. M. Hirsch, C. A. Smith, Effects of *Rhizobium meliloti* nif and fix mutants on alfalfa root nodule development. *J. Bacteriol.* **169**, 1137–1146 (1987).
64. A. M. Hirsch, M. Bang, F. M. Ausubel, Ultrastructural analysis of ineffective alfalfa nodules formed by nif::Tn5 mutants of *Rhizobium meliloti*. *J. Bacteriol.* **155**, 367–380 (1983).
65. J. Prell, P. Poole, Metabolic changes of rhizobia in legume nodules. *Trends Microbiol.* **14**, 161–168 (2006).

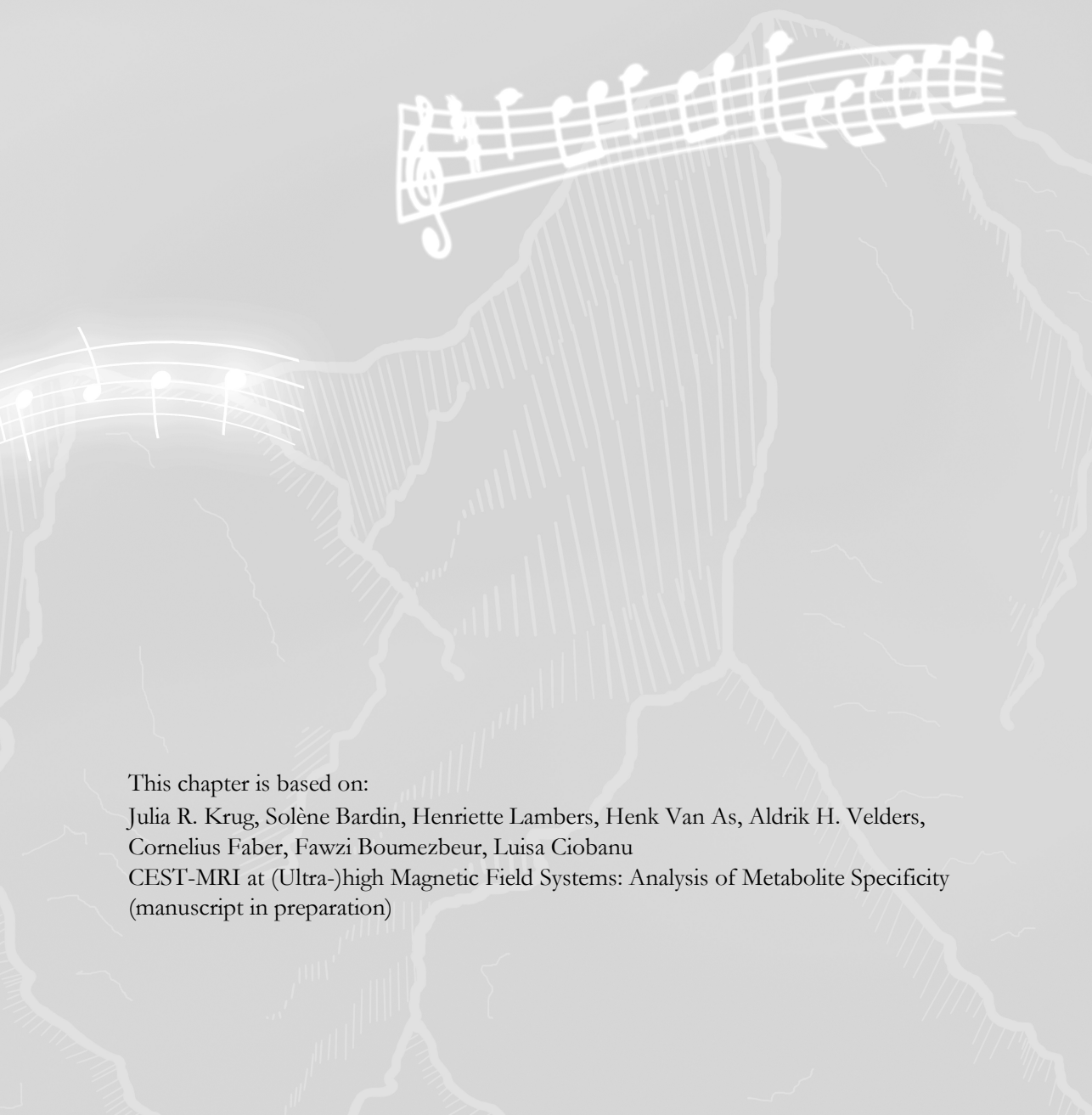
66. N. Hohnjec, A. M. Perlick, A. Pühler, H. Küster, The *Medicago truncatula* Sucrose Synthase Gene MtSucS1 Is Activated Both in the Infected Region of Root Nodules and in the Cortex of Roots Colonized by Arbuscular Mycorrhizal Fungi. *Mol. Plant-Microbe Interact.* **16**, 903–915 (2007).
67. L. O. Yang, M. K. Udvardi, D. A. Day, Specificity and regulation of the dicarboxylate carrier on the peribacteroid membrane of soybean nodules. *Planta* **182**, 437–444 (1990).
68. J. J. Flint, K. Menon, B. Hansen, J. Forder, S. J. Blackband, Metabolic support of excised, living brain tissues during magnetic resonance microscopy acquisition. *J. Vis. Exp.* **2017**, 1–10 (2017).





## Chapter 6

# CEST-MRI at (Ultra-)high Magnetic Field Systems: Analysis of Metabolite Specificity



This chapter is based on:

Julia R. Krug, Solène Bardin, Henriette Lambers, Henk Van As, Aldrik H. Velders,  
Cornelius Faber, Fawzi Boumezbeur, Luisa Ciobanu

CEST-MRI at (Ultra-)high Magnetic Field Systems: Analysis of Metabolite Specificity  
(manuscript in preparation)

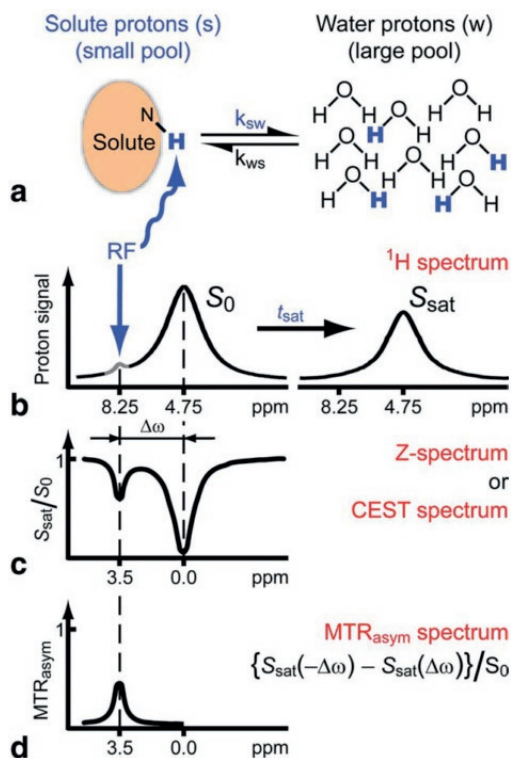
### **Abstract**

Spatially resolved metabolite detection is very useful as it is one of the few methods with which a variety of metabolites can be non-invasively detected. In addition to the direct detection of metabolite protons, the indirect detection by chemical exchange saturation transfer (CEST) of exchangeable protons with water protons has proven to yield significant signal-to-noise ratio (SNR) enhancements. However, the selectivity to a certain metabolite of interest is a challenge using CEST- techniques. In this chapter, we are investigating the selectivity of CEST at ultra-high field of 17.2 T and 22.3 T in phantoms (i.e. glutamate, glucose, lactate and myoinositol) and cherry tomato pericarp. The Z-spectra were found to be better resolved at 22.3 T than at 7.0 T for phantoms and tomato pericarp tissue. The complete disentanglement of metabolites remains a challenge even at the state-of-the-art ultra-high field strength of 22.3 T.

## 6.1 Introduction

Spatially resolved metabolite detection by Magnetic Resonance (MR) techniques is a powerful tool to measure information on the metabolite distribution in living organisms non-invasively (1). Common methods for metabolic imaging are localised spectroscopy and spectroscopic imaging of protons or X-nuclei such as  $^{13}\text{C}$ ,  $^{31}\text{P}$  and more recently  $^2\text{H}$  (2). However, MR techniques are relatively insensitive compared to other spectroscopic techniques and suffer from low signal-to-noise ratios (SNR). This results either in high detection limits, long acquisition times or low spatial resolutions. One method to increase the SNR is to use high magnetic field strength (3) with 17.2 T and 22.3 T currently being among the highest magnetic field strengths for pre-clinical imaging and NMR Microscopy applications, respectively. These emerging ultra-high field strengths open up new possibilities for metabolic imaging techniques, however additional enhancement methods are desirable to improve the detection limit further.

Among the methods used for metabolic imaging, Chemical Exchange Saturation Transfer (CEST) has proven to be a useful technique for sensitivity enhancement (4). As an example, for glutamate, a 700-fold increase in SNR compared to localised spectroscopy was reported (5). The principle of CEST originates from the early study of exchange processes in NMR Spectroscopy (6). Combined with the spatially-resolved MRI, this method can help detect a certain metabolite using the advantage of increased sensitivity compared to direct detection of the metabolite. This increase in sensitivity depends on the combination of chemical shift difference between water and the metabolite and exchange rates between them (7). The CEST-method is based on a saturation transfer of the solute molecules to the solvent molecules, which is bulk water in the case of most biological samples (8). By irradiating the exchangeable protons of the molecule of interest, the subsequent exchange of the solute protons with bulk water leads to the transfer of the saturation to the bulk water (Figure 6-1a+b). By dividing the resulting saturated signal  $S_{\text{sat}}$  by the signal without pre-saturation  $S_0$ , the CEST-spectrum can be obtained (Figure 6-1c). As direct water saturation may interfere with detection of CEST effects, a common procedure for quantification is to employ the so-called MT ratio asymmetry ( $\text{MTR}_{\text{asym}}$ ) analysis (Figure 6-1d). The saturation transfer module can be performed with different options of transfer schemes (e.g. a continuous wave pulse, a pulse train with a short interpulse delay or a label-transfer module which either use a dephasing gradient after each pulse or an inversion pulse) before starting the first RF pulse of the MRI experiment (8).



**Figure 6-1:** a.) The principle of CEST is based on the exchange of protons of a solute molecule with the solvent molecules e.g.  $\text{H}_2\text{O}$ . b.) When irradiating at the resonance frequency of the exchangeable solute proton, the magnetisation will be saturated, which will be transferred to the bulk water upon the exchange. c.) Dividing the spectrum taken with the saturation pulse applied  $S_{\text{sat}}$  by the spectrum without saturation  $S_0$  results in the CEST- or Z-spectrum d.) A common procedure for quantification is to employ the so-called MT ratio asymmetry ( $\text{MTR}_{\text{asym}}$ ) analysis. © 2011 Wiley-Liss, Inc. Wiley. Used with permission from (Peter C. M. van Zijl, Nirbhay N. Yadav, Chemical exchange saturation transfer (CEST): What is in a name and what isn't?, Magnetic Resonance in Medicine and John Wiley and Sons) (8).

Several types of CEST experiments have been developed and classified based on their exchange mechanism, namely proton exchange, molecular exchange and compartmental exchange (8). Numerous chemical compounds have been investigated for application towards CEST, most commonly known is their division into diamagnetic CEST (diaCEST) and paramagnetic CEST (paraCEST) (8). For diaCEST(4),

metabolites (e.g. glucose) are included. For these metabolites, the CEST-mechanism is based on proton exchange with the water protons. Among the compounds tested for endogenous CEST-contrast (9) were lactate (10), glutamate (5, 11), glucose (7, 12, 13), myoinositol (14).

CEST-contrast depends on a number of sample parameters: exchange rate ( $k_{sw}$ ) pH, temperature and the concentration of solutes (11). Another dependence of the CEST-contrast is on MR-parameters, saturation time  $T_{sat}$ , pulse bandwidth, saturation offset, and excitation field strength  $B_1$ . The CEST-condition states that in order to exhibit the CEST effect,  $k_{sw}$  has to be smaller than or equal to the chemical shift difference in frequency units  $\Delta\delta$  [Hz]<sup>1</sup> between the exchangeable metabolite proton and water protons (9). As this chemical shift difference increases with  $B_0$  as it is linear to the magnetic field  $B_0$ (15), the CEST-condition is fulfilled for a larger range of exchange rates  $k_{sw}$  at higher field strengths. Using high field strengths of 17.2 T and 22.3 T results in increased SNR, longer  $T_1$  relaxation times and most importantly, an increased specificity by increased spectral resolution (8). Here, we aim to test whether low concentrated metabolites can be imaged at ultra-high strengths with increased selectivity.

To this end, we tested a phantom consisting of solutions of the selected metabolites lactate, glucose and glutamate and a mix of the three afore-mentioned metabolites on three different field strengths (7.0 T, 17.2 T and 22.3 T). Additionally, myoinositol was tested at 17.2 T and 22.3 T. The CEST-parameters were optimised on each field strength  $B_0$  and the phantom was tested with the optimised parameters to conduct a specificity analysis towards each metabolite given a specific field strength and CEST parameters. Then, a cherry tomato was used to evaluate CEST specificity on a biological specimen. The  $B_1$  field was varied to optimise the selectivity and finally, CEST-MRI experiments were performed.

<sup>1</sup> In this chapter, we use the abbreviation of  $\Delta\omega$  [Hz] to indicate the field-dependent chemical shift difference, as this notation is common in most literature and formulas. However, to compare at different field strengths, these chemical shift difference are converted to the field-independent shift difference  $\Delta\delta$  [ppm] (15) in the results section.

## 6.2 Experimental Methods

### Phantom Solutions for Optimisation of $B_1$ -parameter

The phantoms were prepared using 0.01 M PBS buffer in  $H_2O$  and the metabolites of interest to the final concentrations of 1. 20 mM L-Glutamic Acid (Glutamate), 2. 20 mM D-Glucose (Glucose), 3. 40 mM L-(+)-Lactic Acid (Lactate) and 4. a mix of 1-3. 5. 20 mM Myoinositol. All solutions were adjusted to the pH of 7 and azide was added when the solution was not tested immediately.

### MRI-Equipment

MRI experiments were done on different systems 1.) a 7.0 T PharmaScan (Bruker, BioSpin, Ettlingen, Germany) with a maximum possible gradient strength of 760 mT/m and a 38 ID mm  $^1H$  resonator 2.) a 17.2 T Biospec system (Bruker, BioSpin, Ettlingen, Germany) with a maximum possible gradient field strengths of 1 T/m and a 25 mm ID quadrature birdcage coil 3.) a 22.3 T Advance III HD (Bruker, BioSpin, Ettlingen, Germany) with a maximum possible gradient field strengths of 3 T/m and a 5 mm  $^1H$  birdcage coil. All systems were equipped with ParaVision 6.0.1.

### CEST-Experiments

Prior to all experiments, a FID-shim procedure up to second order was performed on the entire sample. A  $B_0$  map was recorded and for each scan, MAPSHIM was used to calculate the optimal shim settings for the region of interest and iterative shimming was performed to improve the  $B_0$ -field homogeneity. A Local Frequency adjustment for CEST-PRESS and Basic Frequency Adjustment for CEST-RARE was repeated prior to each scan.

A CEST-PRESS sequence was used with the following parameters: 1.) CEST module consists of 35 block pulses of pulse length ( $t_p$  50 ms) with an interpulse delay 10  $\mu$ s, saturation time ( $T_{sat}$ ) 1.75 s, saturation offset range from 10 ppm to -10 ppm with a resolution of 0.1 ppm between 4.3 and -4.3 ppm alternating positive and negative saturation offsets, 2.) PRESS parameters: repetition time (TR) 2.5 s, echo time (TE) 15.2 ms, spectral acquisition time 560 ms, total acquisition time ( $t_{acq}$ ) 4 min 10 s, number of averages (NA) 1. Voxel sizes and  $B_1$ -field strength varied for different experiments and are reported in the results section. 2.) RARE parameters: TR 3 s,  $TE_1$  4.72 ms, receiver bandwidth 50 kHz, rarefact 6, NA 1,  $t_{acq}$  11 min 10 s. Voxel sizes and  $B_1$ -field strength varied for different experiments and are reported in the results section.

The CEST-RARE images were acquired with the following parameters 1.) CEST module consists of 35 block pulses of  $t_p$  50 ms with an interpulse delay 10  $\mu$ s,  $T_{sat}$  1.75 s, saturation offset range from 4 ppm to -4 ppm with a resolution of 0.4 ppm alternating positive and negative saturation offsets. Additionally, reference images with a saturation offset of 38 and -38 ppm. Geometries and matrix sizes vary and are reported in the results section. A Water Saturation Shift Referencing (WASSR)-experiment was performed with saturation offsets from -1 ppm to 1 ppm with a resolution of 0.1 ppm and a  $B_1$ -field strength of 0.2  $\mu$ T. Rare factors were 6 and 1 at 17.2 and 22.3 T, respectively.

### Data Processing

CEST-PRESS data was analysed with the  $MTR_{asym}$  analysis (Equation 1) using MATLAB.

For  $MTR_{asym}$  maps, a WASSR map was recorded to correct for  $B_0$ -inhomogeneities prior to the  $MTR_{asym}$ -analysis (see S 6-5). For data processing, MATLAB-scripts were used. The  $MTR_{asym}$  ratio for CEST-PRESS spectra and CEST-RARE was determined using the asymmetry analysis (Equation 6-1) (8). This is based on calculating the difference between the signal intensity  $S_{sat}(-\Delta\omega)$  at the (field-dependent) saturation offset  $-\Delta\omega$  [Hz] and a control acquisition to account for the effect of direct water saturation (16). The saturation offset  $\Delta\omega$  is given by the frequency difference between the excitation frequency and the frequency of the water protons. Additionally, this difference is normalised by the signal intensity  $S_0$  corresponding to a saturation offset (-38 ppm) from the water saturation (8).

$$MTR_{asym}(\Delta\omega) = \frac{S_{sat}(-\Delta\omega) - S_{sat}(\Delta\omega)}{S_0} \quad (6-1)$$



### 6.3 Results

After optimisation of the CEST parameters (i.e. saturation offset and  $B_1$ -field strength) in section 6.3.1, the selectivity with optimal parameters was determined and evaluated on spectrometers with different field strengths in section 6.3.2. Z-spectra CEST-RARE experiments on a cherry tomato were evaluated in section 6.3.3.

#### 6.3.1. Optimisation of CEST-MRI Parameters at Different Magnetic Field Strengths

The optimal CEST-parameters were determined on phantoms of the individual metabolites (Table 6-1). For  $B_1$ -optimization, Z-spectra at different field strengths were evaluated for 1. a large intensity in  $MTR_{\text{asym}}$  values with 2. minimal line broadening for increased specificity (S 6-3).  $B_1$ - optimisation was performed on CEST-PRESS spectra with constant CEST-module parameters of  $T_{\text{sat}} = 1.75$  s at all field strength to limit the maximum repetition time with the objective to use a fast MRI sequence. In different phantom experiments, the maximum in the  $MTR_{\text{asym}}$  ratio for gluCEST shifted between the saturation offset 2.8-2.9 ppm and for glucose from 1.1-1.2 ppm. For consistency, the offset 2.8 ppm is reported for gluCEST in all experiments, while the offset for glucoCEST is reported at 1.2 ppm.

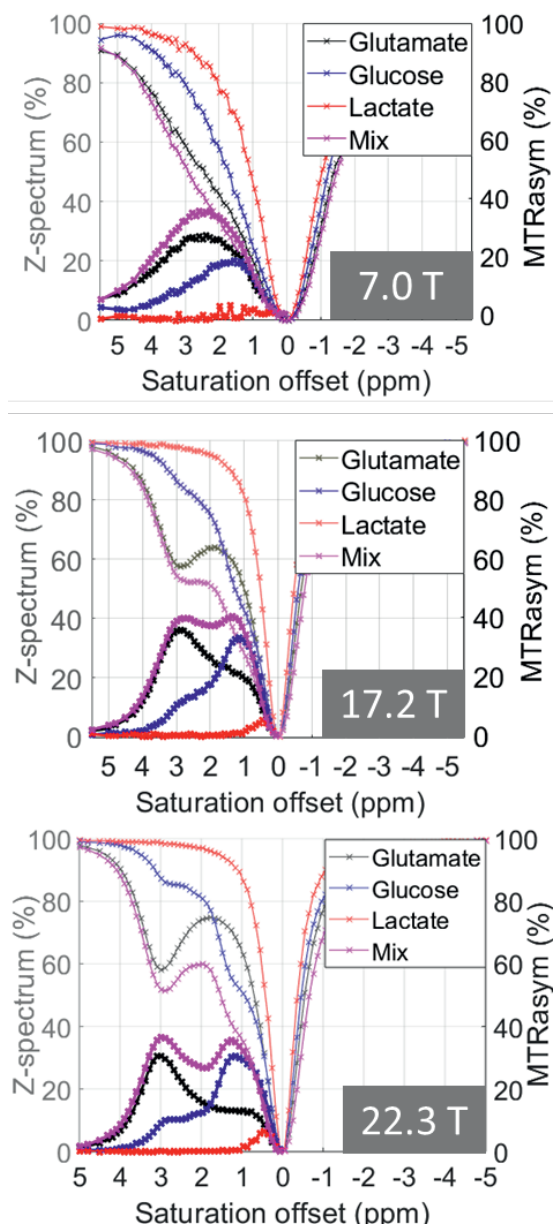
**Table 6-1:** Exchange rates  $k_{\text{sw}}$ , saturation offset  $\Delta\delta$ , and optimised  $B_1$ -field strengths at different static magnetic field strengths. All experiments were conducted on liquid phantoms (pH 7 in 0.01 M PBS buffer).

Concentrations of metabolites in pH 7 and 0.01M PBS	$k_{\text{sw}}$ [ $\text{s}^{-1}$ ] (at pH 7 from literature)	$\Delta\delta$ [ppm]	$B_1$ [ $\mu\text{T}$ ] @ 7 T	$B_1$ [ $\mu\text{T}$ ] @ 17.2 T	$B_1$ [ $\mu\text{T}$ ] @ 22.3 T
Glutamate [20 mM]	$7490 \pm 90$ (19)	2.8	7	7	7
Glucose [20 mM]	$3940 \pm 260$ (19)	1.2	3	5	5
Lactate [40 mM]	$\sim 350 \pm 50$ (10)	0.4	1.5	2.6	2.6
Myoinositol [20 mM]	$2090 \pm 100$ (19)	0.8	-	4	5

### 6.3.2 Specificity Analysis Using the $MTR_{\text{asym}}$ -analysis

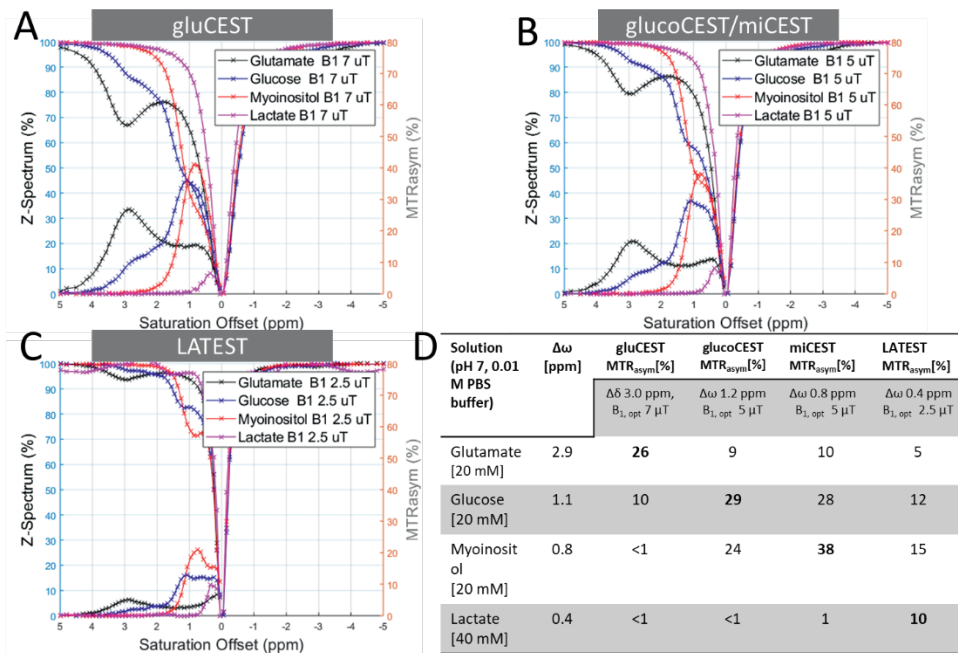
Z-spectra and corresponding  $MTR_{\text{asym}}$ -spectra of the metabolites (glutamate, glucose, lactate and the mix) at different  $B_0$ -field strengths and at optimised parameters to favour gluCEST contrast are shown in Figure 6-2. The Z-spectra at 7.0 T show that the Z-spectrum of glutamate shows the highest  $MTR_{\text{asym}}$  ratio. The maximum of the  $MTR_{\text{asym}}$  peak of glutamate is observed around 2.8 ppm for glutamate. The peak of glucose is visible around the expected offset at 1.2 ppm, while for lactate no peak can be observed in the  $MTR_{\text{asym}}$ -spectrum (Figure 6-2A),

For 17.2 T and 22.3 T, the  $MTR_{\text{asym}}$  spectra peak at the expected saturation offsets (Figure 6-1B and C). Furthermore, the spectra are more resolved than at 7.0 T, with the best resolution at 22.3 T. However, the  $MTR_{\text{asym}}$  spectra of the glucose solution at all field strength show a significant contribution at the saturation offset for glutamate at optimised parameters. This results in a contribution of glucose in the gluCEST contrast, and vice versa a contribution of glutamate to the glucoCEST contrast was observed. This proves that even at the current state-of-the-art ultra-high field strength for MRI and MRS, the metabolite contributions, though being better resolved, cannot be completely disentangled.



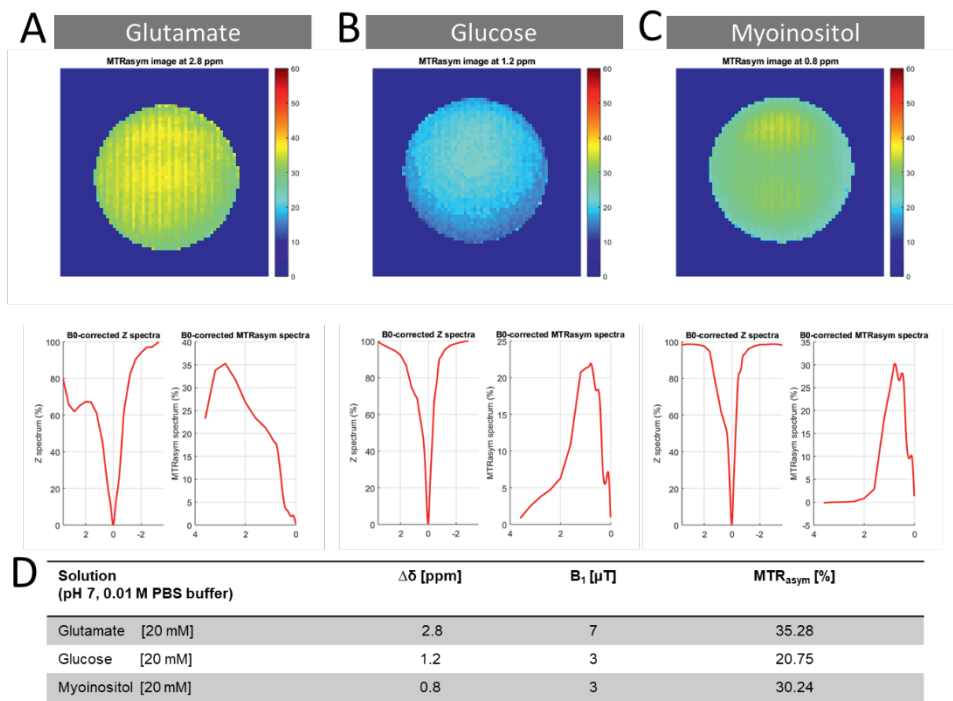
**Figure 6-2:** Z-spectra acquired with optimised parameters for gluCEST-contrast at 7.0 T, 17.2 T and 22.3 T (all Z-spectra acquired with B<sub>1</sub> 7 μT, voxel dimensions 2 x 2 x 4 mm<sup>3</sup>). The Z-spectra (thin line) show the proton signal intensity after saturating at the respective saturation offset with a B<sub>1</sub>-field strength of 7 μT. The asymmetric MTR analysis of the Z-spectrum yields the MTR<sub>asym</sub>-spectra (bold line), which eliminates the effect of direct water saturation.

While the ultra-high field allows for increased specificity, the contrast is not solely originating from the targeted metabolite (Figure 6-3). For example, considering the gluCEST contrast with optimised  $B_1$ -field strength of  $7\ \mu\text{T}$ , we obtain an  $\text{MTR}_{\text{asym}}$ -ratio at 2.8 ppm of 26% but a glucose contribution of 10% (Figure 6-3A and D). The contributions of myoinositol and lactate, are, however, negligible to the gluCEST-contrast, which allows for a distinction of these metabolites. However, the proximity of glucose and myoinositol both in terms of saturation offset ( $\Delta\delta_{\text{gluco}}$  1.2 ppm and myoinositol  $\Delta\delta_{\text{mi}}$  0.8 ppm) and optimal  $B_1$ -field strengths of  $5\ \mu\text{T}$  makes them indistinguishable in the  $\text{MTR}_{\text{asym}}$  contrast (Figure 6-3B and D). Using the LATEST parameters ( $\Delta\delta_{\text{lac}}$  0.4 ppm and  $B_1$   $2.5\ \mu\text{T}$ ) an  $\text{MTR}_{\text{asym}}$  ratio of 10% can be achieved which is exceeded by the  $\text{MTR}_{\text{asym}}$  ratios of myoinositol and glucose with 12% and 9% respectively.



**Figure 6-3:** Z-spectra and  $\text{MTR}_{\text{asym}}$ -spectra for optimised parameters for A.) gluCEST B.) glucoCEST/ miCEST-contrast C.) LATEST contrast and D)  $\text{MTR}_{\text{asym}}$  ratios for each gluCEST, gluco/miCEST and LATEST experiment from the Z-spectra in A.-C)

CEST-RARE images with the optimised  $B_1$ -field strengths were recorded on a phantom consisting of 20 mM Glucose, 20 mM Glucose and 20 mM Myoinositol (Figure 6-4A). The inhomogeneities in the image stem from  $B_1$ - inhomogeneity as the typical excitation profile of a birdcage coil is observed in the image.

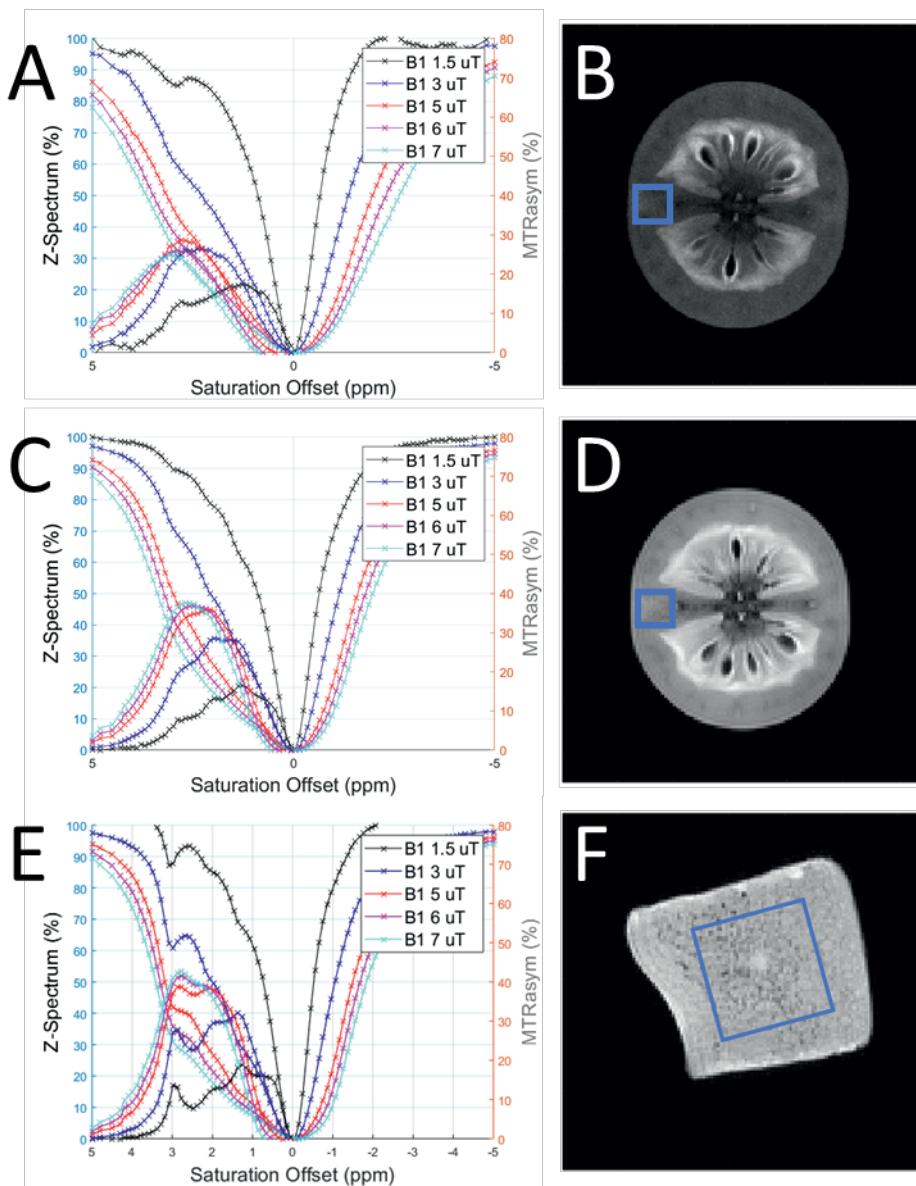


**Figure 6-4:** Phantoms at 22.3 T were investigated using CEST-RARE experiments on A.) Glutamate, B.) Glucose, and C.) Myoinositol. The images are color-coded for the obtained  $MTR_{asym}$  at the indicated saturation offset. The spectra show the Z-spectra and  $MTR_{asym}$ -spectra for a region of interest in the center of each phantom. D.) The table shows the  $MTR_{asym}$  ratios on pure phantom solutions.

### 6.3.3. CEST-effect Studied on a Cherry Tomato

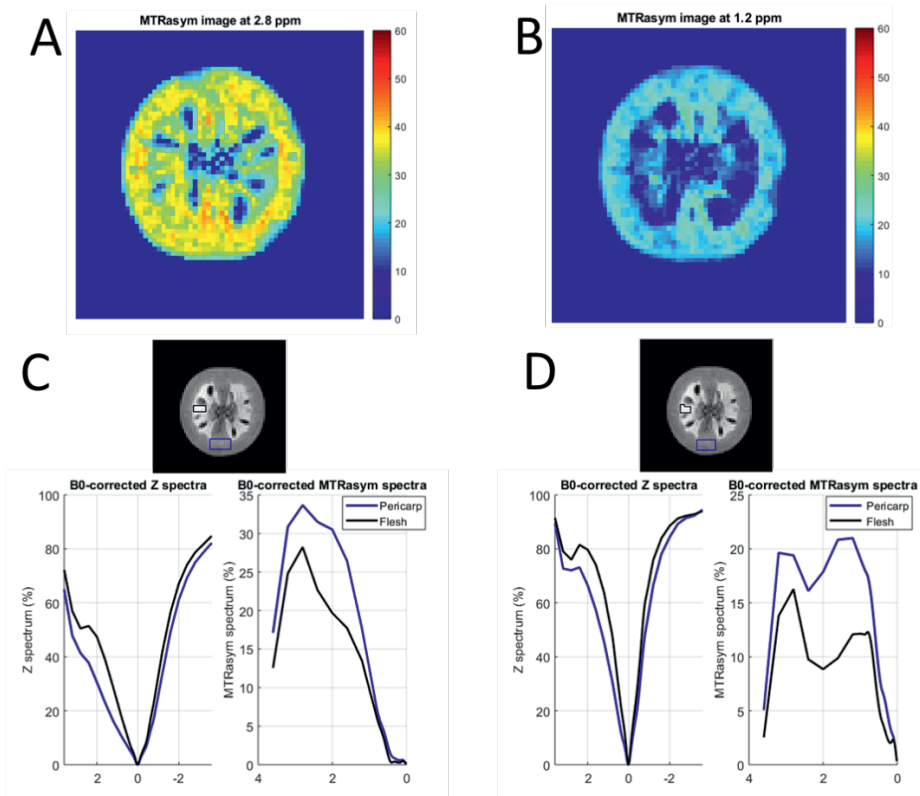
To investigate the usefulness of CEST for studying tomatoes or similar biological specimen,  $B_1$ -field strength optimisation was conducted at 7.0 T, 17.2 T and 22.3 T using CEST-PRESS (Figure 6-5A-C) on a cherry tomato (*S. lycopersicum*). At all three field strengths, a shift of the  $MTR_{\text{asym}}$  peak from 1.2 ppm at low  $B_1$ -field strengths ( $B_1 = 1.5 \mu\text{T}$ ), to 2.8 ppm at higher  $B_1$  field strength ( $B_1 = 7 \mu\text{T}$ ) was observed, which signifies a shift of selectivity from glucose to glutamate. Additionally, an enhanced separation of peaks in the  $MTR_{\text{asym}}$  spectrum with narrower linewidth could be observed, especially at 22.3 T (Figure 6-5C).

Complementary, localised spectroscopy was performed to detect the presence of metabolites (S 6-4). Localised spectroscopy being semiquantitative in this case, can be used to indicate the presence of the metabolites glucose and glutamate, which are known to be major metabolites in tomatoes (20, 21). Myoinositol is also predicted to be present in tomato at lower concentrations (20), however as the proton resonances of myoinositol are located in the carbohydrate region of the spectrum, it is difficult to assign this metabolite. Peak fitting might be the method of choice, but prior knowledge of the metabolite composition of tomato would be recommended.



**Figure 6-5:** Z-spectra from a CEST-PRESS spectrum with different  $B_1$ -field strengths on the pericarp tissue of the same tomato for A.) 7.0 T and C.) 17.2 T. E.) At 22.3 T, a piece of excised tomato pericarp tissue in perfluorodecalin was used for CEST-PRESS spectra. The corresponding 2D RARE images are shown in B.) at 7.0 T D.) at 17.2 T and F.) at 22.3 T. The blue box indicates representative voxel locations of the dimensions  $3 \times 3 \times 3 \text{ mm}^3$  at 7.0 T and 17.2 T and  $1.5 \times 1.5 \times 1.5 \text{ mm}^3$  at 22.3 T.

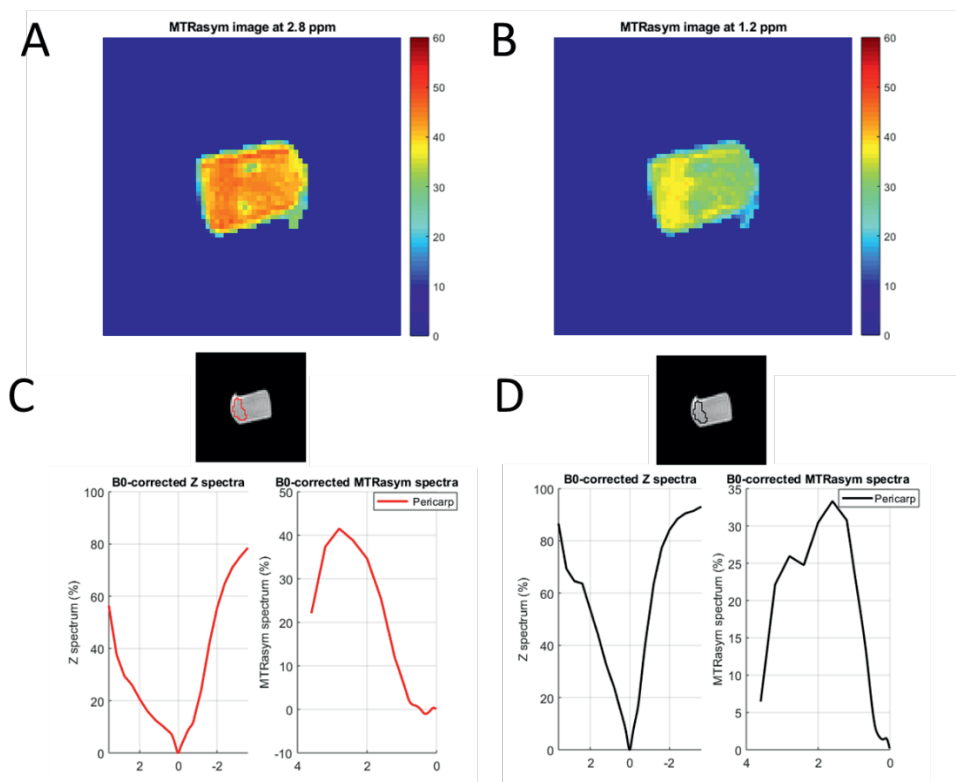
Using CEST-RARE on a cherry tomato, CEST-images were acquired at 17.2 T for preferred gluCEST (Figure 6-6A) and glucoCEST-parameters (Figure 6-6B). Here, the  $B_1$ -field strength of  $7\ \mu\text{T}$  was chosen for optimal gluCEST contrast, while  $3\ \mu\text{T}$  was chosen for optimal glucoCEST contrast based on the maximum of the  $\text{MTR}_{\text{asym}}$  in the Z-spectra of the CEST-PRESS experiment (Figure 6-6). The corresponding Z-spectra are shown in Figure 6-6C and D. In the tomato, the pericarp tissue exhibits a higher  $\text{MTR}_{\text{asym}}$  ratio at the saturation offset of 2.8 ppm than the flesh (Figure 6-6A). Likewise, the pericarp shows a higher  $\text{MTR}_{\text{asym}}$  ratio than the flesh for the saturation offset of 1.2 ppm. However, due to the dependence of the  $\text{MTR}_{\text{asym}}$  ratio on several factors, the quantification of the concentrations is not feasible only based on the  $\text{MTR}_{\text{asym}}$  ratio at one saturation offset.



**Figure 6-6:** CEST-RARE images at 17.2 T for A.) gluCEST contrast (Saturation offset 2.8 ppm,  $B_1\ 7\ \mu\text{T}$ ) with the corresponding Z-spectrum of an ROI located at the pericarp and the flesh of a tomato B.) glucoCEST contrast (Saturation offset 1.2 ppm,  $B_1\ 3\ \mu\text{T}$ ). Both images have a matrix size of  $64 \times 64$  and a field-of-view of  $10 \times 10\ \text{mm}^2$



At 22.3 T, the  $MTR_{asym}$  ratios in the tomato pericarp are increased with respect to 17.2 T. For gluCEST parameters (Saturation offset 2.8 ppm,  $B_1$  7  $\mu$ T), this  $MTR_{asym}$ -increase is from 34 % (Figure 6-6C) to 41 % (Figure 6-7C). For glucoCEST (Saturation offset 1.2 ppm,  $B_1$  3  $\mu$ T), the  $MTR_{asym}$  from 21 % to 31% (Figure 6-7D). However, as it is not the same tomato (Note that this in contrast to the experiments in Figure 6-5 which were conducted on the same tomato), it is not feasible to conclude whether this difference stems from a higher metabolite concentration or a higher  $MTR_{asym}$  ratio as an effect of the increasing field strengths. Additionally, excising the tomato might have an effect on the metabolite distribution.



**Figure 6-7:** CEST-RARE images at 22.3 T for A.) gluCEST contrast (Saturation offset 2.8 ppm,  $B_1$  7  $\mu$ T) with the corresponding Z-spectrum of an ROI located at the pericarp and the tomato flesh B.) glucoCEST contrast (Saturation offset 1.2 ppm,  $B_1$  3  $\mu$ T). Both images have a matrix size of 64 x 64 and a field-of-view of 10 x 10 mm<sup>2</sup>

## 6.4 Discussion

$B_1$  strength optimisation is necessary for a CEST-experiments as the selectivity for a metabolite of interest can be optimised by applying the optimised  $B_1$ -value at the saturation time  $T_{\text{sat}}$  (19). When using a phantom for  $B_1$ -optimization, additional parameters such as temperature, pH-value, metabolite concentrations and buffer concentration should be matched as these sample conditions influence Z-spectra (11). For the results presented in section 6.3, we used a fixed saturation time  $T_{\text{sat}}$  in the CEST-preparation module, as CEST was optimised keeping reduced acquisition times into account. As the  $T_1$  increases at increasing field strengths  $B_0$ , also the saturation time  $T_{\text{sat}}$  could have been increased to achieve a higher CEST-contrast at 22.3 T, compared to 17.2 T, due to more efficient saturation. However, for consistency the choice was made to keep the TR constant.

The CEST-SNR could be calculated to quantify the effect of varying the  $B_0$ -field strength on the sensitivity (22). To compare the SNR of the systems, the volume-normalised  $\text{SNR}_{v,k=1}$  increases by a factor 22.5 between a 25 mm  $^1\text{H}$  (quadrature) birdcage coil at 17.2 T to and a 5 mm  $^1\text{H}$  birdcage coil at 22.3 T (S 6-1). This does not only stem from the difference in magnetic field strength, as the theoretical SNR-increase from 17.2 T to 22.3 T only accounts for a factor 1.6 due to the SNR dependence on  $B_0^{7/4}$  (23). Additional factors to explain this SNR difference are the difference in coil diameter and other hardware differences (e.g. preamplifier).

Quantitative CEST analysis is a big challenge within the biomedical domain. Most CEST-studies which aimed to investigate a certain metabolite by CEST contrast used an infusion to prove a qualitative change in the CEST contrast. At lower field strength spectral resolution is reduced as the spectral resolution scales with the main magnetic field strengths  $B_0$ . Using ultra-high field strength for CEST improves the separation of metabolite contributions. Unfortunately, it does not lead to a complete disentanglement of the metabolite contributions to a CEST-contrast at a particular saturation offset when using the CEST-contrast based on the asymmetry analysis. Therefore, the observed gluCEST contrast and glucoCEST contrast in the cherry tomato cannot uniquely be attributed to glutamate or glucose, respectively, and a further step to uniquely select the metabolite of interest is necessary.

To quantify the CEST-contrast in model-based solutions, the fitting to the modified Bloch-McConnell equations (24) has been reported. The drawback of the fitting of the Z-spectrum using the Bloch-McConnell equations is that the recording of a full Z-spectrum is too time-consuming for applications where fast acquisition times are needed, e.g. for fMRI experiments.

Regarding the acquisition, several other methods are proposed to increase the specificity towards a certain metabolite with an optimised acquisition strategy using either e.g. chemical exchange spin-lock imaging (CESL) (25) or frequency-labelled exchange (FLEX) (26, 27). The advantage of CESL is the possibility for separation of metabolites according to their exchange rate  $k_{\text{exch}}$ , while FLEX is able to simultaneously separate several exchangeable metabolite protons. For CEST imaging,  $B_0$  homogeneity is crucial as the saturation pulse bandwidth is small and shift in resonant frequency caused by  $B_0$ -inhomogeneities can lead to the excitation at a displaced chemical shift. Therefore, optimising the  $B_0$ -homogeneity is crucial and might potentially be a drawback at ultra-high field. One approach to correct for  $B_0$ -inhomogeneities is the Water Saturation Shift Referencing (WASSR) approach (28), where the Z-spectrum around the saturation offset of 0 ppm is experimentally recorded with a CEST-MRI sequence (e.g. CEST-RARE) and fitted to determine the frequency shift due to  $B_0$ -inhomogeneities per voxel. This shift is then used to extrapolate to the expected saturation offset in this voxel and the  $\text{MTR}_{\text{asym}}$ -ratio can be corrected for it. However, for an accurate extrapolation, this approach requires the acquisition of CEST-MRI images with different saturation offsets and adds to the acquisition time of the experiments. Additionally, if  $B_1$ -inhomogeneities are present in the region of interest, a simultaneous  $B_0$  and  $B_1$ -mapping can be performed using WASABI (29).

## 6.5 Conclusion and Outlook

CEST has been proven to be a promising technique for experiments where the Signal-to-Noise is limited. Furthermore, ultra-high field strengths and optimised detectors are advantageous due to their increase in SNR, which in turn increased the SNR due to CEST.

Most importantly, CEST-contrast specificity towards certain metabolites increase with increasing field strengths, which manifested itself by higher resolved  $MTR_{\text{asym}}$ -spectra. While this might be a powerful method in a well-defined system with a single compound which changes in concentration, model-free CEST contrast alone cannot serve to identify a compound in a complex system with several metabolites, which change in opposite directions. As most biological specimens contain a complex mixture of metabolites, it is needed to refine the methods either by employing more selective acquisition strategies (e.g. FLEX, see general discussion, chapter 7) or by data analysis strategies which succeed in the disentanglement of the contributions or a combination of both.

## 6.6 Acknowledgements

J.R.K. was supported by the NWO-funded Netherlands' Magnetic Resonance Research School (NMARRS) graduate school [022.005.029] and by the ERASMUS+ programme for the mobility period at CEA/Neurospin in Saclay. Experiments at the 950 MHz instrument were supported by uNMR-NL, an NWO-funded National Roadmap Large-Scale Facility of the Netherlands [184.032.207]. Experiments at the 17.2 T were supported by the ANR-DFG 'BAMBOO'-project and the 'Bottom-Up' programme at CEA. We thank Julien Flament for providing us the CEST-sequences and the WASSR correction Matlab script.

## 6.7 Supporting Information

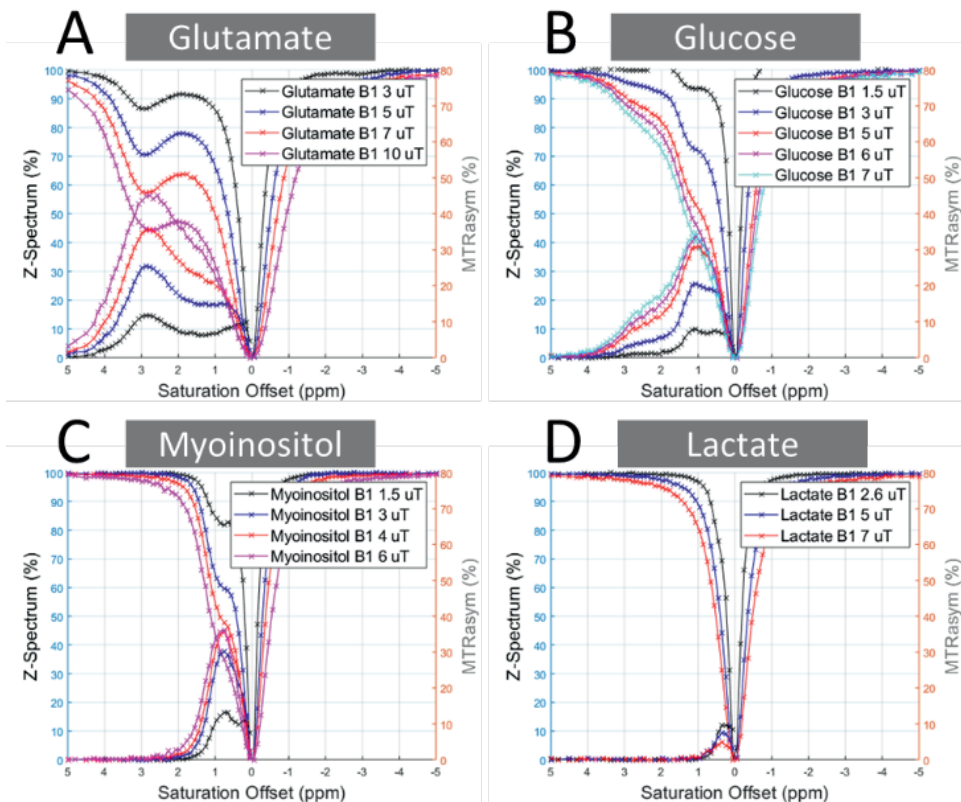
**S 6-1:** SNR comparison between the 7.0 T, 17.2 T and 22.3 T system. An MSME experiment was recorded with the following parameters (TR 1s, TE 7 ms, 1 average, rBW 100 kHz,  $t_{acq}$  4 min 16 s, matrix size 256 x 256). The reference solution used to acquire this image was 20% (v/v) H<sub>2</sub>O, 80% (v/v) D<sub>2</sub>O and 6.3 mM CuSO<sub>4</sub>.

Main magnetic field $B_0$ [T]	RF - detector	RF inner diameter [mm]	SNR <sub>i</sub>	Voxel volume [mm <sup>3</sup> ]	SNR <sub>i,v, k=1</sub> [mm <sup>-3</sup> ]
7.0	<sup>1</sup> H resonator	38	12	$9.5 \times 10^{-3}$	5
17.2	<sup>1</sup> H (quadrature) birdcage	25	25	$4.4 \times 10^{-3}$	22
22.3	<sup>1</sup> H birdcage	5	35	$2.7 \times 10^{-3}$	495

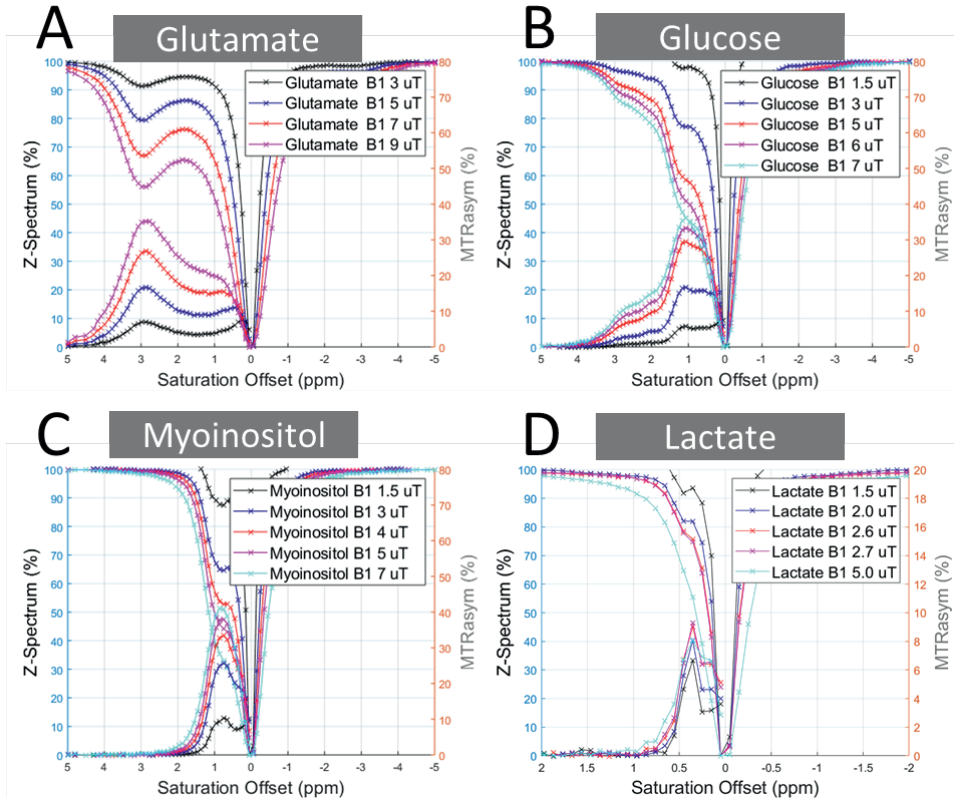
The image SNR of a (magnitude) image on a CuSO<sub>4</sub> was determined by subtracting the mean of the signal ROI  $\mu_S$  by the mean of the noise ROI  $\mu_N$  and divide this by the standard deviation of the noise  $\sigma_N$ . To compensate for differences in acquisition parameters, we additionally normalised to account for differences in matrix sizes  $M_x$  and  $M_y$  (18) (S 6-1). Other acquisition parameters which influence the SNR were kept constant.

$$SNR_{v,k=1} = \frac{\mu_S - \mu_N}{\sigma_N * V_{Voxel} * \sqrt{M_x * M_y}} \quad (S\ 6-1)$$

**S 6-2:**  $B_1$ -optimization at 17.2 T for A.) 20 mM Glutamate (voxel dimension:  $3 \times 3 \times 3 \text{ mm}^3$ ) B.) 20 mM Glucose (voxel dimension:  $3 \times 3 \times 3 \text{ mm}^3$ ) C.) 20 mM Myoinositol (voxel dimension:  $3 \times 3 \times 3 \text{ mm}^3$ ) D.) 40 mM Lactate (voxel dimension:  $2 \times 2 \times 4 \text{ mm}^3$ ).

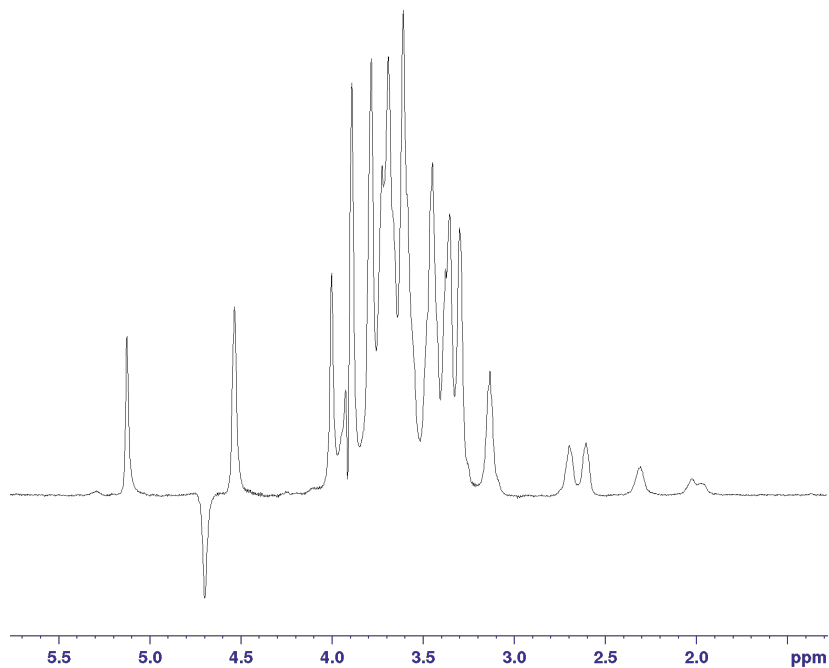


**S 6-3:** B<sub>1</sub>-optimization for 22.3 T A.) 20 mM Glutamate (voxel dimension: 3 x 3 x 3 mm<sup>3</sup>) B.) 20 mM Glucose (voxel dimension: 3 x 3 x 3 mm<sup>3</sup>) C.) 20 mM Myoinositol (voxel dimension: 3 x 3 x 3 mm<sup>3</sup>) D.) 40 mM Lactate (voxel dimensions: 2 x 2 x 4 mm<sup>3</sup>)

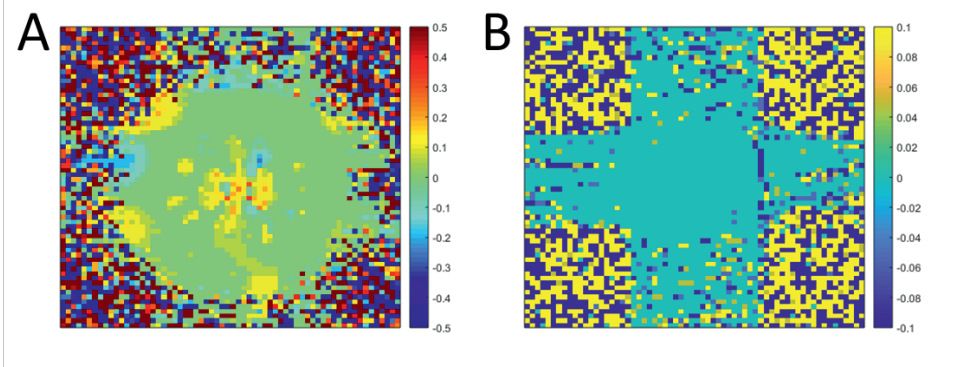




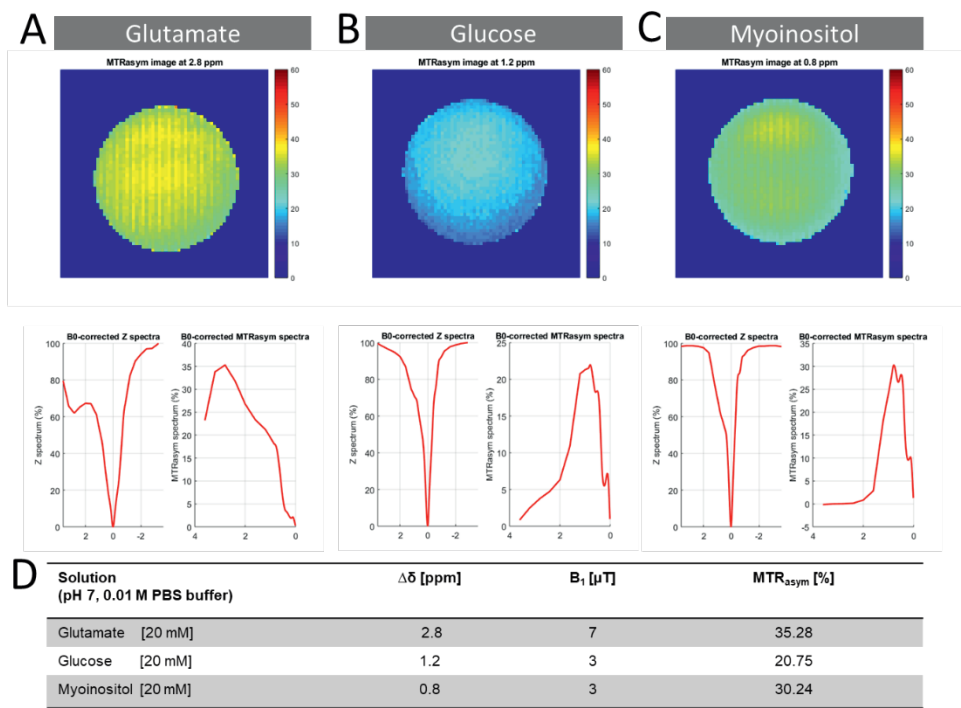
**S 6-4:** Localized spectroscopy (LASER) at 22.3 T (TR 12 s, TE 25 ms, 128 averages,  $t_{\text{acq}}$  25 min and 36 s, excitation chemical shift 3.7 ppm, spectral width 8012 Hz, excitation pulse adiabatic half passage, refocussing pulses hyperbolic secant 4, R=20) indicated the presence of glutamate and carbohydrates (e.g. glucose).



**S 6-5:** WASSR- maps of cherry tomato at 17.2 T (left) and 22.3 T (right). At 17.2 T the  $B_0$ -inhomogeneities are larger than at 22.3 T, however on the 17.2 T an entire cherry tomato has been imaged. The seeds and possible air cavities can contribute to  $B_0$  inhomogeneities. At 22.3 T only a tomato pericarp tissue was excised which was additionally submerged in perfluorodecalin, a compound which dissolves air and thus prevents susceptibility artefacts.



**S 6-6:** Phantoms at 17.2 T were investigated using CEST-RARE experiments on A.) Glutamate, B.) Glucose, and C.) Myoinositol. D.) The table shows the  $MTR_{\text{asym}}$  ratios on pure phantom solutions. Note that B.) Glucose and C.) Myoinositol were acquired with a  $B_1$  value below optimal  $B_1$  field strength as determined in (S 6-2).

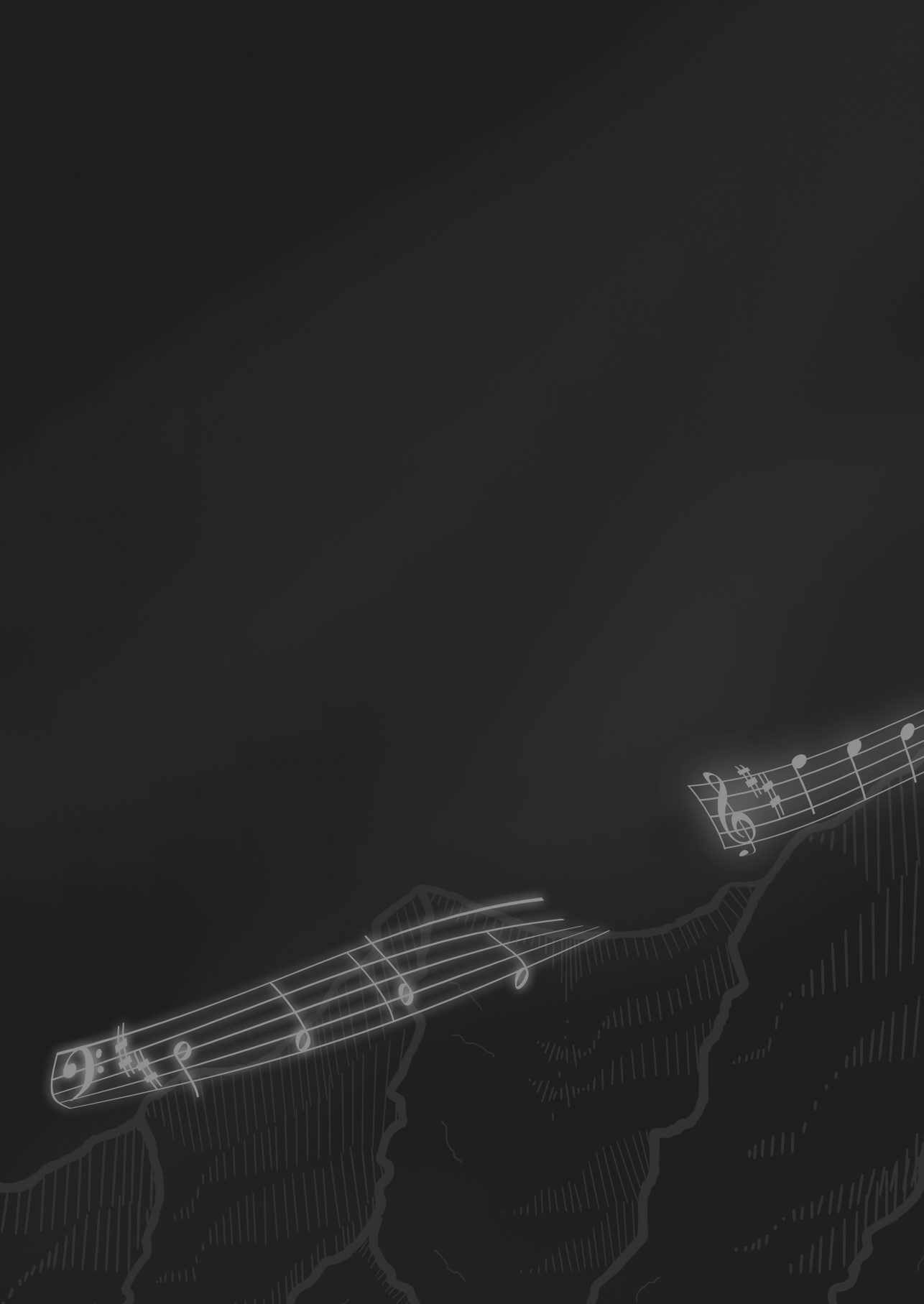


## 6.8 References

1. D. P. Soares, M. Law, Magnetic resonance spectroscopy of the brain: review of metabolites and clinical applications. *Clin. Radiol.* **64**, 12–21 (2009).
2. R. A. De Graaf, *In vivo NMR spectroscopy: principles and techniques* (John Wiley & Sons, 2019).
3. A. Webb, Increasing the sensitivity of magnetic resonance spectroscopy and imaging. *Anal. Chem.* **84**, 9–16 (2012).
4. M. T. McMahon, A. A. Gilad, J. W. M. Bulte, P. C. M. Van Zijl, *Chemical Exchange Saturation Transfer Imaging: Advances and Applications* (CRC Press, 2017).
5. K. Cai, M. Haris, A. Singh, F. Kogan, J. H. Greenberg, H. Hariharan, J. A. Detre, R. Reddy, Magnetic resonance imaging of glutamate. *Nat. Med.* **18**, 302–306 (2012).
6. J. Zhou, P. C. M. Van Zijl, Chemical exchange saturation transfer imaging and spectroscopy. **48**, 109–136 (2006).
7. T. Roussel, L. Frydman, D. Le Bihan, L. Ciobanu, Brain sugar consumption during neuronal activation detected by CEST functional MRI at ultra-high magnetic fields. *Sci. Rep.* **9**, 4423 (2019).
8. P. C. M. van Zijl, N. N. Yadav, Chemical exchange saturation transfer (CEST): What is in a name and what isn't? *Magn. Reson. Med.* **65**, 927–948 (2011).
9. E. Vinogradov, A. D. Sherry, R. E. Lenkinski, CEST: From basic principles to applications, challenges and opportunities. *J. Magn. Reson.* **229**, 155–172 (2013).
10. C. Debrosse, R. Prakash, R. Nanga, P. Bagga, K. Nath, Lactate Chemical Exchange Saturation Transfer (LATEST) Imaging in vivo: A Biomarker for LDH Activity. *Nat. Publ. Gr.*, 1–10 (2016).
11. F. C. Wermter, C. Bock, W. Dreher, Investigating GluCEST and its specificity for pH mapping at low temperatures. *NMR Biomed.* **28**, 1507–1517 (2015).
12. F. A. Nasrallah, G. Pagès, P. W. Kuchel, X. Golay, K. H. Chuang, Imaging brain deoxyglucose uptake and metabolism by glucoCEST MRI. *J. Cereb. Blood Flow Metab.* **33**, 1270–1278 (2013).
13. K. W. Y. Chan, M. T. McMahon, Y. Kato, G. Liu, J. W. M. Bulte, Z. M. Bhujwalla, D. Artemov, P. C. M. Van Zijl, Natural D -Glucose as a Biodegradable MRI Contrast Agent for Detecting Cancer. **1773**, 1764–1773 (2012).
14. M. Haris, A. Singh, K. Cai, K. Nath, R. Crescenzi, F. Kogan, H. Hariharan, R. Reddy, MICEST: A potential tool for non-invasive detection of molecular changes in Alzheimer's disease. *J. Neurosci. Methods.* **212**, 87–93 (2013).
15. M. H. Levitt, *Spin dynamics: basics of nuclear magnetic resonance* (John Wiley & Sons, 2001).
16. V. Guivel-Scharen, T. Sinnwell, S. D. Wolff, R. S. Balaban, Detection of proton chemical exchange between metabolites and water in biological tissues. *J. Magn. Reson.* **133**, 36–45 (1998).
17. P. Z. Sun, J. Lu, Y. Wu, G. Xiao, R. Wu, Evaluation of the dependence of CEST-EPI measurement on repetition time, RF irradiation duty cycle and imaging flip angle for enhanced pH sensitivity. *Phys. Med. Biol.* **58**, N229–N240 (2013).
18. M. T. Vlaardingerbroek, J. A. Boer, *Magnetic resonance imaging: theory and practice* (Springer Science & Business Media, 2013).
19. V. Khlebnikov, W. J. M. van der Kemp, H. Hoogduin, D. W. J. Klomp, J. J. Prompers, Analysis of chemical exchange saturation transfer contributions from brain metabolites to the Z-spectra at various field strengths and pH. *Sci. Rep.* **9**, 1089 (2019).

20. J. N. Davies, R. J. Kempton, Changes in the individual sugars of tomato fruit during ripening. *J. Sci. Food Agric.* **26**, 1103–1110 (1975).
21. A. Sorrequieta, G. Ferraro, S. B. Boggio, E. M. Valle, Free amino acid production during tomato fruit ripening: a focus on L-glutamate. *Amino Acids*. **38**, 1523–1532 (2010).
22. P. Z. Sun, J. Lu, Y. Wu, G. Xiao, R. Wu, Evaluation of the dependence of CEST-EPI measurement on repetition time, RF irradiation duty cycle and imaging flip angle for enhanced pH sensitivity. *Phys. Med. Biol.* **58**, N229–N240 (2013).
23. D. I. Hoult, R. E. Richards, The signal-to-noise ratio of the nuclear magnetic resonance experiment. *J. Magn. Reson.* **24**, 71–85 (1976).
24. J. Kim, Y. Wu, Y. Guo, H. Zheng, P. Z. Sun, A review of optimization and quantification techniques for chemical exchange saturation transfer MRI toward sensitive in vivo imaging. *Contrast Media Mol. Imaging*. **10**, 163–178 (2015).
25. T. Jin, J. Autio, T. Obata, S. Kim, Spin-Locking Versus Chemical Exchange Saturation Transfer MRI for Investigating Chemical Exchange Process Between Water and Labile Metabolite Protons. **1460**, 1448–1460 (2011).
26. J. I. Friedman, M. T. McMahon, J. T. Stivers, P. C. M. Van Zijl, Indirect detection of labile solute proton spectra via the water signal using frequency-labeled exchange (FLEX) transfer. *J. Am. Chem. Soc.* **132**, 1813–1815 (2010).
27. N. N. Yadav, C. K. Jones, J. Xu, A. Bar-Shir, A. A. Gilad, M. T. McMahon, P. C. M. van Zijl, Detection of rapidly exchanging compounds using on-resonance frequency-labeled exchange (FLEX) transfer. *Magn. Reson. Med.* **68**, 1048–1055 (2012).
28. P. C. M. van Zijl, B. A. Landman, M. Kim, J. Gillen, J. Zhou, Water saturation shift referencing (WASSR) for chemical exchange saturation transfer (CEST) experiments. *Magn. Reson. Med.* **61**, 1441–1450 (2009).
29. P. Schuenke, J. Windschuh, V. Roeloffs, M. E. Ladd, P. Bachert, M. Zaiss, Simultaneous mapping of water shift and B1 (WASABI)—application to field-inhomogeneity correction of CEST MRI data. *Magn. Reson. Med.* **77**, 571–580 (2017).





# Chapter 7

## General Discussion





## **Abstract**

In this chapter, the main insights and conclusions from the experimental chapters are summarized. Technical and experimental insights from ultra-high field MRI and MRS are discussed and perspectives for different applications are provided. Finally, perspectives for the ultra-high-field at 22.3 T and beyond are mentioned.

## 7.1 Main Insights and Conclusions

In this thesis, we have investigated the potentials and challenges of ultra-high field MRI and MRS at (ultra-)high magnetic field (UHF) strengths.

In **chapter 2** we systematically analysed how the newly installed (2015-unmr-nl system at Utrecht University) 22.3 T system compared to other NMR-spectrometers, namely a 14.1 T spectrometer and a 17.6 T spectrometer equipped with Micro5-probes for imaging. We found that the volumetric Signal-to-Noise Ratio ( $\text{SNR}_{i,v}$ ) was significantly higher for a 5 mm birdcage coil at the 22.3 T. This led to acquisition times being 24 times accelerated at 22.3 T compared to the 14.1 T. However, we also realised the difference between theoretical and experimentally achievable SNR. This underlines the importance of the entire hardware setup of the MR system and not solely the main magnetic field strength. To this end, a 1.5 mm solenoid coil was fabricated and tested for small specimens (<1 mm in diameter).  $\text{SNR}_{i,v}$  was 5.9 times increased compared to the 5 mm birdcage coil on the same magnetic field strength 22.3 T. Additionally, contrast in FLASH images ( $T_2^*$ ) increased from 14.1 T to 22.3 T.

In **chapter 3**, we have focused on describing a protocol for sample preparation and the use of dedicated coils at UHF, which can also be applied to the same system at lower field strength. At UHF it is especially crucial to avoid air spaces in the sample during sample preparation to increase the image quality, i.e. obtaining artefact-free images. Dedicated equipment can help to increase the  $\text{SNR}_{i,v}$  even further if e.g. the rf-coil is adjusted to the sample geometry. This protocol is the result of how to calibrate a new rf-coil on a microimaging system. As magnetic field homogeneity is of utmost importance for certain applications such as metabolite imaging in (cf. chapter 5 and 6), possible shimming strategies for different applications are listed.

The use of UHF MRI was investigated for a research question related to biofilm visualisation and quantification on activated carbon granules for microbial fuel cells in **chapter 4**. However, susceptibility problems arising from paramagnetic ions were found to be detrimental for imaging. While this problem was solved with protocol optimisation and sample pretreatment for 14.1 T, it remained a problem for frequency-encoded sequences at 22.3 T, resulting in image artefacts which distorted biofilm visualization and impeded quantification. Possible strategies such as pure-phase encoding techniques were suggested.

In **chapter 5**, the application of UHF MRI on plant sciences are discussed. A high-resolution 3D-FLASH with a spatial resolution of  $7 \times 7 \times 7 \mu\text{m}^3$  was recorded on a root nodule of *Medicago truncatula* in an acquisition time of 34 h 24 min. The high spatial resolution allowed to distinguish individual plant cells, while the  $T_2^*$  contrast allowed a distinction of cells filled with bacterioids of *S. meliloti*. While this was achieved with high SNR and good contrast on a vacuum-infiltrated and fixed specimen, images with a reduced SNR and contrast were obtained from a freshly excised root nodule i.e. the root nodule was excised from the intact plant and directly imaged (after a short sample preparation with PFD). Nevertheless, localized spectroscopy results with voxel sizes of  $200 \times 350 \times 350 \mu\text{m}^3$  were obtained on these fresh nodules, which enabled to make a spatial metabolite profile across the relevant nodule zones.

One of the possibilities of ultra-high field is to use the sensitivity for metabolite imaging. In clinical imaging chemical shift saturation transfer (CEST) has been proposed and is explored for different metabolites. However, one of the questions is if ultra-high field CEST imaging can, next to the increase in SNR, also contribute through an additional aspect, namely the increased spectral resolution. In **chapter 6**, we compared the CEST spectra across a wide variety of systems and concluded that the increased spectral resolution indeed results in a better selectivity towards metabolites. Selectivity still remains a challenge, as even at 22.3 T the metabolite of interest cannot be disentangled completely.

In the remainder of this chapter, we will discuss the lessons we can take from ultra-high field strength from the hardware and experimental point-of-view. Perspectives of ultra-high field MRI and MRS in different research fields are discussed, and we conclude with a perspective for future state-of-the-art ultra-high field strength of 28 T.

## 7.2 Lessons from Ultra-high Magnetic Field Strengths

Increasing the magnetic field strengths does not only extrapolate SNR-values and expected image quality. As an example of field extrapolation, the transition of clinical MRI from 3 T to 7 T-systems was a big step and problems, particular in  $B_1$ -field homogeneity, are still essential considerations in clinical imaging today. Here, we want to discuss lessons and critical points from ultra-high field MR Microscopy and Spectroscopy, namely the need for strong gradients, dedicated radiofrequency coils, susceptibility effects, chemical shift differences, other means to increase SNR and sequence optimisation.

### 7.2.1 Dilemma of Gradient Strengths

At the start of the field of MRI Microscopy, SNR was clearly the main factor for limiting achievable spatial resolutions with the highest resolutions achieved being  $10 \times 10 \times 100 \mu\text{m}^3$  in 1990 (1). This limit explains the need for higher magnetic field strengths. However, the higher we go in spatial resolutions, the more we are limited by other factors such as  $T_2$  and diffusion limits(1–3). These factors can typically be overcome by a stronger gradient, which are not ubiquitously available and might limit the available sample space. Developments in stronger tri-axial gradients might be needed when the SNR has improved, and the actual resolution becomes limited by the gradient strength. We have shown in **chapter 2** that we can reach a nominal resolution of  $(5.5 \mu\text{m})^3$  on a phantom with poly-methylmethacrylate beads of  $40 \mu\text{m}$  in diameter. This spatial resolution is close to the limit of achievable resolution for the maximum gradient field strength of 3 T/m of the Micro5-probe used, which is around  $4 \mu\text{m}$  (4). For the phase encoding direction, the limit is slightly lower. However, to reach the current benchmark resolutions even at UHF, stronger gradient field strengths are needed as have been used to achieve the resolution records as listed in Table 7-1. These researchers made use of dedicated radiofrequency coils as well as dedicated gradient hardware to reach the benchmark resolutions.

**Table 7-1:** Comparison of spatial resolutions obtained in literature on phantom samples

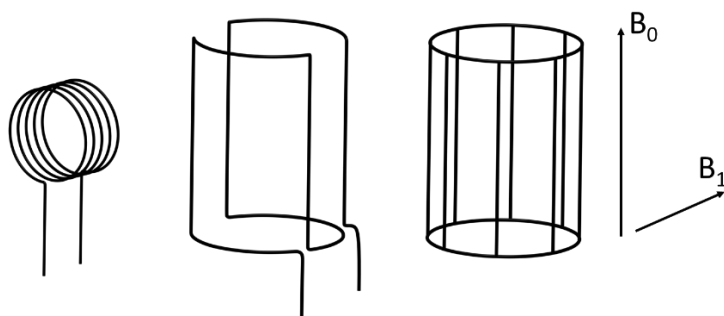
Reference	Coil type/ diameter	B <sub>0</sub> [T]	G <sub>max</sub> [T/m]	Field-of-View [μm <sup>3</sup> ]	Spatial Resolution [μm <sup>3</sup> ]	Acquisition Time/ Number of averages
Ciobanu <i>et al.</i> (5)	Solenoid 74 μm	9	1.6 5.8 5.7	237 x 66 x 66	3.7 x 3.3 x 3.3	30 h
Weiger <i>et al.</i> (6)	Planar 20 μm	18.8	65	384 x 384 x 192	3 x 3 x 3	59 h
Lee <i>et al.</i> (7) <sup>1</sup>	Solenoid 500 μm	14.1	13.5 11.2 12.3	500 x 500 x 75	1 x 1 x 75	56 min
Lee <i>et al.</i> (8)	Solenoid ~820 μm	14.1	13.5 11.2 12.3	500 x 500 x 75	1 x 2 x 75	32 h
Moore and Tycko (9)	Solenoid 170 μm	9.38	4	160 x 160 x 160	5 x 5 x 5	150 h
Chen and Tycko (10)	Solenoid 150 μm (ID) T= 28 K	9.38	G <sub>max</sub> used ~ 6.3	218 x 95 x 95	2.8 x 2.8 x 2.8	53 h
Chapter 2	Solenoid 1500 μm	22.3	3	1575 x 1050 x 1050	5.5 x 5.5 x 5.5	58 h

Not only the spatial resolution limit can be increased by higher gradient field strength. Chemical shift displacement and susceptibility artefacts in the slice direction and frequency encoding direction can be mitigated by stronger gradient or larger receiver bandwidth, which in turn reduces the SNR.

<sup>1</sup> The difference between the work of Lee *et al.*, 2001 (7) and Lee *et al.*, 2009 (8) lies in the object sizes being 13 μm and 3-6 μm respectively.

### 7.2.2. Dedicated Radiofrequency Coils

It is well-known that adapting the size and geometry of the radiofrequency (RF) coil to a sample gives improvement in terms of filling factor, especially for mass-limited samples in NMR spectroscopy (11–13). While in NMR spectroscopy the SNR of the entire sample contributes to the signal amplitude in the spectrum, in MRI the SNR per unit volume is measured and decreasing the coil diameter leads to an increase of SNR per unit volume proportional to  $\frac{1}{d_{coil}}$  and  $\frac{1}{\sqrt{d_{coil}}}$  for solenoidal coils (14). Additionally, when possible to adjust the rf-geometry, the solenoidal geometry (Figure 7-1A) is 3 times more sensitive compared to the saddle or birdcage geometry (15) (see Figure 7-1B for saddle geometry and Figure 7-1C for birdcage geometry). Next to sensitivity,  $B_1$ -homogeneity of detector coils in transmission mode in the region of interest is crucial for most MR experiments.



**Figure 7-1:** Scheme of the different coil geometries used in this thesis, i.e. a solenoid (left), saddle (middle) and birdcage coil (right scheme). The directions of the main magnetic field  $B_0$  and the excitation field  $B_1$  are indicated (modified based on reference (16)).

Next to efforts to maximising the SNR, the ease of sample handling and suitability for the experimental workflow are important aspects when choosing the coil design. The solenoid design and orientation requires the removal of the probe for exchanging the sample. This step is time-consuming and should be considered when designing the coil insert for a specific type of specimen or applications. Coil designs where the sample can be loaded from the top by the airlift, have an advantage for a higher throughput of samples. This should be especially taken into account when the gain in MRI acquisition time (by SNR increase) for the desired experiment is in the same order as the probe exchange time, or if the experiment has to be conducted very fast after the sample

preparation due to changes in the specimen. Additionally, the horizontal orientation of the sample in a solenoid coil can cause the sample to move along the sample capillary during the measurement. To this end, the sample needs to be stationary in its position which could not be ensured for example in **chapter 4** as the fixing into a stable position might have damaged the biofilm on the activated carbon granule.

### 7.2.3 Susceptibility Effects

Susceptibility differences can be detrimental to image quality at ultra-high field MRI. These susceptibility differences can manifest as artefacts in the MR image and are often caused by paramagnetic ions or air spaces can cause severe image artefacts. Pure phase encoding sequences e.g. single point imaging (SPI) have been proposed for samples with susceptibility effects in frequency encoding sequences. These sequences often come at the expense of longer measurement times and should be combined with an accelerated acquisition scheme as proposed in (17, 18). Additionally, it is important during sample preparation to avoid the inclusion of large air cavities in the sample whenever possible.

Susceptibility effects related to the difference in susceptibility between coil material (e.g. copper wire) and surrounding air can cause additional artefacts close to the edge of the sample. This can be mitigated by either submerging the coil in a susceptibility matching reservoir (**Chapter 3**) or using zero-susceptibility wire (19).

Next to causing artefacts, susceptibility differences within a sample offer a method to increase contrast at ultra-high field. In chapter 2, we could observe a stronger  $T_2^*$ -contrast by the cell walls of a lily root at 22.3 T compared to 14.1 T. MRI of air spaces can be useful as a measure to quantify the microporosity in fruits and vegetables (20). Additionally, there are developments to use superparamagnetic nanoparticles (SPIO) as a contrast agent (21). SPIO's will have a strong effect on the contrast at ultra-high field due to the proportionality of magnetic field variations caused by susceptibility differences with main magnetic field strength  $B_0$  (22, 23). In MR Microscopy, SPIO's were proposed for use in an *in vitro* MR assay (24).

### 7.2.4 Chemical Shift Displacement

For metabolite imaging, several options are possible for ultra-high field MRS, namely single-voxel or multivoxel techniques with different selection approaches. Using single-

voxel localized spectroscopy at ultra-high field can be a powerful tool since lower concentrations are detectable compared to lower field strengths due to the SNR-increase. A disadvantage, however, is the high chemical shift displacement of the compounds within a localized spectroscopy spectrum due to the higher chemical shift dispersion at ultrahigh field. This can be seen in cf. **chapter 5** (Figure 5-3a) by the displacement of the voxel of the metabolite betaine with respect to the voxel at the center resonance frequency. To this end, the pulse bandwidth or gradient strengths can be increased or the working frequency offset can be chosen to match the compound of interest if there is one specific metabolite of interest. For multivoxel spectroscopic imaging techniques such as chemical shift selective imaging (nowadays referred to as CSSI, originally published as CHESS (25)) both the SNR-increase and the larger chemical shift dispersion at ultra-high field are beneficial but  $B_0$  homogeneity can be critical for a uniform excitation of the correct chemical shift.

### 7.2.5 Comparison between Different MR Systems

For comparing different MR-systems in **chapter 2**, phantoms were chosen carefully but it remains difficult to choose optimal phantoms. A standard sample used to compare coil performance is 20 % (v/v)  $H_2O$ , 80% (v/v)  $D_2O$  and 6.3 mM  $CuSO_4$ . The  $CuSO_4$  is added as it shortens the  $T_1$  and  $T_2$ -relaxation times of the solution and allows faster scanning (22). For the image comparison, we chose a fixed plant material, as fixed material does not significantly change its internal structure between the measurements at different spectrometers. In this research, we have chosen to compare images with identical parameters while they do not necessarily have the same contrast. Also, the compared spectrometers had similar hardware components i.e. 5 mm RF coils which made a comparison based on the same MR-parameters feasible. In case it would be desired to compare RF coils which are significantly different in diameter, the volume-normalized  $SNR_{i,v}$  has to be normalised additionally to the number of data acquisition points  $k$  (i.e. the matrix which is sampled) to yield  $SNR_{i,v,k=1}$  as differences in matrix size also contribute to a difference in  $SNR_{i,v}$  (26). Likewise, differences in receiver bandwidth and other MR parameters such as echo time, repetition time, number of averages have to be accounted for when comparing the  $SNR_{i,v}$  of different sequences(26).



### 7.2.6 Sequence Optimisation

For UHF MRI sequences, it is advantageous to optimise the sequences for minimal echo time, as the  $T_2$ -relaxation time shortens with increasing field strengths. Depending on the hardware, excitation and refocusing pulse bandwidths and gradient strengths can be increased, to shorten the echo time considerably. Additionally as mentioned in section 7.3.2, the pulse bandwidth can be increased in spatially resolved spectroscopy sequences to reduce the chemical shift displacement.

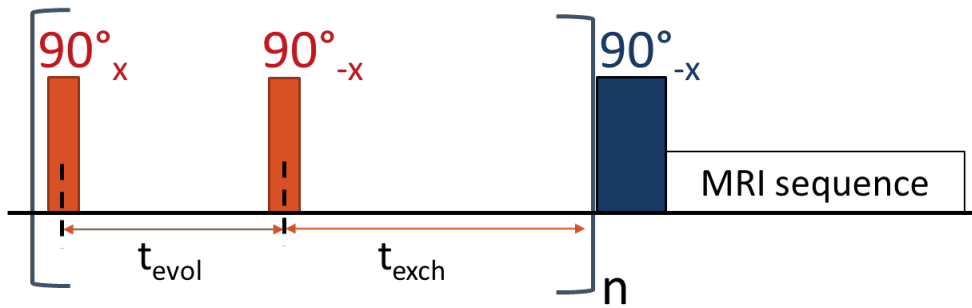
### 7.2.7 SNR-increase for Metabolite Imaging by Chemical Exchange

Using chemical exchange saturation transfer (CEST), the Boltzmann equilibrium remains undisturbed. Instead, the excess presence of water protons and the exchange of protons from metabolites with the water protons is used to increase the SNR of the metabolites. As shown in this thesis, this method can be used to enhance the SNR for metabolite imaging. While the specificity towards certain metabolites increases with magnetic field strengths, it remains necessary to increase the specificity even further, as discussed in **chapter 6**.

CEST imaging has been investigated at ultra-high field (**Chapter 6**). For this method, the higher chemical shift dispersion at ultra-high field strengths is beneficial, as the saturation offset of the exchangeable metabolite can be excited more selective. However, even at state-of-the-art UHF of 22.3 T, it is not possible to entirely disentangle the metabolite contributions and other methods might be possible.

To increase the selectivity towards the desired metabolite, Frequency Labeled EXchange (FLEX) transfer seems to be a promising option, as specificity is increased while retaining the advantage of CEST of increasing the SNR for metabolite detection by exchange of the metabolite protons with water protons. For off-resonance FLEX, a  $90^\circ$  pulse is applied with a pulse bandwidth to reach all chemical shift offsets of the exchangeable metabolite protons except the water resonance (Figure 7-2) (27, 28). During the evolution time  $t_{\text{evol}}$  the magnetisation can evolve due to the chemical shift and is flipped at the end of  $t_{\text{evol}}$  with a  $90^\circ$  pulse along the -x-axis. During the exchange period  $t_{\text{exch}}$  the metabolite protons can exchange with water protons. This FLEX-module is repeated n-times in order to use the excess of the water protons with respect to the metabolite protons to enhance the SNR of the signal, similar to the CEST-module. Subsequently,  $t_{\text{evol}}$  varied during the next repetition of the experiment to obtain

the next point with a different chemical shift evolution. With this method, a free induction decay (FID) is obtained, which can be fourier-transformed to yield a spectrum. Using FLEX, several metabolites can be detected during one complete FLEX experiment. However, a FLEX-experiment comes at the expense of elongated measurement times, as FLEX experiment requires a number of repetitions (e.g. 16 or 32) with different  $t_{\text{evol}}$  periods in order to construct FID signal with enough data points for a fourier-transformation. The minimal number of repetitions for CEST-MRI with MTR<sub>asym</sub> analysis is 3, due to the three different saturation offsets ( $-\Delta\omega$ ;  $\Delta\omega$  and  $\sim -40$  ppm).



**Figure 7-2:** Scheme of FLEX pulse sequence (27). A  $90^\circ_x$  pulse selectively excites the exchangeable metabolite protons which have a magnetization  $M_0$ , which are given  $t_{\text{evol}}$  to evolve due to the chemical shift offset. After the time period  $t_{\text{evol}}$ , a second  $90^\circ_{-x}$  pulse selectively flips back the y component of the magnetization  $M_0 \cdot \cos(\omega t_{\text{evol}})$ . Subsequently, during  $t_{\text{exch}}$  the metabolite protons can exchange with water protons, transferring the reduction in magnetization to the water peak. Any MRI or spatially-resolved sequence can be used to spatially resolve the water proton information. The sequence is repeated with different steps of  $t_{\text{evol}}$ .

### 7.2.8 Other Methods to Enhance SNR

In this thesis, we investigated the SNR- increase due to an increase in main magnetic field strengths  $B_0$ , and to a certain extent SNR-increase to an increase in detector sensitivity. Additional possibilities to increase the SNR of an MR experiment include reducing the random thermal noise or hyperpolarisation techniques.

The random thermal noise can be reduced by cryoprobe systems, where the coil is cooled to the temperature of liquid helium. The advantage of a cryoprobe is that the thermal noise in the rf-coil is reduced leading to higher SNR-values by a factor 2.5 (29)

at the same magnetic field strengths. The same 3D-RARE experiment as used in section 4.3.1 could have been acquired a factor 6 accelerated at the same magnetic field strength of 14.1 T. Furthermore, an MRI cryoprobe at lower field strength could have been chosen for the experiments in **chapter 4**. This strategy would use the fact that susceptibility effects are less pronounced at lower field strengths as it is proportional to the field strength. The practical reason for which a cryoprobe was not used here is that no MRI cryoprobe was available at the Magnetic Resonance Facility in Wageningen.

Hyperpolarisation techniques such as dynamic nuclear polarisation (DNP)(30), signal amplification by reversible exchange (SABRE) (31) and photo-chemical induced dynamic nuclear polarisation (photoCIDNP) (32) are currently under development towards MRI for signal enhancement. For DNP, a compound (e.g.  $^{13}\text{C}$ -pyruvate) is hyperpolarised and subsequently injected into a specimen to see an enhanced contrast due to the presence of the hyperpolarised compound in a specific part of the specimen. SABRE is readily used to hyperpolarise several metabolites for analytical applications (31, 33) and currently biocompatible catalysts are tested as next step towards its use in *in vivo* MRI (34). PhotoCIDNP for MRI is a hyperpolarisation method which can enhance  $^{19}\text{F}$  NMR signals (32). In contrast to the previously discussed factors  $B_0$  and detector sensitivity for SNR-increase, these hyperpolarisation approaches do not uniformly enhance the SNR of all spins present in the specimen or proximity to the radiofrequency coil, but enhance the SNR of a selected chemical compound of which the fate can be detected by the increased SNR with respect to the surrounding tissue.

### 7.3. Perspectives for Applications

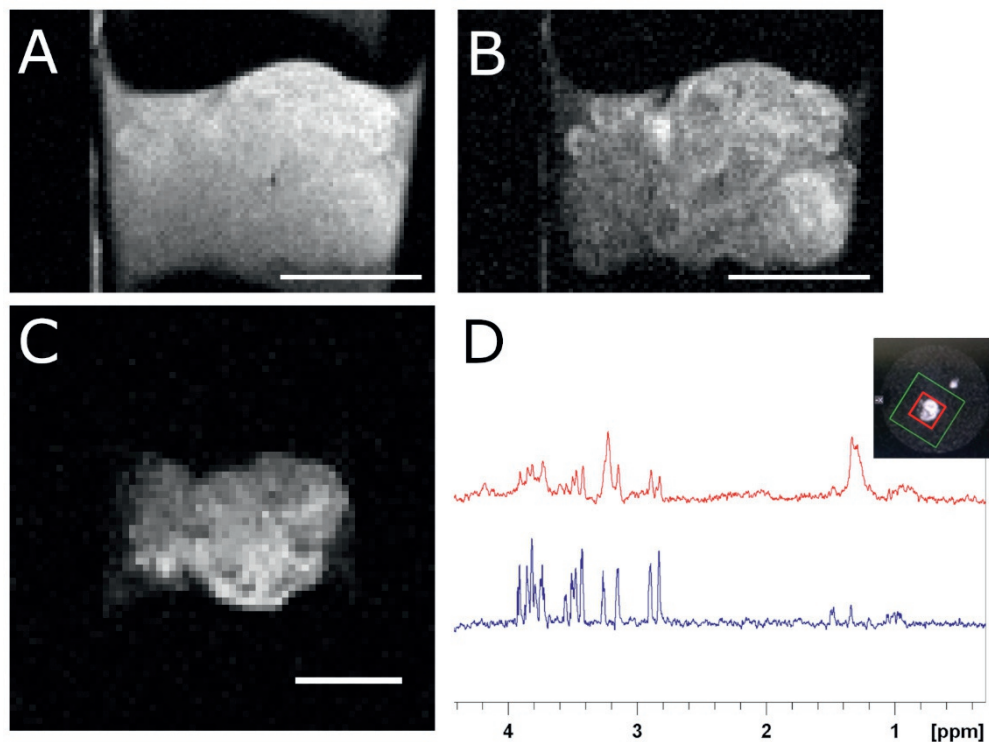
This thesis shows a limited amount of applications. Within the project which led to this thesis, however, we have investigated the feasibility for different applications. This short outlook lists ultra-high field MRI and MRS applications for future research in clinical research (Section 7.3.1), environmental sciences and wastewater treatment (Section 7.3.2), and plant sciences (Section 7.3.3).

#### 7.3.1. Clinical Research Applications

While non-invasive clinical whole-body MRI might not be desirable with the wavelength limitations, ultra-high field MRI can contribute to clinical research by solving different questions on organoids or tissue biopsies and thereby complement other methods in clinical research questions

##### 7.3.1.1. Brain Organoids

In neuroscience research and clinical research, there are still unsolved problems around the mechanism of diseases, such as e.g. spinocerebellar ataxia (35). Human brain organoids in this context are promising to study the pathogenesis (36). Ultra-high field MRI allows to non-invasively study these brain organoids in terms of diffusion, structure and metabolites. The ultra-high field strength of 22.3 T provides us with the sensitivity needed to perform these experiments at the relevant spatial and temporal resolution while the gradient strength might allow in the future to separate components over slower diffusion time scales. One of the challenges at 22 T is to create a contrast between water and the brain organoids (Figure 7-3A). T<sub>2</sub>-weighting provided contrast between the tissue water and surrounding free water (Figure 7-3B), but diffusion-weighting (Figure 7-3C) was the method of choice, as the magnetisation of the free water protons surrounding the brain organoids was dephased. Metabolite analysis using single-voxel MRS provide additional information on the metabolites which are detectable (Figure 7-3D). The primary metabolites which could be detected were choline and lactate. Further studies are in progress to determine and quantify the metabolites within the brain organoids. The main challenge in this application for metabolite imaging will be to keep the organoids under *in situ* conditions with a constant gas flow and shaking especially if a longitudinal study is desired.



**Figure 7-3:** A.) MRI experiments of a 2D plane through a brain organoid in a droplet of water in perfluorodecalin without contrast preparation (echo time 3.3 ms) and B.) with T<sub>2</sub>-weighting at an echo time of 16.4 ms (Acquired with a spin-echo sequence TR 5 s; TE 3.3 ms; number of echoes 12; FOV 3 x 2 mm; matrix size 96 x 64; rBW 100 kHz, slice thickness 0.062 mm; 64 averages, 10 slices;  $t_{acq}$  5 h 41 min) C.) with a small diffusion-weighting step (acquired with a spin-echo sequence with a small diffusion step  $b_{eff} = 947$  s/mm<sup>2</sup>; TR 5 s; TE 11.3 ms, FOV 4 x 4 mm; MX 64 x 64; rBW 50 kHz, slice thickness 0.1 mm; 4 averages, 10 slices,  $t_{acq}$  21 min). Depicted scale bars in A-C indicate 1 mm. D.) PRESS-spectrum (TR 10 s; TE 9 s;  $t_{acq}$  10 min 40 s; voxel dimensions 1 x 1 x 0.8 mm<sup>3</sup>, 64 averages) of voxel on brain organoid (red) and voxel on medium (blue). The inset shows the screenshot with in red marked the voxel location on the brain organoid (Unpublished results by Krug, Van As, Velders, Buijsen, van Roon-Mom, Webb, Ronen).

### 7.3.1.2 *Ex Vivo* Tissues and Biopsies

Ultra-high field can give access to information on diffusion, metabolites and structural information at a lower detection limit, but at the same time it is limited to small sample

sizes of 5 mm - 10 mm (in future potentially 25 mm if wide-bore ultra-high field systems become available). UHF might also be useful for tissue biopsies or *ex vivo* MRI. Next to the increased SNR to explore different modalities, it can be used to investigate the *ex vivo* samples (e.g. biopsies) at a higher spatial resolution than on clinical scanners. Lymph nodes have previously been investigated with high field (14.1 T) MRI to correlate the effect of superparamagnetic iron nanoparticles with photoacoustic imaging (37).

### 7.3.2 Environmental Technology and Wastewater Treatment

We investigated applications in environmental technology and wastewater treatment, namely using wastewater as a resource to produce electricity (Section 7.3.2.1) and anaerobic granules for the production of volatile fatty acids as a starting material for bioplastics (Section 7.3.2.2). Specifically, we investigated the potential of MRI and MRS to answer research questions with respect to biomass structure and chemical compounds, which benefit from using a non-invasive technique.

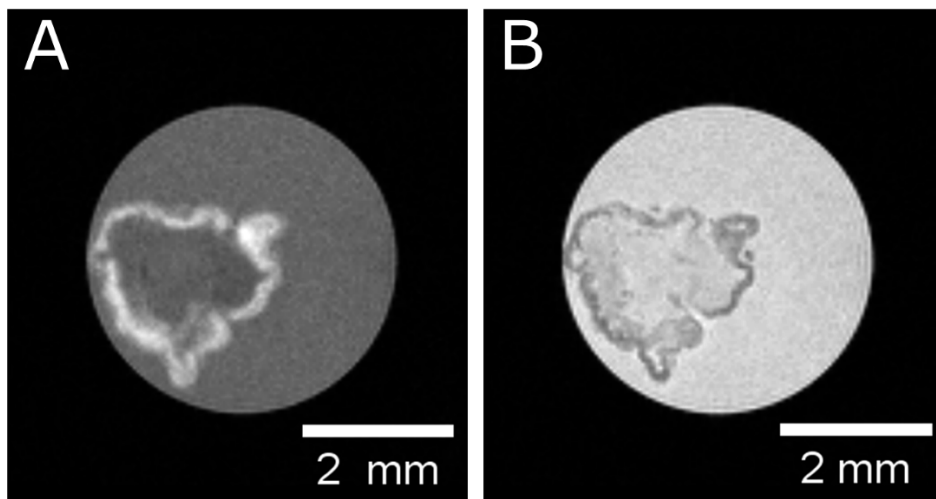
#### 7.3.2.1 Biofilm in Microbial Fuel Cells

**Chapter 4** shows an example of a biofilm grown on an activated carbon granule. This is one example of an application but could not be extended to ultra-high field due to the susceptibility artefacts arising from the paramagnetic ions in the activated carbon electrode. However, for a wider range of biofilms, ultra-high field MRI offers opportunities for high-resolution 3D structural information, transport phenomena and metabolite information. Beneficial for biofilm applications at ultra-high field will be that the materials are not causing image artefacts such as air bubbles or paramagnetic ions. In a large number of applications (38) the biofilm is either not attached to a support or the support is not paramagnetic, so ultra-high field MRI provides an excellent technique. In future, spatially-resolved spectroscopy could be attempted for thicker biofilms if the concentrations in combination with the achievable volume sizes can be detected. This might require a customised reactor setup such as has been developed for flat biofilms (39) to keep the biofilm viable during longer acquisition times.

#### 7.3.2.2 Volatile-fatty Acid Producing Bacteria

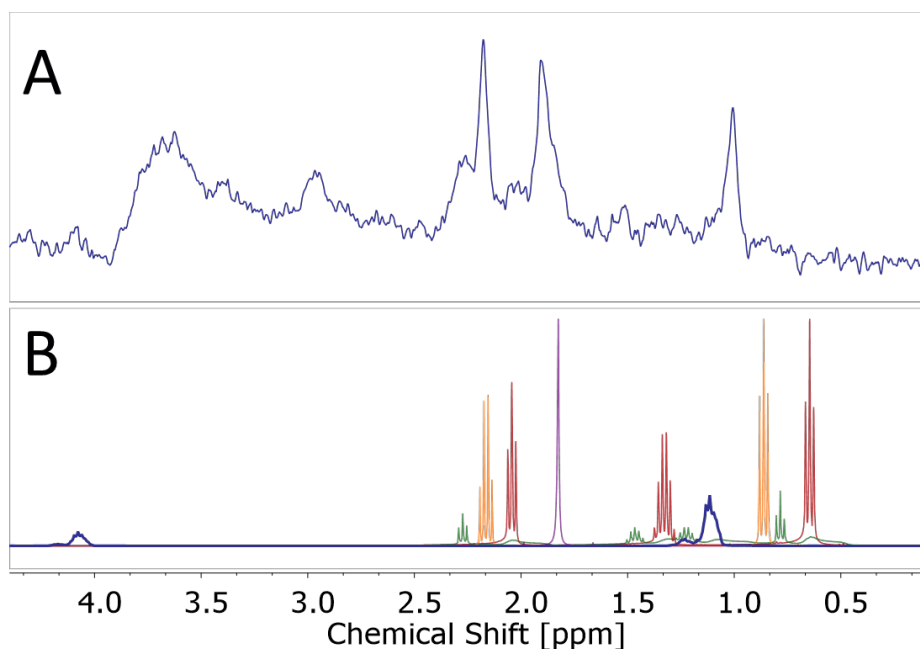
Granular sludge from a lab-scale reactor producing volatile fatty acid were tested initially as a control when investigating the aerobic granular sludge granules. Opposite to prior assumptions, the core of the granules seemed to be hollow or contain biomass density

as seen in both  $T_1$ -contrast images (Figure 7-4A) and  $T_2$ -contrast images (Figure 7-4B). As it was previously assumed that the lab granules were homogeneous in biomass density, this finding suggested implications for different metabolic activity in different depths of the granule.



**Figure 7-4:** 2D-MRI images of VFA-granules at 22.3 T A.) with  $T_1$ -weighted contrast (MSME; TR 5 s; TE 5.3 ms; FOV 6 x 6 mm<sup>2</sup>; MX 128 x 128;  $t_{acq}$  9 min 23 s; rBW 50 kHz ), B.) with  $T_2$ -weighted contrast (MSME; TR 5s; TE 5.3 ms; FOV 6 x 6 mm<sup>2</sup>; MX 128 x 128;  $t_{acq}$  10 min 40 s; rBW 50 kHz) (Unpublished results by Krug, Hendriks, Kirkland, Vergeldt, Toja Ortega, Kreuk, Velders and Van As).

To investigate whether spatially resolved spectroscopy would be feasible to detect and potentially quantify the gradient of VFA's within the biomass, we used Point Resolved Spectroscopy (PRESS) at ultra-high field strength of 22.3 T (Figure 7-5A). While chemical shifts in the lipid region, most likely corresponding to acetate and propionate, could be detected in a volume of (300  $\mu$ m)<sup>3</sup>, the spatial resolution was not high enough to detect metabolites in the biomass. Additionally, the granule size in the bioreactor decreased over the course of this project, which made attempts to detect metabolites along a gradient in an irregular-shaped 3D structure unfeasible. In future, to distinguish metabolites between the medium and the biomass, within a chosen volume, localised diffusion-weighted spectroscopy could be used. The metabolites in bacteria and medium can most likely be distinguished by their difference in diffusion constant.

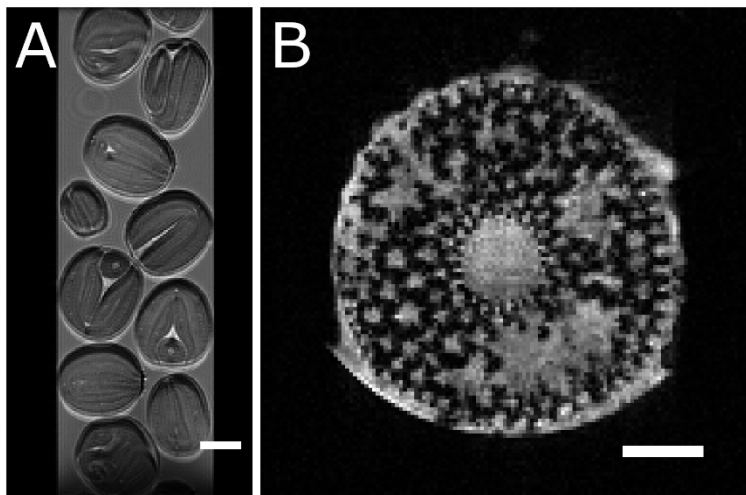


**Figure 7-5:** A.) Localized spectrum of a voxel on a VFA granule (PRESS, Voxel dimensions  $(0.3 \text{ mm})^3$ , TR 1 s, TE 15.2 ms, NA 4096,  $t_{\text{acq}}$  1 h 8 min,  $B_0$  22.3 T; RF-coil 1.5 mm solenoid) B.) Reference NMR-spectra of expected VFA-compound present in VFA granules: namely lactic acid (blue), acetic acid (purple), propionic acid (orange), valeric acid (green), butyric acid (red) ( $\omega(^1\text{H})$  400 MHz, compounds dissolved in  $\text{H}_2\text{O}$ ) (Unpublished results by Krug, Hendriks, Kirkland, Vergeldt, Toja Ortega, Kreuk, Velders and Van As).



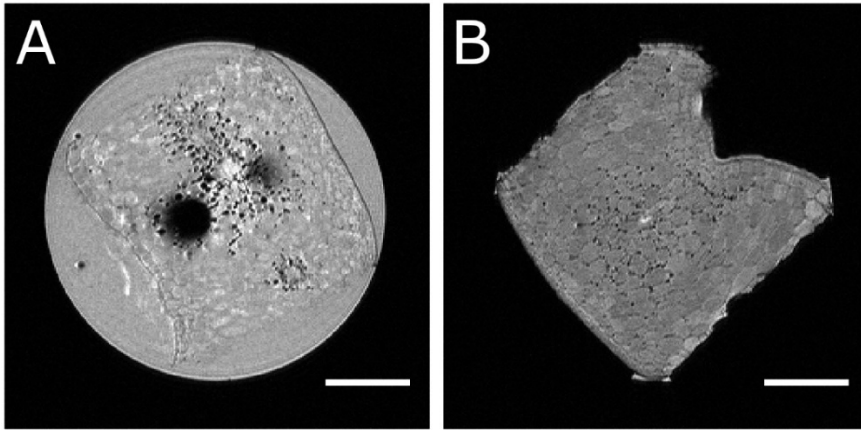
### 7.3.3 Plant Sciences

Ultra-high field MRI can offer both high-resolution images and spatially resolved metabolite information of plant specimens, such as plant seeds and roots (Figure 7-6).



**Figure 7-6:** Examples of MRI of plant specimen at 22.3 T A.) A plane of a 3D-MSME experiment of cabbage seeds in water is shown (*Brassica rapa*, type “Optiko”) in a 5 mm RF coil (TR 2 s, TE 2.4 ms,  $t_{\text{acq}}$  36 h 24 min, FOV 12 x 6 x 6 mm<sup>3</sup>, MX 256 x 128 x 128, rBW 200 kHz). Magnitude data is presented here and the scale bar indicates 1 mm. B.) A 2D-FLASH of Alfafa submerged in PFD in a 1.5 mm solenoid coil at 22.3 T (TR 130 ms, TE 2.6 ms,  $t_{\text{acq}}$  2h 21 min, NA 512, FA 30°, FOV 1.2 x 1.2 mm<sup>2</sup>, ST 0.1 mm, MX 128 x 128, rBW 50 kHz). Magnitude data is presented here and the scale bar indicates 200  $\mu\text{m}$ .

Additionally, we have shown on root nodules that metabolites in different zones of a root nodule can be detected and that we can obtain high-resolution 3D images (7 x 7 x 7  $\mu\text{m}^3$ ) on fixated root nodules (40). Main challenges for ultra-high field non-invasive MRI and spatially-resolved spectroscopy on plants are specifically related to air spaces inside plant tissue. During the fixation step, a vacuum treatment is included to infiltrate the tissue with the fixation liquid. This, however, also extracts the air spaces, which is convenient for MRI. In contrast to anatomical imaging by MRI, this fixation step is not useful for spatially-resolved spectroscopy, as it most likely alters metabolite concentrations. For this *in situ* measurements were performed as the next step where the root was excised to fit in the solenoid coil but was not fixated by the fixative.



**Figure 7-7:** 2D images of excised pericarp tissue of a tomato in A.) H<sub>2</sub>O and B.) PFD. A RARE-experiment with the following parameters was recorded ((TR 3 s, TE 8.0 ms, rarefact 4,  $t_{acq}$  3 h 25 min, FOV 5 x 5 mm<sup>2</sup>, MX 256 x 256, 3 slices, NA 64, rBW 50 kHz). Magnitude data is presented here and the scalebar indicates 1 mm.

The difficulty with *in situ* measurements without vacuum treatment are air spaces present in the tissue as can be seen when an excised tomato pericarp tissue is imaged in H<sub>2</sub>O (Figure 7-7A). In the middle of the slice the black circle is the effect of an air bubble causing a distortion in the image due to susceptibility mismatches between air and water as discussed in section 7.2.2. This can be solved for *in situ* samples by using perfluorodecaline as immersion liquid (as discussed in **Chapter 3**). No susceptibility effects are seen in the tomato pericarp tissue which is immersed in PFD (Figure 7-7B). PFD has the ability to fill up the extracellular air spaces by dissolving the air which reduces the susceptibility effects.

Finally, ultra-high field MRI might be useful for *in vivo* imaging in plants as complete non-invasive imaging and spectroscopy of biological specimen are usually given the preference. MRI offers this unique advantage compared to other techniques, so either appropriate acquisition methods or sample preparation protocol have to be developed to optimally accommodate for plant specimen. Pure phase encoding techniques could be used for susceptibility-free imaging (41). To this end, a system should be implemented which can supply the plant with light, fresh water and potentially nutrients. Previously, this has been done on e.g. tomato plants on a 0.72 T (42) and a 3 T MRI-system (43) at Wageningen University. The limited space of the 22.3 T poses additional

challenges which would be needed to overcome by e.g. microfluidic systems and suitable sized whole plants or plant organs (i.e. *Arabidopsis* or roots of *Medicago Truncatula*).

## 7.4 Perspectives for 22.3 T and Beyond

One crucial lesson from the 22.3 T UHF MRI was that the optimal result can be achieved when the coil is designed for a specific sample configuration (44) and all coil parameters including susceptibility matching are be considered (40).

Increased time resolution can be very useful for longitudinal studies, if it is ensured that the specimen is viable over the study period and the process (i.e. structural changes or metabolite changes) can be followed within the temporal resolution as given by the total acquisition time of the experiments. To this end, appropriate systems for e.g. perfusion with biofilms or light and water supply for plants should be designed and tested. Due to the limited space, microfluidic applications could be investigated.

The higher the  $B_0$ -field, the shorter the  $T_2$ -relaxation time of water protons becomes while the  $T_1$ -relaxation time increases (45). One might think that a shorter  $T_2$  relaxation time could be advantageous for achieving higher contrast, but as an additional factor  $T_2$  converges at the resolutions which are used at ultra-high field imaging (46). To mitigate the effect of signal loss due to decreasing  $T_2$  relaxation times, pulse sequence optimization can be employed to shorten the effective echo time during image acquisition.

The research project shown in this thesis has focused on the  $^1\text{H}$ -nucleus which is the most sensitive nucleus due to the high gyromagnetic ratio  $\gamma$ . However, ultra-high field also holds advantages for X-nuclei such as  $^2\text{H}$ ,  $^{13}\text{C}$ ,  $^{23}\text{Na}$  and  $^{31}\text{P}$ , which are less sensitive than  $^1\text{H}$  due to their lower gyromagnetic ratio  $\gamma$ , as SNR is proportional to  $\gamma^3$  (47). At ultra-high field the SNR-increase can also be used for spatially resolving these X-nuclei at higher spatial resolutions compared to lower field strengths. Hardware requirements are a dual coil or double-tuned coil, which depending on the circuit and the desired experiment, allow either the switching between  $^1\text{H}$  and X-channel or the simultaneous excitation of both nuclei.

While ultra-high field already proved to be useful for a number of applications, we conclude that the possibilities for applications can be further exploited if this state-of-the-art ultra-high magnetic field system is combined with strong gradient strengths,

optimized detector coils, sequence optimization and implementing novel sequences and methods. Additionally, several biological applications would profit from a customized support to maintain the specimen under study viable.

## 7.5 References

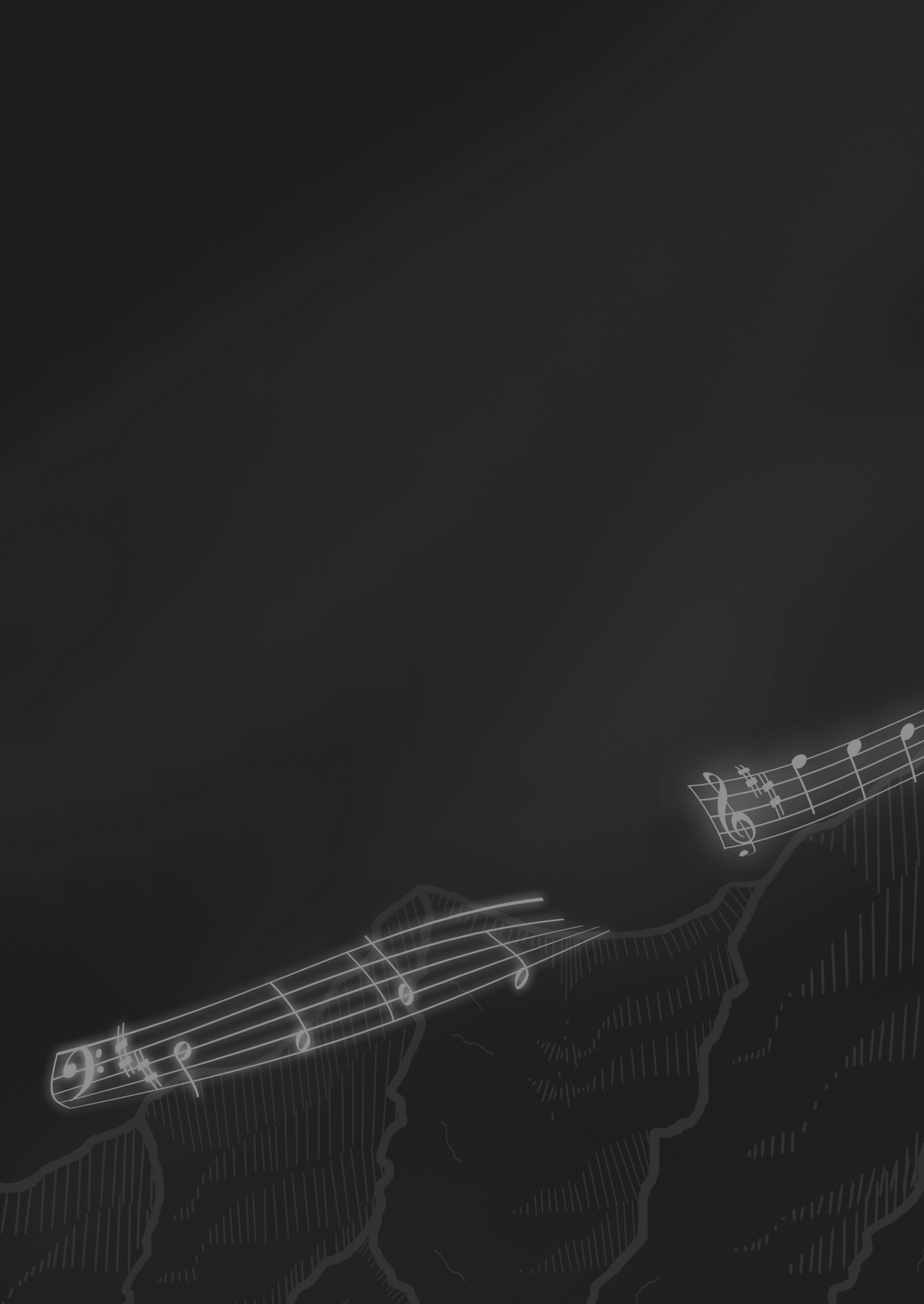
1. W. Kuhn, NMR Microscopy—Fundamentals, Limits and Possible Applications. *Angew. Chemie Int. Ed.* **29**, 1–19 (1990).
2. P. T. Callaghan, *Principles of nuclear magnetic resonance microscopy* (Oxford University, 1993).
3. P. T. Callaghan, C. D. Eccles, Sensitivity and resolution in NMR imaging. *J. Magn. Reson.* **71**, 426–445 (1987).
4. T. Neuberger, A. Webb, Radiofrequency coils for magnetic resonance microscopy. *NMR Biomed.* **22**, 975–981 (2009).
5. L. Ciobanu, D. Seeber, C. Pennington, 3D MR microscopy with resolution 3.7  $\mu\text{m}$  by 3.3  $\mu\text{m}$  by 3.3  $\mu\text{m}$ . *J. Magn. Reson.* **158**, 178–182 (2002).
6. M. Weiger, D. Schmidig, S. Denoth, C. Massin, F. Vincent, M. Schenkel, M. Fey, NMR microscopy with isotropic resolution of 3.0  $\mu\text{m}$  using dedicated hardware and optimized methods. *Concepts Magn. Reson. Part B Magn. Reson. Eng.* **33B**, 84–93 (2008).
7. S. C. Lee, K. Kim, J. Kim, S. Lee, H. Y. Jeong, W. K. Sung, K. S. Ha, C. Cheong, One micrometer resolution NMR microscopy. *J. Magn. Reson.* **150**, 207–213 (2001).
8. S. C. Lee, K. Kim, J. Kim, J. H. Yi, S. Lee, C. Cheong, MR microscopy of micron scale structures. *Magn. Reson. Imaging.* **27**, 828–833 (2009).
9. E. Moore, R. Tycko, Micron-scale magnetic resonance imaging of both liquids and solids. *J. Magn. Reson.* **260**, 1–9 (2015).
10. H. Y. Chen, R. Tycko, Low-temperature magnetic resonance imaging with 2.8  $\mu\text{m}$  isotropic resolution. *J. Magn. Reson.* **287**, 47–55 (2018).
11. A. P. M. Kentgens, J. Bart, P. J. M. Van Bentum, A. Brinkmann, E. R. H. Van Eck, J. G. E. Gardeniers, J. W. G. Janssen, P. Knijn, S. Vasa, M. H. W. Verkuijlen, High-resolution liquid-and solid-state nuclear magnetic resonance of nanoliter sample volumes using microcoil detectors. *J. Chem. Phys.* **128**, 52202 (2008).
12. R. M. Fratila, A. H. Velders, Small-volume nuclear magnetic resonance spectroscopy. *Annu. Rev. Anal. Chem.* **4**, 227–49 (2011).
13. A. G. Webb, Chapter 4 - Microcoil Nuclear Magnetic Resonance Spectroscopy. *J. Pharm. Biomed. Anal.* **38**, 83–130 (2008).

14. T. L. Peck, R. L. Magin, P. C. Lauterbur, Design and Analysis of Microcoils for NMR Microscopy. *J. Magn. Reson. Ser. B.* **108**, 114–124 (1995).
15. J. Mispelter, M. Lupu, A. Briguet, *NMR probeheads for biophysical and biomedical experiments: theoretical principles & practical guidelines* (Imperial College Press, 2006).
16. W. A. Edelstein, Radiofrequency Systems and Coils for MRI and MRS in *Encycl. Magn. Reson. eds-in-chief R. K. Harris R. Wasylishen, John Wiley Chichester*. doi:10.1002/9780470034590.emrstm0444.
17. D. Xiao, B. J. Balcom, Restricted k-space sampling in pure phase encode MRI of rock core plugs. *J. Magn. Reson.* **231**, 126–132 (2013).
18. M. Halse, J. Rioux, S. Romanzetti, J. Kaffanke, B. MacMillan, I. Mastikhin, N. J. Shah, E. Aubanel, B. J. Balcom, Centric scan SPRITE magnetic resonance imaging: optimization of SNR, resolution, and relaxation time mapping. *J. Magn. Reson.* **169**, 102–117 (2004).
19. R. Kc, I. D. Henry, G. H. J. Park, A. Aghdasi, D. Raftery, New solenoidal microcoil NMR probe using zero-susceptibility wire. *Concepts Magn. Reson. Part B Magn. Reson. Eng.* **37B**, 13–19 (2010).
20. M. Musse, H. Van As, NMR imaging of air spaces and metabolites in fruit and vegetables. *Mod. Magn. Reson.*, 1765–1779 (2018).
21. Y.-X. J. Wang, Superparamagnetic iron oxide based MRI contrast agents: Current status of clinical application. *Quant. Imaging Med. Surg.* **1**, 35 (2011).
22. J. F. Schenck, The role of magnetic susceptibility in magnetic resonance imaging: MRI magnetic compatibility of the first and second kinds. *Med. Phys.* **23**, 815–850 (1996).
23. K. M. Lüdeke, P. Röschmann, R. Tischler, Susceptibility artefacts in NMR imaging. *Magn. Reson. Imaging.* **3**, 329–343 (1985).
24. P. Mowat, F. Franconi, C. Chapon, L. Lemaire, J. Dorat, F. Hindré, J. Benoit, P. Richomme, J. Le Jeune, Evaluating SPIO-labelled cell MR efficiency by three-dimensional quantitative T MRI. *NMR Biomed.* **20**, 21–27 (2007).
25. A. Haase, J. Frahm, W. Hanicke, D. Matthaei, <sup>1</sup>H NMR chemical shift selective (CHESS) imaging. *Phys. Med. Biol.* **30**, 341 (1985).
26. M. T. Vlaardingerbroek, J. A. Boer, *Magnetic resonance imaging: theory and practice* (Springer Science & Business Media, 2013).

27. J. I. Friedman, M. T. McMahon, J. T. Stivers, P. C. M. Van Zijl, Indirect detection of labile solute proton spectra via the water signal using frequency-labeled exchange (FLEX) transfer. *J. Am. Chem. Soc.* **132**, 1813–1815 (2010).
28. N. N. Yadav, C. K. Jones, J. Xu, A. Bar-Shir, A. A. Gilad, M. T. McMahon, P. C. M. van Zijl, Detection of rapidly exchanging compounds using on-resonance frequency-labeled exchange (FLEX) transfer. *Magn. Reson. Med.* **68**, 1048–1055 (2012).
29. C. Baltes, N. Radzwill, S. Bosshard, D. Marek, M. Rudin, Micro MRI of the mouse brain using a novel 400 MHz cryogenic quadrature RF probe. *NMR Biomed.* **22**, 834–842 (2009).
30. J. H. Ardenkjaer-Larsen, Hyperpolarized MR – What’s up Doc? *J. Magn. Reson.* **306**, 124–127 (2019).
31. P. J. Rayner, S. B. Duckett, Signal amplification by reversible exchange (SABRE): From discovery to diagnosis. *Angew. Chemie Int. Ed.* **57**, 6742–6753 (2018).
32. J. Bernarding, F. Euchner, C. Bruns, R. Ringleb, D. Müller, T. Trantzsche, J. Bargon, U. Bommerich, M. Plaumann, Low-cost LED-based Photo-CIDNP Enables Biocompatible Hyperpolarization of  $^{19}\text{F}$  for NMR and MRI at 7 T and 4.7 T. *ChemPhysChem.* **19**, 2453–2456 (2018).
33. N. Eshuis, B. J. A. van Weerdenburg, M. C. Feiters, F. P. J. T. Rutjes, S. S. Wijmenga, M. Tessari, Quantitative trace analysis of complex mixtures using SABRE hyperpolarization. *Angew. Chemie Int. Ed.* **54**, 1481–1484 (2015).
34. A. Manoharan, P. J. Rayner, M. Fekete, W. Iali, P. Norcott, V. Hugh Perry, S. B. Duckett, Catalyst-Substrate Effects on Biocompatible SABRE Hyperpolarization. *ChemPhysChem.* **20**, 285–294 (2019).
35. R. A. M. Buijsen, L. J. A. Toonen, S. L. Gardiner, W. M. C. van Roon-Mom, Genetics, Mechanisms, and Therapeutic Progress in Polyglutamine Spinocerebellar Ataxias. *Neurotherapeutics.* **16**, 263–286 (2019).
36. E. Di Lullo, A. R. Kriegstein, The use of brain organoids to investigate neural development and disease. *Nat. Rev. Neurosci.* **18**, 573 (2017).
37. D. J. Grootendorst, J. Jose, R. M. Fratila, M. Visscher, A. H. Velders, B. Ten Haken, T. G. Van Leeuwen, W. Steenbergen, S. Manohar, T. J. M. Ruers, Evaluation of superparamagnetic iron oxide nanoparticles (Endorem®) as a photoacoustic contrast agent for intra-operative nodal staging. *Contrast Media Mol. Imaging.* **8**, 83–91 (2013).

38. M. P. Herrling, S. Lackner, H. Nirschl, H. Horn, G. Guthausen, Recent NMR/MRI studies of biofilm structures and dynamics. *Annu. Reports NMR Spectrosc.* **97**, 163 (2019).
39. P. D. Majors, J. S. McLean, G. E. Pinchuk, J. K. Fredrickson, Y. A. Gorby, K. R. Minard, R. A. Wind, NMR methods for in situ biofilm metabolism studies. *J. Microbiol. Methods.* **62**, 337–344 (2005).
40. R. van Schadewijk, J. R. Krug, D. Shen, K. B. S. S. Gupta, F. J. Vergeldt, T. Bisseling, A. G. Webb, H. Van As, A. H. Velders, H. J. M. de Groot, Magnetic Resonance Microscopy at Cellular Resolution and Localised Spectroscopy of *Medicago truncatula* at 22.3 Tesla. *Sci. Rep.* **10**, 1–11 (2020).
41. I. V. Mastikhin, B. J. Balcom, Centric SPRITE MRI of Biomaterials with Short  $T_2^*$ . *Encycl. Magn. Reson.* **1**, 783–788 (2012).
42. C. W. Windt, F. J. Vergeldt, P. A. De Jager, H. Van As, MRI of long-distance water transport: a comparison of the phloem and xylem flow characteristics and dynamics in poplar, castor bean, tomato and tobacco. *Plant. Cell Environ.* **29**, 1715–1729 (2006).
43. A. Prusova, thesis, Wageningen University, Wageningen (2016).
44. T. W. J. Scheenen, thesis, Wageningen University, Wageningen (2001).
45. R. A. de Graaf, P. B. Brown, S. McIntyre, T. W. Nixon, K. L. Behar, D. L. Rothman, High magnetic field water and metabolite proton  $T_1$  and  $T_2$  relaxation in rat brain in vivo. *Magn. Reson. Med.* **56**, 386–394 (2006).
46. H. T. Edzes, D. van Dusschoten, H. Van As, Quantitative  $T_2$  Imaging of Plant Tissues By Means Of Multi-Echo MRI Microscopy. *Magn. Reson. Imaging.* **16**, 185–196 (1998).
47. A. Webb, Increasing the sensitivity of magnetic resonance spectroscopy and imaging. *Anal. Chem.* **84**, 9–16 (2012).





## Summary



Magnetic Resonance Imaging (MRI) and spatially resolved spectroscopy are valuable Magnetic Resonance (MR) techniques ranging from clinical diagnostics and research to applications in environmental and plant sciences. The key advantage is the ability to non-invasively and non-destructively yield information which other techniques cannot provide. A disadvantage of MR techniques, however, is their relatively low sensitivity, which poses limitations to the minimal spatial resolution and target concentration or comes at the expense of long experiment times. The Signal-to-Noise Ratio (SNR) can generally be increased by increasing the main magnetic field strength  $B_0$ , increasing the sensitivity of the detector, reducing the noise of the coil or enhancing the signal by hyperpolarisation techniques. In this thesis, we mainly focussed on SNR increase by increasing the  $B_0$  (cf. **chapters 2-6**) and to a certain extent by increasing the detector sensitivity (cf. **chapters 2,3 and 5**), as well as the enhancement by chemical shift saturation transfer (cf. **chapter 6**).

Ultra-high magnetic field strength for MRI and spatially resolved spectroscopy are anticipated by the research community both with excitement as well as with precaution. Opportunities in terms of increase of both SNR and spectral resolution meet the challenges concerning susceptibility artefacts which cause image distortions and line broadening. During the research project leading to this thesis, we have identified both opportunities as well as challenges on phantoms and biological specimen.

In **chapter 1**, the main milestones in the discovery of the fundamental physical phenomenon of nuclear magnetic resonance (NMR) and MRI techniques, as well as the road towards the different applications, are explained. The basics of MRI and spatially resolved spectroscopy are discussed, including MR image formation and the most commonly used sequences. The research field of Magnetic Resonance Microscopy (MRM) is set into context, and main hardware differences between the different research areas of MRI, i.e. clinical, preclinical and microimaging, are highlighted. The limitations to MR techniques, being the low SNR, and opportunities to increase the SNR are discussed. In terms of additional benefits and challenges at ultra-high field, susceptibility mismatches which represent a significant challenge in high field MRI are highlighted. A short introduction to spatially resolved spectroscopy methods is given.

In **chapter 2**, the SNR-increase was quantified systematically across different high-field microimaging systems. We found that using the same detector dimensions (5 mm saddle and birdcage coils) the volumetric SNR could be increased by a factor of 5.9 from 14.1 T to 22.3 T, while a factor of 2.2 could be gained from 17.6 T to 22.3 T. As the SNR

increase from 14.1 T to 22.3 T exceeded the theoretical expectation, this underlines the importance of considering other hardware components as well, such as using optimised radiofrequency detectors; in fact, the 5 mm saddle coil at 14.1 T appeared to underperform. Using a 1.5 mm microcoil at 22.3 T, we found an increase of a factor 3.5 with respect to the 5 mm birdcage coil at the same magnetic field strength. This underlines the importance of adjusting the detector coil to accommodate the correct sample dimensions optimally. Our highest resolution obtained  $(5.5 \mu\text{m})^3$  was on a phantom with doped water with the 1.5 mm solenoid coil, using a 3D-FLASH experiment with a matrix size of 288 x 192 x 192 in 58 h and 34 min. An additional effect from increasing the field strengths is the increase in  $T_2^*$  contrast, which could be observed by imaging with identical parameters on a specimen of lily root.

In **chapter 3**, we describe a method protocol for using the uNMR-nl ultra-high field spectrometer (22.3 T) and calibrate new or home-built microcoils. Sample preparation for using solenoid coils is described, and adjustments for MRI experiments are described. As pre-scan adjustments and especially a good  $B_0$ -homogeneity is essential to a number of applications at ultra-high field, the necessary adjustments, such as shimming, are outlined in the protocol.

A case study for samples posing challenges to ultra-high field MRI due to susceptibility problems is shown in **chapter 4**. The preamble of this chapter describes the initial trials with respect to different activated carbon materials and sample pre-treatment strategies. An acid pre-treatment was found to reduce the iron content in activated carbon material. Biofilm visualisation and quantification of activated carbon electrodes by MRI on a 14.1 T high field imaging system was successfully correlated with the electrochemical performance and total mass by total nitrogen analysis. Strategies to deal with these susceptibility artefacts are discussed.

In **chapter 5**, magnetic resonance imaging and spatially resolved spectroscopy were combined to evaluate the potential of ultra-high field MRI for plant sciences. A high-resolution image of a fixed *Medicago truncatula* root nodule with a resolution of  $7 \times 7 \times 7 \mu\text{m}^3$  was obtained. These root nodules form in response to growing in nitrogen-deficient soil and are a symbiotic interaction with bacteroids (*Sinorhizobium meliloti*). In this image, plant cells are well resolved, while the presence of bacteroids can be distinguished by  $T_2^*$  contrast in the interior of infected plant cells. However, when freshly excising the root nodules, contrast and SNR decreases, most likely due to air cavities. This underlines the need for robust approaches when susceptibility is involved.

Additionally, spatially resolved spectroscopy was used to obtain spectral information from relevant zones in the nodule in a voxel of  $200 \times 350 \times 350 \mu\text{m}^3$ .

While the ultra-high magnetic field is suitable for spatially resolved spectroscopy due to the increased SNR improving the detection limit, chemical exchange saturation transfer (CEST) imaging can further improve the detection limit significantly for a number of metabolites which contain exchangeable protons. In **chapter 6**, we investigated the additional advantage of CEST at ultra-high field, namely the increase of the selectivity towards the desired metabolite on 7.0 T, 17.2 T and 22.3 T systems. An increase in selectivity was observed with increasing field strengths, but it remains a challenge to uniquely select for a specific metabolite.

In the general discussion (**Chapter 7**), we summarise the main findings and conclusions of this thesis. The lessons from ultra-high field MRI and spatially resolved spectroscopy are discussed from a hardware and experimental point of view. We highlight that both the main magnetic field strength and other hardware components, such as gradient strength and detector sensitivity, are important. Experimental considerations, which in particular have to be taken into account when working at ultra-high-field strengths are the chemical shift displacement when performing localised spectroscopy, strategies to reduce susceptibility effects and sequence optimisation. Other strategies for SNR increase, such as cryoprobes and hyperpolarisation, are briefly discussed for a future outlook. As ultra-high field MRM is a research field which usually comes together with small sample sizes, perspectives for different applications such as clinical research, environmental sciences, wastewater treatment, and plant sciences are discussed. Finally, this chapter concludes with an outlook for ultra-high field MRI and spatially resolved spectroscopy for magnetic field strengths beyond 22.3 T.

Overall, we conclude that ultra-high field MRI and spatially resolved spectroscopy are highly beneficial as it leads to higher spatial resolutions, faster acquisition times and improved detection limits for metabolites. These advantages can be in the future further extended to a variety of applications. Novel acquisition approaches, hardware and sample preparation, can be additionally optimised for each application to benefit maximally from the state-of-the-art 22.3 T system.

## **Samenvatting**

Kernspintomografie (MRI) en ruimtelijk-opgeloste spectroscopie zijn waardevolle methoden in de kernspinresonantie, variërend van klinische diagnostiek- en onderzoeksmethoden tot toepassingen in de milieu- en plantenwetenschappen. Het belangrijkste voordeel ten opzichte van andere technieken is de mogelijkheid om niet-invasief en niet-destructief te meten. Een nadeel van de kernspinmethodes is de relatief lage gevoeligheid. Deze lage gevoeligheid stelt limieten aan het ruimtelijke oplossingsvermogen en de benodigde concentratie van kernspins tenzij de experimentele duur verlengd wordt. De signaal-ruis verhouding (ook wel afgekort met SNR) kan in het algemeen vergroot worden door een verhoogde magneetveldsterkte  $B_0$ , een verhoogde gevoeligheid van de detector, het verlagen van het ruisniveau of het versterken van het signaal door middel van hyperpolarisatiemethoden. In deze dissertatie focussen we op het vergroten van de SNR door bij extreem hoge magneetvelden te meten (zie **hoofdstukken 2-6**) en door de gevoeligheid van de detector te vergroten (zie **hoofdstukken 2,3, en 5**). Bovendien kijken we naar de SNR-verhoging door chemische shift saturatie transfer (zie **hoofdstuk 6**).

De wetenschappelijke gemeenschap keek uit naar ultrahoge magnetische velden voor kernspintomografie en ruimtelijk opgeloste spectroscopie met zowel grote verwachtingen als met enige terughoudendheid. Aan de ene kant zijn er vooruitzichten in de vorm van SNR-verhoging en verhoogde spectrale oplossing en aan de andere kant zijn er uitdagingen rondom susceptibiliteitseffecten, die beeldvervalsingen en lijnverbreding kunnen veroorzaken.

In **hoofdstuk 1** worden de mijlpalen in de ontdekking van het onderliggende fysische fenomeen van kernspinresonantie (NMR)- en MRI-technieken en het pad naar de verschillende toepassingen uitgelegd. De basis van MRI en ruimtelijk-opgeloste spectroscopie, MRI-beeldvorming en de meest gebruikte sequenties worden behandeld. Het onderzoeksveld van kernspinresonantie-microscopie (MRM) wordt in context geplaatst en verschillen in hardware tussen de verschillende gebieden in MRI worden uitgelicht. De limitaties voor de kernspintechnieken, zijnde de lage SNR en mogelijkheden om de SNR te vergroten, worden bediscussieerd. Daarnaast worden de zogeheten susceptibiliteitsverschillen benadrukt, omdat deze een belangrijke uitdaging in ultrahoogveld MRI zijn.

In **hoofdstuk 2** wordt de SNR-verhoging van verschillende micro-imaging systemen systematisch gekwantificeerd. We hebben vastgesteld dat de SNR met een factor van 5.9 kan stijgen van een 14.1 T spectrometer naar een 22.3 T spectrometer, door radiofrequentie-spoelen met dezelfde dimensies (5 mm zadel en birdcage spoelen) te gebruiken, terwijl van 17.6 T naar 22.3 T een factor 2.2 te behalen was. Het feit dat de SNR-verhoging van 14.1 T naar 22.3 T groter is dan de theoretische verwachtingen, laat zien hoe belangrijk de hardware en met name een geoptimaliseerde radiofrequentiespoel is. De 5 mm spoel op de 14.1 T bleek niet optimaal te presteren. Met een 1.5 mm microspoel op 22.3 T hebben we een verhoging van de SNR met een factor 3.5 ten opzichte van de 5 mm spoel bij dezelfde magneetveldsterkte gerealiseerd. Dit laat zien dat het van belang is om de spoel qua dimensies optimaal op de dimensies van het monster af te stemmen. De hoogst gemeten ruimtelijke oplossing was  $(5.5 \mu\text{m})^3$  op een fantoom met gedoteerd water in de 1.5 mm solenoïde spoel. Hierbij hebben we gebruik gemaakt van een 3D-FLASH experiment met een matrixgrootte van  $288 \times 192 \times 192$  in 58 uur en 34 min. Een bijkomend effect van het verhogen van de veldsterkte is de verhoging in  $T_2^*$  contrast, die geobserveerd kon worden door het opnemen van een MRI-beeld bij identieke parameters op een monster van een leliewortel.

In **hoofdstuk 3** beschrijven we een protocol om de uNMR-nl ultrahoogveld spectrometer (22.3 T) te gebruiken en om nieuwe microspoelen te kalibreren. De voorbereiding van een monster voor een solenoïde spoel en de afregelingen voor een MRI-experiment worden beschreven. Daarnaast worden voor een aantal toepassingen bij ultrahoog veld de noodzakelijke pre-scan optimalisaties beschreven. Met name  $B_0$ -homogeniteit is essentieel bij ultrahoogveld en daarom wordt het homogeniseren van het magneetveld expliciet beschreven.

Een casus voor uitdagende monsters wordt gepresenteerd in **hoofdstuk 4**. Het gaat hierbij om monsters die susceptibiliteitsproblemen geven in MRI bij ultrahoog veld. De inleiding van dit hoofdstuk beschrijft de eerste experimenten met verschillende materialen van actieve kool en de verschillende strategieën voor voorbehandeling. Een voorbehandeling met zuurverminderde de ijzer hoeveelheid in de geteste actieve kool. Visualisatie en kwantificatie van biofilm op actieve kool op een 14.1 T hoogveld MRI systeem correleerde met de elektrochemische prestatie en totale massa op basis van het totale stikstofgehalte. Strategieën om met de susceptibiliteitsartefacten om te gaan worden bediscussieerd.



In **hoofdstuk 5** worden MRI en ruimtelijk-opgeloste spectroscopie technieken gecombineerd om het potentieel van ultrahoogveld MRI te onderzoeken voor toepassing in de plantenwetenschappen. Van een gefixeerde *Medicago truncatula* wortelknolletje werden beelden verkregen met een ruimtelijke oplossing van  $7 \times 7 \times 7 \mu\text{m}^3$  in 34 uur en 24 min. *M. truncatula* vormt wortelknolletjes als reactie op een stikstofarme grond en in de cellen in deze wortelknolletjes bevinden zich in symbiose bacterioiden (*Sinorhizobium meliloti*). In de verkregen MRI beelden kunnen door middel van  $T_2^*$  contrast zowel de plantencellen als de aanwezigheid van bacterioiden in de plantencellen onderscheiden worden. Beelden van een vers afgesneden wortelknolletje hebben een verminderd contrast, waarschijnlijk vanwege de aanwezige luchtholtes. Deze susceptibiliteitsproblemen benadrukken het belang van een robuuste benadering. Daarnaast werd ruimtelijk opgeloste spectroscopie gebruikt om spectrale informatie uit relevante zones in het knolletje in een voxelgrootte van  $200 \times 350 \times 350 \mu\text{m}^3$  te verkrijgen.

Ultrahoog veld is geschikt voor ruimtelijk opgeloste spectroscopie door een verhoogde detectielimiet, die voortkomt uit een verhoogde SNR. Chemical Exchange Saturatie Transfer (CEST)-beeldvorming kan deze detectielimiet significant verbeteren voor een aantal metabolieten die uitwisselbare protonen hebben. In **hoofdstuk 6** hebben we het bijkomend voordeel van CEST bij ultrahoog veld onderzocht, met name de verhoging in selectiviteit voor bepaalde metabolieten in 7.0 T, 17.2 T en 22.3 T systemen. Een hogere selectiviteit werd gevonden bij hogere veldsterktes, maar het blijft een uitdaging om specifiek één metaboliet te selecteren.

In de algemene discussie (**Hoofdstuk 7**) vatten we de voornaamste resultaten van dit proefschrift samen. De belangrijkste bevindingen van ultrahoogveld MRI en ruimtelijk opgeloste spectroscopie worden bediscussieerd met de focus op hardware en experimentele aspecten. We benadrukken dat zowel de magneetveldsterkte als de gevoeligheid van de detector van belang zijn. Experimentele factoren waar rekening mee moet worden gehouden bij ultrahoog veld zijn de chemische shift verschuiving bij ruimtelijk-opgeloste spectroscopie, strategieën om susceptibiliteit te verminderen en sequentie optimalisatie. Andere strategieën voor SNR-verhoging, zoals cryoprobes en hyperpolarisatie, worden kort bediscussieerd in het kader van toekomstig onderzoek. Omdat ultrahoogveld MRM een onderzoeksveld is dat vaak gepaard gaat met kleine monstergroottes, worden de mogelijkheden van ultrahoogveld MRI in verschillende

gebieden zoals klinisch onderzoek, milieuwetenschappen en plantenwetenschappen, bediscussieerd. Tenslotte sluit dit hoofdstuk af met de vooruitzichten van ultrahoogveld MRI en ruimtelijk-opgeloste spectroscopie met magneetveldsterktes hoger dan 22.3 T.

Samenvattend concluderen we dat ultrahoogveld MRI en ruimtelijk-opgeloste spectroscopie veelbelovend zijn, vanwege de hogere oplossingsvermogens, snellere acquisitietijden en verbeterde detectielimieten voor metabolieten. Deze voordelen kunnen in de toekomst uitgebreid worden voor verschillende toepassingen. Bovendien kunnen nieuwe meetmethodes, hardware en monstervoorbereiding geoptimaliseerd worden voor elke specifieke toepassing om maximaal van het 22.3 T systeem te kunnen profiteren.



## **Zusammenfassung**

Magnetresonanztomographie (MRT) und ortsauflösende Spektroskopie sind wertvolle Magnetresonanz(MR)-Techniken deren Anwendungen von klinischer Diagnostik und Forschung bis zu Umwelt- und Pflanzenwissenschaften reichen. Der Hauptvorteil ist die Möglichkeit Informationen nicht invasiv und nicht destruktiv zu erhalten, die andere Techniken nicht hergeben. Ein Nachteil der Magnetresonanztechniken ist jedoch die niedrige Sensitivität, die die räumliche Auflösung und die Spinkonzentration limitiert oder lange Experimentdauer mit sich bringt. Das Signal-Rausch-Verhältnis (SRV) kann normalerweise erhöht werden, indem man das Hauptmagnetfeld  $B_0$  oder die Sensitivität des Detektors erhöht, das Rauschniveau der Spule reduziert oder das Signal durch Hyperpolarisierung steigert. In dieser Doktorarbeit lag der Focus auf der SRV-Steigerung durch  $B_0$ -Erhöhung konzentriert (siehe **Kapitel 2-6**) und bis zu einem gewissen Grad der Erhöhung der Detektorsensitivität (siehe **Kapitel 2, 3 und 5**), sowie der Steigerung durch *Chemical Exchange Saturation Transfer (CEST)* (siehe **Kapitel 6**) gewidmet.

Ultrahohe Magnetfeldstärken für MRT und ortsaufgelöste Spektroskopie werden durch die Forschungsgemeinschaft mit Spannung erwartet, aber auch mit Vorsicht betrachtet. Den Chancen der SRV-Steigerung und höheren spektralen Auflösung stehen Herausforderungen durch Suszeptibilitätartefakte gegenüber, die Bildverzerrungen und Linienverbreiterungen zur Folge haben können. In diesem Forschungsprojekt wurde bei Messungen von Modellproben und biologischen Proben sowohl Möglichkeiten als auch Herausforderungen gesehen.

In **Kapitel 1** werden die wichtigsten Eckdaten der Entdeckung des fundamentalen physikalischen Phänomens der Kernresonanz (NMR) und MRT-Techniken genauso wie der Weg zu den verschiedenen Anwendungen dargelegt. Die Grundlagen von MRT und ortsaufgelöster Spektroskopie werden erörtert, einschließlich der MR Bilderzeugung und die meist benutzten Sequenzen. Das Forschungsfeld der Magnetresonanzmikroskopie (MRM) wird in den Kontext eingebettet und wichtige Hardwareunterschiede zwischen den verschiedenen MRT-Gebieten werden hervorgehoben. Die Limitierung der MR-Techniken, nämlich die niedrige SRV, und die Möglichkeiten zur SRV-Steigerung werden diskutiert. Den zusätzlichen Nutzen und die Herausforderungen von ultrahohen Magnetfeldstärken betreffend werden Suszeptibilitätsunterschiede herausgestellt, die eine besondere Herausforderung in Hochfeldmethoden darstellen. Es wird eine kurze Einleitung in ortsaufgelöste Spektroskopie gegeben.

In **Kapitel 2** wird die SRV-Steigerung systematisch über mehrere Hochfeld-Microimaging-Systeme quantifiziert. Wir fanden heraus, dass mit den gleichen Dimensionen des Detektors (5 mm Sattel- und Vogelkäfigspule) das volumetrische SRV um einen Faktor 5.9 erhöht werden konnte mit einer Erhöhung des Magnetfeldes von 14.1 T auf 22.3 T, während ein Faktor 2.2 erreicht wurde mit einer Erhöhung von 17.6 T auf 22.3 T. Da die SRV-Erhöhung mit der Erhöhung von 14.1 T auf 22.3 T die theoretischen Erwartungen übertrifft, unterstreicht dies den Einfluss der Hardware, wie zum Beispiel den Gebrauch von optimierten Radiofrequenzdetektoren, da die 5 mm Sattelspule bei 14.1 T nicht ihre optimale Leistung erbringt. Mit einer 1.5 mm Mikrospeule wurde bei 22.3 T SRV-Steigerung von 3.5 gegenüber der 5 mm Vogelkäfigspule bei gleicher Magnetfeldstärke gefunden. Dies unterstreicht die Bedeutung der optimalen Anpassung der Dimensionen der Detektorspule an die Dimensionen der Probe. Die höchste erreichte Auflösung in dieser Arbeit war  $(5.5 \mu\text{m})^3$  an einer Modellprobe mit dotiertem Wasser mit der 1.5 mm Zylinderspule, in einem 3D-FLASH Experiment mit einer Matrizengröße von  $288 \times 192 \times 192$  in 58 Stunden und 34 Minuten. Ein zusätzlicher Effekt der Magnetfeldstärkenerhöhung ist die Zunahme des  $T_2^*$ -Kontrastes, die durch die Aufnahme eines MRI-Bildes mit identischen Parametern an einer Lilienwurzel detektiert werden konnte.

In **Kapitel 3** wird ein Methodenprotokoll beschrieben um das unmr-nl Ultrahochfeldspektrometer (22.3 T) zu verwenden und um neue oder selbstgebaute Mikrospeulen zu kalibrieren. Das Vorbereiten der Probe für die Zylinderspule wird beschrieben und ebenso Prä-Scan Einstellungen für MRT-Experimente. Da Prä-Scan Einstellungen und vor allem eine gute  $B_0$ - Homogenität wesentlich sind für zahlreiche Anwendungen bei Ultrahochfeld, werden diese in diesem Protokoll beschrieben.

Eine Fallstudie für Proben, die durch Suszeptibilitätsprobleme Herausforderungen bei Ultrahochfeld-MRT aufzeigen, ist in **Kapitel 4** dargestellt. Die Präambel für dieses Kapitel beschreibt die Initialexperimente in Bezug auf verschiedene Aktivkohlematerialien und Strategien zur Vorbehandlung der Probe. Eine Säurevorbehandlung hat ergeben, dass der Eisengehalt in dem Aktivkohlematerial reduziert wurde. Biofilmvisualisierung und – quantifizierung auf Aktivkohlematerial mittels MRT auf einem 14.1 T Hochfeldbildgebungssystem wurde erfolgreich an der elektrochemischen Leistung und Gesamtmasse durch Gesamtstickstoffbestimmungsanalyse korreliert. Strategien zum Umgang mit Suszeptibilitätproblemen sind dargelegt.

In **Kapitel 5** wurden MRT und orts aufgelöste Spektroskopie kombiniert, um das Potenzial von Ultrahochfeld-MRT für Pflanzenwissenschaften auszuwerten. Ein hoch aufgelöstes Bild von einer fixierten *Medicago truncatula* Wurzelknöllchen mit einer Auflösung von  $(7\ \mu\text{m})^3$  wurde in 34 Stunden und 24 Minuten erreicht. Diese Wurzelknöllchen formen sich, wenn die Pflanzen auf stickstoffarmen Boden wachsen, und sind eine symbiotische Interaktion mit Bakterioiden (*Sinorhizobium melioli*). In diesem Bild sind die Pflanzenzellen gut aufgelöst, während die Anwesenheit von Bakterioiden mittels  $T_2^*$ -Kontrastbildgebung im Innern der infizierten Pflanzenzellen nachgewiesen werden kann. Bei frisch geschnittenen Wurzelknöllchen ist sowohl Kontrast als auch SRV reduziert, wahrscheinlich durch die Lufthohlräume. Dies unterstreicht die Notwendigkeit von robusten Methoden, wenn Suszeptibilität beteiligt ist. Des Weiteren wurde orts aufgelöste Spektroskopie benutzt, um spektrale Informationen aus relevanten Zonen in dem Knöllchen in einem Voxel von  $200 \times 350 \times 350\ \mu\text{m}^3$  zu erhalten.

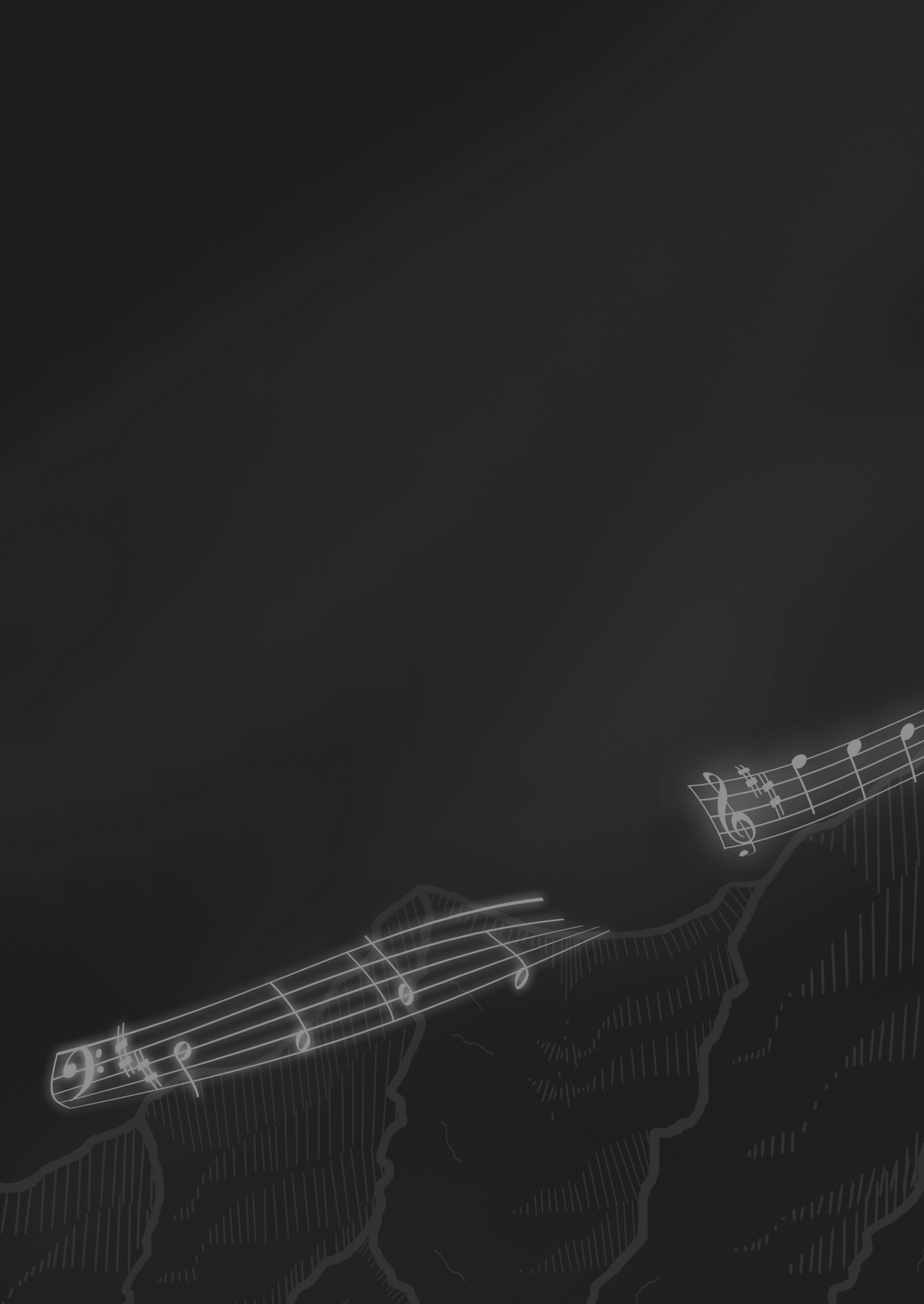
Während Ultrahochmagnetfeld aufgrund der SRV-Steigerung für orts aufgelöste Spektroskopie geeignet ist, kann CEST-Bildgebung die Nachweisgrenze einer Anzahl von Stoffwechselprodukten, die austauschbare Protonen haben, signifikant verbessern. In **Kapitel 6** haben wir den zusätzlichen Vorteil von CEST bei Ultrahochfeld untersucht, nämlich die erhöhte Selektivität für bestimmte Stoffwechselprodukte bei 7.0 T-, 17.2 T- und 22.3 T-Systemen. Eine Steigerung in Selektivität wurde festgestellt, aber es bleibt eine Herausforderung, ein bestimmtes Stoffwechselprodukt zu selektieren.

In der allgemeinen Diskussion (**Kapitel 7**) werden die Hauptergebnisse und Schlussfolgerungen dieser Doktorarbeit zusammengefasst. Die Lektionen von Ultrahochfeld-MRT und orts aufgelöster Spektroskopie werden aus experimenteller und technischer Sicht erörtert. Wir unterstreichen, dass sowohl die Hauptmagnetfeldstärke als auch andere Hardwarekomponenten wie Gradientenstärke und Detektorsensibilität wichtig sind. Experimentelle Aspekte, die bei Ultrahochfeld erwogen werden müssen, sind chemische Verschiebungen, Strategien zur Reduzierung von Suzeptibilitätseffekten und Sequenzoptimierung. Andere Strategien für SRV-Steigerung wie zum Beispiel Kryosonden und Hyperpolarisierung werden kurz hinsichtlich ihrer zukünftigen Perspektiven angesprochen. Da Ultrahochfeld-MRM ein Forschungsfeld ist, das normalerweise mit kleinen Proben dimensionen einhergeht, werden Perspektiven für verschiedene Anwendungen wie zum Beispiel klinische Forschung, Umweltwissenschaften, Wasseraufbereitung und Pflanzenwissenschaften erörtert.

Dieses Kapitel schließt mit einem Ausblick für Ultrahochfeld-MRT und orts aufgelöster Spektroskopie für Magnetfelder über 22.3 T hinaus ab.

Zusammenfassend lässt sich sagen, dass Ultrahochfeld-MRT und orts aufgelöste Spektroskopie sehr vorteilhaft sind, da sie zu höheren Auflösungen, schnelleren Experimentzeiten und verbesserten Nachweisgrenzen für Stoffwechselprodukte führen. Diese Vorteile können in der Zukunft noch weiter für verschiedene Anwendungen benutzt werden. Neue Experimentmethoden, Hardware und Probenvorbereitung können für jede Anwendung ergänzend optimiert werden, um maximal von dem neuesten Stand der Technik (dem 22.3 T-Spektrometer) zu profitieren.

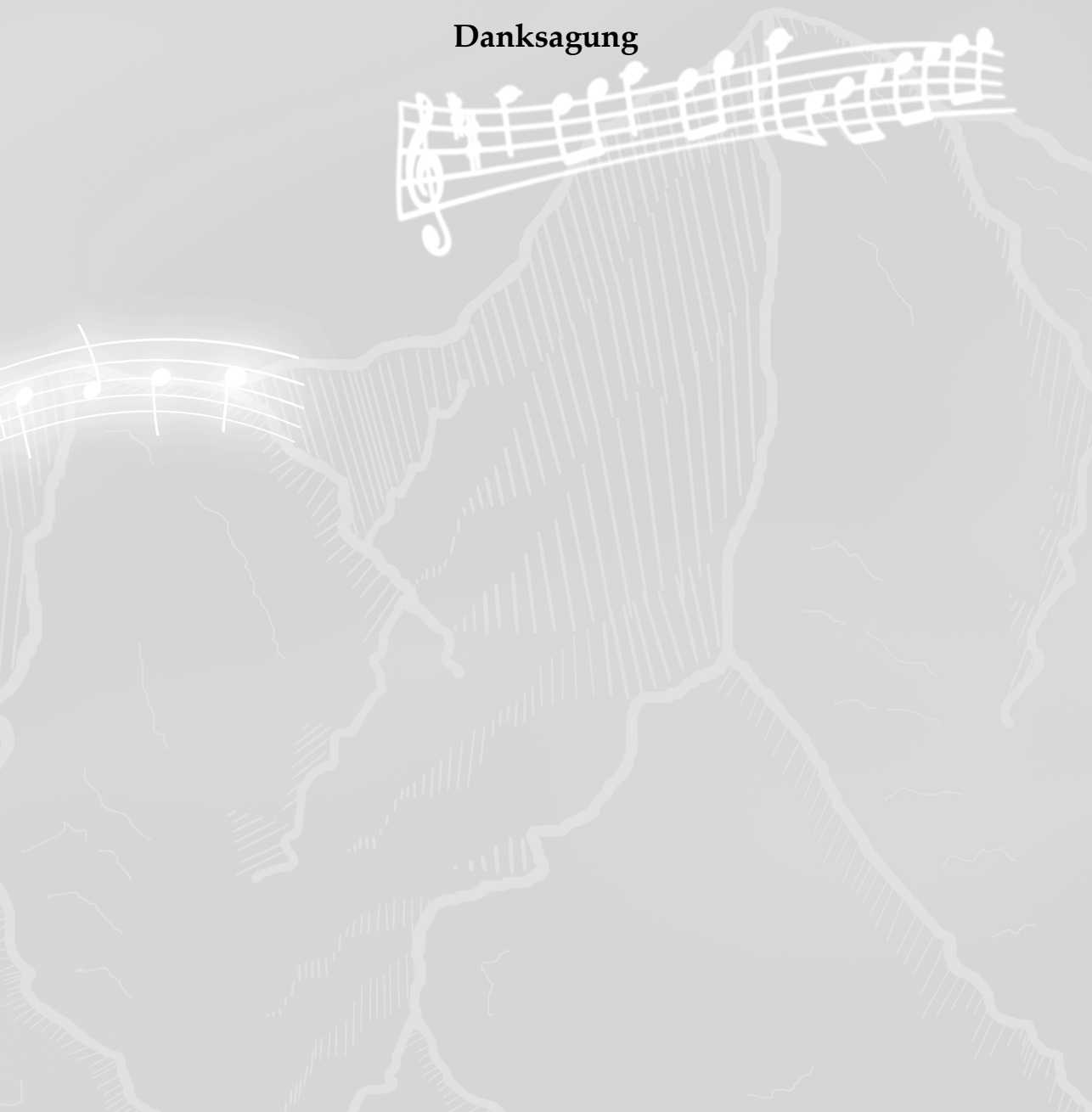




# **Acknowledgements**

**Dankwoord**

**Danksagung**



I had the privilege to share my PhD-trajectory with a big support team of advisors, colleagues, collaborations, friends and family. This last and most important chapter of my thesis is for you.

Allereerst wil ik mijn begeleiders danken voor hun begeleiding en feedback de afgelopen jaren. *Aldrik*, jou heb ik veel te danken. Je open deur was altijd een hulp als ik niet verder kwam. De mogelijkheden die ik onder jouw begeleiding kreeg om mezelf professioneel en als persoon te ontwikkelen waardeer ik ten zeerste. *Henk*, heel erg bedankt voor de vrijheid in het onderzoek en je grote enthousiasme voor nieuwe projecten. Met je ervaring en netwerk in dit onderzoeksveld heb je me veel geholpen en hebben we tijdens mijn PhD-project heel interessante samenwerkingen met andere groepen kunnen doen. *Frank*, door jouw kritische blik en de discussies met jou heb ik dingen scherper kunnen zien. Je hebt me zo vaak geholpen als ik vastzat en ik wil jou danken voor alle hulp. *John Philippi*, wat hat ik zonder jou gedaan? Alle spoelen die je voor mij hebt gebouwd of als ik weer aankwam met dat problemen aan het equipment van de 600 me aan het verder werken hinderden. Ik zal nooit vergeten hoe we samen alle ventilatoren van de AQS-unit binnen de kortste tijd hebben vervangen.

*Remco*, onze samenwerking gedurende een groot gedeelte van mijn PhD was erg leuk. Ik heb veel van je geleerd, sommige dingen vrij onverwacht over Science communication en film compositie. Ik wens je ontzettend veel succes bij het verwezenlijken van je visie en ik weet dat je gaat brillieren in wat je gaat doen. I also would like to express my gratitude to *Andrew*, for your help and input in this project. Thank you very much for all your help and encouragement already from the very beginning of my PhD project when I came to the coil course in Italy. *Alia* and *Huub*, thank you for the comments on the work and the collaboration.

*Cat*, I really enjoyed our collaboration especially at the beginning of my PhD and I learned a lot from you. *Merle*, bedankt voor je enthousiasme voor samenwerking en de meetdagen achter de 950. *Alexander*, *Lenno* and *Sara*, thank you for your help and input during our projects.

*Luisa*, thank you very much for the opportunity for me to do my PhD internship in your lab and under your supervision. I really enjoyed the time at Neurospin and to work on the CEST-project. *Solène*, merci d'avoir travaillé avec moi sur ce projet et pour m'avoir encouragé à rendre mes explications sur l'IRM mieux accessible. *Solène* et *Roxane*, merci de votre patience quand je n'arrivais pas à trouver les bons mots ou quand j'utilisais du 'Franglais'. Mes remerciements vont également à *Clement*, *Tom*, *Tangi*, *Fawzi*, *Henriette*, *Boucif* et aux autres membres de l'équipe CIEL et Neurospin.

*Itamar*, I really enjoy working with you and both our scientific and societal discussions. The energy and positivity made our measurements on brain organoids so much more fun. Thank you very much for all your advices.

*Klaartje Houben*, *Joban van der Zwan*, *Marie Renault*, *Andrei Gurinov* thank you very much for facilitating the MRI-experiments at the unmr-nl facility. Also, I would like to thank the entire NMR group in Utrecht for the support during my measurement slots. *Volker Lehmann*, danke ich ganz besonders für die schnelle Hilfe, wenn ich Probleme mit einem der Spektrometer hatte

*Leire*, isn't it amazing how "your" beautiful granules turned out with "my" amazing MRI? Your astonishing perseverance and passion for this project had a huge contribution to its success. I enjoyed our discussions on biofilm and MRI. *Roos*, thank you for your efforts in the initial stage of this project. *Annemiek* en *Mieke*, bedankt voor jullie altijd motiverend feedback op dit werk.

At this point I would like to thank my former academic supervisors and co-workers. *Nan Esbuis* en *Marco Tessari*, bedankt voor jullie begeleiding bij mijn allereerste onderzoeksthesis. *Prof. Zauscher*, thank you for having given me the opportunity to do a research internship at your lab. I admire the way you stimulate collaborations within your lab and with other labs. *Kate*, I can't thank you enough, not only did we work together, you were also very important for me to feel home during my time in Durham. All the members of the *Zauscher Lab*, thank you very much for your kindness and hospitality. *Luc-Jan*, heel erg bedankt voor je adviezen tijdens mijn bachelor als mijn studieadviseur, je hebt me erg geholpen om me in die tijd goed te oriënteren. Finally, I want to thank all my academic mentors and teachers, for their passion for science and their mentoring. A big thanks also goes to the *NMARRS graduate school* and the committee behind the idea. It was a huge privilege to be able to perform the PhD research with a grant from this initiative.

*Anton*, mijn kantoorgenoot, bedankt ervoor dat je me deze vier jaar altijd hebt geholpen, wat zou BNT zonder je zijn. *Banu*, bedankt voor al je steun, je bent zo een ontzettend sterk persoon. Natuurlijk, *Jack*, bedankt voor je geduldige en luisterend oor. *Gerben*, je perspectief en mening was heel belangrijk en onmisbaar in alle discussies aan de koffietafel. *JB*, mijn klimaatje en collega, bedankt voor alle uitjes en gesprekken. *Koen*, mijn enige "full colleague" bij zowel BNT als BIP, bedankt voor je tips en adviezen. *Laura*, je brengt altijd goede adviezen in en ik hoop je de komende tijd weer vaker te kunnen spreken. *Maria*, thanks for the advices in my first year, I was glad to meet you again at Euromar. *Pieter*, je hulp met de NMR-experimenten, probewissels, spectrometer troubleshooting jij zorgde ervoor dat het allemaal draaiende bleef. *Rebecca*, leuk dat we nog langer collega's zijn en eventueel kunnen samenwerken. *Rosa*, *Sander* and *Fatemeh*, the NMR-team, often only you understood my jokes and references at the coffee table. *Stan*, het is altijd leuk met je in discussie te gaan, en te horen wat je doet. *Stijn*, het was leuk en interessant je bij je Bachelor-thesis te mogen begeleiden. *Vittorio*, thanks a lot for all advices and stimuli to learn new methods. I admire your creativity and innovative ideas. *Yurdanur* and *Ningy*, thank you for the conversations at the coffee table and for sharing your thoughts and experience. To all the BNT-students and former members, thank you very much for your feedback, input and coffee breaks. *Jackie*, bedankt voor de gesprekken tijdens gezamenlijke koffiepauzes, je bent altijd zo positief en energiek. Also, I would like to thank everyone of the *PCC-group* for their support, especially in the beginning of my PhD, when we were still together on the Dreijen. Grote Dank aan *Mara*, door jouw inspanning heb ik toch nog mijn PhD project op tijd kunnen beginnen.

The support from the colleagues at *BIP* was very valuable both scientifically as well as morally during this PhD stretch so my gratefulness goes to my colleagues *Netty*, *Daan*, *Shazja*,

*Carel, Yashar, Arjen, Emilie, Herbert, Rob, Cor, Elena, Mattia, Ahmad, Folkert, Johannes, Morwarid, Donny, Suyeon, Klandia, Wouter, Abbas.* Special thanks to the NMR/MRI-part of the group *Camilla, John v.D., Tatiana, Raquel* and *Ana* for your very helpful feedback and input for conference presentations and learning new research topics. *Tatiana*, we were not only PhD colleagues but you were also a big support in reflecting on PhD life. *Raquel*, thanks a lot for all your advices and support, especially through the last year. You helped me a lot to see a new perspective both scientifically and personally. *Edo* and *Alena*, thank you a lot for all the help at the beginning with MRI. *Eleni* and *Simba*, it was really nice to get to know you on the PhD trip. I always enjoy our conversations on very diverse topics.

*Nicolas, Yunting, Mica* from the Rietveld Academy, you opened my mind on the more artistic side of the PhD project during our Art-meets-Science collaboration. *Science Café committee*, I really like to be part of the committee and enjoy our brainstorm and the Science Café events.

*Edgar, Elisa, Eva*, thanks a lot for your support and the daily conversations. *Fede* and *Mirko*, you are each supporting a strong, independent woman and I always enjoy the rare times when we all meet. *Lena, Dina, Tommy*, tusen takk for tiden da jeg bodde i Norge. Jeg liker å tenke tilbake på det. *Climbing lemurs*, the climbing evenings and weekends were helping a lot to disconnect from my work. *Mes amis de la groupe Café et Trailwalker de Paris*, merci de m'avoir accueilli et merci pour toutes les conversations intéressantes et l'aide pour améliorer mon français pendant mes séjours à Paris.

*Pjotr*, jouw mening en adviezen waren en zijn onmisbaar voor mij, bedankt voor je steun door de afgelopen jaren heen. *Annelies, Joshua* en *Joke*, bedankt voor jullie steun.

I also would like to acknowledge all the people whom I am not listing by name but who have made a difference, maybe only for one moment or only for a day, but it is the small encounters and not the big gestures which can mean a lot in the everyday life.

*Camilla*, not only have you been my colleague but much more my friend and PhD companion. Without our coffee breaks and dinners, endless conversations about life, philosophy and equity, we would be definitely less rich in experiences, perspectives, reflections and also our titles 'Doctor of Philosophy' would certainly contain less philosophy. We developed a lot in these four years, and I could not have imagined a better PhD companion. Grazie mille!!

Tien jaar geleden, kwam ik naar Nederland, en nooit had ik verwacht hier zo lang te blijven en dit mijn thuis te maken. Ik werd met open armen ontvangen en geïntegreerd, bedankt aan iedereen die me hier thuis heeft laten voelen. *Renske* en *Sjors*, mijn Nederlandse "familie", jullie zijn mijn wegbegeleiders al sinds tien jaar. Jullie deur staat altijd open voor mij en jullie steunen me altijd door alle ups-and-downs. *Renate*, altijd een grote steun bij de grote en de kleine gelegenheden. We komen elkaar altijd opzoeken waar we ook zijn. *Tine*, onze discussies en reflecties hebben me altijd geholpen dingen uit een ander perspectief te zien. Wie had er toen gedacht dat de eerste personen met wie ik in Nederland sprak, gelijk zo hechte vrienden zouden worden.

*Mark, Abby, Elianne en Stijn*: van studieavonden in de FNWI-bibliotheek van toen naar de diners en dagjes uit van nu, jullie zijn altijd een grote steun en *Mark*, je pragmatisme helpt altijd om dingen weer in perspectief te plaatsen.

*Vanessa und Steffi*, wir können uns Monate nicht sehen, aber wenn wir uns wiedersehen ist doch wieder alles beim Alten, als wäre die Zeit stehen geblieben.

Nun ist es Zeit meiner *Familie* zu danken für eure ständige und bedingungslose Unterstützung durch all die Jahre. *Tante Liz* und *Onkel Kurt*, vielen Dank für euer Interesse an meiner Arbeit und meinem Weg. *Thomas* und *Marlies*, danke für eure Unterstützung, ich weiß, dass ich immer bei euch anknöpfen kann. *Anna-Lena*, wir finden immer wieder Möglichkeiten uns zu sehen und auszutauschen, ich bin stolz auf dich wie du deinen Weg gehst und alles meisterst. *Ann-Katrin* und *Marie-Luise*, wir gehen alle drei unserer unterschiedlichen Wege, und doch halten wir zusammen. Vielen Dank für eure Unterstützung und Aufmunterung. *Ulrike* und *Andreas*, ganz besonderen Dank für eure Unterstützung. *Andreas*, dein Humor hilft durch viele schwierige Situationen. *Ulrike*, ich bewundere dich für deine Ansichten und deine Stärke. In meinem Garten bist du die Leitblume, an der man sich orientieren kann, die mit viel Geduld darüber wacht ob das Blumenbeet noch in Ordnung ist.

*Opa Willi*: *Oma Leni* und du, ihr habt mich auf der einen Seite immer unterstützt weiter zu machen, mir aber auch immer das Gefühl gegeben, dass ich mich durch Rückschläge nicht entmutigen lassen muss.

*Alberto*, I am so happy to have you at my side, thank you so much for all your support especially during the final phase of my PhD and my future path. Thank you for being this wonderful person in my life and for sharing the same views on life. Estoy ansiosa por saber adónde nos llevará la vida y espero poder descubrirlo juntos. *Juani y Juan*, gracias por una gran bienvenida en vuestra familia, ha sido un gran placer conoceros y aprender todas esas nuevas palabras de Extremadura. Gracias también a *Raquel y David* por vuestra hospitalidad.

Meine lieben Großeltern, *Oma Margarete* und *Opa Helmut*, die nicht ihr mehr bei uns seid: Ihr habt mein Leben geprägt, mir Wichtiges mit auf den Weg gegeben und ich werde euch mein ganzes Leben lang vermissen.

Ein altes Sprichwort besagt, man solle seinen Kindern Wurzeln und Flügel geben. *Mama und Papa*, ihr habt sogar viel mehr als das getan. Flugstunden habt ihr mir gleich mit dazu gegeben und mir gezeigt wie ich selbst navigieren kann. Damit ich meiner Wege ziehen kann und ab und an nach Hause zurückfinde. Euer Vertrauen hat mir Mut gegeben vieles aus zu probieren und dies wird mich mein ganzes Leben lang begleiten. Nur ihr wisst wie viel mir dies bedeutet und wie dankbar ich euch für alles bin.



## About the author

The author was born in Witten, Germany. She completed her High School at the Schiller-Gymnasium Witten. During this time, she spent a High school year (2006/2007) abroad in Scotland and Norway. After the Abitur, she came to the Netherlands to study Natural Sciences and Chemistry at the Radboud University, Nijmegen. To broaden her perspective, she participated in the Interdisciplinary Honours Programme with courses on philosophy, psychology and a think tank on scientific integrity and valorisation. She was active in the participation committees and study association Leonardo da Vinci. For her Master's programme, she came to Wageningen University, where she completed the Master Molecular Life Sciences with a Minor in Environmental Sciences in 2015. Her MSc thesis she completed at the Laboratory of Biophysics under supervision of Dr. Henk Van As. For her MSc research internship, she went for seven months to Prof. Zauscher's lab at Duke University in North Carolina, United States. During her Master programme, she worked on her PhD research proposal for ultra-high field MRI and MRS in collaboration with her PhD advisors. The proposal was submitted and was funded by Netherlands' Magnetic Resonance Research School. She started her PhD programme in January 2016 at the Laboratory of BioNanoTechnology and Laboratory of Biophysics under supervision of Prof. Aldrik Velders and Dr. Henk Van As. She spent a half-year PhD internship at the lab of Dr. Luisa Ciobanu at CEA/ Neurospin in France. The outcomes of the PhD research are presented in this thesis.





## List of Publications

K.E. Marusak, **J.R. Krug**, Y. Feng, Y. Cao, L. You, S. Zauscher, Bacterially driven cadmium sulfide precipitation on porous membranes: Toward platforms for photocatalytic applications. *Biointerphases*, 13(1), 011006 (2018).

L. Caizán-Juanarena\*, **J.R.Krug\***, F.J.Vergeldt, J.M. Kleijn, A.H. Velders, H. Van As, A.ter Heijne, 3D biofilm visualization and quantification on granular bioanodes with magnetic resonance imaging. *Water Research*, 115059 (2019) \*Shared first author

R. van Schadewijk, **J. R. Krug**, D. Shen, K. B. S. S. Gupta, F. J. Vergeldt, T. Bisseling, A. G. Webb, H. Van As, A. H. Velders, H. J. M. de Groot, A Alia, Magnetic Resonance Microscopy at Cellular Resolution and Localised Spectroscopy of *Medicago truncatula* at 22.3 Tesla, *Scientific Reports* 10, 1–11 (2020).

**J.R. Krug**, R. van Schadewijk, F.J. Vergeldt, A.G. Webb, H.J.M. de Groot, A Alia, H. Van As, A.H. Velders, Assessing spatial resolution, acquisition times and signal-to-noise ratios for commercial microimaging systems at 14.1, 17.6 and 22.3 T, *manuscript submitted*

R. van Schadewijk, R., **J. R. Krug.**, A. G. Webb., H. Van As, A. H. Velders, H. J. M. de Groot, A Alia, Magnetic Resonance Microscopy using Microcoils at 22 T: Coil Performance Calibration and Usage Demonstrated on *Medicago sativa* Roots, *under review at Journal of Visualized Experiments*

C.M. Kirkland, **J.R.Krug**, F.J. Vergeldt, L. van den Berg, A.H. Velders, J.D. Seymour, S.L. Codd, H. Van As, M.K. de Kreuk, Characterizing the structure of aerobic granular sludge using magnetic resonance, *manuscript submitted*

**J.R. Krug**, S. Bardin, H. Lambers, H. Van As, A. H. Velders, C. Faber, F. Boumezbeur, L. Ciobanu, Metabolic Specificity Analysis of CEST-techniques at ultra-high magnetic field strengths, *manuscript in preparation*





*Netherlands Research School for the  
Socio-Economic and Natural Sciences of the Environment*

# D I P L O M A

*for specialised PhD training*

The Netherlands research school for the  
Socio-Economic and Natural Sciences of the Environment  
(SENSE) declares that

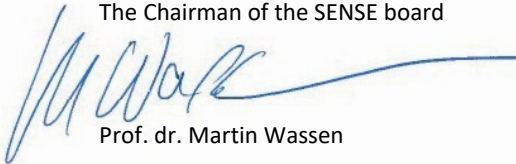
***Julia Ramona Krug***

born on 18 September 1990 in Witten, Germany

has successfully fulfilled all requirements of the  
educational PhD programme of SENSE.

Wageningen, 24 April 2020

The Chairman of the SENSE board



Prof. dr. Martin Wassen

the SENSE Director of Education



Dr. Ad van Dommelen

*The SENSE Research School has been accredited by the Royal Netherlands Academy of Arts and Sciences (KNAW)*



K O N I N K L I J K E N E D E R L A N D S E  
A K A D E M I E V A N W E T E N S C H A P P E N





The SENSE Research School declares that **Julia Ramona Krug** has successfully fulfilled all requirements of the educational PhD programme of SENSE with a work load of 44.8 EC, including the following activities:

#### SENSE PhD Courses

- o Environmental research in context (2016)
- o Research in context activity: 'Communicating science projects: Physics with Industry (2018) and Art meets Science in Cross-Pollination (2018)'

#### Other PhD and Advanced MSc Courses

- o Interpersonal communication, Wageningen University (2016)
- o Effective behaviour in your professional surroundings, Wageningen University (2016)
- o Media Training, Wageningen University (2018)
- o Efficient Writing Strategies, Wageningen University (2018)
- o Project and Time Management, Wageningen University (2018)

#### External training

- o *In Vivo* NMR course, AMC Amsterdam, The Netherlands (2016)
- o RF coil course, ESMRMB, Italy and *In Vivo* MR Spectroscopy, ESMRMB, Austria (2016)
- o Programming in ParaVision, Bruker, Germany (2018)
- o Research internship on CEST-MRI techniques at CEA/Neurospin, France (2019)

#### Selection of Management and Didactic Skills Training

- o Organisation committee National PhD Day, Promovendi Network Netherland (2018)
- o Supervising BSc student with thesis 'Monitoring chemical reactions and solute diffusion inside agarose based hydrogels using Molecular and Spatially Resolved Imaging Techniques' (2017)
- o Assisting practicals of the BSc/MSc courses 'Nanomedicine' (2016-2019) and the MSc course 'Advances in Magnetic Resonance' (2016-2018)
- o Lecturer in the BSc/MSc course 'Biophysical imaging' (2016-2018)
- o Lecturer PhD course '*In vivo* NMR' (2018)

#### Selection of Oral Presentations

- o *Improving detection limits by using a 22 T magnet and microcoils*, EUROMAR 2018, 1-5 July 2018, Nantes, France
- o *Metabolic Specificity Analysis of CEST-techniques at (Ultra-)High Fields*. International conference on Magnetic Resonance Microscopy (ICMRM), 18-22 August 2019, Paris, France
- o *Ultra-high MRI and MRS: Opportunity and challenges for biological specimens*. EUROMAR/ISMAR, 25-30 August 2019, Berlin, Germany

SENSE coordinator PhD education

Dr. ir. Peter Vermeulen

This research was funded by the NWO-funded graduate school Netherlands' Magnetic Resonance Research School [022.005.029]. Financial support from Wageningen University for printing this thesis is gratefully acknowledged.

Cover designed by Alberto Belmonte Parra and the author

Printed by ProefschriftMaken ([www.proefschriftmaken.nl](http://www.proefschriftmaken.nl))

This thesis is printed on FCS certified paper.





